




12-2015

Solution and Surface Properties of Architecturally- and Compositionally-Complex Block Copolymers and their Binary Mixtures

Jesse Lawrence Davis

University of Tennessee - Knoxville, jdavi190@vols.utk.edu

Follow this and additional works at: https://trace.tennessee.edu/utk_graddiss

 Part of the [Materials Chemistry Commons](#), [Nanoscience and Nanotechnology Commons](#), [Polymer and Organic Materials Commons](#), [Polymer Chemistry Commons](#), and the [Polymer Science Commons](#)

Recommended Citation

Davis, Jesse Lawrence, "Solution and Surface Properties of Architecturally- and Compositionally-Complex Block Copolymers and their Binary Mixtures. " PhD diss., University of Tennessee, 2015.
https://trace.tennessee.edu/utk_graddiss/3570

This Dissertation is brought to you for free and open access by the Graduate School at TRACE: Tennessee Research and Creative Exchange. It has been accepted for inclusion in Doctoral Dissertations by an authorized administrator of TRACE: Tennessee Research and Creative Exchange. For more information, please contact trace@utk.edu.

To the Graduate Council:

I am submitting herewith a dissertation written by Jesse Lawrence Davis entitled "Solution and Surface Properties of Architecturally- and Compositionally-Complex Block Copolymers and their Binary Mixtures." I have examined the final electronic copy of this dissertation for form and content and recommend that it be accepted in partial fulfillment of the requirements for the degree of Doctor of Philosophy, with a major in Chemistry.

S. Michael Kilbey II, Major Professor

We have read this dissertation and recommend its acceptance:

Jimmy W. Mays, Ziling Xue, Andy Sarles

Accepted for the Council:

Carolyn R. Hodges

Vice Provost and Dean of the Graduate School

(Original signatures are on file with official student records.)

**Solution and Surface Properties of Architecturally- and Compositionally-
Complex Block Copolymers and their Binary Mixtures**

A Dissertation Presented for the

Doctor of Philosophy

Degree

The University of Tennessee, Knoxville

Jesse Lawrence Davis

December 2015

Copyright © 2015 by Jesse L. Davis

Dedication

*This dissertation is dedicated to my loving parents, Eugene and Noelyn Davis, my fiancée
April Stephens, and my brothers, Jason and Joel Davis.*

Acknowledgements

I would like to extend my everlasting gratitude to my advisor, Prof. S. Michael Kilbey II, for molding me into a responsible researcher and citizen of the scientific community. His well-balanced guidance and mentorship has been instrumental in my development as a materials scientist here at The University of Tennessee.

I would also like to acknowledge a number of family members, friends, and colleagues who have supported and encouraged me during my Ph.D. studies at The University of Tennessee. First, I thank my fiancée April Stephens and my parents, Noelyn and Eugene Davis, for their encouragement and unconditional love. Each of you are special to me, and your love has been a steady source of inspiration and support. I appreciate my parents for having sacrificed personal life goals in order to see me attain my goals in life. From the early morning training sessions to the late night tutoring and private lessons, I have seen the fruit of their investment in my brothers and me. I would also like to extend my gratitude to my brother Jason, who himself is going through the Ph.D. process at Georgia Regents University, my youngest brother Joel, and my cousin Vanessa Davis for their support, love and encouragement. My colleague and life-long friend William Michael Kochemba has provided me with great inspiration throughout my early years in graduate school.

Special thanks go to Suk-kyun Ahn, David Uhrig, Brad Lokitz, and Juan Pablo Hinestrosa of Oak Ridge National Laboratory for their mentorship, insight and advice on a broad range of scientific questions and proposals. Professor Paul Russo is thanked for helpful light scattering discussions. Dr. John Dunlap of the Advanced Microscopy and Imaging Center at The

University of Tennessee-Knoxville is gratefully acknowledged for his assistance with transmission electron microscopy studies. I truly thank Dr. Xu Wang for the considerable role he played in teaching me to critically analyze every scientific problem and demonstrating how to develop excellent and careful scientific techniques. His hard work and brilliance will always be remembered.

Finally, I am grateful to all of the members (past and present) of the Kilbey research group for their friendship, support, advice, and engaging conversations. These members include Juan Pablo Hinestrosa, Chaitra Deodhar, Camile Kite, William Michael Kochemba, Kamlesh Bornani, Bethany Aden, Zach Seibers, Xu Wang, Graham Collier, Rachel Ramirez, Jiadi Hou, and Dayton Street. This work would not be possible without the financial support from the National Science Foundation and the U.S. Army Research Office.

Abstract

The spontaneous generation of complex structures from polymeric building blocks provides a simple yet effective route to create useful soft matter structures having potential application in a variety of nanotechnologies. The topology, chemical structure, block composition, and sequence of the constituent building blocks of polymers are tunable through synthetic chemistry. This tunability offers attractive opportunities to generate complex, yet well-defined structures with control over the geometry, packing symmetry, and microdomain structure. This thesis work involves the study of the self-assembly behaviors of architecturally complex amphiphilic block copolymers (ABCs). ABCs are composed of two or more chemically distinct blocks that are covalently bonded together. Because of the thermodynamic incompatibility between the blocks, they self-organize through microphase separation. Systems studied include multiblock linear copolymers, star-like copolymers and graft copolymers.

The self-assembly behaviors of polystyrene-poly(2-vinylpyridine) (PS-PVP) block copolymers have been systematically investigated in solution and in thin films. Binary mixtures containing linear diblock and triblock copolymers of different block lengths and star block copolymers having different numbers of constituent arms and composition were also investigated. In general, the ensembles that consist of monomodal PS-PVP block copolymers exhibit simple nanoparticle-like structures. In contrast, binary mixtures of PS-PVP block copolymers with different component architectures produce a wider variety of micellar aggregates, including particle-like, worm-like and hierarchical structures, owing to the complex architecture-induced diversity of microphase segregation behaviors in the mixed systems.

In addition to studies of copolymer mixtures, the links between sequence, and composition on the self-assembly properties of a series of PLA-PEG containing bottlebrush copolymers were investigated in solution. It is found that the composition and sequence of the side-chains dictated the stability, thermodynamics, and size of micelle formation.

These studies clarify the self-assembly properties of ABCs and provide new insights into how micellar structures can be controlled by tuning macromolecular architecture, sequence, and polymer composition, as well as, in the case of mixtures, blend ratio. This work is expected to be valuable for understanding the self-assembly of complex copolymeric systems, which may find use in a variety of applications ranging from personalized medicine to environmental remediation, and lays the groundwork for self-assembly processing.

Table of Contents

Chapter 1: Introduction	1
1.1 Self-assembly of amphiphilic block copolymers	2
1.2 Motivation.....	4
1.3 Polymer design as a tool to tune self-assembly properties	7
1.4 Models of behavior of micellar systems	11
1.5 Research objectives.....	15
Chapter 2: Experimental and Theoretical Considerations of Dynamic and Static Light Scattering	
Characterization Techniques.....	22
2.1 Static light scattering.....	23
2.2 Dynamic light scattering	27
2.3 Cleaning techniques	31
2.4 Data analysis	32
Chapter 3: Control of Self-Assembled Structure through Architecturally and Compositionally	
Complex Block Copolymer Surfactant Mixtures	41
3.1 Abstract.....	42
3.2 Introduction.....	43
3.3 Experimental.....	46
3.3.1 Materials.	46
3.3.2 BCP preparation.....	47
3.3.3 Film preparation.....	49

3.3.4 Characterization	49
3.4 Results and discussion	51
3.4.1 Self-assembly of BCPs in solution.	51
3.4.2 BCP assemblies in thin films.	56
3.4.3 Compositionally complex binary BCP mixtures.	70
3.5 Conclusions.....	76
Chapter 4: Solution Properties of Architecturally Complex Multiarm Star Diblock Copolymers in	
Non-selective and Selective Solvents for the Inner Block.....	77
4.1 Abstract.....	78
4.2 Introduction.....	79
4.3 Experimental	83
4.3.1 Materials	83
4.3.2 Block copolymer solution preparation.....	84
4.3.3 Characterization by light scattering and theory	86
4.3.4 Characterization by transmission electron microscopy	86
4.4 Results and discussion	87
4.4.1 Hydrodynamics of architecturally and compositionally diverse star copolymers	87
4.4.2 Concentration study	95
4.4.3 TEM.....	99
4.5 Conclusions.....	103
Chapter 5: Effects of Sequence and Composition on the Self-assembly of Poly(lactic acid)-	
Poly(ethylene glycol) Bottlebrush Copolymers.....	104

5.1 Abstract	105
5.2 Introduction.....	106
5.3 Experimental	108
5.3.1 Materials	108
5.3.2 Materials synthesis.....	109
5.3.3 Methods and characterization	110
5.4 Results and Discussions.....	111
5.4.1 Synthesis of bottlebrush copolymers	111
5.4.2 Effect of composition and concentration on self-assembly in solution	114
5.4.3 Effect of sequence on self-assembly.....	125
5.4.4 Self-assembly in aqueous solution.....	130
5.5 Conclusions.....	136
Chapter 6: Summary, Conclusions and Future Work	138
6.1 Summary and conclusions	139
6.2 Future work.....	143
List of References	146
Appendices.....	170
Appendix A - Chapter 3: Control of Self-Assembled Structure through Architecturally and Compositionally Complex Block Copolymer Surfactant Mixtures.....	171
Appendix B - Chapter 4: Solution Properties of Architecturally Complex Multiarm Star Diblock Copolymers in Non-selective and Selective Solvents for the Inner Block.....	196

Appendix C - Chapter 5: Effects of Sequence and Composition on the Self-assembly of
Poly(lactic acid)-Poly(ethylene glycol) Bottlebrush Copolymers203
Vita.....214

List of Tables

Table 1-1. Molecular characteristics of architecturally- and compositionally-complex ABCs....	17
Table 1-2. Molecular characteristics of bottlebrush copolymers.....	18
Table 3-1. Molecular characteristics and self-assembly properties of surfactant-like PS-PVP BCPs in toluene.....	48
Table 3-2. Mixing strategy by varying component architecture and self-assembly properties of PS–PVP BCP mixtures at a mixing ratio of 1:1 (by weight) in toluene solutions and in thin film form.....	61
Table 3-3. Mixing strategy by varying blend composition.....	74
Table 4-1. Macromolecular properties of 26- and 40-arm star diblock copolymers.	85
Table 4-2. Static light scattering results for 26- and 40-arm star diblock copolymers.	94
Table 4-3. Hydrodynamic and frictional interactions for 26- and 40-arm star diblock copolymers.	98
Table 5-1. Molecular characteristics of PLA-PEG bottlebrush copolymers, where r indicates random and b indicates a block copolymer and their macromonomers.....	112
Table 5-2. Hydrodynamic sizes of PLA-PEG bottlebrush copolymers in methanol as a function of concentration.	118

Table 5-3. Hydrodynamic radii of PLA-PEG random and block bottlebrush copolymers in water as a function of copolymer design and concentration..... 133

Table A-1. Hydrodynamic radii of PS-PVP block copolymer mixtures (polymer I:polymer II = 1:1, w:w) in toluene at a concentration of 1.0 mg/mL..... 195

List of Figures

Figure 1-1. Microphase separation of polystyrene-block-poly(2-vinylpyridine) (PS-PVP) in a selective solvent, which in this case is thermodynamically good for PS blocks but a poor solvent for PVP blocks.	3
Figure 1-2. Traditional morphologies accessed from the self-assembly of diblock copolymers in a solvent that is selective for the red block above the CMC. From left to right micelles comprised of diblock copolymers mainly form spheres, rods, or vesicles.	6
Figure 1-3. Schematic showing behavior of systems that follow the closed association model, represented in a plot of inverse micellar molecular weight, $(M_{w,mic})^{-1}$ versus concentration, c , in a thermodynamically good solvent for the red block. Zone I consists of only free chains in solution. Zone II displays coexistence between free chains and aggregates in solution. Zone III is marked by a shift in the equilibrium toward the self-assembled aggregates. Concept for figure was taken from Voulgaris <i>et al.</i> ⁵⁸	13
Figure 2-1. Scheme showing (A) the scattering volume that is as a result of the angle, θ , between I_o (\vec{K}_i) and the optical aperture used for observing, I_s , (\vec{K}_f) and (B) a diagram of the definition of the scattering wave vector $\vec{q} = \vec{K}_f - \vec{K}_i$. ⁶¹	24
Figure 2-2. Scheme showing the intensities of the standard, solvent, and solution as a functions of time, t . In SLS, only the excess scattering intensity is taken into consideration during the measurement of the solution in question.	25

Figure 2-3. Schematic showing the intensity fluctuations (blue line) and the corresponding autocorrelation function. The solid black line models the average intensity, which is used in SLS. ⁶³	28
Figure 2-4. Screen shot of ALV_SLS.exe program written in Visual Basic by Dr. Masashi Osa.	34
Figure 2-5. Screen shot of ALV_SLS.exe program after analysis of input data at a specific concentration and 16 different angles.	36
Figure 2-6. Screen shot of ALV_DLS.exe software package with model results from the first detector.....	37
Figure 2-7. Screen shot of the input window for the ALV_Gamma_vs_q.exe software program.	39
Figure 3-1. Light intensity autocorrelation functions (a), hydrodynamic radii, R_h , distributions (b) and apparent diffusion coefficient D_{app} versus q^2 (c) for sample T1 in toluene. Insets in (a) are the chemical structures of styrene (left) and 2-vinylpyridine (right).....	52
Figure 3-2. AFM height images ($2 \mu\text{m} \times 2 \mu\text{m}$) of BCP films. The sample IDs correspond to Table 3-1. Brighter areas are higher than darker areas. The Z scale is 15 nm for D1, T1, S1, S4, and S7, and 3 nm for the other images.....	56
Figure 3-3. Horizontal radius (a) and vertical height (b) of the microdomains, and RMS roughness values calculated for the films (c) as a function of S/V ratio. Error bars are computed from the standard deviation of replicate measurements ($n = 3$ for roughness and $n = 20$ for radius and height).	58

Figure 3-4. AFM height images ($2\ \mu\text{m} \times 2\ \mu\text{m}$) of the films of BCP mixtures of D1+T1 (a), D1+S1 (b), D1+T2 (c), D1+S2 (d), D1+T3 (e), D1+S3 (f), D1+S4 (g) and D1+S7 (h) at a mixing ratio of 1:1 by weight. The Z scale is 15 nm for (a, b), 5 nm for (c, d, e, and f), and 20 nm for (g, h). 63

Figure 3-5. AFM height images ($2\ \mu\text{m} \times 2\ \mu\text{m}$) of the films of triblock/star copolymer mixtures of T1+S1 (a), T1+S4 (b), T1+S7 (c), S1+T2 (d), T1+S2 (e), S1+T3 (f) and T1+S3 (g) at a mixing ratio of 1:1 by weight. The Z scale is 15 nm for (a-d) and 40 nm for (e-g). (h) TEM image of the film in (g) with PVP blocks stained by iodine vapor, the inset is the large area TEM image..... 66

Figure 3-6. (a-c) Cryo-TEM images of the BCP mixtures of D1+T1 (a), D1+S1 (b) and T1+S3 (c) at a mixing ratio of 1:1 by weight in toluene. The scale bar is 200 nm. 69

Figure 3-7. AFM height images ($2\ \mu\text{m} \times 2\ \mu\text{m}$) of the films of BCP mixtures of D1+T1 (a, b), D1+S1 (c, d) and T1+S3 (e, f) at mixing ratios of 3:1 (a, c, e) and 1:3 (b, d, f) by weight. The Z scale is 15 nm for (a-d) and 40 nm for (e, f). 72

Figure 3-8. (a) Horizontal radius and vertical height of the microdomains in the films of D1+T1 BCP mixtures as a function of the mass fraction of T1. The error bars reflect the standard deviation of replicate measurements ($n = 20$). (b) Dependence of film morphologies of three typical BCP mixtures as a function of the mass composition of the blended BCPs..... 75

Figure 4-1. (A) Light intensity autocorrelation functions for the 26-arm stars and (B) the 40-arm stars in toluene at $c = 2.5\ \text{mg/mL}$ at a scattering angle of 88° . (C) Apparent hydrodynamic radii, R_h , distributions for the 26-arm stars and (D) the 40-arm stars at $c = 2.5\ \text{mg/mL}$ and a scattering

angle of 88° . The colors and symbols are assigned and used consistently in other plots presenting data from DLS measurements in toluene. Concentrations are nominal values. 88

Figure 4-2. Mean decay rates, Γ , versus q^2 for the (A) 26-arm stars in toluene at $c = 2.5$ mg/mL and for the (B) 40-arm stars in toluene at $c = 2.5$ mg/mL. For plots (A) and (B) the solution diffusion coefficient, D_s , is obtained from the slope of the best-fit lines. The data, when recast as Γ/q^2 versus q^2 , allow $\langle D \rangle_z$ to be obtained for the (C) 26-arm stars in toluene at $c = 2.5$ mg/mL and the (D) 40-arm stars in toluene at $c = 2.5$ mg/mL by extrapolating the best fit line to $q^2 = 0$. The dependence of Γ/q^2 with respect to q^2 for all samples suggests that in a selective solvent for the inner block, the star diblock copolymers do not behave as hard spheres. Concentrations are nominal values. 91

Figure 4-3. Zimm plots for star $[\text{PS}_{103.8}\text{-PVP}_{11.5}]_{26}$ in toluene, a selective solvent for the inner PS blocks (left), and in THF, a non-selective good solvent (right). Properties determined from the extrapolations to zero scattering angle, $q^2 = 0$, and to zero concentration, $c = 0$ are set above each Zimm plot..... 93

Figure 4-4. Dependence of R_h on concentration for 26- and 40-arm stars in toluene (A). Dependence of $\langle D \rangle_z$ on concentration for 26- and 40-arm stars in toluene (B). Comparison of the concentration dependence of R_h for samples $[\text{PS}_{103.8}\text{-PVP}_{11.5}]_{26}$ and $[\text{PS}_{106.3}\text{-PVP}_{21.3}]_{40}$ in toluene and THF (C), the concentration dependence of R_g for 26- and 40-arm stars in toluene (D). (Solid lines in (B) are fits to the data obtained from equation 2.17 while the dashed lines in (A), (C) and (D) are trend lines to guide the eye.) 97

Figure 4-5. TEM images of (A) the 40-arm star $[\text{PS}_{53.8}\text{-PVP}_{53.8}]_{40}$, and (B) the 26-arm star $[\text{PS}_{50}\text{-PVP}_{50}]_{26}$ drop cast from toluene solutions with PVP blocks stained by iodine vapor. TEM image

of (C) [PS_{53.8}-PVP_{53.8}]₄₀ drop cast from toluene solution with both PS and PVP blocks stained using RuO₄. TEM image of doubly-stained (D) [PS_{53.8}-PVP_{53.8}]₄₀ deposited from a toluene solution containing gold (III), which coordinates with PVP blocks. The dried film is subsequently exposed to RuO₄ vapors. This double staining method renders the PVP blocks appear darker than the PS blocks, as described in text. Based on this series of images, a drawing (inset) of how the stars rearrange in toluene, a selective solvent for the PS (red) blocks, is developed. 102

Figure 5-1. Results from DLS measurements on *g*-[PLA₄₁-*r*-PEG₅₉], including (A) normalized light intensity autocorrelation function for *g*-[PLA₄₁-*r*-PEG₅₉] and the corresponding (B) normalized amplitude distribution of decay rates. In plots (C) and (D), D_{app} is obtained by extrapolating the best fit line through the data cast as Γ/q^2 versus q^2 to $q^2 = 0$. Resulting apparent R_h values are presented in Table 5-2. 116

Figure 5-2. Representative TEM image showing aggregates formed from *g*-[PLA₄₁-*r*-PEG₅₉] at (A) 5.0 mg/mL, and (B) and (C) cryo-TEM images acquired from solutions at 10.0 mg/mL in methanol at two different size scales. 117

Figure 5-3. (A) Normalized light intensity autocorrelation function and (B) normalized amplitude distribution of decay rates for *g*-[PLA₁₃-*r*-PEG₈₇] in methanol as a function of concentration. For plots (C) and (D), D_{app} is obtained by extrapolating the best fit line through data cast as Γ/q^2 versus q^2 to $q^2 = 0$. Resulting apparent R_h values are presented in Table 5-2. While a small population of larger scatterers seems to be present at 1.0 and 2.0 mg/mL, as described in the text,

careful data analysis at all scattering angles does not support the conclusion that both modes are, in fact, present. 121

Figure 5-4. Representative TEM images for g -[PLA₁₃- r -PEG₈₇] in methanol at (A) and (B) 5.0 mg/mL at two different image size scales and (C) a cryo-TEM image for g -[PLA₁₃- r -PEG₈₇] at 10.0 mg/mL. 122

Figure 5-5. (A) Light intensity autocorrelation function for g -[PLA₇- r -PEG₉₃] and (B) normalized amplitude distribution of decay rates. For plots (C) and (D), D_{app} for g -[PLA₇- r -PEG₉₃] is obtained by extrapolating the best fit line through the data cast as Γ/q^2 versus q^2 to $q^2 = 0$. The apparent hydrodynamic radii are given in Table 5-2. 124

Figure 5-6. Cryo-TEM images acquired from a region on a lacey carbon film grid where there was a high density of aggregates. Images (A) and (B) are acquired for g -[PLA₇- r -PEG₉₃] at 10.0 mg/mL in methanol. 125

Figure 5-7. (A) Light intensity autocorrelation functions for g -[PLA₃₆- b -PEG₆₄] at various concentrations in methanol, and (B) normalized amplitude distribution of decay rates, which suggest that micelles are formed at all of the concentrations studied. For plots (C), (D), (E) and (F), D_{app} is obtained by extrapolating the best fit line through the data cast as Γ/q^2 versus q^2 to $q^2 = 0$ for g -[PLA₃₆- b -PEG₆₄]. Values of $R_{h,app}$ are presented in Table 5-2. 129

Figure 5-8. TEM images for g -[PLA₃₆- b -PEG₆₄] in methanol at (A) 1.0 mg/mL (B) 2.0 mg/mL, (C) 5.0 mg/mL, and (D) 10.0 mg/mL. The large aggregates are large compound micelles and smaller aggregates are also observed. 130

Figure 5-9. (A) Normalized light intensity autocorrelation function, and (B) normalized amplitude distribution of decay rates for g -[PLA₄₁- r -PEG₅₉] at $c \approx 0.5$ mg/mL in water. (C) D_{app}

for g -[PLA₄₁- r -PEG₅₉] in aqueous solution at $c \approx 0.5$ mg/mL is obtained by extrapolating the best fit line through the data cast as Γ/q^2 versus q^2 to $q^2 = 0$. Data presented in (B) and (C) clearly indicate two populations of scatterers of different size. Values of $R_{h,app}$ are presented in Table 5-2..... 132

Figure 5-10. (A) Normalized light intensity autocorrelation function at five different concentrations for g -[PLA₁₃- r -PEG₈₇] in aqueous solution, and (B) normalized amplitude distribution of decay rates at five different concentrations for g -[PLA₁₃- r -PEG₈₇]. Both plots reflect similar behaviors at all concentrations studied..... 134

Figure 5-11. (A) Normalized light intensity autocorrelation function at three different concentrations for sample g -[PLA₇- r -PEG₉₃] in aqueous solution, and (B) normalized amplitude distribution of decay rates at three different concentrations for sample g -[PLA₇- r -PEG₉₃] in aqueous solution. The data reflect strong micellization behavior..... 136

Figure A-1. Light intensity autocorrelation function (a), hydrodynamic radii, R_h , distributions (b) and apparent diffusion coefficient D_{app} versus q^2 (c) for sample D1 in toluene at $c = 1.0$ mg/mL. 174

Figure A-2. Light intensity autocorrelation function (a), hydrodynamic radii, R_h , distributions (b) and apparent diffusion coefficient D_{app} versus q^2 (c) for sample D2 in toluene at $c = 1.0$ mg/mL. 174

Figure A-3. Light intensity autocorrelation function (a), hydrodynamic radii, R_h , distributions (b) and apparent diffusion coefficient D_{app} versus q^2 (c) for sample D3 in toluene at $c = 1.0$ mg/mL. 175

Figure A-4. Light intensity autocorrelation function (a, d), hydrodynamic radii, R_h , distributions (b, e) and apparent diffusion coefficient D_{app} versus q^2 (c, f) for sample T2 in toluene at $c = 1.0$ mg/mL (a, b, c) and at $c = 8.0$ mg/mL (d, e, f). 175

Figure A-5. Light intensity autocorrelation function (a, d), hydrodynamic radii, R_h , distributions (b, e) and apparent diffusion coefficient D_{app} versus q^2 (c, f) for sample T3 in toluene at $c = 1.0$ mg/mL (a, b, c) and at $c = 8.0$ mg/mL (d, e, f). 176

Figure A-6. Light intensity autocorrelation function (a, d), hydrodynamic radii, R_h , distributions (b, e) and apparent diffusion coefficient D_{app} versus q^2 (c, f) for sample S1 in toluene at $c = 1.0$ mg/mL (a, b, c) and at $c = 8.0$ mg/mL (d, e, f). 177

Figure A-7. Light intensity autocorrelation function (a, d), hydrodynamic radii, R_h , distributions (b, e) and apparent diffusion coefficient D_{app} versus q^2 (c, f) for sample S2 in toluene at $c = 1.0$ mg/mL (a, b, c) and at $c = 8.0$ mg/mL (d, e, f). 178

Figure A-8. Light intensity autocorrelation function (a, d), hydrodynamic radii, R_h , distributions (b, e) and apparent diffusion coefficient D_{app} versus q^2 (c, f) for sample S3 in toluene at $c = 1.0$ mg/mL (a, b, c) and at $c = 8.0$ mg/mL (d, e, f). 179

Figure A-9. Light intensity autocorrelation function (a), hydrodynamic radii, R_h , distributions (b) and apparent diffusion coefficient D_{app} versus q^2 (c) for sample S4 in toluene at $c = 1.0$ mg/mL. 180

Figure A-10. Light intensity autocorrelation function (a), hydrodynamic radii, R_h , distributions (b) and apparent diffusion coefficient D_{app} versus q^2 (c) for sample S5 in toluene at $c = 1.0$ mg/mL. 180

Figure A-11. Light intensity autocorrelation function (a), hydrodynamic radii, R_h , distributions (b) and apparent diffusion coefficient D_{app} versus q^2 (c) for sample S6 in toluene at $c = 1.0$ mg/mL..... 181

Figure A-12. Light intensity autocorrelation function (a), hydrodynamic radii, R_h , distributions (b) and apparent diffusion coefficient D_{app} versus q^2 (c) for sample S7 in toluene at $c = 1.0$ mg/mL..... 181

Figure A-13. Light intensity autocorrelation function (a), hydrodynamic radii, R_h , distributions (b) and apparent diffusion coefficient D_{app} versus q^2 (c) for sample S8 in toluene at $c = 1.0$ mg/mL..... 182

Figure A-14. Light intensity autocorrelation function (a), hydrodynamic radii, R_h , distributions (b) and apparent diffusion coefficient D_{app} versus q^2 (c) for sample S9 in toluene at $c = 1.0$ mg/mL..... 182

Figure A-15. Light intensity autocorrelation function (a), hydrodynamic radii, R_h , distributions (b) and apparent diffusion coefficient D_{app} versus q^2 (c) for mixture D1+T1 in toluene at $c = 8.0$ mg/mL..... 183

Figure A-16. Light intensity autocorrelation function (a), hydrodynamic radii, R_h , distributions (b) and apparent diffusion coefficient D_{app} versus q^2 (c) for mixture D1+T2 in toluene at $c = 8.0$ mg/mL..... 183

Figure A-17. Light intensity autocorrelation function (a), hydrodynamic radii, R_h , distributions (b) and apparent diffusion coefficient D_{app} versus q^2 (c) for mixture D1+T3 in toluene at $c = 8.0$ mg/mL..... 184

Figure A-18. Light intensity autocorrelation function (a), hydrodynamic radii, R_h , distributions (b) and apparent diffusion coefficient D_{app} versus q^2 (c) for mixture D1+S1 in toluene at $c = 8.0$ mg/mL..... 184

Figure A-19. Light intensity autocorrelation function (a), hydrodynamic radii, R_h , distributions (b) and apparent diffusion coefficient D_{app} versus q^2 (c) for mixture D1+S2 in toluene at $c = 8.0$ mg/mL..... 185

Figure A-20. Light intensity autocorrelation function (a), hydrodynamic radii, R_h , distributions (b) and apparent diffusion coefficient D_{app} versus q^2 (c) for mixture D1+S3 in toluene at $c = 8.0$ mg/mL..... 185

Figure A-21. Light intensity autocorrelation function (a), hydrodynamic radii, R_h , distributions (b) and apparent diffusion coefficient D_{app} versus q^2 (c) for mixture D1+S4 in toluene at $c = 8.0$ mg/mL..... 186

Figure A-22. Light intensity autocorrelation function (a), hydrodynamic radii, R_h , distributions (b) and apparent diffusion coefficient D_{app} versus q^2 (c) for mixture D1+S7 in toluene at $c = 8.0$ mg/mL..... 186

Figure A-23. Light intensity autocorrelation function (a), hydrodynamic radii, R_h , distributions (b) and apparent diffusion coefficient D_{app} versus q^2 (c) for mixture T1+S1 in toluene at $c = 8.0$ mg/mL..... 187

Figure A-24. Light intensity autocorrelation function (a), hydrodynamic radii, R_h , distributions (b) and apparent diffusion coefficient D_{app} versus q^2 (c) for mixture T1+S2 in toluene at $c = 8.0$ mg/mL..... 187

Figure A-25. Light intensity autocorrelation function (a), hydrodynamic radii, R_h , distributions (b) and apparent diffusion coefficient D_{app} versus q^2 (c) for mixture T1+S3 in toluene at $c = 8.0$ mg/mL..... 188

Figure A-26. Light intensity autocorrelation function (a), hydrodynamic radii, R_h , distributions (b) and apparent diffusion coefficient D_{app} versus q^2 (c) for mixture T1+S4 in toluene at $c = 8.0$ mg/mL..... 188

Figure A-27. Light intensity autocorrelation function (a), hydrodynamic radii, R_h , distributions (b) and apparent diffusion coefficient D_{app} versus q^2 (c) for mixture T1+S7 in toluene at $c = 8.0$ mg/mL..... 189

Figure A-28. Light intensity autocorrelation function (a), hydrodynamic radii, R_h , distributions (b) and apparent diffusion coefficient D_{app} versus q^2 (c) for mixture S1+T2 in toluene at $c = 8.0$ mg/mL..... 189

Figure A-29. Light intensity autocorrelation function (a), hydrodynamic radii, R_h , distributions (b) and apparent diffusion coefficient D_{app} versus q^2 (c) for mixture S1+T3 in toluene at $c = 8.0$ mg/mL..... 190

Figure A-30. Light intensity autocorrelation function (a), hydrodynamic radii, R_h , distributions (b) and apparent diffusion coefficient D_{app} versus q^2 (c) for sample T1 in THF at $c = 1.0$ mg/mL. 190

Figure A-31. Light intensity autocorrelation function (a), hydrodynamic radii, R_h , distributions (b) and apparent diffusion coefficient D_{app} versus q^2 (c) for sample S1 in THF at $c = 0.5$ mg/mL. 191

Figure A-32. Light intensity autocorrelation function (a), hydrodynamic radii, R_h , distributions (b) and apparent diffusion coefficient D_{app} versus q^2 (c) for sample S6 in THF at $c = 0.5$ mg/mL.	191
Figure A-33. Light intensity autocorrelation function (a), hydrodynamic radii, R_h , distributions (b) and apparent diffusion coefficient D_{app} versus q^2 (c) for sample S8 in THF at $c = 0.5$ mg/mL.	192
Figure A-34. 3D AFM image of disperse micelles made by drop-casting from S7 toluene solution at $c = 3.0$ μ g/mL on a silicon substrate.	192
Figure A-35. AFM height (a) and phase (b) images ($10 \mu\text{m} \times 10 \mu\text{m}$) of the film made from T1+S2 block copolymer mixture at a mixing ratio of 1:1 by weight.....	193
Figure A-36. AFM height (a) and phase (b) images ($10 \mu\text{m} \times 10 \mu\text{m}$) of the film made from S1+T3 block copolymer mixture at a mixing ratio of 1:1 by weight.....	193
Figure A-37. AFM height (a) and phase (b) images ($10 \mu\text{m} \times 10 \mu\text{m}$) of the film made from T1+S3 block copolymer mixture at a mixing ratio of 3:1 by weight.....	194
Figure B-1. Zimm plot for $[\text{PS}_{50}\text{-PVP}_{50}]_{26}$ in toluene, a selective solvent for the inner PS block. Properties determined from the extrapolations to zero scattering angle, $q^2 = 0$, and to zero concentration, $c = 0$, are set above the Zimm plot.	197
Figure B-2. Zimm plot for $[\text{PS}_{102.5}\text{-PVP}_{20.5}]_{26}$ in toluene, a selective solvent for the inner PS block. Properties determined from the extrapolations to zero scattering angle, $q^2 = 0$, and to zero concentration, $c = 0$, are set above the Zimm plot.	198

Figure B-3. Zimm plot for [PS_{53.8}-PVP_{53.8}]₄₀ in toluene, a selective solvent for the inner PS block. Properties determined from the extrapolations to zero scattering angle, $q^2 = 0$, and to zero concentration, $c = 0$, are set above the Zimm plot. 199

Figure B-4. Zimm plot for sample [PS_{106.3}-PVP_{21.3}]₄₀ in toluene, a selective solvent for the inner block (top), and THF a non-selective solvent (bottom), with results from the extrapolation to zero scattering angle, $q^2 = 0$, and zero concentration, $c = 0$, are set above the Zimm plot..... 200

Figure B-5. Zimm plot for [PS₁₀₈-PVP₁₂]₄₀ in toluene, a selective solvent for the inner PS block. Properties determined from the extrapolations to zero scattering angle, $q^2 = 0$, and to zero concentration, $c = 0$, are set above the Zimm plot. 201

Figure B-6. These two images show a comparison of the morphology of the 40-arm star [PS_{53.8}-PVP_{53.8}]₄₀ from THF solution (a thermodynamically good solvent for both blocks) obtained from two different staining techniques. (A) TEM image of the 40-arm star [PS_{53.8}-PVP_{53.8}]₄₀ drop cast from a THF solution with both PS and PVP blocks stained with RuO₄. Here, RuO₄ stains the double bonds in the PS and PVP blocks allowing the entire structure on the copper supported carbon film TEM grid to be imaged. (B) TEM image of the 40-arm star [PS_{53.8}-PVP_{53.8}]₄₀ drop cast from THF solution with only the PVP blocks stained by iodine vapor..... 202

Figure C-1. Zimm plot produced from SLS measurements on sample *g*-[PLA₄₁-*r*-PEG₅₉] in DMF, a non-selective good solvent, at three different concentrations ($c = 1.0, 3.0,$ and 9.0 mg/mL). Set below the plot are results from the extrapolation to zero scattering angle, $q^2 = 0$, and zero concentration, $c = 0$. $M_w(c)$ is the molecular weight that is calculated from extrapolation to

$c = 0$ and $M_w(q^2)$ is the molecular weight that is calculated from the extrapolation to $q^2 = 0$. Concentrations are nominal values. 204

Figure C-2. (A) Normalized light intensity autocorrelation function and (B) normalized amplitude distribution of decay rates for g -[PLA₄₁- r -PEG₅₉] in DMF at $c = 9.0$ mg/mL. (C) angularly-dependent characteristic decay rate, Γ , for g -[PLA₄₁- r -PEG₅₉] in DMF at $c = 9.0$ mg/mL, plotted as Γ/q^2 versus q^2 . Extrapolating the best fit line through the data to $q^2 = 0$ yields the z -average apparent diffusion coefficient, D_{app} . The numerical value of D_{app} is then substituted into the Stokes-Einstein equation to calculate $R_h = 9.0$ nm. Concentrations are nominal values. 205

Figure C-3. (A) Zimm plot produced from SLS measurements on sample g -[PLA₁₃- r -PEG₈₇] in DMF, a non-selective good solvent, at three different concentrations ($c = 1.0, 3.0,$ and 9.0 mg/mL). Set below the plot are results from the extrapolation to zero scattering angle, $q^2 = 0$, and zero concentration, $c = 0$. $M_w(c)$ is the molecular weight that is calculated from extrapolation to $c = 0$ and $M_w(q^2)$ is the molecular weight that is calculated from the extrapolation to $q^2 = 0$. Concentrations are nominal values. 206

Figure C-4. (A) Normalized light intensity autocorrelation function and (B) normalized amplitude distribution of decay rates for g -[PLA₁₃- r -PEG₈₇] in DMF at $c = 9.0$ mg/mL. (C) angularly-dependent characteristic decay rate, Γ , for g -[PLA₁₃- r -PEG₈₇] in DMF at $c = 9.0$ mg/mL, plotted as Γ/q^2 versus q^2 . Extrapolating the best fit line through the data to $q^2 = 0$ yields the z -average apparent diffusion coefficient, D_{app} . The numerical value of D_{app} is then substituted into the Stokes-Einstein equation to calculate $R_h = 9.0$ nm. Concentrations are nominal values. 207

Figure C-5. Zimm plot produced from SLS measurements on sample g -[PLA_{7- r} -PEG₉₃] in DMF, a non-selective good solvent, at three different concentrations ($c = 1.0, 3.0, \text{ and } 9.0 \text{ mg/mL}$). Set below the plot are results from the extrapolation to zero scattering angle, $q^2 = 0$, and zero concentration, $c = 0$. $M_w(c)$ is the molecular weight that is calculated from extrapolation to $c = 0$ and $M_w(q^2)$ is the molecular weight that is calculated from the extrapolation to $q^2 = 0$. Concentrations are nominal values. 208

Figure C-6. (A) Normalized light intensity autocorrelation function and (B) normalized amplitude distribution of decay rates for g -[PLA_{7- r} -PEG₉₃] in DMF at $c = 9.0 \text{ mg/mL}$. (C) angularly-dependent characteristic decay rate, Γ , for g -[PLA_{7- r} -PEG₉₃] in DMF at $c = 9.0 \text{ mg/mL}$, plotted as Γ/q^2 versus q^2 . Extrapolating the best fit line through the data to $q^2 = 0$ yields the z -average apparent diffusion coefficient, D_{app} . The numerical value of D_{app} is then substituted into the Stokes-Einstein equation to calculate $R_h = 9.0 \text{ nm}$. Concentrations are nominal values. 209

Figure C-7. (A) Normalized light intensity autocorrelation function and (B) normalized amplitude distribution of decay rates for g -[PLA_{36- b} -PEG₆₄] in aqueous solution at $c = 0.1 \text{ mg/mL}$. (C) angularly-dependent characteristic decay rate, Γ , for g -[PLA_{36- b} -PEG₆₄] in aqueous solution at $c = 0.1 \text{ mg/mL}$, plotted as Γ/q^2 versus q^2 . Extrapolating the best fit line through the data to $q^2 = 0$ yields the z -average apparent diffusion coefficient, D_{app} . Concentrations are nominal values. 210

Figure C-8. Plots showing the angular dependence of the characteristic decay rates, Γ , cast as Γ/q^2 versus q^2 . (A) g -[PLA_{13- r} -PEG₈₇] in MeOH at $c = 1.0 \text{ mg/mL}$. D_{app} is obtained by extrapolating the best fit lines through the data to $q^2 = 0$. From those intercepts, Stokes-Einstein

relation gives $R_{h,slow\ mode} = 12\text{ nm}$, and $R_{h,fast\ mode} = 150\text{ nm}$. (B) g -[PLA_{13-*r*}-PEG₈₇] in MeOH at $c = 2.0\text{ mg/mL}$. D_{app} is obtained by extrapolating the best fit line through the data to $q^2 = 0$, and the resulting D_{app} values give $R_{h,fast\ mode} = 8.0\text{ nm}$, and $R_{h,slow\ mode} = 270\text{ nm}$. Concentrations are nominal values. As explained in Chapter 5 (Section 5.4.2), the need to select only certain scattering angles to obtain R_h values for the slow mode that are (nearly) consistent with the size range suggested by the amplitude distribution function make it difficult to conclude that the second (slow) mode is real..... 211

Figure C-9. Plots showing the angular dependence of the characteristic decay rates, Γ , cast as Γ/q^2 versus q^2 for g -[PLA_{13-*r*}-PEG₈₇] in aqueous solution at (A) $c = 0.1\text{ mg/mL}$, (B) $c = 0.5\text{ mg/mL}$, (C) $c = 1.0\text{ mg/mL}$ (D) $c = 5.0\text{ mg/mL}$, and (E) $c = 10.0\text{ mg/mL}$. Concentrations are nominal values. 212

Figure C-10. Plots showing the angular dependence of the characteristic decay rates, Γ , cast as Γ/q^2 versus q^2 for g -[PLA_{7-*r*}-PEG₉₃] in aqueous solution at (A) $c = 1.0\text{ mg/mL}$, (B) $c = 5.0\text{ mg/mL}$, and (C) $c = 10.0\text{ mg/mL}$. Concentrations are nominal values. 213

List of Schemes

Scheme 3-1. Model structures of BCP micelles with different core and corona sizes formed in selective solvents and on solid surfaces through spin-assisted assembly.	60
Scheme 5-1. Reaction scheme used to make PLA- <i>r</i> -PEG bottlebrush random copolymers.	113
Scheme 5-2. Reaction scheme used to make PLA- <i>b</i> -PEG bottlebrush block copolymers.	113
Scheme 5-3. Schematic representation of how block and random bottlebrush copolymers self-assemble to form single micelles in a solvent that is selective for the blue side chains.	127
Scheme A-1. Model architectures of different PS-PVP block copolymers. The unimolecular micelles formed from multiarm stars generally have asymmetrical PVP-PS core-corona structures in toluene, the detailed self-assembly behaviors of multiarm stars in selective/non-selective solvents is more complex as described in Chapter 4.	172
Scheme A-2. Effect of solvent removal on the self-assembly behaviors of PS-PVP block copolymers in thin films. In these drawings, the color red represents PS domains and the color blue represents PVP domains.	173

Chapter 1: Introduction

1.1 Self-assembly of amphiphilic block copolymers

Self-assembly is the spontaneous process whereby complex structures are generated from simple building blocks. Self-assembly drives most environmental processes,¹ and it can be used as a tool in chemistry and materials science to produce well-organized constructs in which the properties and interactions can be accurately predicted and controlled.² The two main types of self-assembly processes that exist are static and dynamic self-assembly. In static self-assembly the system undergoes energy minimization and reaches global or local equilibrium. On the other hand, in dynamic self-assembly well-organized constructs arise from local interactions between components within the system;¹ However, if the energy dissipation is altered, the system transitions to a new state, which could include disassembly.³ Self-assembled systems have found many applications, including as templates for nanoparticle synthesis⁴ and patterned surfaces,⁵ and as scaffolds for cell growth.⁶

Block copolymers have been the subject of intense research over the past 30 years,⁷⁻¹² in part because they mimic simplified versions of complex polymeric systems found in Nature. Amphiphilic (“dual loving”) block copolymers (ABCs) are long-chain amphiphiles that contain a solvophobic (solvent-fearing) block and a solvophilic (solvent-loving) block that are linked by a covalent bond. Common examples include polystyrene-*block*-poly(2-vinylpyridine) (PS-PVP), which contains hydrophobic PS and hydrophilic PVP blocks. ABCs based on PS-PVP have been used extensively in this work. In a solvent such as toluene, which is thermodynamically good for PS but poor for PVP, and above the critical micelle concentration (CMC), PS-PVP block copolymers can undergo microphase-separation, self-assembling into micellar ensembles, as shown in Figure 1-1. This self-assembly process is thermodynamically driven and kinetically

controlled and this allows the insoluble PVP blocks to segregate to the inside or “core” of the micelle, while the soluble PS blocks remain in contact with the solvent toluene, creating what is referred to as the “corona”. Because of this disparity in solubility of the two blocks, toluene is referred to as a “selective” solvent.

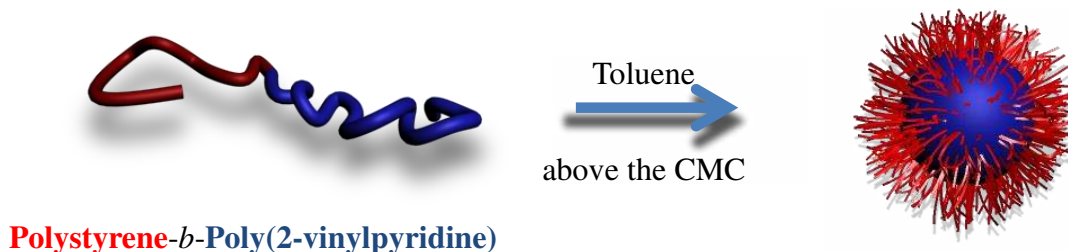


Figure 1-1. Microphase separation of polystyrene-block-poly(2-vinylpyridine) (PS-PVP) in a selective solvent, which in this case is thermodynamically good for PS blocks but a poor solvent for PVP blocks.

The self-assembly of ABCs has been extensively studied in solution and thin film because of its versatility as a way to access new, larger, or useful structures.¹³⁻¹⁵ Depending on the size of the BCP and volume fraction, a wide range of morphologies such as cylinders, spheres, vesicles, and hierarchical assemblies can be accessed without the need for complicated synthetic procedures.⁸ The self-assembly of ABCs has found use in lithography where the goal is to pattern surfaces in order to create smaller, faster, and more efficient electronic devices.¹⁶ One of the most widely proposed uses for self-assembled micellar systems is in biotechnological applications, where micelles serve as nanocarriers that encapsulate useful cargoes, such as drug

molecules, viral vectors, or imaging agents.¹⁷⁻²⁰ ABCs can also be used to encapsulate inorganic nanoparticles, which have therapeutic and diagnostic use in medicine, but require a polymeric coating to enhance circulation and delivery.²¹

The goals of this research are to investigate the links between architectural variations and compositional precision of PS-PVP block copolymers and their ability to undergo supramolecular assembly in solution and thin films. Though a substantial portion of this study will be focused on characterization of the single component parent systems, a key hallmark of this work will be on studying self-assembly behaviors of binary copolymer blends. Binary mixtures may be a useful route to access hierarchical structures that are otherwise inaccessible by the single component, parent systems. In addition to binary mixtures of PS-PVPs, my thesis work involves studying self-assembly behaviors of ABCs of unusual architecture, such as poly(D,L-lactide)-poly(ethylene glycol) (PLA-PEG) bottle brush copolymers.

1.2 Motivation

Self-assembly of ABCs depends on the ability to generate well-organized structures by controlling the chemical and physical properties such as size, shape, sequence, connectivity and surface properties of the constituent blocks.²² Recent advancement in modern synthetic techniques has provided materials chemists with a variety of methods to encode chemical information into macromolecules that gives rise to organized structures with properties that are different from the molecular constituents.²³⁻²⁶ Specifically, in this research I plan to investigate how architectural and compositional variations of single component systems impact self-

assembly properties such as stability, dynamics, and kinetics, both in solution and when deposited on surfaces. Furthermore, this research explores how binary blends of single component (parent) systems of architecturally- and compositionally-complex ABCs impacts self-assembly, both in solution and at surfaces.

Synthetic ABCs present a great opportunity to study the dynamics, structure and interactions of soft matter. Polymers and copolymers are technologically important materials encountered in everyday life, and they also represent simplified versions of complex systems created by nature (e.g., proteins). The traditional architectures of ABCs include diblock, triblock and other linear block copolymers, as well as non-linear architectures such as star-like or bottlebrush copolymers. At fixed temperature, the micellization of block copolymers occurs at a specific concentration, referred to as the critical micelle concentration (CMC). The size and shape of the micelle is dependent on the constituent blocks and their ability to microphase segregate in a selective solvent.^{10,27-29} The assembly is driven by a balance of interactions between the blocks and the solvent.³⁰ The extent of microphase separation is determined by the segregation product, χN . In most cases and where there are no strong specific interactions, such as hydrogen bonding, χ_{AB} is small and positive and is inversely dependent upon temperature. By tuning temperature and χN , the incompatibility between the constituent blocks can be controlled.⁸ There exists no breaking and reforming of bonds as in traditional bench chemistry because self-assembly is completely thermodynamically driven by the polymer-polymer and polymer-solvent interactions.²⁸

There are three main parameters that determine the extent of microphase separation of AB diblock copolymers: (1) the degree of polymerization ($N = N_A + N_B$), (2) the volume fraction of A and B blocks (f_A and f_B), and the Flory-Huggins interaction parameter, χ_{AB} , which determines the incompatibility between the two blocks. There has been a great deal of work on the solution self-assembly of diblock copolymers.^{8,31-33} While a full review is beyond the scope of this document, in short, the shape of the micellar aggregate depends on copolymer composition, monomer type, solvent quality, processing pathway, concentration, pH, temperature, and other factors (e.g. electrostatic interactions). Diblock copolymers can self-assemble into a variety of shapes. As depicted in Figure 1-2, these well-documented morphologies include: (1) spheres, (2) rods, and (3) vesicles.

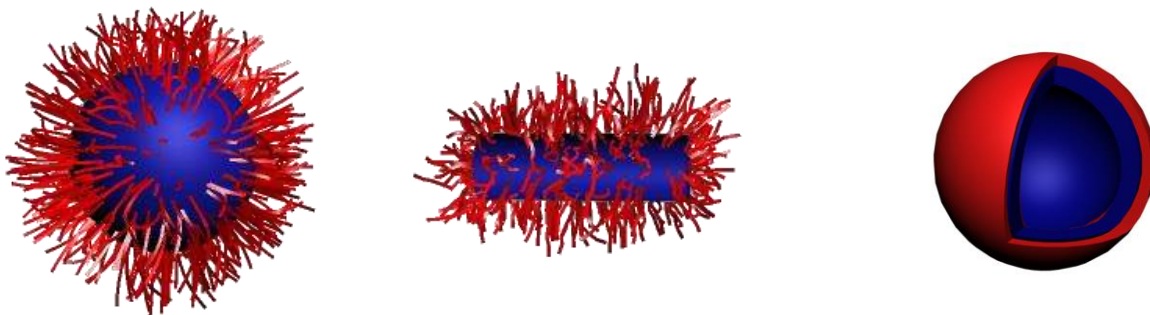


Figure 1-2. Traditional morphologies accessed from the self-assembly of diblock copolymers in a solvent that is selective for the red block above the CMC. From left to right micelles comprised of diblock copolymers mainly form spheres, rods, or vesicles.

1.3 Polymer design as a tool to tune self-assembly properties

Theoretical and experimental results have shown that block sequence and connectivity can affect the self-assembly of ABCs.^{9,34-37} Balsara *et al.* studied the solution properties of BAB triblocks comprising of PVP-PS-PVP in toluene, a selective solvent for the PS block. They found that the triblocks formed spherical micelles with a PVP core surrounded by loops of the PS-blocks. Previously, theoretical and experimental work suggested that due to the entropic penalty associated with the looping of the triblock, micelle formation would not be possible. This seminal work, in fact, proved that micelle formation is possible for BAB triblocks in a thermodynamically good solvent for the middle block. The authors also made the important finding that the molecular weight of the middle block plays a significant role in the micellar properties.³⁶

It is also possible to generate more complex topologies from linear block copolymers.^{25,38-39} The cyclization of ABCs can be achieved by reactively coupling the chain ends of an AB linear diblock copolymer.⁴⁰ The resulting cyclic architecture can have a significant effect on the stability, morphology, and dimension of the self-assembled aggregate.³⁹ The self-assembly of cyclic and linear diblock copolymers of the same degree of polymerization was investigated by Minatti *et al.* They showed that linear polystyrene-*b*-polyisoprene (PS-PI) formed classical spherical micelles, and the stability of the micellar structure was constant over the concentration range studied. In contrast, the cyclic PS-PI copolymers formed giant wormlike aggregates. In addition, the size and morphology can be tuned by adjusting the concentration of

the cyclic copolymer solution. At low concentrations the cyclic PS-PI formed “sunflower-like” micelles and at high concentrations giant wormlike micelles were accessed.⁴¹

Recently, a more exotic cyclic architecture was created and the corresponding self-assembly properties has been investigated in solution.³⁸ Wang *et al.* synthesized a figure 8-shaped ABC where each loop was a different type of repeating unit. To do this, they first synthesized a 4-arm star having 2 PS arms and 2 poly(acrylic acid) (PAA) arms using ATRP. They then “clicked” pairs of arms together to create the (PS-*b*-PAA)₂ figure 8-shaped ABC. They compared the structure formed by self-assembly in solution with that formed by its linear counterpart. Their results showed that both architectures formed micelles, but the figure 8-shaped cyclic copolymer resulted in micelles having smaller aggregation numbers (N_{agg}) but larger hydrodynamic radii (R_h). This behavior was attributed to the topological constraint imposed by the hydrophobic segments that are constrained within the figure 8-shaped chain. Compared to their linear analogues, the figure-8 chains self-associate less in water, forming larger but less well-organized aggregates. In general, the entropically disfavored self-assembly of cyclic copolymers can lead to interesting aggregate properties as a result of its unique architecture. Furthermore, the cyclization of polymers can lead to improved properties of the aggregates such as increased thermal stability and robustness toward salt additives.³⁹

Branching has been proven to have significant effects on the self-assembly properties of ABCs in solution and at surfaces.⁴²⁻⁴⁶ In comparison to an enormous number of studies focused on linear ABCs, there are few reports on solution and surface self-assembly properties of star block copolymers.⁴⁷⁻⁵¹ Using poly(n-butylacrylate)-*b*-poly(methyl methacrylate) (PBA-PMMA),

Nese *et al.* demonstrated that star block copolymers with large number of arms possess superior mechanical and thermal properties as compared to their corresponding linear counterparts of similar composition.⁴⁷ Star diblock copolymers with a large number of arms can also form stable unimolecular micelles in solution and at surfaces because of intra-molecular steric repulsion between the arms.⁵⁰⁻⁵¹ Pang *et al.* reported the synthesis and self-assembly of a novel 21-arm star in which each arm was made of a coil-rod polystyrene-*b*-poly(3-hexylthiophene) (PS-P3HT) diblock copolymer. In a thermodynamically good solvent for both blocks it was found that the PS-P3HT stars formed static unimolecular micellar structures due to the large number of arms present.⁵¹ Pang *et al.* also investigated the self-assembly properties of a star diblock copolymer comprising 21-arms of poly(acrylic acid)-*b*-poly(3-hexylthiophene) (PAA-P3HT) in dimethylformamide (DMF), a nonselective good solvent. Using dynamic light scattering (DLS), transmission electron microscopy (TEM) and atomic force microscopy (AFM), they showed that because of the compact nature of the PAA-P3HT star, it formed unimolecular structures in solution and at surfaces. The average hydrodynamic diameter, D_h , of the well solvated star was 20 nm, and TEM images showed that the core-forming PAA block was 9 nm, which is half of the size of the star measured by DLS.⁵⁰ These studies of ABCs of different design and ABCs of high molecular weight stars of varying design and chemical nature show that formation of micellar systems depends on their thermodynamic and kinetic properties above their CMC in solution. As a result, their dynamic stability and characteristics (e.g. shape and size) depends greatly on temperature, pH, concentration, and the properties of the selective solvent. In contrast, the high molecular weight and arm number of star diblock copolymers endows them with the unique

ability to form unimolecular constructs, whose properties are not governed by the traditional rules of self-assembly for soft matter.

Beyond these conventional, single component systems, the structures accessed from mixed systems inspire new ideas about how novel soft matter constructs can be created, and this vein of study has contributed to a better understanding of self-assembly processes.^{27,52-55} For example, Lodge and coworkers created “hamburger-like” micelles from a binary blend of a mikto-arm star terpolymer and diblock copolymer. The diblock was composed of polyethylene-*b*-poly(ethylene oxide) while the mikto-arm star was made by chemically attaching an acid chloride functionalized poly(perfluoro-propylene oxide) homopolymer at the junction between the blocks of the polyethylene-*b*-poly(ethylene oxide) diblock copolymer, resulting in a 3-arm star. The authors concluded that the hamburger micelles were a result of micelle fusion, and these asymmetric, multicompartment micellar structures were a result of multiple steps that included micelle collision, fusion, and fission over a prolonged period of time.⁵⁴ Eisenberg and coworkers investigated the effects of solvent, water content, and mixture composition on the morphology of binary mixtures of PS-PAA and PS-P4VP diblock copolymers. Using transmission electron microscopy (TEM) and differences in electrophoretic mobility, they demonstrated that the water content affects both the size and shape of the aggregates because it acts as a precipitant for the hydrophobic PS blocks. The work also revealed that the mixing ratio of the block copolymers can affect the morphology of the mixed system. This was highlighted in a series of studies where they increased the PS-P4VP content, which resulted in a morphological change from large compound micelles (LCMs) to a bimodal sample of small spherical micelles and LCMs, and finally to vesicles. This work highlighted the

sensitivity of binary ABC mixtures to external stimuli and blend composition, and also illustrates the complexity of behaviors that exist within mixed systems.⁵²

Processing (mixing) protocols have been shown to affect the properties self-assembled structures.⁵⁶⁻⁵⁷ Yoo *et al.* studied binary mixtures of linear PS_{33k}-P4VP_{8k} and PS_{20k}-P4VP_{19k} diblock copolymers (subscripts refer to block molecular weight in thousands) using three different mixing protocols: (1) They independently prepared micellar solutions and mixed them, which is denoted as “a mixture from a micellar state” or “postmixing;” (2) They also created mixtures by combining two dissimilar ABCs in a powdery state, mixed the blend, and subsequently added a thermodynamically selective solvent; (3) Finally they made mixtures from a blended state by “premixing,” in which they dissolved the block copolymer surfactants in a non-selective good solvent to create a blend of chains and then, after removing the solvent, the blend was re-dissolved in a selective solvent. The formation of a bimodal sample of small and large micelles or a mixture of small and hybridized micelles was governed by the difference in the mixing procedure. The difference in the micellar properties in solution was attributed to differences in the kinetics of micelle formation due to the change in mixing protocols. These results suggest that processing parameters have a significant effect on the aggregate structures adopted by mixed systems.⁵⁶

1.4 Models of behavior of micellar systems

There are two main models that describe micellization. The first is the *open association model*, which describes the formation of micelles with no unimers in solution. However, this

model is rarely appropriate because it suggests that a CMC does not exist; the copolymers aggregate, forming micelles with no well-defined number of chains. The second model is the *closed association model*, which describes the formation of micelles at and above the CMC and the establishment of a thermodynamic equilibrium between the aggregates and single chains present in solution. Figure 1-3 shows the three zones of the closed association model, expressed in terms of inverse micellar molecular weight, $(M_{w,mic})^{-1}$, versus solution concentration, c . Zone I encompasses the presence of single chains. The concentration at which aggregates first appear is defined as the CMC. Once micelles form, there is a coexistence between free chains and micelles (zone II). In zone III the system has reached dynamic equilibrium however; this equilibrium is shifted towards self-assembled aggregates. The equilibrium is dependent on the size and connectivity of the blocks, the solvent quality, solution temperature²⁹ and, in cases where aqueous solutions are used, the pH.^{28,30}

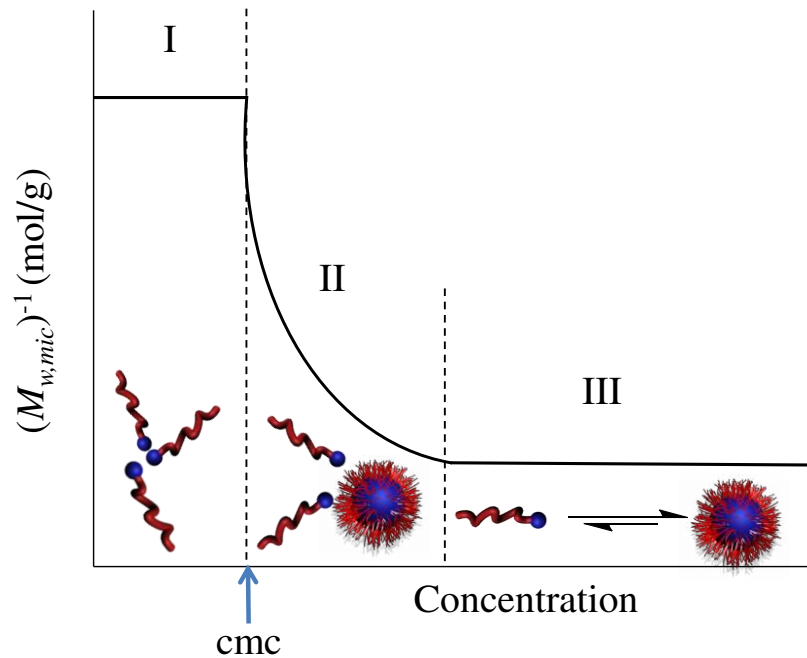


Figure 1-3. Schematic showing behavior of systems that follow the closed association model, represented in a plot of inverse micellar molecular weight, $(M_{w,mic})^{-1}$ versus concentration, c , in a thermodynamically good solvent for the red block. Zone I consists of only free chains in solution. Zone II displays coexistence between free chains and aggregates in solution. Zone III is marked by a shift in the equilibrium toward the self-assembled aggregates. Concept for figure was taken from Voulgaris *et al.*⁵⁸

The self-assembly of micelles (shown schematically in Figure 1-1) can be described by the Gibbs free energy of micellization at standard conditions, ΔG_{mic}° :

$$\Delta G_{mic}^{\circ} = RT \ln(cmc) \quad (1.1)$$

Here T is the absolute temperature (e.g. in Kelvin) and R is the ideal gas constant. For a process to be spontaneous, ΔG_{mic}° and the standard enthalpy of formation, ΔH_{mic}° must be less than 0.

The standard enthalpy of micelle formation is given by:

$$\Delta H_{mic}^{\circ} = R \frac{d \ln(cmc)}{d\left(\frac{1}{T}\right)} \quad (1.2)$$

From equations 1.1 and 1.2, the standard Gibbs free energy and the standard enthalpy of micelle formation can be calculated once the CMC and solution temperature is known. This is important because the possibility of micelle formation can be predicted without the need for time consuming experimental procedures.

The free energy per chain, F_{chain} , as described by Zhulina *et al.*²⁹ contains three contributions:

$$F_{chain} = F_{interface} + F_{core} + F_{corona} \quad (1.3)$$

where:

$$F_{interface} = \gamma s \quad (1.4)$$

In these equations s is area per chain and γ is the free energy per unit area of the core-corona interface. F_{core} and F_{corona} are the contributions due to the core and corona respectively. F_{corona} is the free energy associated with stretching the corona chains and F_{core} captures the free energy gained when the non-solvated core blocks remove themselves from solution into the core.

In short, the self-assembly process sacrifices the entropy of the single chains; however, a large unfavorable enthalpic penalty due to poorly solvated blocks having to remain in solution is prevented, and so the overall total free energy of the system is lowered ($\Delta G < 0$). These theoretical models, formulated for single component systems, provide more support to the idea that mixed or blended systems offer new opportunities to access new, unusual, or sophisticated structures. This is because of the gain in entropy that results upon mixing, which is analogous to that of mixing two dissimilar gases within a system. Mixed micelles having complementary chemical functionalities are also expected to be more thermodynamically stable than single component micellar systems because of attractive interactions. As a result of these features, more exotic structures may be accessed without the need for complicated synthetic procedures.

1.5 Research objectives

Block copolymers serve as model systems for studying the dynamics, structure, and interactions of soft matter in solution and at surfaces. The scientific focus of this dissertation research is to investigate the stability, dynamics, and kinetics of self-assembly of architecturally- and compositionally-complex ABCs and their binary mixtures in solution and at surfaces. To accomplish this, fifteen model polymer systems comprising PS-PVP, listed in Table 1-1, and four model systems of poly(lactic acid)-poly(ethylene glycol) (PLA-PEG) bottlebrush copolymers, listed in Table 1-2, that differ in block chemistry, sequence, composition, structure, and topology are used in this study. These differences in polymer design enable me to investigate

the links between architectural diversity, compositional precision, and the dynamics, kinetics, and stability of the resulting self-assembled structure in solution and at surfaces.

The 15 PS-PVP block copolymers used as model polymer amphiphiles in this study were synthesized by living anionic polymerization, which allows block copolymers with narrow polydispersity indices (PDI) to be made. The scope of anionic polymerization is beyond this work; however the interested reader can refer to the literature.^{24,59-60} The linear block copolymers, both PS-PVP diblocks and the PVP-PS-PVP triblocks have a variety of block sizes and styrene to vinylpyridine ratios (S/V) that range from ~1 to 10. The star block copolymers were synthesized by initiating through a divinylbenzene core to produce arms having PS inner- and PVP outer-blocks. The star block copolymers are distinguished by their number of arms, f . As observed in Table 1-1 $f = 8, 26, \text{ or } 40$ and within each subset the S/V ranges from ~1 to 9. The four bottle brush copolymers made of PLA-PEG differ by composition by controlling the relative amount of the two types of side chains used to make the copolymer and also by topological sequence (block versus random). The aforementioned differences in composition, sequence, and architecture are important because they serve as a means to advance our understanding of self-assembly as a suitable means for nanomanufacturing ensembles formed from surfactant-like block copolymers.

Table 1-1. Molecular characteristics of architecturally- and compositionally-complex ABCs.

sample ID	ABCs	M_w (kg/mol) ^a	PDI	S/V ^b
D1	PS-PVP	[100-60]	1.08	1.7
D2	PS-PVP	[54-14]	1.11	3.9
D3	PS-PVP	[255-24]	1.06	10.6
T1	PVP-PS-PVP	[31.25-62.5-31.25]	1.40	1
T2	PVP-PS-PVP	[12-96-12]	1.20	4
T3	PVP-PS-PVP	[6.2-124-6.2]	1.20	10
S1	[PS-PVP] ₈	[27-27] ₈	1.18	1
S2	[PS-PVP] ₈	[42-14] ₈	1.09	3
S3	[PS-PVP] ₈	[42-6] ₈	1.23	7
S4	[PS-PVP] ₂₆	[50-50] ₂₆	1.23	1
S5	[PS-PVP] ₂₆	[102.5-20.5] ₂₆	1.45	5
S6	[PS-PVP] ₂₆	[103.8-11.5] ₂₆	1.36	9
S7	[PS-PVP] ₄₀	[53.75-53.75] ₄₀	1.26	1
S8	[PS-PVP] ₄₀	[106.25-21.25] ₄₀	1.16	5
S9	[PS-PVP] ₄₀	[108-12] ₄₀	1.30	9

^aTotal molecular weight of linear copolymers is the sum of the values in square brackets (individual block molecular weights), and total molecular weight of star copolymers is the product of the sum of the block molecular weights (in square brackets) and the average number of arms (subscript). ^bPolystyrene-*b*-poly(2-vinylpyridine) ratios, defined as S/V.

Table 1-2. Molecular characteristics of bottlebrush copolymers.

Sample ID	PLA (wt %)	PEG (wt %)	M_w (kDa)	PDI
Block bottlebrush copolymer				
PLA ₄₃ - <i>b</i> -PEG ₅₇	43	57	188.8	1.14
Random bottlebrush copolymer				
PLA ₄₃ - <i>r</i> -PEG ₅₇	43	57	153.0	1.06
PLA ₁₄ - <i>r</i> -PEG ₈₆	14	86	196.8	1.10
PLA ₆ - <i>r</i> -PEG ₉₄	6	94	179.4	1.10

The overarching aim of this work is to quantify and enumerate the links between composition, architecture, sequence and block chemistry and various key factors (kinetics, structure, dynamics, etc.) that are innately linked in the self-assembly of soft matter. My focus will be on mixtures and blends of well-defined copolymers to tailor the free energy of the system through tuning the polydispersity and interfacial curvature in order to induce novel self-assembly properties that are not accessible by the single component parent systems. This work was inspired in part by the work of Jain and Bates.²⁷ These authors demonstrated this concept using linear poly(ethylene oxide)-*block*-poly(butadiene) (PEO-PB) diblock copolymers, which when mixed formed many complex and interesting aggregates due to the non-ergodic nature of the micellar system. My research objectives include:

- i. Investigating the self-assembly properties of architecturally- and compositionally-complex ABCs in solution and at surfaces in a selective solvent and in a non-selective solvent;

- ii. Understanding the self-assembly properties of binary blends of different architectures at a 1:1 (weight ratio) and comparing behaviors with properties of the single-component parent systems;
- iii. Examining how the mixing ratio affects the self-assembly properties of binary blends of different architectures and comparing behaviors with those of the single component, parent systems and with the symmetric (1:1) blends; and
- iv. Investigating how composition, sequence, concentration and solvent quality affect the self-assembly properties of PLA-PEG bottlebrush copolymers.

To complete these studies, the characterization techniques of dynamic and static light scattering (DLS and SLS respectively), atomic force microscopy (AFM), and cryogenic transmission electron microscopy (cryo-TEM), and regular TEM will be used. Light scattering is very important to my work because it is a non-invasive technique that gives information about the size of aggregates in its solution environment. It can also be used to study the kinetics and thermodynamics of self-assembly in solution. In light of this, Chapter 2 will focus on the theory and experimental set-up of both DLS and SLS.

In Chapter 3, investigations of the self-assembly properties (at 25 °C) of all of the 15 ABCs listed in Table 1-1 in solution and at surfaces are described. DLS experiments were completed at either 1.0 mg/mL or 8.0 mg/mL, depending on the CMC of the parent system. All binary mixtures were investigated at 1.0 mg/mL and 8.0 mg/mL. At high concentration, (8.0 mg/mL) there was an increase in the polydispersity of the kinetically frozen system and this led in part to the formation of complex hierarchical structures. AFM was used to study the surface

topology of the self-assembled block copolymers and their binary blends. It was found that all of the parent systems formed spherical aggregates when cast on silicon surfaces. However, as the S/V and number of arms were increased, the film thickness and aggregate size decreased. While spherical structures were often observed, worm-like aggregates and an unusual hierarchical aggregate having a structure that looked like a brain coral also were observed.

In Chapter 4, the solution properties of novel, high molecular weight 26- and 40-arm PS-PVP stars were studied in selective (toluene) and non-selective (tetrahydrofuran, THF) solvents. The phase behavior of these highly dense stars was investigated through a wide range of concentrations with the use of DLS, SLS, and TEM. The hydrodynamics of the 26- and 40-arm stars remained constant throughout the concentration range studied, and the stars remain as isolated aggregates both in THF and in toluene. Remarkably, TEM images reveal a segregated morphology driven by intramolecular microphase separation within the star diblocks in a selective solvent for the inner PS block, despite the high geometric constraint that exists in these dense stars.

In Chapter 5, I describe the synthesis and self-assembly of PLA/PEG random and block brush copolymers. The self-assembly behavior of these model amphiphilic systems were investigated in solvents selective for the PEG side chains (methanol and water), and in a thermodynamically non-selective good solvent for both side chains (DMF). The block composition directly affected the size and structure of the micellar aggregates in solution as seen by DLS and cryo-TEM. At constant PLA and PEG brush composition, the arrangement of PLA

and PEG side-chains (block versus random) played the leading role in the micellar structure and size.

Finally, Chapter 6 summarizes the main findings from my dissertation work and its impact on the self-assembly processing of soft matter ensembles. Chapter 6 also describes particular themes of future research that would be promising to pursue.

Chapter 2: Experimental and Theoretical Considerations of Dynamic and Static Light Scattering Characterization Techniques

Scattering in its simplest terms is the reradiation of a wave due to changes in the medium through which it is propagating. Dynamic and static light scattering (DLS and SLS) provides a wealth of information on the diffusion and size distribution of particles in solution. Mean decay rates, Γ , can be used to provide information on the apparent diffusion coefficient, D_{app} , which is then used to gain an understanding of the hydrodynamic radius, R_h , of the scattering particles in their native environment. Careful analysis of DLS and SLS data can be used to detect small changes in the average size, and distribution of sizes as solvent type, temperature, pH and other properties are changed. Also, SLS is often used to obtain information on the molecular weight, M_w , solvent quality, and characteristic size of the scattering particles within the system. When SLS and DLS is used in tandem they can be powerful tools for understanding the structure and behavior of the constituents within the scattering volume.

In this chapter, theoretical and experimental background of both DLS and SLS will be presented. These techniques are used extensively in my dissertation work therefore it is relevant to (1) to highlight a few mathematical relations for the practice of light scattering and (2) to present an overview of the experimental preparation and set-up for both DLS and SLS measurements, and (3) briefly describe data analysis procedures.

2.1 Static light scattering

As shown in Figure 2-1, the scattering volume depends on the scattering angle, θ , which is formed by the intersection of the incident light beam described by the vector quantity, (\vec{K}_i) having intensity I_0 , and the optical aperture used for observing the scattered light intensity I_s that

is described by the vector (\vec{K}_f). For particles in solution, the absolute scattered intensity is described by the Rayleigh ratio, R :

$$\Delta R = (I_{solution} - I_{solvent}) \left(\frac{I_{abs,std}}{I_{std}} \right) \quad (2.1)$$

ΔR takes into account the contribution of light scattered from the solvent, $I_{solvent}$, and the absolute scattered intensity of the standard, $I_{abs,std}$, which is normalized by the intensity for a scattering standard, I_{std} . These quantities, based specifically on identifying the standard to be toluene and the solvent to be THF, are illustrated in Figure 2-2.

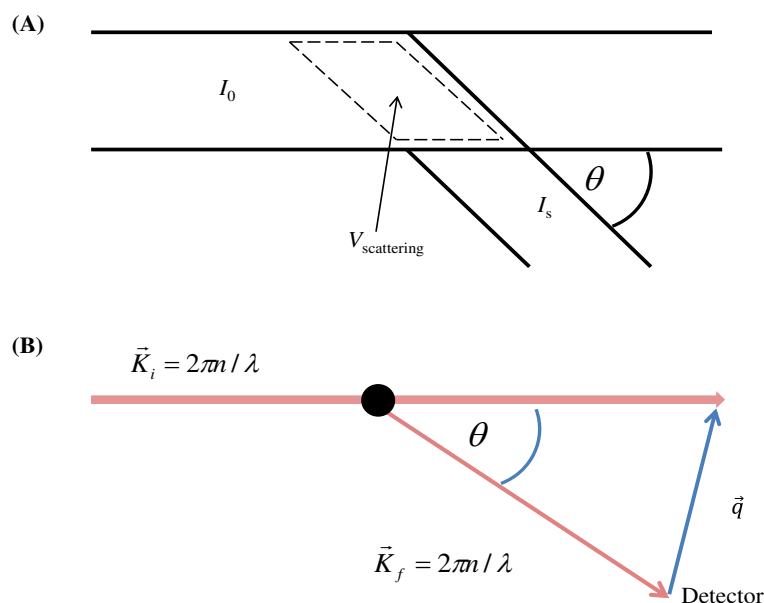


Figure 2-1. Scheme showing (A) the scattering volume that is as a result of the angle, θ , between I_0 (\vec{K}_i) and the optical aperture used for observing, I_s , (\vec{K}_f) and (B) a diagram of the definition of the scattering wave vector $\vec{q} = \vec{K}_f - \vec{K}_i$.⁶¹

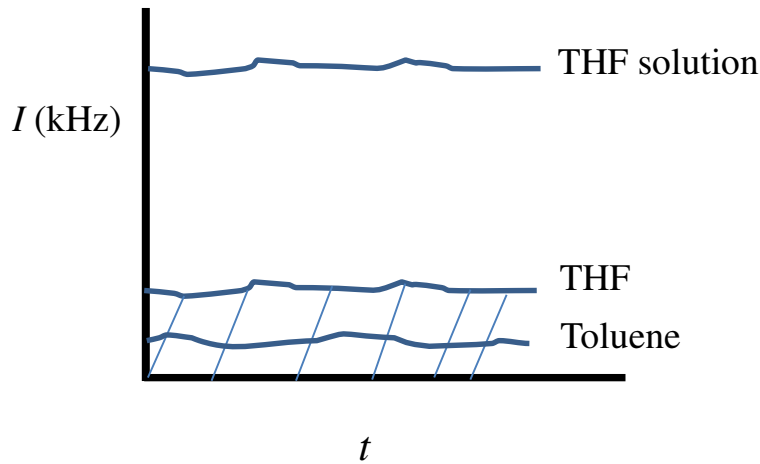


Figure 2-2. Scheme showing the intensities of the standard, solvent, and solution as a functions of time, t . In SLS, only the excess scattering intensity is taken into consideration during the measurement of the solution in question.

Figure 2-1B, which illustrates the scattering geometry, allows the scattering wave vector \vec{q} to be derived from the propagating and scattered waves:

$$q^2 = |\vec{K}_f - \vec{K}_i|^2 \quad (2.2)$$

$$q^2 = |\vec{K}_f|^2 + |\vec{K}_i|^2 - 2\vec{K}_i \cdot \vec{K}_f \quad (2.3)$$

$$q^2 = 2|\vec{K}_i|^2 - 2|\vec{K}_i|^2 \cos \theta = 2\vec{K}_i^2 (1 - \cos \theta) \quad (2.4)$$

$$q^2 = 2\vec{K}_i^2 \cdot 2\sin^2 \frac{\theta}{2} = 4\vec{K}_i^2 \sin^2 \frac{\theta}{2} \quad (2.5)$$

$$q = 2 \left\{ \frac{2\pi n}{\lambda} \right\} \sin \left(\frac{\theta}{2} \right) = \frac{4\pi n}{\lambda} \sin \left(\frac{\theta}{2} \right) \quad (2.6)$$

As shown in equation 2.6, \bar{q} depends on the solvent refractive index, n , the wavelength of light, λ , and θ . To take into account the effects of particle concentration, and solute-solvent interactions on the measured scattered intensity, the thermodynamics of concentration fluctuations have to be used. This is derived in Chapter 7 of Hiemenz and Lodge.⁶²

In my typical SLS experiments, several scattering angles between 20° to 146° were accessed by using 9 goniometer angles on the ALV instrument. Toluene was used as the calibration standard. A “dust-filter” option of 3% was utilized for the measured scattered intensity at each scattering angle and three runs of 10 s each were averaged. If the average count rate for any of the 10 s runs at any scattering angle differs by more than 3% from the ensemble average, the set of three measurements was repeated until the criterion of deviating by less than 3% of the ensemble average is satisfied. The z -average radius of gyration, $R_g \equiv \left[\langle S^2 \rangle_z \right]^{1/2}$, was determined using the truncated form of the virial expansion for the scattered intensity:⁶³

$$\frac{Kc}{\Delta R} = \frac{1}{M_{w,app} P(q)} + 2A_2 \quad (2.8)$$

As mentioned above, ΔR is the normalized absolute scattering intensity,⁶³ which is calculated according to equation 2.1. A_2 is the second virial coefficient and c is the solution concentration. K is the contrast factor, which is defined as:⁶³

$$K = \frac{16\pi^2}{\lambda^4 N_a} n^2 \left(\frac{dn}{dc} \right)^2 \quad (2.9)$$

Here N_a is Avogadro's number, $\lambda = 632.8$ nm (the ALV uses a HeNe laser) and n is the solvent refractive index. The refractive index increment, dn/dc , was determined using a Wyatt OptiLab Rex differential refractometer, which contains a laser operating at $\lambda = 658$ nm. Naturally it is assumed that the dn/dc measured at 658 nm is the same as that at 632.8 nm. For comparatively small particles ($q^2 R_g^2 \ll 1$), $P(q)$ can be expressed as:⁶³

$$P(q) = 1 - \frac{q^2 R_g^2}{3} \quad (2.10)$$

2.2 Dynamic light scattering

When scattering particles are moving, temporal fluctuations in the scattered intensity are a direct consequence of their Brownian motion, which occurs because of collisions between the scattering particle and the motion of the smaller solvent particles. Changes in the interparticle position causes a change in the detected scattered intensity measured at a given scattering angle, q .⁶³ The basic principle of how the fluctuating scattered intensity, $I(q,t)$, is treated in a dynamic light scattering experiment is illustrated in Figure 2-3.

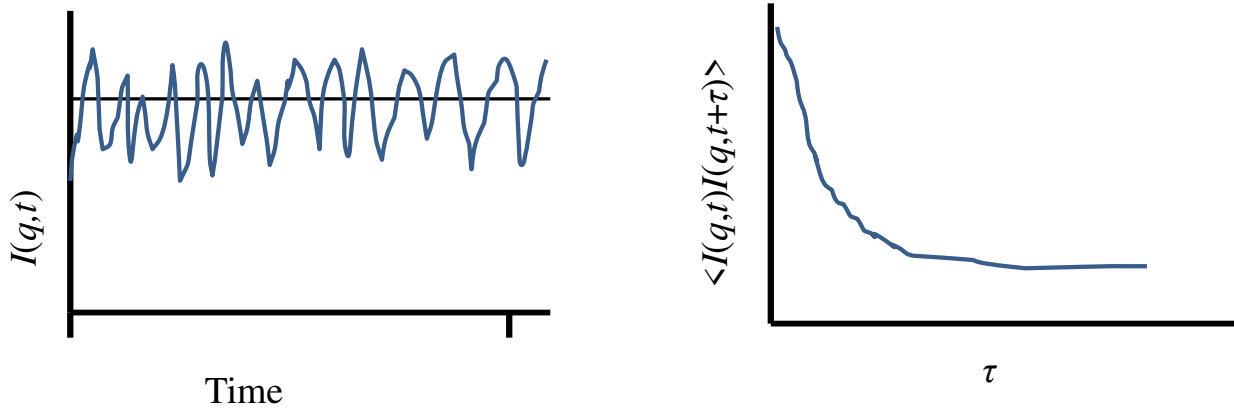


Figure 2-3. Schematic showing the intensity fluctuations (blue line) and the corresponding autocorrelation function. The solid black line models the average intensity, which is used in SLS.⁶³

The plot on the left in Figure 2-3 shows the signal detected by the photomultiplier at a given scattering angle. The fluctuating pattern (represented by the solid blue line) can be mathematically translated by an electronic device (a multichannel digital correlator) into a light intensity autocorrelation function. This is done by multiplying the time-dependent scattered intensity by itself after it has been shifted by a lag time τ , and averaging that product over the total measurement time. This light intensity autocorrelation function, $\langle I(q,t) \cdot I(q,t+\tau) \rangle$, which does not depend on t but only on the lag time τ , is calculated for various values of τ , ranging from in our case 125 ns to several seconds. At very small τ , the intensity is strongly correlated, but at longer τ , because the Brownian motion is random, the correlation is lost. The normalized scattered light intensity autocorrelation function, $g_2(q,\tau)$, is related to the first-order electric field time correlation function, $g_1(q,\tau)$, by the Siegert relation:

$$g_2(q, \tau) = 1 + g_1(q, \tau)^2 = \frac{\langle I(q, \tau)I(q, t + \tau) \rangle}{\langle I(q, \tau)^2 \rangle} \quad (2.11)$$

Here $I(q, t)$ is the scattered light intensity at time t and $g_1(q, \tau)$ is the first-order electric field time correlation function, which depends on the lag time τ and the scattering wave vector, q . As mentioned earlier, q depends on the scattering angle θ , λ , and the solvent refractive index, n : $q = (4\pi n/\lambda)\sin(\theta/2)$. The autocorrelation function obtained at each scattering angle is analyzed first by the CONTIN algorithm⁶⁴ to determine the amplitude distribution of decay rates, $A(\Gamma)$, which provides insight into the population(s) of scatterers in the scattering volume. CONTIN uses a regularization method in order to resolve $A(\Gamma)$ such that it satisfies the expression

$$[g_2(\tau) - 1]^{1/2} = g_1(\tau) = \int_0^{\infty} A(\Gamma) e^{-\Gamma\tau} d\Gamma \quad (2.12)$$

For systems where the CONTIN analysis shows one peak in the distribution of decay rates, the method of cumulants is used to determine the mean decay rate, or first cumulant, Γ_1 , and the normalized variance, μ_2/Γ_1 , at each scattering angle according to:

$$\frac{1}{2} \ln[g_2(\tau)] = \Gamma_0 - \Gamma_1\tau + \frac{\mu_2}{2} \tau^2 \quad (2.13)$$

Γ_0 is a constant independent of τ . In situations where the solutions exhibit two or three decay modes, a double or triple exponential distribution, expressed by equations 2.14 or 2.15, respectively, are used for the analysis:

$$g_1(\tau) = A_1 \exp(-\Gamma_1\tau) + A_2 \exp(-\Gamma_2\tau) \quad (2.14)$$

$$g_1(\tau) = A_1 \exp(-\Gamma_1\tau) + A_2 \exp(-\Gamma_2\tau) + A_3 \exp(-\Gamma_3\tau) \quad (2.15)$$

Here A_1 , A_2 and A_3 are the relative amplitudes of each characteristic decay mode Γ_1 , Γ_2 and Γ_3 .

The apparent diffusion coefficient, D_{app} , of scattering particles having a mean decay rate Γ_i can be determined by⁶²

$$D_{\text{app}}(q) = \frac{\Gamma_i}{q^2} \quad (2.16)$$

The z-average diffusion coefficients, $\langle D \rangle_z$, obtained from the y-intercept of a plot of Γ/q^2 versus q^2 , where Γ is the characteristic decay rate at a given scattering angle, is determined from analysis of the light intensity auto-correlation function that is computed in a DLS experiment.^{63,65} The diffusion coefficient determined in this way is the z-average over the molar mass distribution,⁶⁶ and reflects translational diffusion of the scatterer (no contributions due to rotation or segmental fluctuations) at a given concentration. As a result of this concentration dependence, the hydrodynamic radius determined using the Stokes-Einstein relation is an apparent hydrodynamic radius, $R_{\text{h,app}}$: $R_{\text{h,app}} = kT/6\pi\eta_0\langle D \rangle_z$. Here k is the Boltzmann constant, T is the absolute temperature and η_0 is the solvent viscosity (0.555 cp for toluene and 0.454 cp for THF at 25 °C).⁶³ An alternate method by which the solution diffusion coefficient, D_s , can be determined is to extract it from the slope of a plot of Γ versus q^2 . (Recall that as Γ is the characteristic decay rate, plotting Γ versus q^2 is simply another way to express the angular dependence of the decay rate.) This method was also used in Chapter 4 in order to present a comparison between the two different fitting methods. According to Brown, the effect of concentration on $\langle D \rangle_z$ can be described using the following equation, which is a virial expansion in concentration:⁶⁵

$$\langle D \rangle_z = D_0(1 + k_D c + \dots) \quad (2.17)$$

Here k_D is the diffusion virial coefficient, which takes into account polymer-polymer equilibrium interactions and polymer-polymer hydrodynamic interactions.⁶⁵ D_0 is the diffusion

coefficient at infinite dilution, and it is obtained by extrapolating the concentration dependent $\langle D \rangle_z$ values to $c = 0$. The true hydrodynamic radius, $R_{h,0}$, which is independent of concentration, is obtained from the corresponding D_0 value by using the Stokes-Einstein relation.

2.3 Cleaning techniques

Dust and other stray particles that are significantly larger in size than the particle trying to be observed will scatter light more strongly than the polymers (or their aggregates) in solution. The presence of unwanted particles in the solution can give rise to significant and undesirable errors in the acquired data. Therefore, it is essential to prepare dust free solutions in order to complete an acceptable light scattering experiment. There are numerous cleaning techniques. It is almost an art, but the most common method involves cleaning the DLS tubes and scintillation vials with soap and deionized water and sonicating for at least one hour. The DLS tubes are then rinsed with copious amounts of deionized water and stored (upside down) in a clean, dry environment covered by perforated foil. To clean the solvent, filtration is the quickest and most reliable procedure.⁶⁷ I have developed a double syringe filtration technique that has significantly increased the quality of the solvent used in my light scattering experiments. This involves filtering the solvent through two simultaneously connected Millipore PTFE filters into a pre-cleaned scintillation vial. To test the cleanliness of the solvent, a SLS experiment is first completed. If there are no significant spikes in the scattered intensity when measuring the solvent and if the count rates remain very low, then the solvent is determined to be acceptable for light scattering experiments.

A clean polymer solution is also essential to a successful light scattering experiment. Firstly, a stock solution is gravimetrically prepared at the desired concentration in a previously cleaned dust-free vial with the use of filtered solvent (0.2 μm PTFE). Secondly, prior to a light scattering experiment, aliquots are taken from the stock solution and gravimetrically diluted into clean vials with filtered solvent to achieve a series of solutions with desired concentration. It also should be noted that a polymer solution should never be rapidly forced through a small filter because any self-assembled aggregates can be degraded by shear forces when filtered. Finally, a clean polymer solution is defined as one in which no large spikes in signal appear (due to dust) when the scattered intensity is observed (measured) at a low angle (e.g. 20°) for a minimum of 15 minutes. If no large spikes in intensity are observed, the solution is determined to be clean, and a full set of light scattering experiments are started.

2.4 Data analysis

All static and dynamic light scattering (SLS and DLS) measurements were done on a four detector, goniometer-based ALV system equipped with a linearly polarized 22 mW HeNe laser operating at a wavelength, λ , of 632.8 nm. The instrument is mounted on an optical table to reduce the effects of vibrations. The incident beam is reflected by two mirrors, and any increased scattered intensity that may occur is reduced by a liquid crystal attenuator before being analyzed by a built-in quadrant-photodiode equipped with a beam splitter plate. The laser light is then focused into the sample cell that is positioned in the center of the scattering cell filled with toluene. The scattering cell is mounted on a motor-driven precision goniometer ($\pm 0.01^\circ$)

equipped with four detectors interleaved by 34° from one another. My typical protocols use up to nine different goniometer angles in DLS experiments, giving rise to signal detection at scattering angles ranging from 20° to 146° . The temperature of the scattering cell is maintained at 25 ± 0.1 °C in all experiments by circulating a mixture of water and ethylene glycol through the cell jacket. The signal is processed using a fast photon count digital correlator (ALV-7000 multiple tau) with an initial sampling time of 125 ns.

The ALV light scattering instrument has software that is sufficient to acquire simultaneously the data from both DLS and SLS experiments. However, the software to analyze the data to determine the R_h , R_g , A_2 and $M_{w,app}$ is lacking. Therefore, the data are analyzed with a software package that was written by Dr. Masashi Osa based on the programs used at Kyoto University. The following section demonstrates how the ALV_SLS.exe and ALV-Zimm_plot.exe external software packages are used to process the “static.txt” data files, which is then used to calculate $Kc/\Delta R$ which is necessary to create Zimm plots.

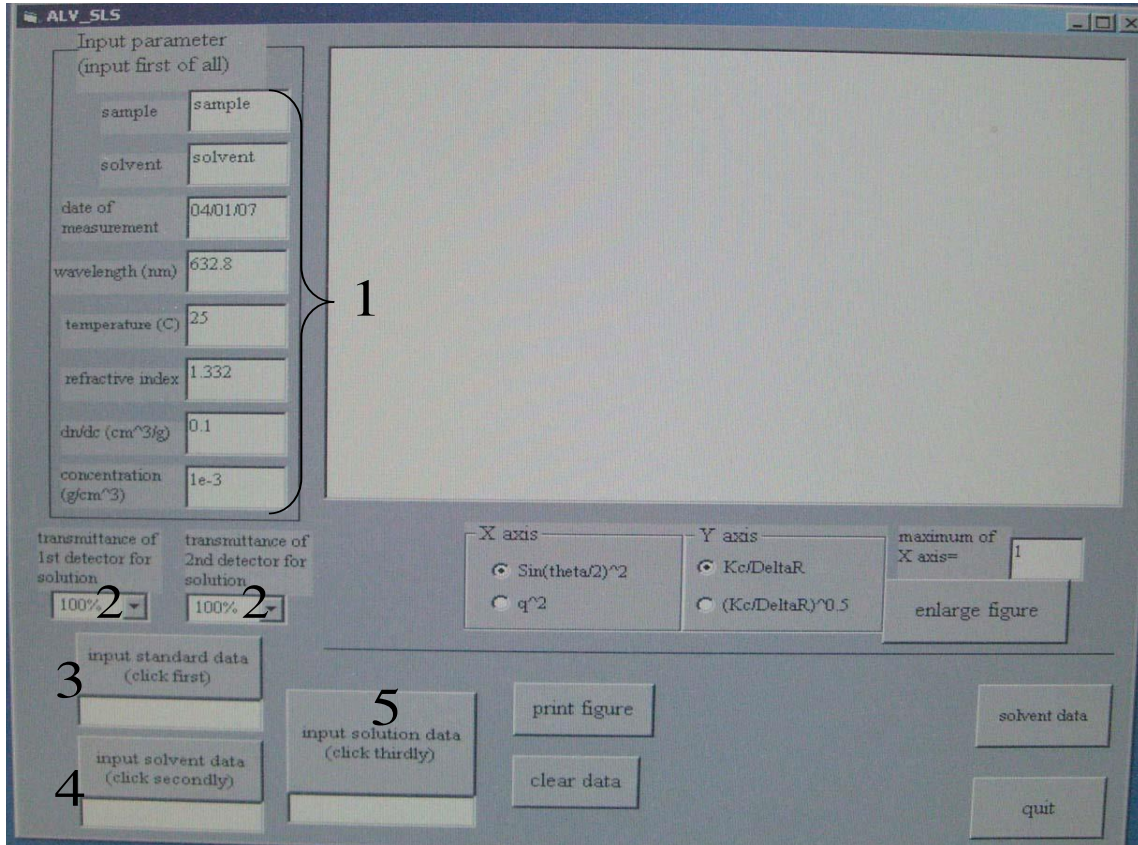


Figure 2-4. Screen shot of ALV_SLS.exe program written in Visual Basic by Dr. Masashi Osa.

Firstly, the ALV_SLS.exe icon is opened and the initial window that is seen is shown in Figure 2-4. The following steps are to be followed, and the step numbers correspond to input boxes in the software, as identified in Figure 2-4:

1. The relevant parameters such as sample name, solvent, date of measurement, wavelength, temperature, refractive index, dn/dc , and concentration are entered.
2. The transmittance values at the 1st and 2nd detectors used during solution analysis are input.

3. In boxes 3-5 the standard data file, solvent data file, and solution data file (previously created and saved on the computer) are selected (a dialog box opens when the buttons are clicked) and loaded into the software program.
6. Once the standard, solution, and data files are loaded, the large plot window (6) displays the data as $Kc/\Delta R$ versus $\sin^2(\theta/2)$. This is displayed in the screen shot in Figure 2-5 at sixteen angles and a finite concentration.
7. The image can be enlarged and the corresponding Zimm or Berry plots can be calculated with at least 2 different concentrations using the ALV-Zimm_plot.exe external software package.

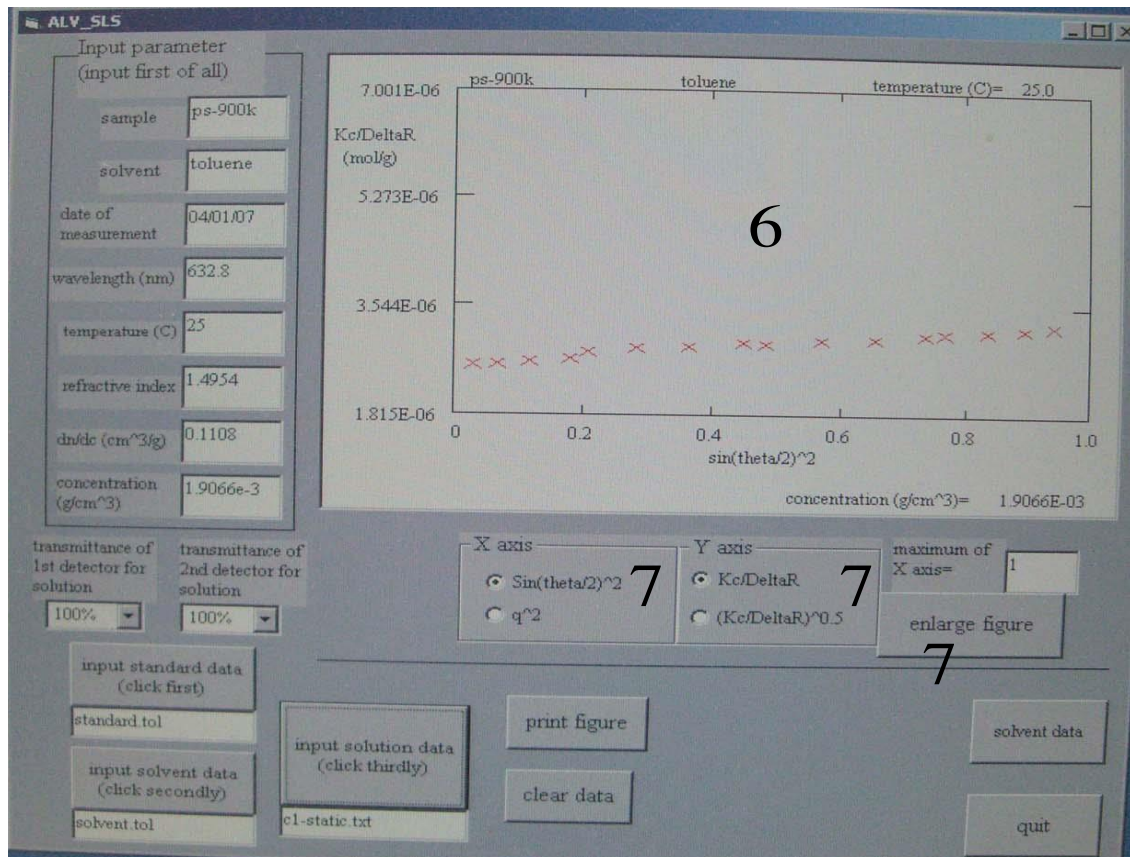


Figure 2-5. Screen shot of ALV_SLS.exe program after analysis of input data at a specific concentration and 16 different angles.

To analyze the DLS data, the ALV_DLS.exe software program is used to process the “.asc” and “dist.txt” data files that are output from the ALV measurement software. This program is used to calculate the first cumulant and the approximate $R_{h,app}$ at finite scattering wave vector q . The ALV_Gamma_vs_q.exe software program is used to make plots of Γ/q^2 versus q^2 , which enables $\langle D \rangle_z$ to be determined at finite concentration. Finally, the

ALV_D_vs_c.exe software program is used to make plots of $\langle D \rangle_z$ versus concentration, which allows D_0 to be obtained. From D_0 , the true hydrodynamic radius at infinite dilution is calculated using the Stokes-Einstein relation. The DLS data analyses using the ALV_DLS.exe and ALV_Gamma_vs_q.exe software programs are summarized in the procedure described next, which draws on labels in Figures 2-6 and 2-7.

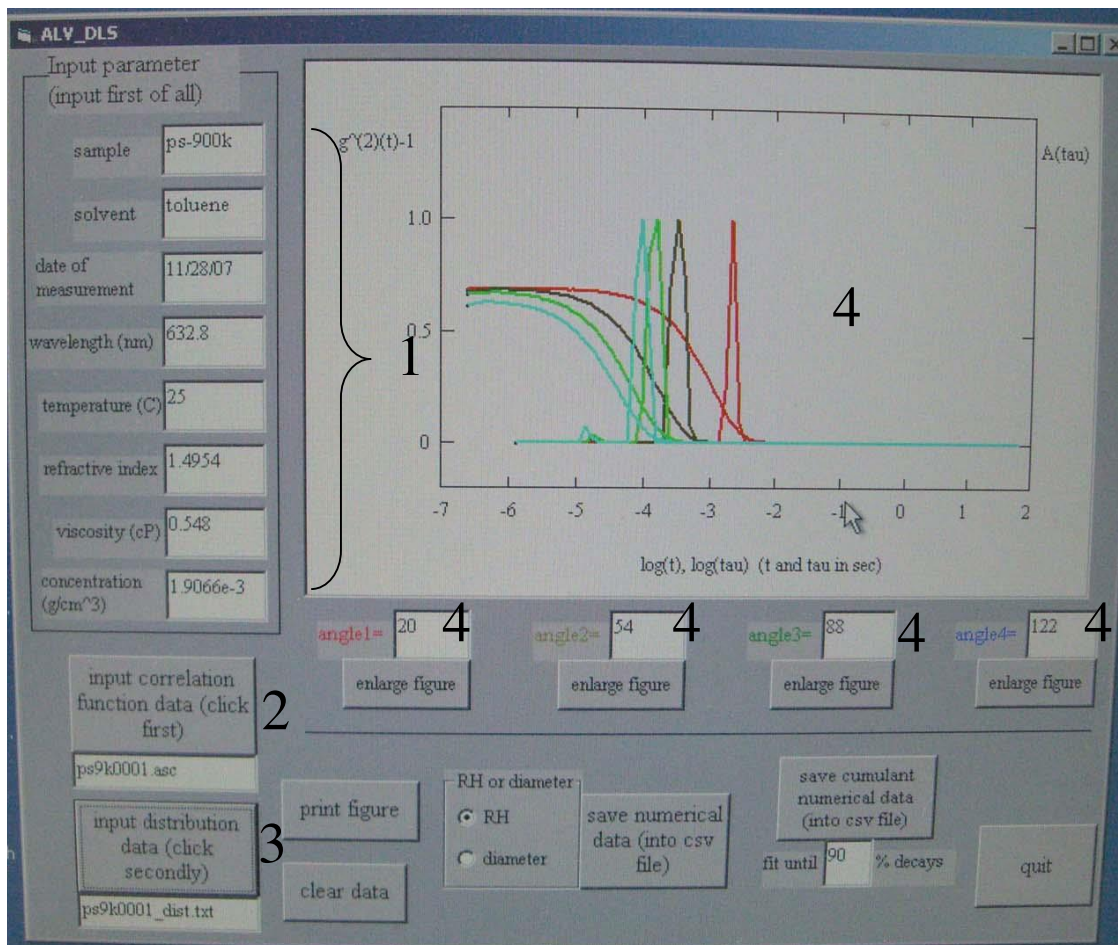


Figure 2-6. Screen shot of ALV_DLS.exe software package with model results from the first detector.

The process used to analyze DLS data is detailed in the following steps, and numbers correspond to input boxes in the software that are identified in Figure 2-6:

1. The relevant parameters such as sample name, solvent, date of measurement, wavelength, temperature refractive index, viscosity, and concentration are input.
2. The correlation function data (sample1.asc file) from the first detector is input.
3. The corresponding distribution data (sample1_dist.txt) is input.
4. The time correlation function, $g^{(2)}(t)-1$, and distribution of relaxation times, $A(t)$, from the first detector and the values of the four scattering angles (identified by number 4) are displayed.

The numerical and cumulant data files are then saved, and steps 1-4 are repeated for the second, third, and fourth detector files. The numerical and cumulant data files at all experimental scattering angles are then combined (by clicking on the ALV_combine_numerical and ALV_combine_cumulant icons) and saved.

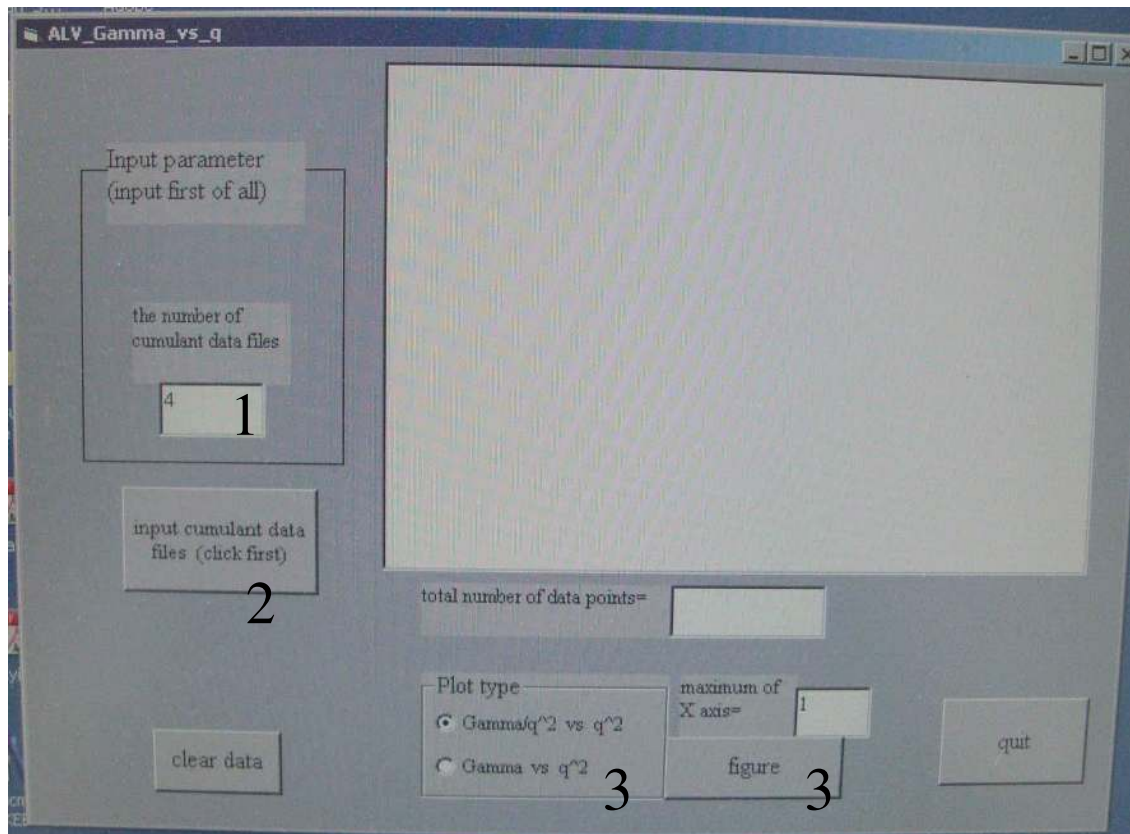


Figure 2-7. Screen shot of the input window for the ALV_Gamma_vs_q.exe software program.

Figure 2-7 shows the initial input window that appears upon opening the ALV_Gamma_vs_q.exe software program. The following steps describe how this software is used to produce Γ/q^2 versus q^2 or Γ versus q^2 plots.

1. The number of the numerical data files for cumulant analyses is entered. For example, if DLS data were acquired at four goniometer angles, you would input “4”.
2. The cumulant data files are loaded through the dialog box that opens.

3. The desired figure option, either “ I/q^2 versus q^2 ” or “ I versus q^2 ”, is chosen. A second window will open with the selected type of figure and the data points displayed.
4. The apparent diffusion coefficient and corresponding $R_{h,app}$ are calculated. The results are then displayed and saved as a CSV file.

The software program described above, written by Dr. Masashi Osa, are quite useful when analyzing DLS and SLS data that are particularly complicated, for example double and triple exponential functions. The data then requires precise and comprehensive external analyses in order to derive the most probable results from the light scattering experiment. External plotting and fitting programs such as OriginLab can also be very useful in analyzing both SLS and DLS data obtained from the ALV light scattering instrument.

**Chapter 3: Control of Self-Assembled Structure through Architecturally and
Compositionally Complex Block Copolymer Surfactant Mixtures**

This chapter describes work published in *Macromolecules* 2014, 47, 7138. I characterized all of the polymers described in this work and coauthored the manuscript. Other coauthors include Dr. Hinestrosa who provided helpful suggestions concerning light scattering, Prof. Jimmy W. Mays, who provided the polymer samples, and Prof. S. Michael Kilbey II, who advised this work.

3.1 Abstract

The self-assembly of binary mixtures of architecturally and compositionally diverse surfactant-like polystyrene-poly(2-vinylpyridine) (PS-PVP) block copolymers (BCPs) in solution and in thin films has been systematically studied. PS-PVP BCPs of different molecular architecture synthesized by living anionic polymerization, including linear diblocks, triblocks, and branched star-like copolymers all having different block sizes, styrene to 2-vinylpyridine ratios, and variations in numbers of arms, were employed as constituent building blocks for the construction of advanced copolymeric ensembles. While ensembles formed from monomodal PS-PVP BCPs exhibit simple spherical aggregate structures in the PS-selective solvent toluene, aggregates created by mixing PS-PVP BCPs of different architecture display structures that include spherical, worm-like and large compound micellar aggregates. This result is attributed to the complex, architecture-induced diversity of microphase segregation in the mixed systems, wherein the fine-scale structures of the resultant ensembles can be further controlled by adjusting the blend composition. For example, unique, hierarchically structured large compound micellar aggregates with spherical primary structures and worm-like secondary structures that resemble a

brain coral were directly created when a 1:1 mixture (by weight) of a triblock copolymer and a star BCP that was cast in thin film form. The present study is valuable for illuminating the range of structures that may be created through architecture- and composition-controlled self-assembly of amphiphilic copolymer mixtures, which generally benefits the development of self-assembly as a method to make soft matter building blocks, as well as connections between self-assembled structures in solution and their thin films.

3.2 Introduction

Self-assembly of copolymeric systems^{8,22} is viewed as a driver of technological advances that rely on the capacity of block copolymers (BCPs) to microphase segregate into well-defined and sometimes complex structures in solution, in bulk, and in thin films.⁶⁸⁻⁷⁸ Amphiphilic BCPs are widely studied due to their surfactant-like nature that promotes self-assembly as well as their ability to straddle interfaces. The combination of the extraordinary ability to control the chemical composition and integrate different monomeric building blocks through advanced polymerization methods inspires their use in many applications, such as templates for preparing inorganic constructs,⁷⁹⁻⁸² nano-carriers for delivery of therapeutic agents⁸³⁻⁸⁵ or bioactive materials,⁸⁶ fabrication of tunable optical materials⁸⁷⁻⁹⁰ or films with self-healing characteristics,⁹¹ to name a few. As a result, elucidating links between BCP design, assembly conditions, and structure continues to be an important theme in soft matter science.^{10,22,69,92-95} In terms of solution behavior, efforts over the past two decades have been devoted primarily to the self-assembly of well-defined linear polymer amphiphiles,^{8,31-32} the self-assembly behaviors of architecturally

complex BCPs^{58,96-98} or mixtures of polymer amphiphiles have been studied much less in comparison.^{27,56,99-107}

In contexts other than biological systems, polymers contain a mixture of chain lengths. While a large polydispersity can drive macrophase segregation of diblock copolymer melts,¹⁰⁸ BCPs are generally robust in the sense that low levels of polydispersities are tolerated within their microphase segregated structures. In amphiphilic systems self-assembled in solution, mixing chains of different degrees-of-polymerization or composition can alter the size and shape of micellar aggregates,¹⁰⁹⁻¹¹⁰ sometimes allowing exotic ensemble structures marked by undulations or distortions to be formed. For example, Mahanthappa and coworkers showed that polydispersity in the core block of poly(ethylene oxide-*block*-1,4-butadiene-*block*-ethylene oxide) (PEO-PB-PEO) triblock copolymers affects the interfacial curvature, allowing ellipsoidal-shaped micelles to form.¹⁰⁹ This ability of BCPs to balance interfacial curvature and stretching of the core and corona blocks has been shown to give rise to even more complex structures in mixed systems: Bates and Jain showed that binary mixtures of nearly monodisperse PEO–poly(1,2-butadiene) (PEO-PBD) diblock copolymers having different compositions and molecular weights in aqueous solution could form sophisticated structures.²⁷ For example, around compositions where single-chain systems formed branched worm-like micelles or network structures, bimodal mixtures formed interesting octopus-like structures that appear to have cylindrical structures with varying local curvature radiating from a central disc-like core.

In terms of blending different types of amphiphilic BCPs, Zhu *et al.* recently reported the construction of multigeometry, soft nanoparticles consisting of disk-sphere and disk-cylinder shapes by blending of two different linear BCPs in a water/THF mixed solvent system. The

multigeometry aggregates form because the incompatible solvophobic blocks locally phase segregate within the assembly, with each type of BCP contributing its characteristic phase segregated structure (bilayer vesicle, cylinder-like, or sphere) to the complex hybrid nanoparticle.¹¹¹ This strategy of kinetic control can be used to construct novel soft matter nanostructures with designed compositions and geometries from simple linear BCPs. The blending of more sophisticated chain architectures can also lead to multigeometry nanoparticles. Lodge and coworkers examined the morphology of 3-arm, ABC star-like terpolymers consisting of mutually immiscible blocks (ethyl-ethylene, ethylene oxide, and perfluoropropylene oxide), and mixed these with the corresponding AB diblock copolymer synthesized as an intermediate to the star terpolymer. The segregation behavior of the 3 arms of the star resulted in multicompartment worm-like micelles of various lengths. Most striking, when the sphere-forming AB diblock was mixed with the star terpolymer, fusion of the aggregates and chain rearrangements within the nanostructures led to the formation of “hamburger-like” micelles. In addition to this interesting structure, the slow evolution through aggregate fusion and break-up yielded asymmetric multicompartment micelles of various size.⁵⁴ In total, these studies highlight the richness of mixing architecturally and compositionally diverse BCP amphiphiles.

Despite the potential for realizing new aggregate shapes and for tuning structure, understanding the self-assembly behavior of complex BCP mixtures is in its infancy. In particular, there have been no systematic studies of the self-assembly of BCP mixtures with both architectural and compositional variations. With this in mind, we examine the structures adopted in solution and in thin films when amphiphilic polystyrene-poly(2-vinylpyridine) (PS-PVP) BCP amphiphiles are self-assembled in the PS-selective solvent toluene. Binary mixtures created from

pairs of diblock+triblock, diblock+star and triblock+star copolymers are explored across a range of compositions and, in the case of the stars, with varying number of diblock copolymer arms. While self-assembly of the single component PS-PVP BCPs tends to yield spherical structures – either spherical micelles in the case of the linear BCPs or unimolecular micelles for the stars with a large number of arms – the mixtures adopt more complex architectures depending on the diversity of component architecture and macromolecular composition.

3.3 Experimental

3.3.1 Materials.

The diblock, triblock and star copolymers comprising polystyrene (PS) and poly(2-vinylpyridine) (PVP) blocks were synthesized via anionic polymerization using custom-built, all-glass reactors with breakseals. The synthesis of these materials has been published separately^{24,59-60} and, therefore, is not repeated here. The polymers were characterized by a combination of size exclusion chromatography, multi-angle laser light scattering, ¹H NMR spectroscopy, and elemental analysis,^{24,59-60} and the results are summarized in Table 3-1. In terms of molecular topology, the triblocks have a center PS block connected to PVP end blocks, and the arms of the stars have a diblock structure with PS as the first block emanating from the central core and PVP as the outer block. The chemical structures of styrene and 2-vinylpyridine monomers are shown in the inset in Figure 3-1a. Throughout this paper we refer to the BCPs by the molecular weight of the PS and PVP blocks (in kg/mol), styrene to 2-vinylpyridine ratio (S/V), and architecture using D for diblock, T for triblock, and S for star.

3.3.2 BCP preparation

Binary mixtures of BCPs were created using a premixing method in which the constituent BCPs were separately dissolved in the non-selective solvent THF at a concentration of 8.0 mg/mL. After equilibration for 3 days, the solutions were mixed together (in different proportions, including v:v = w:w = 1:1, 3:1 or 1:3) and subjected to ultrasonication for 10 min. The mixtures were dried at room temperature for 48 h and then dried further under vacuum at 60 °C for 6 h to completely remove any remaining THF. After cooling to room temperature, the blends were dissolved in toluene to make solutions having concentrations of either 1.0 or 8.0 mg/mL, and then ultrasonicated for 10 min. These toluene solutions containing mixtures of BCPs were then stored in sealed vessels at room temperature for a minimum of 5 days before use. The structure adopted by self-assembly of each parent PS-PVP BCP was also characterized, and for these experiments, solutions of the BCPs in toluene at 1.0 or 8.0 mg/mL were prepared gravimetrically, subjected to ultrasonication for 10 min. to aid dissolution, and then allowed to equilibrate for at least 5 days.

Table 3-1. Molecular characteristics and self-assembly properties of surfactant-like PS-PVP BCPs in toluene.

sample					dn/dc	concentration	micellization	R_{h1}	R_{h2}
ID	BCP	M_w (kg/mol) ^a	PDI	S/V	(mL/g)	(mg/mL)	property ^b	(nm) ^c	(nm) ^c
D1	PS-PVP	[100-60]	1.08	1.7	0.199	1.0	I, M	11	166
D2	PS-PVP	[54-14]	1.11	3.9	0.195	1.0	I, M	6	88
D3	PS-PVP	[255-24]	1.06	10.6	0.189	1.0	I, M	14	142
T1	PVP-PS-PVP	[31.3-62.5-31.3]	1.40	1	0.099	8.0	I, M	9	285
T2	PVP-PS-PVP	[12-96-12]	1.20	4	0.113	8.0	I, M	8	130
T3	PVP-PS-PVP	[6.2-124-6.2]	1.20	10	0.108	8.0	I, M	8	134
S1	[PS-PVP] ₈	[27-27] ₈	1.18	1	0.086	8.0	I, M	19	102
S2	[PS-PVP] ₈	[42-14] ₈	1.09	3	0.117	8.0	I, M	16	189
S3	[PS-PVP] ₈	[42-6] ₈	1.23	7	0.086	8.0	U	26	
S4	[PS-PVP] ₂₆	[50-50] ₂₆	1.23	1	0.104	1.0	U	40	
S5	[PS-PVP] ₂₆	[102.5-20.5] ₂₆	1.45	5	0.097	1.0	U	61	
S6	[PS-PVP] ₂₆	[103.8-11.5] ₂₆	1.36	9	0.106	1.0	U	53	
S7	[PS-PVP] ₄₀	[53.8-53.8] ₄₀	1.26	1	0.107	1.0	U	52	
S8	[PS-PVP] ₄₀	[106.3-21.3] ₄₀	1.16	5	0.106	1.0	U	75	
S9	[PS-PVP] ₄₀	[108-12] ₄₀	1.30	9	0.085	1.0	U	77	

^aTotal molecular weight of linear copolymers is the sum of the values in square brackets (individual block molecular weights), and total molecular weight of star copolymers is the product of the sum of the block molecular weights (in square brackets) and the average number of arms (subscript). ^bMicellization properties of BCPs in toluene at concentrations above the CMCs (using I for isolated chains, M for multimolecular micelles, and U for unimolecular micelles). ^cResults obtained from DLS in toluene at $c = 1.0$ mg/mL for diblocks, 26- and 40-arm stars, and at $c = 8.0$ mg/mL for triblocks and 8-arm stars.

3.3.3 Film preparation

Diced silicon substrates obtained from Silicon Quest were ultrasonically cleaned successively in toluene, 2-propanol, methanol and deionized water, each for 15 min, and then immersed in a “piranha acid” solution (a 1:3 v/v mixture of 30% H₂O₂ and 98% H₂SO₄) and heated until no bubbles evolved. After this cleaning, the silicon substrates were rinsed with copious amounts of distilled water and then dried with N₂ flow. Thin films were made on silicon substrates by spin-coating 50 μL of the polymer solution (in toluene at a polymer concentration of 8.0 mg/mL) at 2000 rpm for 1 min using a Laurell WS-400B-6NPP-LITE spin coater. The as-prepared film thicknesses are ~40 nm, as measured using a Beaglehole Instruments Picometer ellipsometer at multiple angles of incidence ranging from 80° to 60° using 1° increments.

3.3.4 Characterization

The theory and procedure for the dynamic light scattering (DLS) can be found in Chapter 2. In short, once $\langle D \rangle_z$ values are obtained, the hydrodynamic radius, R_h is calculated using the Stokes–Einstein equation as $R_h = kT/6\pi\eta_o\langle D \rangle_z$ where k is the Boltzmann constant, T is the absolute temperature and η_o is the solvent viscosity (0.555 cp for toluene and 0.454 cp for THF).⁵¹ It is emphasized here that while the R_h values reported herein are *apparent* hydrodynamic radii determined at finite concentration (either at 1 mg/mL or 8 mg/mL), for convenience I refer to them simply as the hydrodynamic radius.

The refractive index increment, dn/dc , for each of the PS-PVP BCPs in toluene was obtained from refractive index measurements²² made using a Wyatt OptiLab Rex differential refractometer at $\lambda = 658$ nm. These dn/dc values are reported in Table 3-1.

Atomic force microscopy (AFM) images were collected using a Veeco Instruments Nanoscope IIIa multimode atomic force microscope in tapping mode using silicon cantilevers from Applied NanoStructures, Inc. (Mountain View, CA). Root mean square (RMS) roughness and particle size analysis of the images were performed using the NanoScope Analysis v140r1sr4 software.

Transmission electron microscopy (TEM) images were acquired using a Zeiss Libra 200 MC transmission electron microscope that is equipped with a Gatan UltraScan US1000XP CCD camera. For thin polymer films, the solution was spin-coated onto a carbon film grid that was affixed to a silicon wafer following the same procedure described for spin-coating on silicon substrates. The samples were stained by iodine vapor for 24 h. The iodine reacts preferentially with PVP, rendering the PVP microdomains dark in the TEM images. Images were acquired at the column temperature, which was close to room temperature.

For cryogenic-transmission electron microscopy (cryo-TEM), the toluene solution of polymer at a concentration of 8.0 mg/mL was cooled to 4 °C in order to slow the evaporation of the solvent while blotting excess liquid from the lacey carbon films. Droplets of the solution were placed on lacey carbon film grids. Excess fluid was blotted to create ultrathin layers of the suspension spanning the holes of perforated carbon films. The grids were immediately plunged into liquid nitrogen. Vitrified samples were transferred under liquid nitrogen into the transmission electron microscope using the Gatan 626 cryo-holder and stage. Sample temperature was held at -175 °C.

3.4 Results and discussion

Here the analysis of the structures adopted by the amphiphilic BCPs examined is segmented into two parts. In the first, the behavior of the parent PS-PVP BCPs is presented, beginning with their solution behavior in the selective solvent toluene and then in terms of the structures imaged when solutions are spin cast into thin films. This is followed by sets of results obtained on binary mixtures of the copolymers. For the mixed systems, results obtained when the copolymers were mixed in equal parts (by mass) are presented first, followed by results obtained when the components are mixed in different ratios.

3.4.1 Self-assembly of BCPs in solution.

Five groups of PS-PVP BCPs with various molecular architectures and S/V ratios were investigated, including three PS-PVP diblock copolymers (referred to as D1, D2, D3), three PVP-PS-PVP triblock copolymers (T1, T2, T3), three 8-arm stars (S1, S2, S3), three 26-arm stars (S4, S5, S6) and three 40-arm stars (S7, S8, S9). Among these BCPs, samples S1, T1, S1, S4, and S7 have small S/V in the range of $1 \leq S/V \leq 1.7$, samples S2, T2, S2, S5, and S8 have moderate S/V of $3.9 \leq S/V \leq 5$, and samples S3, T3, S3, S6, and S9 have large S/V ratios that range from $7 \leq S/V \leq 10.6$.

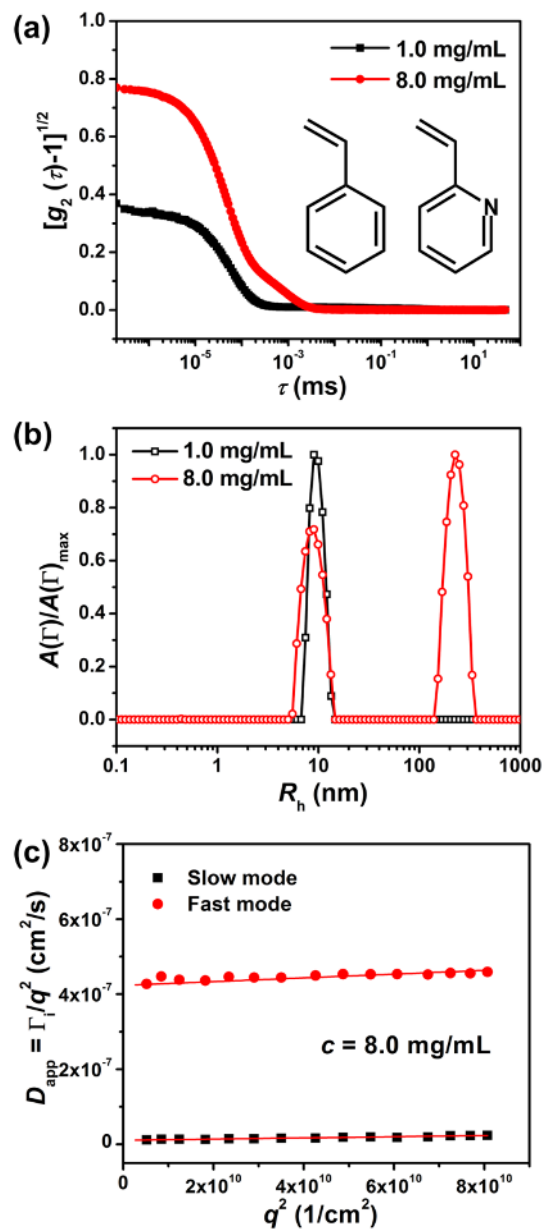


Figure 3-1. Light intensity autocorrelation functions (a), hydrodynamic radii, R_h , distributions (b) and apparent diffusion coefficient D_{app} versus q^2 (c) for sample T1 in toluene. Insets in (a) are the chemical structures of styrene (left) and 2-vinylpyridine (right).

Generally speaking, the amphiphilic nature of PS-PVP BCPs drives their self-assembly in a selective solvent such as toluene, where the PS chains are well solvated and extended while the PVP blocks collapse and aggregate to avoid contact with the solvent. While the self-assembly properties of linear PS-PVP BCPs in toluene have been studied,³² to understand the structures adopted when mixtures of different copolymers are used, it is important to first investigate the parent BCPs. The results obtained from dynamic light scattering (DLS) measurements of the parent copolymers are summarized in Table 3-1. As an example, DLS results for sample T1 in toluene with polymer concentrations below and/or above the critical micelle concentration (CMC) are presented in Figure 3-1. DLS results for all of the other parent copolymers are presented in Appendix A. Figure 3-1a shows the normalized light intensity autocorrelation function for T1 in toluene at the two concentrations studied. A single decay mode is observed at a concentration of 1.0 mg/mL while two decay modes are observed for the solution at 8.0 mg/mL. Additionally, the light intensity autocorrelation function acquired for T1 in toluene at 1.0 mg/mL begins at a much lower value (~ 0.4) and decays more rapidly as compared to that measured at 8.0 mg/mL. The R_h distributions presented in Figure 3-1b show a single, sharp distribution at 1.0 mg/mL but two well-resolved distributions at 8.0 mg/mL. The distribution centered at $R_h \approx 9$ nm is observed at both concentrations and is suggestive of single, isolated chains while the distribution appearing at $R_h \approx 200$ nm in the solution at 8.0 mg/mL suggests self-assembled aggregates. Figure 3-1c shows the apparent diffusion coefficients (determined by fitting the light intensity autocorrelation function with a double exponential decay) for T1 at 8.0 mg/mL as a function of q^2 . The characteristic hydrodynamic radii (R_{h1} for single chains, R_{h2} for micellar aggregates), which are presented in Table 3-1, are calculated using the Stokes–Einstein

relation from the z -average diffusion coefficient. The R_{h1} value for the fast mode observed in Figure 3-1c, $R_{h1} = 9$ nm is similar to that obtained for sample T1 in the non-selective good solvent THF, $R_{h,THF} = 13$ nm (see Appendix A). These results support the conclusion that at $c = 1.0$ mg/mL, T1 in toluene exists as isolated chains. In addition to isolated chains, the “slow” mode observed at $c = 8.0$ mg/mL is attributed to micellar aggregates that appear to be spherical in shape because D_{app} has no q -dependence over the q -range studied.^{44,110} This finding of coexistence of single BCP chains and micellar aggregates indicates that these polymer amphiphiles follow the closed association model.⁹⁶ The DLS results for other linear copolymers are similar to the behaviors exhibited by sample T1, and these are presented in Appendix A.

The results shown in Table 3-1 indicate that PS-PVP diblocks show bimodal size distributions in toluene at a low concentration (1.0 mg/mL), but triblocks only display well-defined bimodal size distributions at a higher concentration (8.0 mg/mL). This observation of the CMC of the triblocks being higher than that of the diblocks is in agreement with previous results showing that the CMCs for PS-PVP triblocks and heteroarm stars are several orders of magnitude higher than that for diblocks.^{36,58} This behavior arises due to unfavorable steric restrictions in triblocks and stars that makes bringing the solvophobic blocks into close proximity more difficult.

The hydrodynamic size distributions for the highly branched 26- and 40-arm stars in toluene at a concentration of 1.0 mg/mL are monomodal, and their correlation functions are fit well by a single exponential decay function. (See Appendix A.) As expected and as reflected by the data in Table 3-1, the 40-arm stars (S7-S9) are larger than the 26-arm stars (S4-S6), and the hydrodynamic sizes for the stars having a constant number of arms at medium and large S/Vs are

similar, but much larger than the R_h of the stars having a small S/V. Because R_h values for these stars range from 40 nm (26 arm, S/V = 1) to 77 nm (40 arm, S/V = 9), two samples were measured in the non-selective good solvent THF to determine if these complex macromolecules are aggregating in toluene at $c = 1.0$ mg/mL. The narrow R_h distributions obtained for these 26- or 40-arm star copolymers (S6 and S8, respectively) in THF and the similarity in their R_h values in toluene and THF (See Appendix A and results in Table 3-1.) suggest that the 26- and 40-arm stars exist as unimolecular micelles in toluene. This behavior is believed to be due to the inability of the poorly solvated PVP to drive aggregation due to the dense topology resulting from the large number of arms and their high molecular weight.

While it is clear that the particular details of the BCP, including block sizes, composition, and architecture, strongly influence the tendency to undergo microphase segregation to form aggregates, in the context of the systems studied here the results given in Table 3-1 indicate that the 8-arm stars appear to be at the boundary of where centro-symmetric star-like copolymers transition from being able to form multimolecular aggregates to only forming unimolecular micelles. The 8-arm stars with small and medium S/V (samples S1 and S2) show multimolecular micellization behaviors similar to that displayed by the linear BCPs. However, the 8-arm star having a large S/V (sample S3) does not form aggregates; instead these stars remain as a unimolecular micelle, in a fashion analogous to the behavior observed for the 26- and 40-arm stars.

3.4.2 BCP assemblies in thin films.

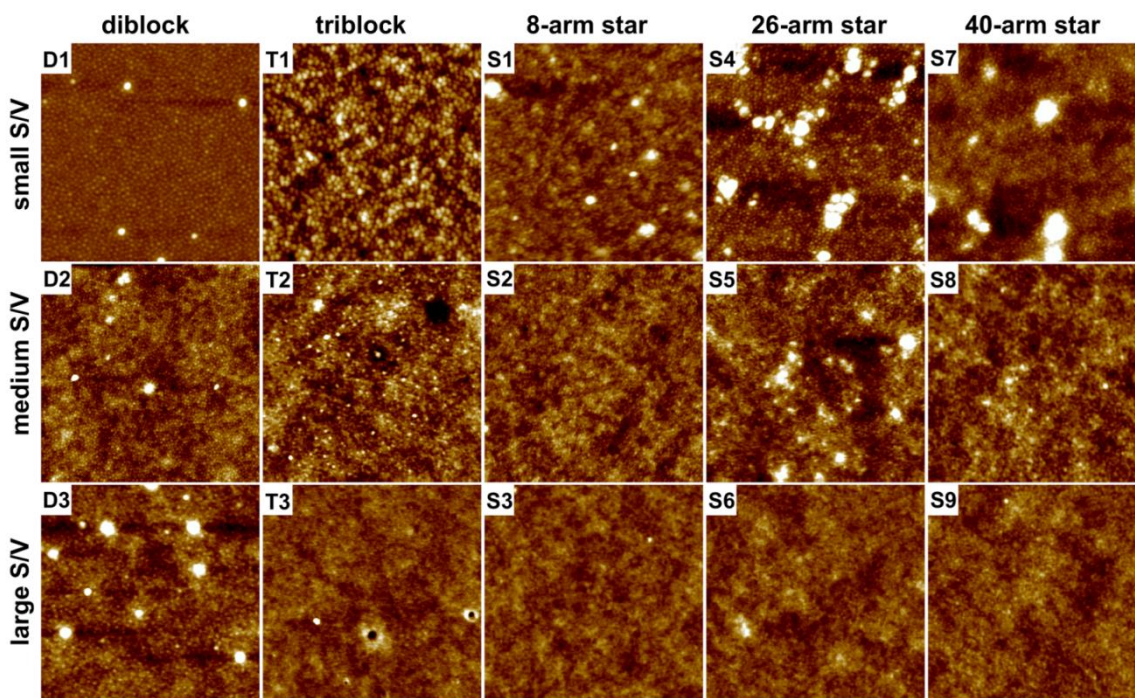


Figure 3-2. AFM height images ($2\ \mu\text{m} \times 2\ \mu\text{m}$) of BCP films. The sample IDs correspond to Table 3-1. Brighter areas are higher than darker areas. The Z scale is 15 nm for D1, T1, S1, S4, and S7, and 3 nm for the other images.

Spin coating of solution-assembled parent BCPs was used in order to image the nanostructures formed by AFM. As the removal of solvent toluene during spin coating is very rapid, the as-spun films are often regarded as representing the morphology of the aggregates in solution.^{81,112} AFM images of the resulting films of the aggregated PS-PVP BCP system formed by self-assembly are presented in Figure 3-2. The horizontal size (radii of the aggregates) and

vertical height of the microdomains, as well as the RMS roughness values calculated for the films, which were determined from a section analysis of the AFM images, are displayed in Figure 3-3. In general, the aggregates appear as circular microdomains (bright regions) covering the film surface, although there are clear differences in the size of the aggregates as the macromolecular architecture or S/V ratio are changed. The circular particles have horizontal dimensions of 40-80 nm (in diameter) for all the films made from BCPs with small S/V ratios, which includes samples D1, T1, S1, S4 and S7 (top row of images in Figure 3-2). It is also worth noting that the films created by spin-casting the self-assembled PS-PVPs having medium or large S/V (center and bottom rows of images in Figure 3-2) are flatter and the particles are smaller than those created using the BCPs having low S/V. Figures 3-3a and 3-3b also show that the horizontal radius and the vertical height of surface deposited aggregates forming the films generally decreases with increasing S/V. In the case of the systems that are able to form micelles in solution, we believe that this is as a direct result larger S/V ratios leading to micelles with smaller PVP cores and larger PS coronae in toluene. We speculate that the PVP domains play a leading role in the morphologies adopted in thin films because the soluble PS domains lose a large amount of solvent and spread on the surfaces during the solvent removal process, as depicted in Scheme A-2 of the Appendix A. In particular, the “softness” of the larger PS corona facilitates the coverage and spreading of the micelles on the surface, as suggested by Scheme 3-1, leading to smoother, more uniform films. This behavior is also reflected in the RMS roughness values calculated for the films. As Figure 3-3c shows, the RMS roughness of the films made by spin casting the self-assembled triblocks and stars tends to decrease with the increased S/V for BCPs having total molecular weights that are similar. While sample D3 shows a larger roughness

compared to sample D2, the former has a much larger total molecular weight and PVP molecular weight as compared to the latter. Presumably, the morphology and the roughness of the films are affected by both the molecular composition (S/V) and the molecular weight of the BCPs.

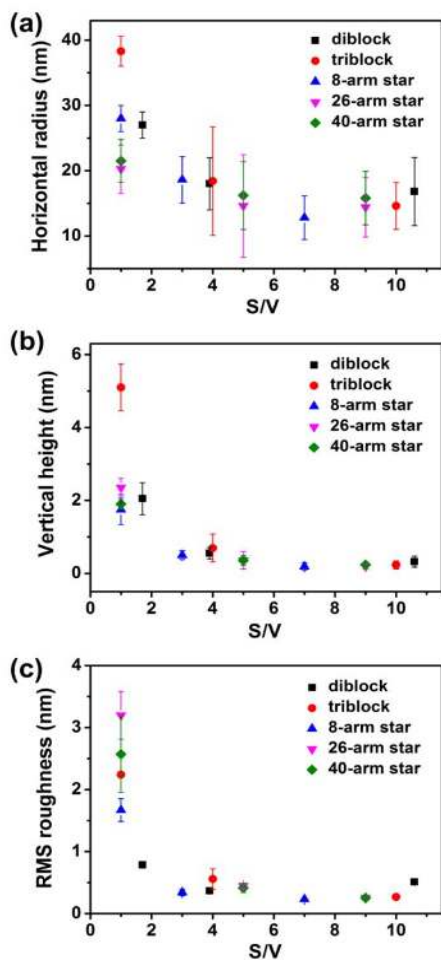
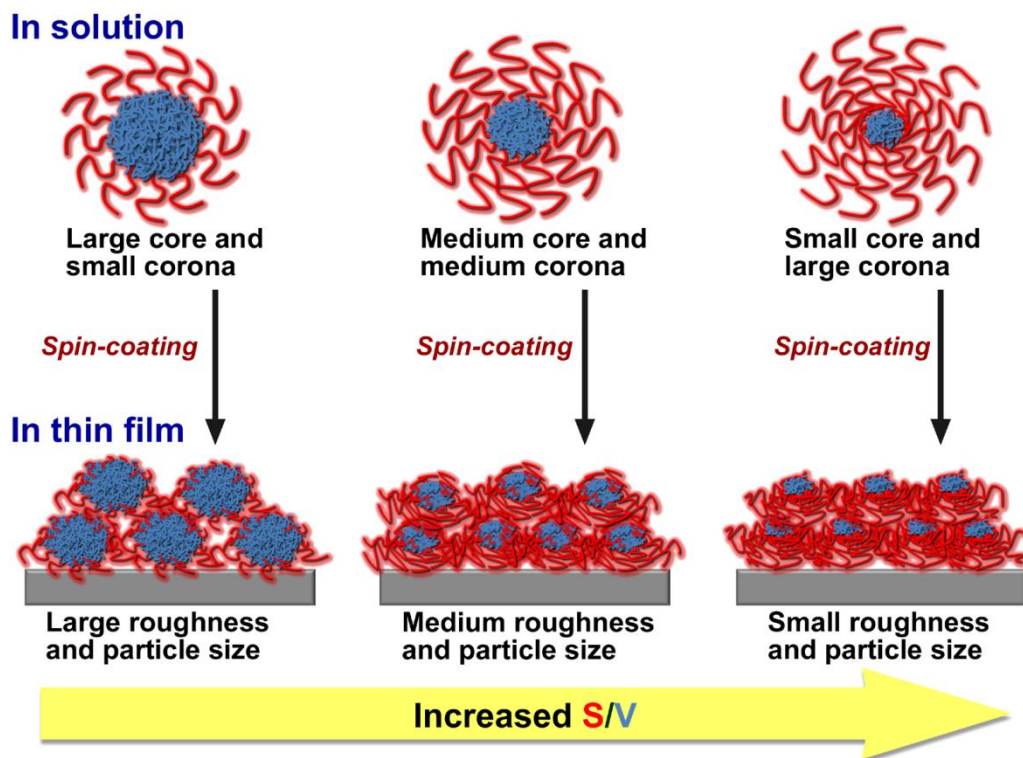


Figure 3-3. Horizontal radius (a) and vertical height (b) of the microdomains, and RMS roughness values calculated for the films (c) as a function of S/V ratio. Error bars are computed from the standard deviation of replicate measurements ($n = 3$ for roughness and $n = 20$ for radius and height).

Overall and as expected, self-assembly in thin films of the single component PS-PVP BCPs from the selective solvent toluene leads to formation of simple spherical aggregate structures regardless of the molecular architecture and composition. In order to demonstrate that the structures imaged from spin cast films are representative of their solution structure, disperse unimolecular micelles on a silicon substrate prepared by drop-casting from sample S7 toluene solution at $c = 3.0 \mu\text{g/mL}$ were imaged by AFM. As shown in Appendix A, an individual unimolecular micelle on a substrate surfaces has a hemispherical shape with a horizontal radius of $\sim 50 \text{ nm}$, which is in good agreement with DLS results ($R_h = 52 \text{ nm}$). However, the characteristic dimension of an individual micelle is larger than the aggregate sizes captured by AFM imaging of thin films made by spin casting: the corresponding film made by spin casting S7 has horizontal feature sizes of $21.5 \pm 3.2 \text{ nm}$. As depicted in Appendix A we believe that this discrepancy arises because the thin film structures imaged by AFM are mainly the non-collapsed parts of the micelles (the “hilltops”), because of how the aggregates spread and cover the surface when forming continuous films. This also manifests in the difference between the hydrodynamic sizes measured by DLS for the micellar aggregates, which are much larger than the characteristic dimensions measured for the thin films. Due to their ability to form spherical micelles in toluene and stability when deposited in thin films diblock D1, triblock T1 and 8-arm star S1, all of which have small S/V ratios, were selected as the common constituents for binary mixtures.



Scheme 3-1. Model structures of BCP micelles with different core and corona sizes formed in selective solvents and on solid surfaces through spin-assisted assembly.

Table 3-2 identifies the variety of binary mixtures made. Diblock sample D1 was mixed with triblocks T1, T2, and T3 and 8-arm stars S1, S2, and S3, which represents blending at varying S/V ratios. Binary mixtures at small S/V were also examined by mixing D1 with stars S1, S4, and S7, which span a range in number of arms, f , from 8 to 26 to 40. Similarly, triblock T1 was mixed with stars S1, S2, S3, S4, and S7, and binary mixtures of star S1 with triblocks T1, T2, and T3 were also made. In all of these experiments, the copolymers were combined at a mixing ratio of 1:1 by weight using the premixing strategy described earlier. Mixing at different ratios is discussed later.

Table 3-2. Mixing strategy by varying component architecture and self-assembly properties of PS–PVP BCP mixtures at a mixing ratio of 1:1 (by weight) in toluene solutions and in thin film form.

mixture ID	polymer I ^a	polymer II ^a	average S/V ^b	R_{h1} (nm) ^c	R_{h2} (nm) ^c	R_{h3} (nm) ^c	RMS roughness (nm) ^d	horizontal radius (nm) ^e	vertical height (nm) ^e	morphology ^f
D1+T1	D1	T1	1.3	21	492		2.0 ± 0.5	29.5 ± 4.4	3.3 ± 0.5	S
D1+T2	D1	T2	2.5	13	325		0.8 ± 0.4	27.6 ± 4.6	1.1 ± 0.3	S
D1+T3	D1	T3	3.3	20	381		0.8 ± 0.3	24.5 ± 2.1	1.1 ± 0.4	S
D1+S1	D1	S1	1.3	16	248	686	2.1 ± 0.3			W
D1+S2	D1	S2	2.2	13	224	456	1.2 ± 0.6	24.2 ± 6.0	1.1 ± 0.3	S
D1+S3	D1	S3	3	13	82	432	0.9 ± 0.4	23.8 ± 4.5	1.0 ± 0.2	S
D1+S4	D1	S4	1.3	31	436		2.3 ± 0.5	25.3 ± 7.1	2.7 ± 0.8	S
D1+S7	D1	S7	1.3	66	670		4.4 ± 0.1	23.3 ± 7.5	1.3 ± 0.6	S
T1+S1	T1	S1	1	22	328		1.9 ± 0.9			W
T1+S2	T1	S2	1.7	12	114		9.5 ± 1.7			H
T1+S3	T1	S3	2.2	14	476		7.1 ± 0.1			H
T1+S4	T1	S4	1	15	68		4.6 ± 1.6			W
T1+S7	T1	S7	1	22	81		2.4 ± 0.5			W
S1+T2	S1	T2	1.9	17	160	595	2.4 ± 0.4	26.8 ± 3.3	1.8 ± 0.8	S
S1+T3	S1	T3	2.4	13	121	347	7.6 ± 0.8			H

^aSample IDs of polymer I and polymer II correspond to the parent BCPs listed in Table 3-1.

^bAverage composition of the blend. ^cDetermined by DLS in toluene at $c = 8.0$ mg/mL. ^dAcquired by AFM roughness analysis with uncertainty expressed by the standard deviation ($n = 3$).

^eMeasured by AFM section analysis of the films with homogeneous spherical aggregate structures with uncertainty expressed by the standard deviation ($n = 20$). ^fMorphology of aggregates observed in thin film: S for spherical aggregate structures, W for worm-like structures, and H for hierarchical structures.

The morphology of the self-assembled structures formed by premixing the amphiphilic BCPs was investigated in thin film form using AFM. Figure 3-4 displays the AFM topography images of thin films resulting from binary mixtures of linear copolymers, namely diblock+triblock mixtures D1+T1, D1+T2, and D1+T3, as well as of diblock+star mixtures D1+S1, D1+S2, D1+S3, D1+S4, and D1+S7. The films of diblock+triblock copolymer pairs show spherical aggregate structures, and the particle sizes slightly decrease as the average composition expressed through the average S/V ratio (given in Table 3-2) of the blends increases. This trend is similar to that for the pure triblocks (T1, T2, T3), but the differences in characteristic particle sizes (radius as measured by AFM) of the diblock+triblock copolymer mixtures are smaller than those determined for the pure triblocks. This finding is similar to the report of Yoo *et al.*,⁵⁶ who showed that when two different micelle-forming diblock copolymers were combined by premixing the copolymers in a common good solvent, the resultant micelles were of a “hybridized” (intermediate) size. Remarkably, most films of diblock/star copolymer mixtures exhibit spherical aggregate structures, only the spin cast film of aggregates formed by premixing D1+S1 (Figure 3-4b) shows cylindrical microdomains oriented parallel to the substrate, which can be described as worm-like or bicontinuous structures. These distorted worm-like structures, which usually exist in films created from blending BCPs,^{56,113} have been proposed by Hashimoto and coworkers to originate from a cosurfactant effect and blending.¹¹³

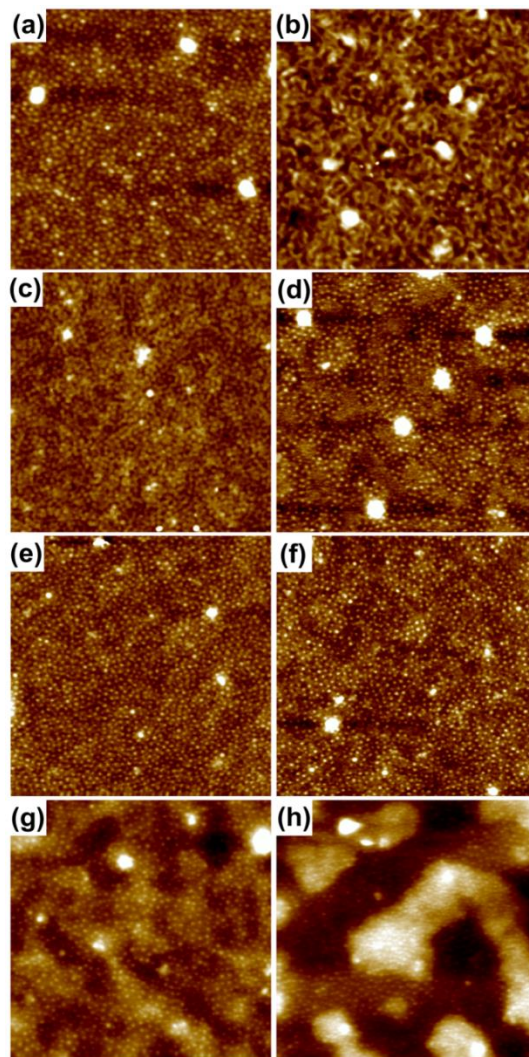


Figure 3-4. AFM height images ($2\ \mu\text{m} \times 2\ \mu\text{m}$) of the films of BCP mixtures of D1+T1 (a), D1+S1 (b), D1+T2 (c), D1+S2 (d), D1+T3 (e), D1+S3 (f), D1+S4 (g) and D1+S7 (h) at a mixing ratio of 1:1 by weight. The Z scale is 15 nm for (a, b), 5 nm for (c, d, e, and f), and 20 nm for (g, h).

As captured by the data presented in Table 3-2, for films created from binary mixtures of diblock and star copolymers, the general trend is that the RMS roughnesses of these films

decrease with increasing average S/V ratios. This behavior, which is consistent with trends observed for the parent materials, is most clearly observed in mixtures D1+S1, D1+S2 and D1+S3, where the number of arms is held constant at $f = 8$. Also, the data in Table 3-2 show that there is also an increase in the RMS roughness as the number of arms of the stars increases, as evidenced through the mixed systems of D1+S1, D1+S4 and D1+S7, which have a constant average composition (average S/V = 1.3). Mixtures of D1 with stars of small S/V, namely D1+S1, D1+S4, and D1+S7, produce films that entirely cover the surface and have large roughness values. This is especially true for D1+S7 mixture, where the RMS roughness is ~4.4 nm due to the present of large bulges on the film surface. The small S/V ratio (large PVP content), highly branched architecture and large molecular weight of S7 seem to facilitate aggregation (as observed in Figure 3-2 for S7), and as a result, blending of S7 with D1 leads to rougher surfaces (Figure 3-4h) compared to the films made from the parent BCPs.

Mixtures of triblocks and star copolymers seem to adopt more complex aggregate structures than blends of diblocks and stars. As shown in Table 3-2, the film RMS roughnesses for triblock+star copolymer are large in comparison and they also do not follow the trend established by the diblock+star mixtures of decreasing with increasing S/V. Moreover, the films cast from mixtures of T1 with stars at a constant S/V = 1 (T1+S1, T1+S4, T1+S7) exhibit worm-like structures (Figures 3-5a-c), similar to the film morphology for D1+S1. The lengths of the cylinders in these films generally decrease with increasing number of arms in the star BCP. As shown in Figure 3-5d, the film of S1+T2 mixture exhibits nearly spherical aggregates (that may be described as intermediate between spheres and short cylinders) with a horizontal particle radius of ~26.8 nm and a vertical particle height of ~1.8 nm. Moreover, some of the triblock+star

copolymer mixtures – specifically T1+S2, S1+T3 and T1+S3 mixtures – can form what appear to be hierarchical morphologies with distinct primary and secondary structures when spin cast as films, as shown in Figures 3-5e-g. The primary structures of these hierarchical morphologies are large-scale cylinders (Figure 3-5e) or spheres (Figure 3-5g) with a secondary structure that appears to be thin worm-like domains on the surfaces of the large aggregates. Among these, aggregates in thin films created from the mixture T1 + S3 are remarkable for their hierarchical structure that consists of a spherical primary structure and worm-like secondary structure, which gives the aggregates the appearance of a brain coral or a walnut. This structure has a horizontal diameter of ~600 nm and a vertical height of ~16 nm (Figure 3-5g). Similar walnut-like hierarchical structures made up of a network of polyaniline nanofibers polymerized on cationic surface-decorated PS microspheres have been reported; however the operative process that leads to the interesting hierarchical structure springs from adsorption of cationic surfactant and its ability to direct the oxidative polymerization.¹¹⁴ A similar hierarchical structure consisting of a sphere with striated domains was created by microphase separation of fluorine-containing diblock copolymers: Zhang and coworkers demonstrated that by controlling the addition of the poor solvent water into a homogeneous solution of the copolymer in THF, soft nanoparticles having diverse internal and hierarchical structures could be created.¹¹⁵ As demonstrated here, spin casting binary mixtures of complex PS-PVP BCPs, i.e. triblock+star copolymer pairs, appears to be another path toward creating supramolecular, hierarchically structured aggregates via self-assembly.

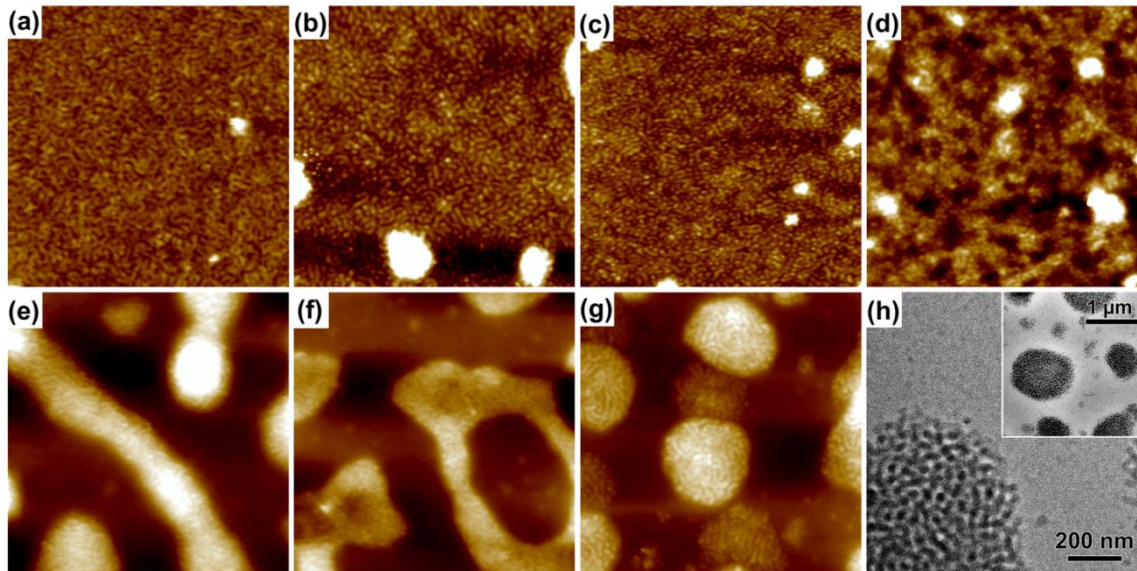


Figure 3-5. AFM height images ($2\ \mu\text{m} \times 2\ \mu\text{m}$) of the films of triblock/star copolymer mixtures of T1+S1 (a), T1+S4 (b), T1+S7 (c), S1+T2 (d), T1+S2 (e), S1+T3 (f) and T1+S3 (g) at a mixing ratio of 1:1 by weight. The Z scale is 15 nm for (a-d) and 40 nm for (e-g). (h) TEM image of the film in (g) with PVP blocks stained by iodine vapor, the inset is the large area TEM image.

In order to provide additional detail of the structure of these hierarchical aggregates, the film of T1+S3 mixture was characterized by TEM after using iodine to stain the PVP segments selectively. As shown in Figure 3-5h and its inset, the PVP blocks (darker regions) are generally organized into spherical domains separated by the brighter PS phase, and the large compound micelles have diameters ranging from ~ 500 to ~ 1000 nm that appear to consist of an aggregation of simple spherical micelles having PVP cores and PS coronae. There are some smaller compound micelles comprised of several simple micelles around the large ones that also can be seen in the AFM image (Figure 3-5g). In total, the results suggest that there are three typical

morphologies adopted in films comprised of self-assembled PS–PVP BCP mixtures, namely (i) spherical, (ii) worm-like, and (iii) hierarchical structures, each of which is represented by the binary mixtures D1+T1, D1+S1, and T1+S3, respectively.

While it is generally accepted that there is correspondence between the structures imaged in thin film form and those present in solution,^{32,113,116} the thin film structures imaged by AFM may be affected by changes in morphology due to solvent evaporation, surface interactions and spreading. Therefore, cryo-TEM imaging provides more direct information regarding the morphologies adopted by the BCP mixtures in solution.^{32,111} The representative mixtures of D1+T1, D1+S1 and T1+S3 were imaged by cryo-TEM at -175 °C, and representative images are presented in Figures 3-6a-c. As shown in Figure 3-6a, simple spherical micelles with an average diameter of 36.7 ± 7.3 nm are clearly seen in the vitrified solution of D1+T1 mixture. The size of the micelles present in the solution as determined from the cryo-TEM images is slightly smaller than the horizontal particle size extracted from images of thin films acquired by AFM. We suspect this discrepancy is because the micelles spread horizontally as they collapse on surfaces due to the transverse shear stress and solvent evaporation during spin-coating. In the D1+T1 mixture, the diblocks and triblocks jointly participate in self-assembly and make up the hybrid micelles which generally consist of a spherical PVP core surrounded by PS coronal chains in toluene. In the case of D1+S1 mixture, no cylindrical aggregates are observed in the bulk solution – only spheres with an average diameter of 24.0 ± 4.6 nm are observed, as shown in Figure 3-6b. This fact indicates that the worm-like structures observed when thin films were imaged are mainly due to the merging of spherical micelles during the spin coating process. The obvious morphological reconstruction in thin films occurs in specific BCP mixed systems and

appears to be linked to certain component architectures. For T1+S3 mixture, as shown in Figure 3-6c, large compound micelles with a diameter of ~350 nm are observed, their sizes are much larger than those of simple spherical micelles, and are highly polydisperse. Notably, no hierarchical structures can be seen on the swollen large compound micelles in toluene solution. Therefore, the hierarchical structures in thin films as shown in Figure 3-5g are also formed during the solvent removal process, due to the substantial collapse of PS microdomains.

The self-assembly properties of PS–PVP BCP binary mixtures in toluene at $c = 8.0$ mg/mL were also investigated by DLS. They exhibit bimodal and even trimodal R_h distributions, as observed from results presented in Appendix A. In Table 3-2 the hydrodynamic sizes of the aggregates are presented using R_{h1} and R_{h2} for the systems with bimodal distributions and R_{h1} , R_{h2} and R_{h3} for the systems having trimodal R_h distributions. The R_{h2} and R_{h3} values in the bimodal or trimodal systems that adopt simple spherical micelles are usually much larger than the sizes deduced from AFM and cryo-TEM imaging (e.g., D1+T1 mixture), suggesting the formation of aggregates.

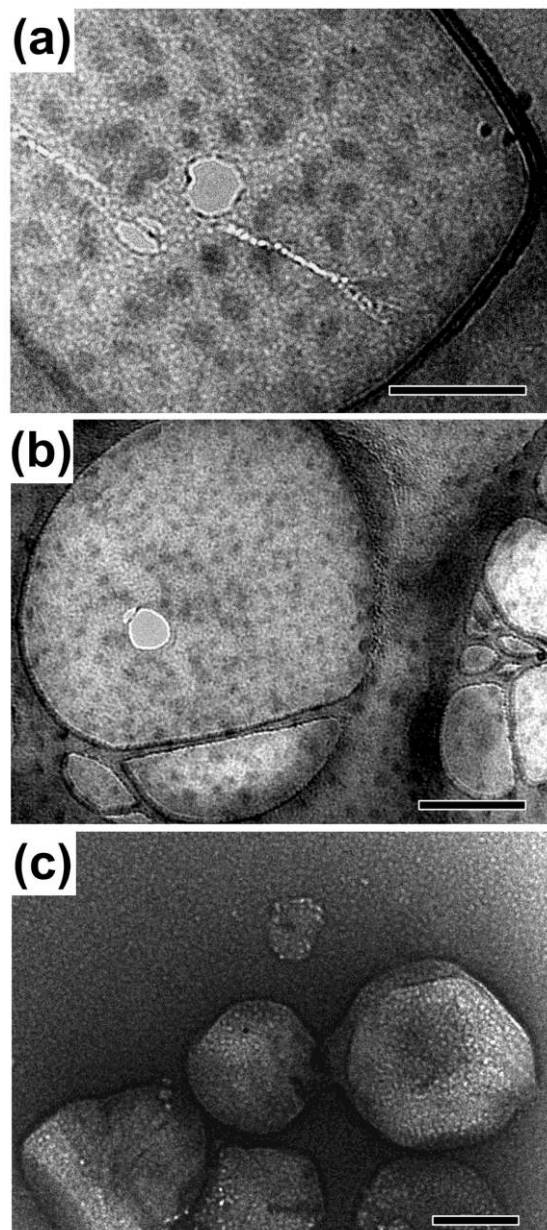


Figure 3-6. (a-c) Cryo-TEM images of the BCP mixtures of D1+T1 (a), D1+S1 (b) and T1+S3 (c) at a mixing ratio of 1:1 by weight in toluene. The scale bar is 200 nm.

The R_{h2} values corresponding to the large compound aggregates present in the bimodal systems are sometimes much smaller than the sizes obtained by AFM (e.g., T1+S2 mixture); we believe this is due to the problem of multiple scattering by the large particles, which leads to a falsification of the angular distribution of scattered light that impacts the measured particle size distribution.¹¹⁷ While multiple scattering can be avoided by using solutions of low concentration (e.g., at 1.0 mg/mL), the micellar aggregates disassemble or the mixtures show different self-assembly behaviors at this concentration (see Appendix A), due to the high CMCs for the parent BCPs.

3.4.3 Compositionally complex binary BCP mixtures.

The average composition of the blend is known to be an important variable that strongly affects the self-assembled structures in systems where the parent BCPs have the same molecular architecture (e.g., diblock+diblock copolymer mixtures).²⁷ In this study, the mixtures are made from two BCPs with different macromolecular architectures. As shown in Table 3-2, BCP mixtures with different component architectures display diverse self-assembled structures in thin films, even though they have an identical average composition. This points to component architecture as a significant factor in the self-assembly behaviors of BCP mixtures, rather than the average composition of the blend. To support this contention, the composition-controlled self-assembly of BCP mixtures is illustrated using three PS-PVP BCP mixtures with BCP components of different architecture. Table 3-3 lists components used and the mixing strategy, and for convenience, we substitute the average composition of the blend for the mass fraction of

the component. In the binary mixtures, the mass fractions of polymer I gradually decrease from 100% to 75% to 50% to 25% to 0%, with the mass fractions of polymer II increasing correspondingly.

As shown in Figures 3-7a and 3-7b (as well as results presented in Figures 3-2 and 3-4), thin films made by mixtures of D1+T1, produce films with spherical aggregate structures for all blend compositions. Figure 3-8a presents the horizontal radii and the vertical heights of the aggregates in the films versus the mass fraction of T1 in D1+T1 mixtures. Both the horizontal and the vertical sizes of the particles formed from D1+T1 mixtures increase with the increasing fraction of T1 component, mainly because of the larger micelle size for T1 than that for D1. As the spherical particles formed from binary BCP mixtures usually show particle sizes that are intermediate or approximately equal to the ensembles made from the parent BCPs (see Tables 3-1 and 3-2), the results show that the particle sizes can be adjusted in a small range by tailoring the mixing ratio.

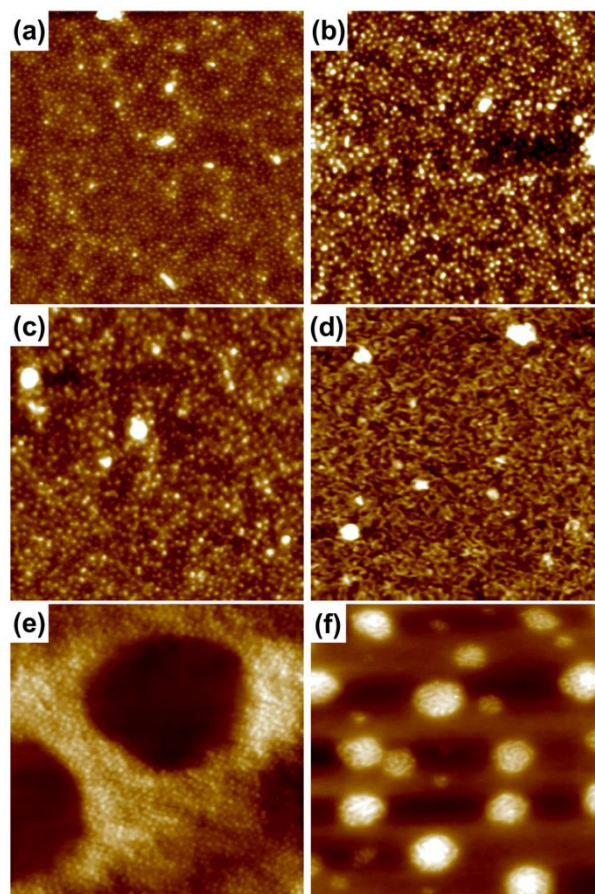


Figure 3-7. AFM height images ($2\ \mu\text{m} \times 2\ \mu\text{m}$) of the films of BCP mixtures of D1+T1 (a, b), D1+S1 (c, d) and T1+S3 (e, f) at mixing ratios of 3:1 (a, c, e) and 1:3 (b, d, f) by weight. The Z scale is 15 nm for (a-d) and 40 nm for (e, f).

As to the self-assembly of D1+S1 copolymer mixtures in thin films, the parent D1 and S1 copolymers adopt simple spherical aggregate structures, as seen in Figure 3-2. The D1+S1 mixture at a mixing ratio of 3/1 by weight (Figure 3-7c) shows spherical aggregate structures with an average horizontal radius (in the plane of the film) of $30.7 \pm 5.6\ \text{nm}$ and an average height (out of the plane of the film) of $3.0 \pm 0.8\ \text{nm}$, while D1+S1 mixtures at mixing ratios of

1:1 (Figure 3-4b) and 1:3 by weight (Figure 3-7d) produce films with cylindrical aggregate (worm-like) structures having horizontal diameters of the cylinders of ~ 34 and ~ 22 nm, respectively. The complex molecular architecture of the star copolymers is likely the origin of structural variation that can be realized in their micellar aggregates. The introduction of a small amount of diblock D1 into the star S1 system allows them to change their structure from spherical to cylindrical aggregates. This is reflected in the small cylindrical aggregates formed when D1+S1 mixture at a mixing ratio of 1:3 by weight is cast into thin films. Further addition of D1 to 50 wt% causes a maximum degree of hybridization in the mixed systems, and the mixture microphase segregates into large cylindrical aggregates. When the fraction of D1 in the mixture reaches 75 wt%, the self-assembly behavior of the mixed system is dominated the self-assembly behavior of D1, and the mixed system recovers the spherical aggregate structures.

Previously it was shown that spin casting the 1/1 mixture of T1+S3 creates the unusual, hierarchically structured aggregates that resemble a brain coral. Self-assembled mixtures of T1+S3 with a T1 fraction of 75 wt% adopt spherical structures when cast as thin films (Figure 3-7e), with the aggregates having an average in-plane radius of 28.1 ± 4.5 nm. In contrast to other mixtures, this film does not completely cover the surface – there are micropores with a horizontal radius of ~ 600 nm and a vertical depth of ~ 40 nm (Figure 3-7e). When the relative amount of S3 is increased to 75 wt%, as shown in Figure 3-7f, hierarchical morphologies with spherical primary and worm-like secondary structures are observed. The primary particles have an average horizontal diameter of 286 ± 94 nm, which is smaller than the brain coral-like aggregates made from the T1+S3 copolymer mixture at a mixing ratio of 1:1 (by weight), due to the low degree of hybridization for the 1/3 mixture of T1+S3.

Table 3-3. Mixing strategy by varying blend composition.

polymer I	polymer II	morphology ^a	mass fraction of polymer II in the blend				
			0 %	25 %	50 %	75 %	100 %
D1	T1	S	1.7 ^b	1.5	1.3	1.1	1
D1	S1	W	1.7	1.5	1.3	1.1	1
T1	S3	H	1	1.4	2.2	3.6	7

^aMorphology of aggregates in thin films at a mixing ratio of w:w = 1:1, using S for spherical aggregate structures, W for worm-like structures, and H for hierarchical structures). ^bAverage composition (average S/V) of the blend.

The film morphologies observed from the three BCP mixtures as a function of blend composition are summarized and presented in Figure 3-8b. As shown in Figure 3-8b, the mixtures exhibit spherical aggregate structures when the mass fraction of linear BCPs – either diblock D1 or triblock T1 – exceeds 50%. However, D1+S1 and T1+S3 copolymer mixtures can form worm-like and hierarchically structured aggregates, respectively, when the fraction of star copolymer in the blend reaches or exceed 50 wt%. We suspect that these complex microphase separated film structures arise because mixing the linear and star block copolymers provides additional degrees-of-freedom in terms of how the macromolecules balance chain stretching and segregation and interface creation during self-assembly.¹¹⁸ From the results of three typical BCP mixtures at different compositions, we can conclude that linear BCPs have the tendency to guide the mixtures to form spherical aggregate structures.

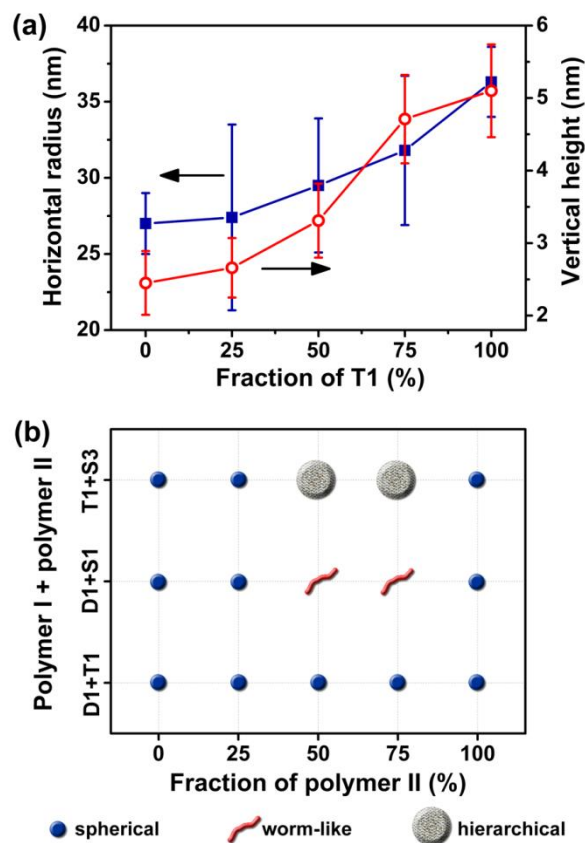


Figure 3-8. (a) Horizontal radius and vertical height of the microdomains in the films of D1+T1 BCP mixtures as a function of the mass fraction of T1. The error bars reflect the standard deviation of replicate measurements ($n = 20$). (b) Dependence of film morphologies of three typical BCP mixtures as a function of the mass composition of the blended BCPs.

In contrast, and although star copolymers tend to adopt spherical aggregate structures on their own, the complex architecture endows them with the latent capacity to dominate the formation of ensembles, steering the mixed system toward more complex shapes. Moreover, while the architectures of the component block copolymers has primary influence on the

structure adopted by the micellar aggregates in binary mixtures, minor changes in the structures can be achieved by adjusting the average composition of the blend.

3.5 Conclusions

We have presented a systematic study on self-assembly of complex surfactant-like BCPs and their binary mixtures that are diverse in their architectures and compositions. Our findings demonstrate that the combination of mixing chains of different architectures and compositions changes the self-assembly behavior, leading in some cases to more complex aggregate structures, particularly upon reconstruction during spin casting, which allows worm-like structures and exotic hierarchical aggregates to be formed. The origin of these behaviors is attributed to the ability of the mixed systems to mediate interfacial curvature and chain stretching. While the rules governing self-assembly of complex BCPs and the relationships between solution and thin film structures are yet to be elucidated, this study points toward new approaches for making unusual and sophisticated structures from simpler building blocks and the development of useful novel nano- and meso-structures and devices based on soft matter.

**Chapter 4: Solution Properties of Architecturally Complex Multiarm Star
Diblock Copolymers in Non-selective and Selective Solvents for the Inner
Block**

4.1 Abstract

In comparison to the behavior of linear block copolymers, much less is known about the structure and properties of highly branched polymeric materials. Motivated by this, the solution properties of a series of 26- and 40-arm polystyrene-poly(2-vinylpyridine) (PS-PVP) star diblock copolymers of different weight-average molecular weight (M_w) and styrene to 2-vinylpyridine (S/V) ratios are studied. These stars are investigated in tetrahydrofuran, THF, a thermodynamically good solvent for both blocks, and in toluene, a solvent that is selective for the inner PS block. It is found that in both THF and toluene the 26- and 40-arm stars remain dispersed as unimolecular star block copolymers. The hydrodynamic radius, R_h , increases with PS M_w and number of arms, with the stars of highest M_w and number of arms having the largest R_h . Concentration studies show that each star maintains its characteristic size: at low and at high concentration, the R_h and the radius of gyration, R_g , remain constant across the concentration range studied. R_g/R_h or ρ ratio is ≈ 1.0 , suggesting that these stars do not behave as homogenous hard spheres, but rather exhibit Gaussian soft sphere characteristics. TEM images indicate that these stars form an asymmetric structure in toluene due to the intramicellar microphase segregation of the arms: The PVP blocks collapse and aggregate within the unimolecular structure while the PS blocks stretch and shield the aggregated PVP domain. Despite the strong tendency of PVP blocks to aggregate in toluene, repulsive steric interactions between solvated PS blocks prevent PVP domains of selectively-solvated stars from aggregating and forming multimolecular aggregates. These results shed new light on how block copolymers of complex architecture organize in solution.

4.2 Introduction

Amphiphilic (“dual loving”) block copolymers (ABCs) are macromolecular analogs of surfactants that contain solvophobic and solvophilic blocks that are linked by covalent bonds. For example, polystyrene-poly(2-vinylpyridine) (PS-PVP) diblock copolymers are archetypal ABCs: when dissolved in a selective solvent such as toluene, which is thermodynamically good for PS but poor for PVP, PS-PVP diblock copolymers can undergo microphase separation, creating micellar ensembles by self-assembly. The size and shape of the aggregate depend on the sizes of the constituent blocks, with spherical, cylindrical and vesicular structures forming due to the tendency of the blocks to microphase segregate in the selective solvent.² The insoluble PVP blocks segregate to the inside, or core, of the micelle in a PS-selective solvent, while the soluble PS blocks remain in contact with the solvent, forming the corona of the micelle.

Micellization of block copolymers occurs at or above the critical micelle concentration (CMC) with the assembly driven by a balance of repulsive interactions between stretched, solvated blocks of the corona, the desire of the non-solvated blocks to minimize contact with the solvent, and the cost of creating an interface between the soluble and insoluble blocks.¹¹⁹ There are two main models that describe micellization. The first is the open association model, which describes the formation of micelles with no unimers in solution. However, this model is rarely appropriate because it suggests that a CMC does not exist: the copolymers readily aggregate, forming structures with no well-defined number of chains (thus leading to a distribution of aggregate sizes). The second, the closed association model, describes the formation of micellar structures at and above the CMC with thermodynamic equilibrium established between those well-defined aggregates and single chains that are present in solution.^{10,120}

The spontaneous generation of complex, well-organized structures from polymeric building blocks in which domain sizes, properties and interactions can be set by the variety of monomer types that can be used, and finely controlled by tailoring block sizes and relative volume fractions has found use in the medical and chemical industries. For example, spherical micelles and vesicles are candidates for the delivery of drugs in the fight against diseases, such as cancer.^{120,121,122} In this application, ABCs enhance drug solubilization/stabilization and the encapsulation alters the pharmacokinetic profile, providing a way to control drug release.²⁸ ABCs may also find application in environmental remediation because they can solubilize contaminants present after an environmental disaster, such as an oil spill.²⁰ ABCs can also be used to form patterned surfaces for microelectronics and bit-patterned media, as well as to pattern catalytic sites.^{123,16}

While the volume fraction, degree of polymerization, and interaction energies dominate the morphological phase behavior of ABCs, architecture (topology) also affects self-assembly.^{10,50} Due to recent advances in living polymerization techniques, architecturally complex star diblock copolymers and homopolymers with numbers of arms ranging from 3 to greater than 100 have been synthesized with low polydispersities.^{124,42,125} In comparison to an enormous number of studies focused on linear ABCs, there are few reports on solution and surface self-assembly properties of multiarm star diblock copolymers.¹²⁶⁻²¹ Highly dense multiarm star block copolymers have the unique ability to form thermodynamically stable unimolecular constructs in solution.^{50,127} They also possess superior mechanical and rheological properties as compared to their linear counterparts of similar weight-average molecular weight (M_w).⁴⁹ Amphiphilic star block copolymers are architecturally different from heteroarm and

miktoarm stars. Heteroarm and miktoarm stars consist of two (or more) distinctly different types of homopolymer arms emanating from a single core, with heteroarm stars having an equal number of arms of each monomer type while miktoarm stars are asymmetric in the number of arms of each type.¹²⁸ Amphiphilic star block copolymers have arms consisting of covalently linked amphiphilic blocks emanating from a single core, which governs their self-assembly behaviors.^{50,51}

There are only a few reports of amphiphilic star block copolymers with a large number of arms having been studied in solution and at surfaces.^{45,50} With respect to varying solvent conditions, Nguyen *et al.* investigated two high molecular weight 18-arm star polyisoprene-*b*-polystyrene (from here on, the inner block is named first) diblock copolymers in six different solvents at 35 °C by light scattering. Two of the solvents used were good solvents for both blocks; another two were chosen such that each was selective for one of the blocks; and the final two were chosen so that they were isorefractive solvents with one of the individual blocks. The authors suggested that the highly stretched polystyrene blocks formed the corona of the star, whereas the polyisoprene blocks formed the core with the overall morphology displaying segregation between PS and PI domains. Furthermore, studies in the isorefractive solvents (chlorobenzene and bromoform, which are isorefractive good solvents for polyisoprene and polystyrene, respectively) showed that the blocks microphase segregated strongly, with the inner PI core being of similar geometric dimension to its corresponding 18-arm homopolyisoprene star.¹²⁹

It has been demonstrated that the number of arms and block composition can also affect the self-assembly behavior of architecturally complex star block copolymers. Strandman *et al.*

investigated the properties of poly(methyl methacrylate)-*b*-poly(acrylic acid) (PMMA-*b*-PAA) amphiphilic 8-arm and 4-arm star block copolymers in aqueous solution. A combination of simulation and experimental techniques was used to investigate the effects of salt, pH, ionic strength and arm number on the self-assembly. The critical aggregation concentration (cac) of the stars was dependent on the length of the hydrophobic PMMA block. Stars with longer hydrophobic blocks had a lower cac, and the aggregation number was dependent on the number of arms. Below the cac and in the absence of added salt, the stars existed as unimolecular micelles. The addition of salt caused a morphological transition in the 4-arm stars from spherical to worm-like aggregates. However, this phase transition was not observed with the more crowded 8-arm stars, due to the shielding effect of its arms.^{130,131,132}

With the knowledge that composition and architecture (geometric constraints) caused by attaching numerous arms about a central junction impact the self-assembly behavior of ABCs, we investigate the solution phase behavior of six PS-PVP star diblock copolymers of different M_w , styrene to 2-vinylpyridine ratio, S/V, and numbers of arms in a thermodynamically non-selective good solvent for both blocks and in a solvent that is selective for the inner PS block. In my previous studies (Chapter 3) focused on the structures adopted when ABCs of different architecture, size and composition are mixed, we characterized these six stars by DLS at the single concentration used for mixed self-assembly.¹³³ Here I use a combination of dynamic and static light scattering (DLS and SLS) and transmission electron microscopy (TEM) to elucidate solution structure and self-assembly behaviors as a function of macromolecular design in a systematic fashion as a function of concentration.

4.3 Experimental

4.3.1 Materials

Multiarm star copolymers were synthesized via anionic polymerization using custom built, all-glass reactors with breakseals. The polystyrene (PS) block is polymerized first in benzene at room temperature from an oligo(styryl)lithium grafted poly(divinylbenzene) core followed by crossover to polymerize 2-vinylpyridine in tetrahydrofuran (THF) at -78 °C. This synthetic approach yields polystyrene-*b*-poly(vinylpyridine) star block copolymers with outer PVP blocks that form the corona and that are covalently linked to the inner PS blocks. More details on the synthesis of these block copolymers can be found in an early publication.²⁴ The samples were characterized by a combination of multiangle laser light scattering, ¹H NMR, and elemental analysis,²⁴ and the results are summarized in the first three columns of Table 4-1. Throughout this Chapter, including in the tables and figures, the multiarm star copolymers are referred to as [PS_mPVP_n]_f where f is the average number of arms and the subscripts m and n refer to the molecular weight (M_w) of the PS and PVP blocks, in thousands, respectively. The styrene to 2-vinylpyridine ratio (S/V) is also reported. It is important to appreciate that the synthetic approach of using a crosslinked core from which the arms are grown and using fractionation to purify the stars naturally leads to a product that is disperse in terms of block length distributions, numbers of arms and, potentially, core size. Thus, even though we capture design variations with average measures (m, n, f and S/V) and one can calculate the average M_w by the product $f(m+n)$ we expect the samples to be more heterogenous even though anionic methods are used. THF (99%) and toluene (HPLC grade) were purchased from Alfa Aesar and used as received.

4.3.2 Block copolymer solution preparation.

THF and toluene stock solutions of the PS-PVP star block copolymers were prepared gravimetrically by adding solvent, filtered through 0.2 μm PTFE filters (Millipore), to bulk copolymer that was weighed into previously cleaned, dust-free vials. Stock solutions were equilibrated at room temperature for at least 5 days. Then, 24 h prior to a light scattering experiment, an aliquot was taken from the stock solution, transferred into a previously cleaned vial, and diluted with filtered solvent (0.2 μm PTFE) to create a solution of the desired concentration. Concentrations examined ranged from nominally 0.001 mg/mL to 10.0 mg/mL. A total of five concentrations were studied.

Table 4-1. Macromolecular properties of 26- and 40-arm star diblock copolymers.

Sample ID ^a	PDI	S/V	c(mg/mL)	$R_{h,app}^b$ (nm)	$R_{h,app}^c$ (nm)	D_0 (cm ² /s) ^d	$R_{h,0}$ (nm) ^d
Toluene							
[PS ₅₀ -PVP ₅₀] ₂₆	1.23	1	2.49	38	50	8.18×10^{-8}	48
[PS _{102.5} -PVP _{20.5}] ₂₆	1.45	5	2.47	57	59	7.01×10^{-8}	56
[PS _{103.8} -PVP _{11.5}] ₂₆	1.36	9	2.48	56	59	7.38×10^{-8}	53
[PS _{53.8} -PVP _{53.8}] ₄₀	1.26	1	2.32	52	61	6.63×10^{-8}	59
[PS _{106.3} -PVP _{21.3}] ₄₀	1.16	5	2.48	79	85	4.63×10^{-8}	85
[PS ₁₀₈ -PVP ₁₂] ₄₀	1.30	9	2.47	71	79	4.99×10^{-8}	79
THF							
[PS _{103.8} -PVP _{11.5}] ₂₆	1.36	9	3.06	60	59	8.99×10^{-8}	54
[PS _{106.3} -PVP _{21.3}] ₄₀	1.16	5	2.06	72	78	5.97×10^{-8}	81

^aThe multiarm star copolymers are referred to as [PS_mPVP_n]_f where f is the number of arms and the subscripts m and n refers to the molecular weight (M_w) of the PS and PVP blocks in thousands, respectively. ^b $R_{h,app}$ calculated from D_s values obtained from the slope of the best fit line of Γ versus q^2 at $c = 2.5$ mg/mL. ^c $R_{h,app}$ calculated from $\langle D \rangle_z$ values, which are obtained by extrapolating to zero scattering angle the best fit line through light scattering data plotted as Γ/q^2 versus q^2 at $c = 2.5$ mg/mL. ^dDiffusion coefficient and hydrodynamic radius found by extrapolation to $c = 0$. Concentrations are nominal values.

4.3.3 Characterization by light scattering and theory

The analysis procedures used with DLS and SLS can be found in Chapter 2.

4.3.4 Characterization by transmission electron microscopy

To prepare samples for imaging by transmission electron microscopy (TEM), a pipette was used to dropcast a small amount of polymer solution onto the carbon film grid, and the films were allowed to dry. Because of the rapid solvent evaporation and the high glass transition temperature, T_g , of PS (104 °C) and PVP (105 °C), the native morphology in solution is expected to be preserved.¹³⁴ Before imaging, the selected sample was stained by exposure to iodine vapor for 24 h, which renders the PVP microdomains dark in the images. Because carbon film grids were used, to facilitate imaging the entire structure, selected samples were also stained using ruthenium tetroxide (RuO₄), which stains both PS and PVP domains.¹³⁵ In addition, to provide contrast between the PS and PVP domains and the solid carbon film, we dissolved gold(III) chloride trihydrate in the star block copolymer solution and stirred for 24 h. The solution was subsequently dropcast and stained on carbon film grid using the procedure previously described. Gold(III) chloride trihydrate preferentially interacts with the PVP domains, rendering it darker than the PS blocks due to the formation of gold nanoparticles under the electron beam during TEM imaging.¹³⁶ Images were acquired at column temperature using a Zeiss Libra 200 MC transmission electron microscope. Gatan UltraScan US1000XP CCD camera was used to record the images using the Digital Micrograph software package.

4.4 Results and discussion

4.4.1 Hydrodynamics of architecturally and compositionally diverse star copolymers

The solution properties of the three 26-arm and the three 40-arm stars with varying block lengths and styrene to 2-vinylpyridine (S/V) ratios in the range of $1 \leq S/V \leq 9$ were investigated. Figures 4-1A and 4-1B show the normalized light intensity autocorrelation function for all of the stars at $c = 2.5$ mg/mL in toluene, which is preferential and thermodynamically good for the PS blocks. The decay of the autocorrelation function depends markedly on the size of the scattering particles, and in this case the light intensity autocorrelation functions are well-fit by a single exponential decay function, which suggests that there is only one population of scatterers in solution for each star. The normalized amplitude distribution functions for the 26-arm and 40-arm stars at $c = 2.5$ mg/mL are shown in Figure 4-1C and 4-1D, respectively. In Figure 4-1C, stars $[\text{PS}_{50}\text{-PVP}_{50}]_{26}$, $[\text{PS}_{103.8}\text{-PVP}_{11.5}]_{26}$ and $[\text{PS}_{102.5}\text{-PVP}_{20.5}]_{26}$ show broad distributions and the peak shifts to higher R_h as the total M_w of the star block copolymers increases. Figure 4-1D shows three relatively narrow distributions for the 40-arm stars with peaks for samples $[\text{PS}_{106.3}\text{-PVP}_{21.3}]_{40}$ and $[\text{PS}_{108}\text{-PVP}_{12}]_{40}$ overlapping, which indicates similar hydrodynamic sizes (size distributions) for these two high M_w 40-arm stars having medium and high S/V ratios. While it is possible to force the fitting to yield two narrower (but overlapping distributions), given the heterogeneity of the stars imparted by the synthesis and purification methods it seems unreasonable to do so.¹³⁷

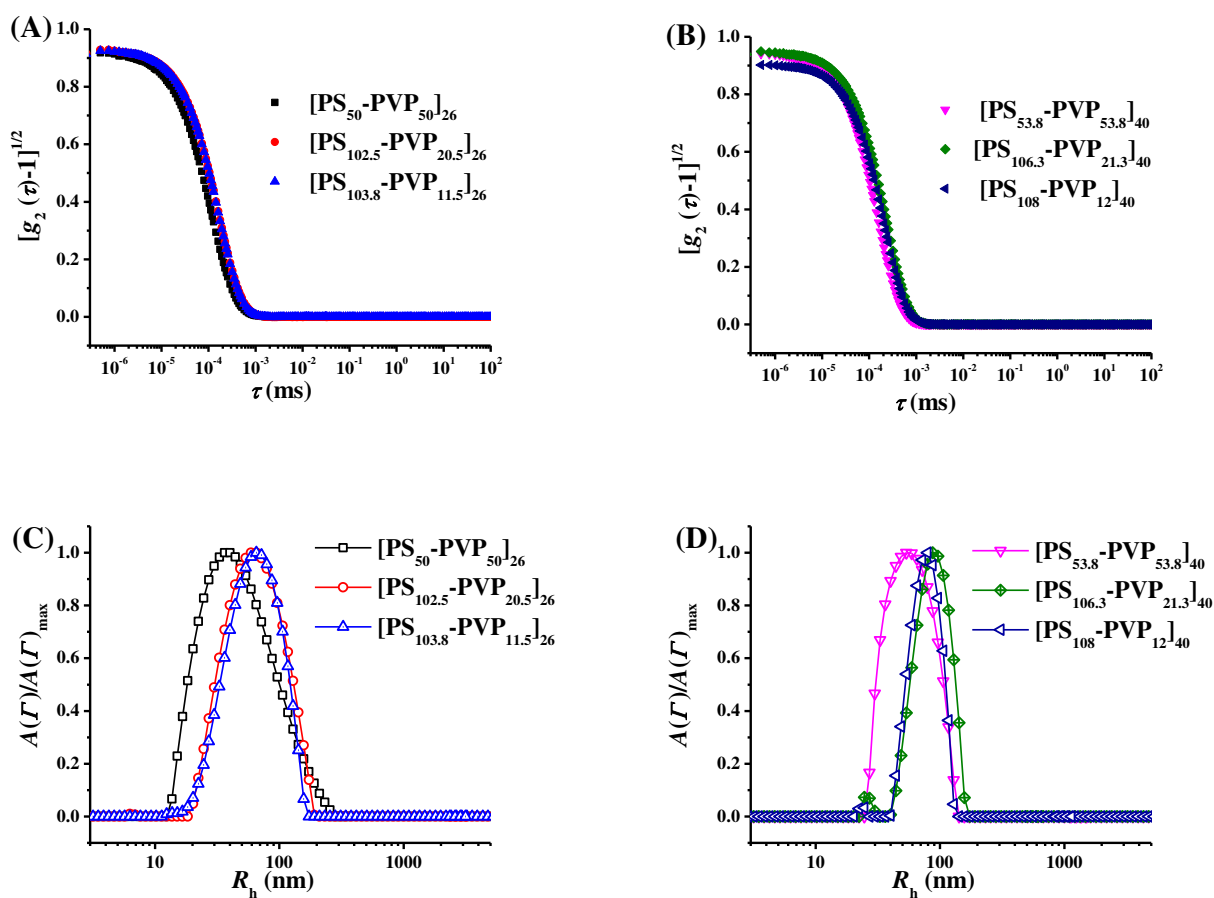


Figure 4-1. (A) Light intensity autocorrelation functions for the 26-arm stars and (B) the 40-arm stars in toluene at $c = 2.5$ mg/mL at a scattering angle of 88° . (C) Apparent hydrodynamic radii, R_h , distributions for the 26-arm stars and (D) the 40-arm stars at $c = 2.5$ mg/mL and a scattering angle of 88° . The colors and symbols are assigned and used consistently in other plots presenting data from DLS measurements in toluene. Concentrations are nominal values.

Figures 4-2A and 4-2B show the fits of the mean decay rate, Γ , versus q^2 for each of the 26-arm and 40-arm stars, at $c = 2.5$ mg/mL in toluene. Because the light intensity autocorrelation functions for the star copolymers were well-fit with a single exponential decay functions, there is a single decay mode that displays a linear dependence on the scattering wave vector, as shown in Figures 4-2A and 4-2B. The slight upturn at high q is a result of the high M_w of the stars.¹³⁷ Best-fit lines intersect the y-axis at $\Gamma \approx 0$, which suggests that the particle motion is governed solely by diffusive processes.⁹⁶ As a result, the slope of the line for each star yields the solution diffusion coefficient, D_s , and from it, the corresponding $R_{h,app}$ can be calculated using the Stokes-Einstein relation. The values of these are given in Table 4-1. The slope of the best-fit line through the data plotted as Γ/q^2 versus q^2 (at 36 different scattering angles) for each of the 26-arm and 40-arm stars shown in Figures 4-2C and 4-2D suggest slight deviation from homogeneous hard sphere diffusive behavior because of the small but noticeable q -dependence over the angular range studied.⁴⁴ The angular dependence also suggests non-rigid particles whose internal motions vary from the center of mass.⁶⁶ This subtle but important characteristic of the solution behavior of the stars will be revisited in a later section. The values of the $R_{h,app}$ obtained from $\langle D \rangle_z$ are reported in Table 4-1.

From the plots in Figure 4-2, it is evident that the 26-arm stars diffuse at a faster rate than the 40-arm, stars and as the total M_w of the stars increases, the stars diffuse at a slower rate, which suggests larger hydrodynamic radii. The two methods of data fitting, using either the slope from Γ versus q^2 or the y-intercept of Γ/q^2 versus q^2 , can yield different apparent hydrodynamic radii, as observed from the values reported in Table 4-1. The 26-arm star [PS₅₀-PVP₅₀]₂₆, which has an S/V ratio of 1, shows the largest difference in $R_{h,app}$ as a result of the two fitting methods.

The $R_{h,app}$ values calculated for the other star block copolymers by the two methods are otherwise consistent. Because the method of Γ/q^2 versus q^2 is more sensitive to dust, noise, and other sources of error, the true R_h at infinite dilution was calculated from $\langle D \rangle_z$ values obtained using data cast in this fashion. These results are discussed in a later section.

The hydrodynamic radius calculated for stars [PS_{103.8}-PVP_{11.5}]₂₆ and [PS_{106.3}-PVP_{21.3}]₄₀ in THF at a concentration of 3.06 and 2.06 mg/mL respectively are shown in Table 4-1. When dissolved in THF, a thermodynamically good solvent, it is expected that both of the blocks are well solvated and resist aggregation. However, it is observed that samples [PS_{103.8}-PVP_{11.5}]₂₆ and [PS_{106.3}-PVP_{21.3}]₄₀ have similar hydrodynamic radii in both the selective and the non-selective good solvents used here. This behavior suggests that even in a solvent selective for the inner PS blocks, these stars are not forming multimolecular aggregates in solution.

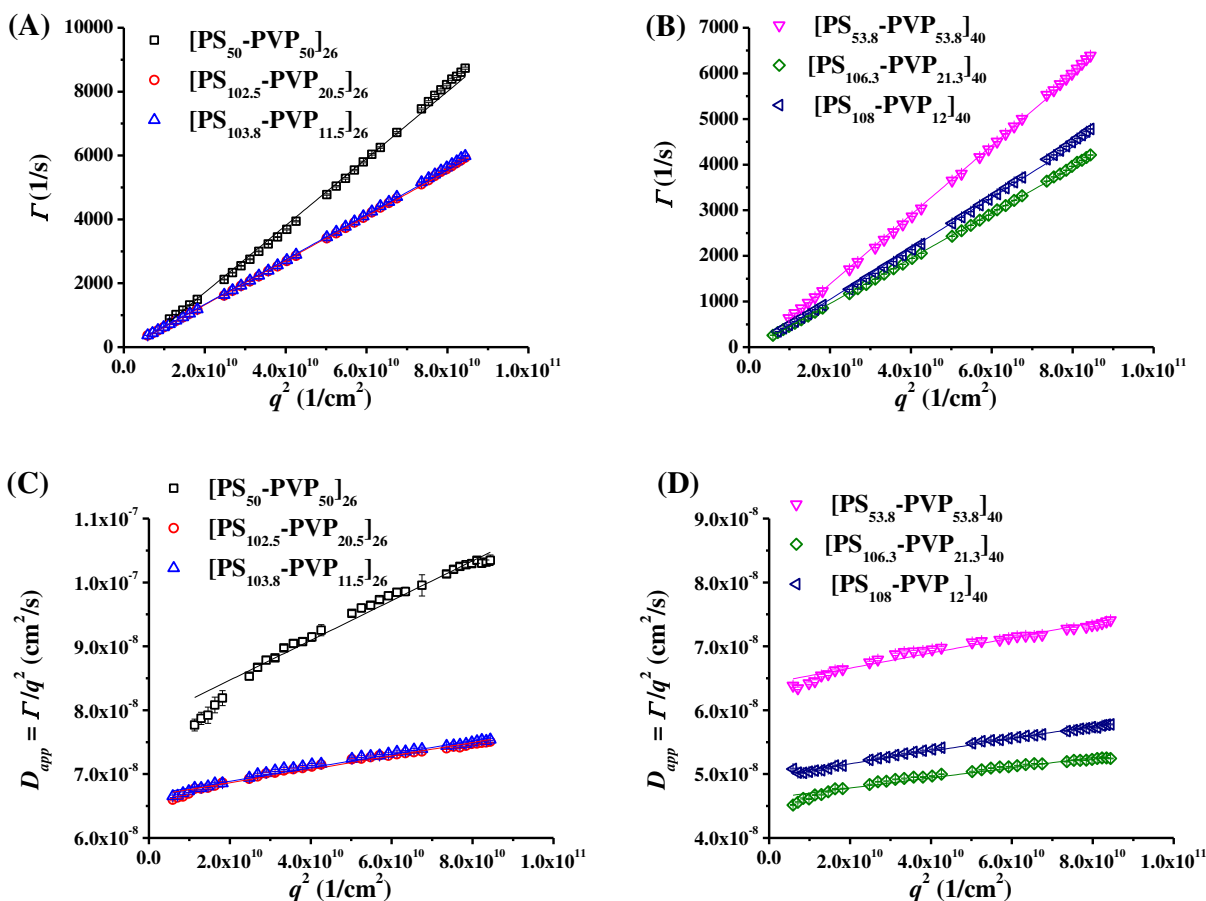


Figure 4-2. Mean decay rates, Γ , versus q^2 for the (A) 26-arm stars in toluene at $c = 2.5$ mg/mL and for the (B) 40-arm stars in toluene at $c = 2.5$ mg/mL. For plots (A) and (B) the solution diffusion coefficient, D_s , is obtained from the slope of the best-fit lines. The data, when recast as Γ/q^2 versus q^2 , allow $\langle D \rangle_z$ to be obtained for the (C) 26-arm stars in toluene at $c = 2.5$ mg/mL and the (D) 40-arm stars in toluene at $c = 2.5$ mg/mL by extrapolating the best fit line to $q^2 = 0$. The dependence of Γ/q^2 with respect to q^2 for all samples suggests that in a selective solvent for the inner block, the star diblock copolymers do not behave as hard spheres. Concentrations are nominal values.

Each of the star block copolymers was investigated by SLS, and representative results are shown in Figure 4-3, which displays the Zimm plots obtained for [PS_{103.8}-PVP_{11.5}]₂₆ in the PS-selective solvent toluene (left), and in the non-selective good solvent, THF (right). Zimm plots for all of the other stars are available in Appendix B. Because the intensity of the scattered light is proportional to the molecular weight of the scattering particle and $(dn/dc)^2$,¹³⁸ SLS provides an absolute measurement of the apparent weight-average molecular weight, $M_{w,app}$. The $M_{w,app}$, R_g , and A_2 values obtained from a series of SLS experiments at different concentrations (at least 2) and at numerous scattering angles⁶¹ are presented in Table 4-2. From Table 4-2 it should be noted that the $M_{w,app}$, R_g , and A_2 are of the same order-of-magnitude in both THF and toluene, which along with the hydrodynamic radii shown in Table 4-1, suggest that the amphiphilic star diblock copolymers remain as isolated, unimolecular stars in a selective solvent as well as in a thermodynamically good solvent for both blocks. SLS yields similar R_g values for the 26-arm stars, with [PS₅₀-PVP₅₀]₂₆ having the smallest R_g value, followed by [PS_{103.8}-PVP_{11.5}]₂₆ and [PS_{102.5}-PVP_{20.5}]₂₆. This pattern of behavior is consistent across the 40-arm stars, where the R_g of [PS_{53.8}-PVP_{53.8}]₄₀, is 1.4 times smaller than the R_g of stars [PS₁₀₈-PVP₁₂]₄₀ and [PS_{106.3}-PVP_{21.3}]₄₀. This trend is a direct result of the $M_{w,app}$ and the S/V ratio: [PS₅₀-PVP₅₀]₂₆ has the smallest R_g because it has the smallest $M_{w,app}$ and S/V ratio, while [PS_{102.5}-PVP_{20.5}]₂₆ has the largest $M_{w,app}$ (and an S/V=5). These results suggest that molecular weight of the PS block defines the size of the individual stars. The 26- and 40-arm stars of S/V=1, which have PS block sizes of nominally 50 kDa, clearly are smaller than the stars having PS block sizes that are nominally 100 kDa. The large difference in R_g between the 40-arm stars and the 26-arm stars is due to the dense topology of the macromolecule. Because of the large number of arms, size and

solution self-assembly is dominated by the intraparticle microphase separation and inter-arm repulsion.

Some insight into the shape of the stars can be gained from light scattering. The ρ -ratio ($\equiv R_g/R_{h,0}$) for each star in toluene is close to 1.0, which indicates Gaussian soft sphere, rather than hard sphere behavior.⁶⁶ In THF, star [PS_{103.8}-PVP_{11.5}]₂₆ has a ρ -ratio of 0.74, which suggests homogeneous hard sphere behavior.⁶⁶ These results point to the possibility that stars have different morphologies depending on solvent type, number of arms, and S/V ratio. Therefore, TEM also was used to image the star block copolymers, and these results are presented later.

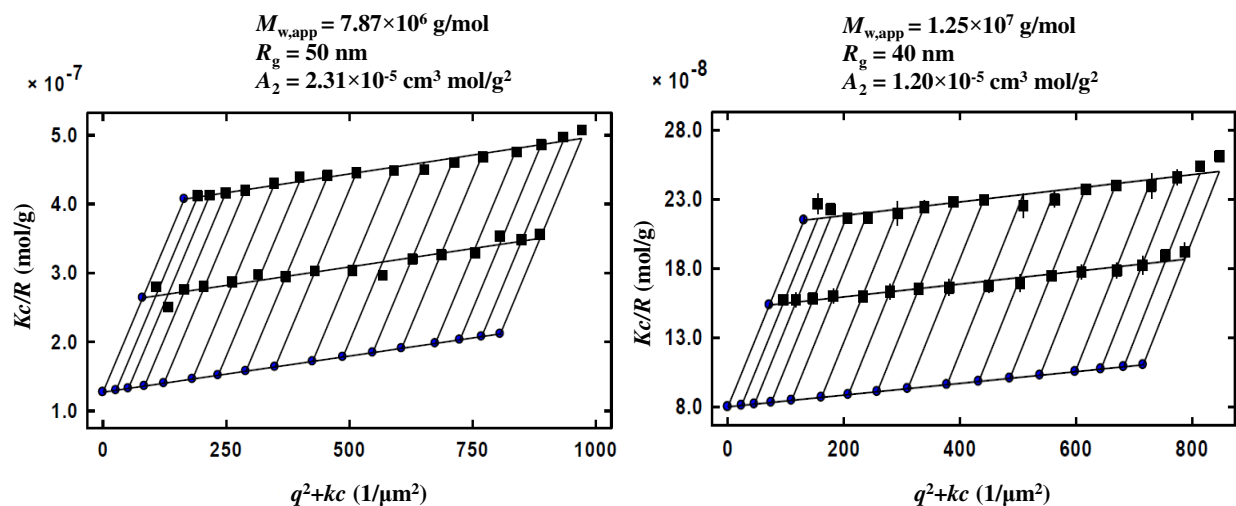


Figure 4-3. Zimm plots for star [PS_{103.8}-PVP_{11.5}]₂₆ in toluene, a selective solvent for the inner PS blocks (left), and in THF, a non-selective good solvent (right). Properties determined from the extrapolations to zero scattering angle, $q^2 = 0$, and to zero concentration, $c = 0$ are set above each Zimm plot.

Table 4-2. Static light scattering results for 26- and 40-arm star diblock copolymers.

Sample ID	S/V	dn/dc ^a (mL/g)	R_g^b (nm)	A_2 (cm ³ mol/g ²)	$M_{w,app}$ (g/mol) ^c	ρ^d	R_T (nm)	V_T^e
Toluene								
[PS ₅₀ -PVP ₅₀] ₂₆	1	0.104	46	5.20×10^{-5}	4.35×10^6	0.96	45	0.94
[PS _{102.5} -PVP _{20.5}] ₂₆	5	0.097	53	5.46×10^{-5}	2.05×10^7	0.95	129	2.3
[PS _{103.8} -PVP _{11.5}] ₂₆	9	0.106	50	2.31×10^{-5}	7.87×10^6	0.94	74	1.85
[PS _{53.8} -PVP _{53.8}] ₄₀	1	0.107	56	3.89×10^{-5}	1.07×10^7	0.95	75	1.27
[PS _{106.3} -PVP _{21.3}] ₄₀	5	0.106	75	3.11×10^{-5}	5.70×10^7	0.88	211	2.5
[PS ₁₀₈ -PVP ₁₂] ₄₀	9	0.085	79	3.91×10^{-5}	1.13×10^7	1.00	77	0.97
THF								
[PS _{103.8} -PVP _{11.5}] ₂₆	9	0.176	40	1.20×10^{-5}	1.25×10^7	0.74	56	1.04
[PS _{106.3} -PVP _{21.3}] ₄₀	5	0.192	75	1.70×10^{-5}	5.33×10^7	0.93	165	2.11

^aMeasured at $\lambda = 658$ nm. ^b R_g determined from Zimm analysis using at least 2 different concentrations. ^cApparent molecular weight, $M_{w,app}$, determined from SLS experiments. ^dThe ρ ratio is defined as $\rho = R_g/R_{h,0}$. ^eRatio describing the thermodynamic and hydrodynamic interactions $V_T = R_T/R_{h,0}$

Additional insight into the interaction between stars in solution can be obtained from values of the thermodynamically effective equivalent sphere radius, R_T . In contrast to $R_{h,0}$ that is derived from extrapolation to zero concentration, R_T is a result of the concentration dependence of light scattered and is calculated according to⁴⁶

$$R_T = \left(\frac{3}{16\pi} \frac{A_2 M_w^2}{N_a} \right)^{1/3} \quad (4.1)$$

R_T values are listed in Table 4-2 for the stars in toluene and THF along with the ratio $V_T = R_T/R_h$, which compares the relative importance of thermodynamic and hydrodynamic interactions between macromolecules and solvent. When this ratio is close to unity, it suggests that the thermodynamic and hydrodynamic interactions act over similar distances and as the ratio approaches zero, the corona makes no contribution to the excluded volume indicating theta solvent conditions.¹³⁹ The V_T for all stars are reported in Table 4-2.

4.4.2 Concentration study

The effect of solution concentration on the size of the star block copolymers was examined using light scattering measurements, and the results are presented in Figure 4-4. Figure 4-4A shows the concentration dependence of R_h for the 26- and 40-arm stars in toluene. For all samples, ranging from low ($c \approx 0.001$ mg/mL) to high concentration (≈ 5.5 mg/mL), the R_h remains constant. This lends further support to the conclusion that these stars form unimolecular micelles in toluene, resisting aggregation as the concentration is increased due to the shielding effects brought about by the large number of arms.⁴³ Because these systems maintain these behaviors over a wide range of concentration, it suggests that amphiphilic star block copolymers

are promising candidates as nano-carriers for a variety of applications.¹⁴⁰ The change in $\langle D \rangle_z$ over the concentration range studied is presented in Figure 4-4B. Values of D_0 were extracted from the y-intercept of the best fit line according to equation 2.17 and k_D values were obtained from the slope. These are presented in Table 4-1 and Table 4-3, respectively. k_D values can be used to gain insight into the thermodynamic and frictional interactions between polymer and solvent. For these stars in toluene, the small but negative k_D values seem to suggest poor solvent conditions due to attractive interactions between the stars,^{36,96,141} but the DLS measurements give no indication of aggregation. According to Lodge *et al.*,³⁶ k_D can be defined as $k_D = 2A_2M_w - k_f$, where k_f characterizes the frictional drag that opposes the motion of the molecule. For all stars in toluene and for star [PS_{103.8}-PVP_{11.5}]₂₆ in THF, A_2 values are all positive. The fact that k_D values of the stars in toluene are less than 0 means that k_f is greater than $2A_2M_w$, which implies that frictional interactions are stronger than thermodynamic star-star interactions. This behavior has also been observed for PI and PS homopolymer stars in good solvents.¹⁴²⁻¹⁴³ For star [PS_{106.3}-PVP_{21.3}]₄₀ in THF, the k_D value is small but positive, which suggests good solvent conditions and that the thermodynamic star-star interactions are greater than frictional interactions. Overall, the k_f values show a very interesting dependence on the design of the star block copolymers: Stars of $S/V = 5$ exhibit greater frictional interactions (k_f) than the other compositions, both in toluene and THF, and the 40-arm stars have larger k_f values compared to their 26-arm analogs.

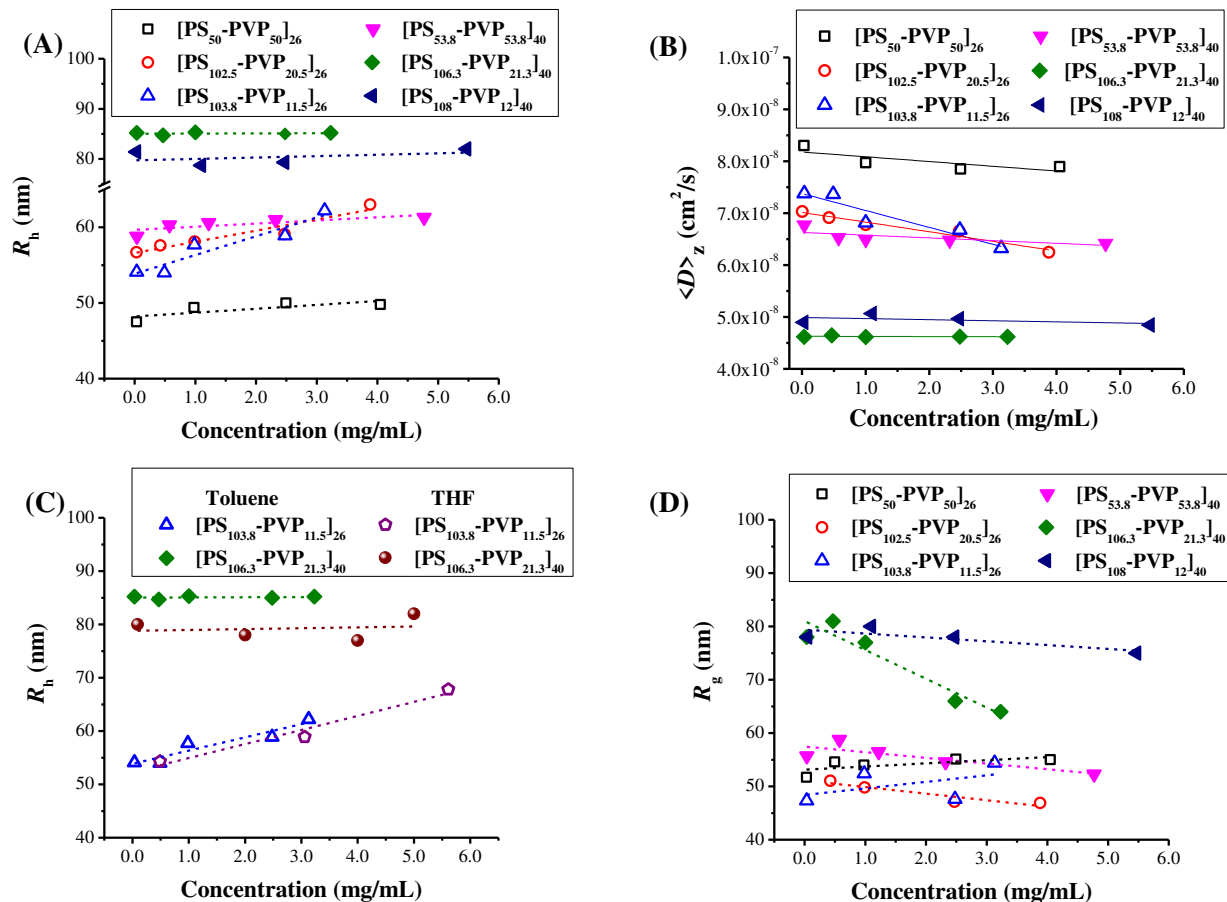


Figure 4-4. Dependence of R_h on concentration for 26- and 40-arm stars in toluene (A). Dependence of $\langle D \rangle_z$ on concentration for 26- and 40-arm stars in toluene (B). Comparison of the concentration dependence of R_h for samples $[PS_{103.8}-PVP_{11.5}]_{26}$ and $[PS_{106.3}-PVP_{21.3}]_{40}$ in toluene and THF (C), the concentration dependence of R_g for 26- and 40-arm stars in toluene (D). (Solid lines in (B) are fits to the data obtained from equation 2.17 while the dashed lines in (A), (C) and (D) are trend lines to guide the eye.)

Table 4-3. Hydrodynamic and frictional interactions for 26- and 40-arm star diblock copolymers.

Sample ID ^a	PDI	S/V	k_D (mL/mg)	k_f (mL/mg)
Toluene				
[PS ₅₀ -PVP ₅₀] ₂₆	1.23	1	-1.12×10^{-2}	0.464
[PS _{102.5} -PVP _{20.5}] ₂₆	1.45	5	-2.65×10^{-2}	2.27
[PS _{103.8} -PVP _{11.5}] ₂₆	1.36	9	-4.42×10^{-2}	0.408
[PS _{53.8} -PVP _{53.8}] ₄₀	1.26	1	-7.88×10^{-3}	0.840
[PS _{106.3} -PVP _{21.3}] ₄₀	1.16	5	-5.72×10^{-4}	3.55
[PS ₁₀₈ -PVP ₁₂] ₄₀	1.30	9	-4.41×10^{-3}	0.834
THF				
[PS _{103.8} -PVP _{11.5}] ₂₆	1.36	9	-3.44×10^{-2}	0.334
[PS _{106.3} -PVP _{21.3}] ₄₀	1.16	5	$+4.74 \times 10^{-3}$	1.81

The effect of concentration on hydrodynamic size, R_h , in selective and non-selective solvents was investigated for two selected stars, [PS_{103.8}-PVP_{11.5}]₂₆ and [PS_{106.3}-PVP_{21.3}]₄₀, and the results are shown in Figure 4-4C. For these 26-arm and 40-arm stars, the same trend is observed in THF and in toluene: the R_h remains constant over the concentration range studied. R_g values were determined from SLS measurements to investigate the effect of branching, M_w , and S/V ratio as a function of concentration, and these results are shown in Figure 4-4D. The R_g

values are basically independent of concentration and S/V , but more dependent on the overall M_w and number of arms, suggesting that as the arms are diblocks of uniform M_w and composition, crowding induced by the number of arms dominates the size of the stars. It should be noted that the same trend in R_h is observed in Figure 4-4A.

4.4.3 TEM

The morphology of the star block copolymers was investigated by TEM using staining techniques involving I_2 , RuO_4 and a combination of RuO_4 and Au (III) stainings, which together can be used to identify the microstructural arrangement of PVP and PS blocks of the star block copolymers. Figure 4-5 displays TEM images of the $[PS_{50}\text{-PVP}_{50}]_{26}$ and $[PS_{53.8}\text{-PVP}_{53.8}]_{40}$ star block copolymers drop cast from toluene on copper-supported carbon film grids. Figure 4-5A shows an image of $[PS_{53.8}\text{-PVP}_{53.8}]_{40}$ stained with I_2 . From this image it appears that the star block copolymers do not have hard sphere morphologies previously inferred from light scattering by Roovers *et al.* for highly dense 64- and 128-arm homopolymer stars in a good solvent.⁴⁶ Rather, the PS-PVP star block copolymers studied here adopt oblate shapes in a selective solvent, with a characteristic diameter of ~ 30 nm. The image also confirms these stars remain as isolated macromolecules in solution. Figure 4-5B, acquired after I_2 staining, shows that $[PS_{50}\text{-PVP}_{50}]_{26}$ stars drop cast from toluene also adopt this structure with a diameter of ~ 20 nm. While I_2 stains PVP only, the overall structure of $[PS_{53.8}\text{-PVP}_{53.8}]_{40}$ sample cast from toluene solution is revealed when RuO_4 is used to stain both PS and PVP blocks.¹⁴⁴ From Figure 4-5C we can see that the entire star has a diameter of approximately 60 nm. Once again, it appears that the stars are not spherical in shape, but slightly oblate.

To clearly identify where the PVP blocks are in relation to the PS blocks and to investigate the degree of microphase separation between the two incompatible blocks, a double staining technique using gold (III) chloride trihydrate and RuO₄ was used. The mechanism of gold (III) chloride trihydrate staining of PVP is described by Spatz *et. al.*¹³⁴ An image of [PS_{53.8}-PVP_{53.8}]₄₀ stained in this fashion is shown in Figure 4-5D. Here the RuO₄ stained PS blocks appear lighter than the gold-coordinated PVP blocks that have higher electron density compared to the PS blocks: Regions containing PVP are marked by a cluster of tiny dark spots, which are generated by the reduction of gold ions by the electron beam during exposure.¹³⁴ The lighter regions that surround the PVP blocks are the RuO₄ stained PS blocks, which otherwise would not be visible because of their low electron density.¹³⁶ From the image, it is seen that the PVP end blocks collapse and aggregate within a region of the star, while the PS blocks stretch to remain in contact with the solution. In so doing, the PS chains shield the PVP blocks from the solvent, forming a type of asymmetric structure that is depicted in the cartoon inset in Figure 4-5D.

The identification of a segregated morphology driven by intramolecular microphase separation that result in PVP blocks collapsing in the inner region seems surprising given the high level of geometric constraint in these star diblock copolymers. Conceptually, it might be reasonable to expect that the poorly solvated PVP blocks would simply collapse upon their contour length, segregating at the PS/PVP interface, or possibly bury themselves within the star as ways to minimize contact with toluene. However, both of these possibilities would lead to more unfavorable contacts between PVP segments and either PS segments or solvent toluene than if multiple PVP blocks were able to “find” each other and segregate themselves from toluene or PS segments. The structure in which PVP blocks are collapsed but at the periphery of

the structure would seem to invite multi-star aggregation. Thus, the type of structure implied by the image produced using dual staining (Figure 4-5D) and depicted in the inset cartoon would allow the stars, particularly those with long PVP blocks, to remain isolated due to repulsive intermolecular interactions between the well-solvated PS blocks that shield the PVP domain. This structural behavior also would seemingly lead to reduce frictional interactions between the stars.

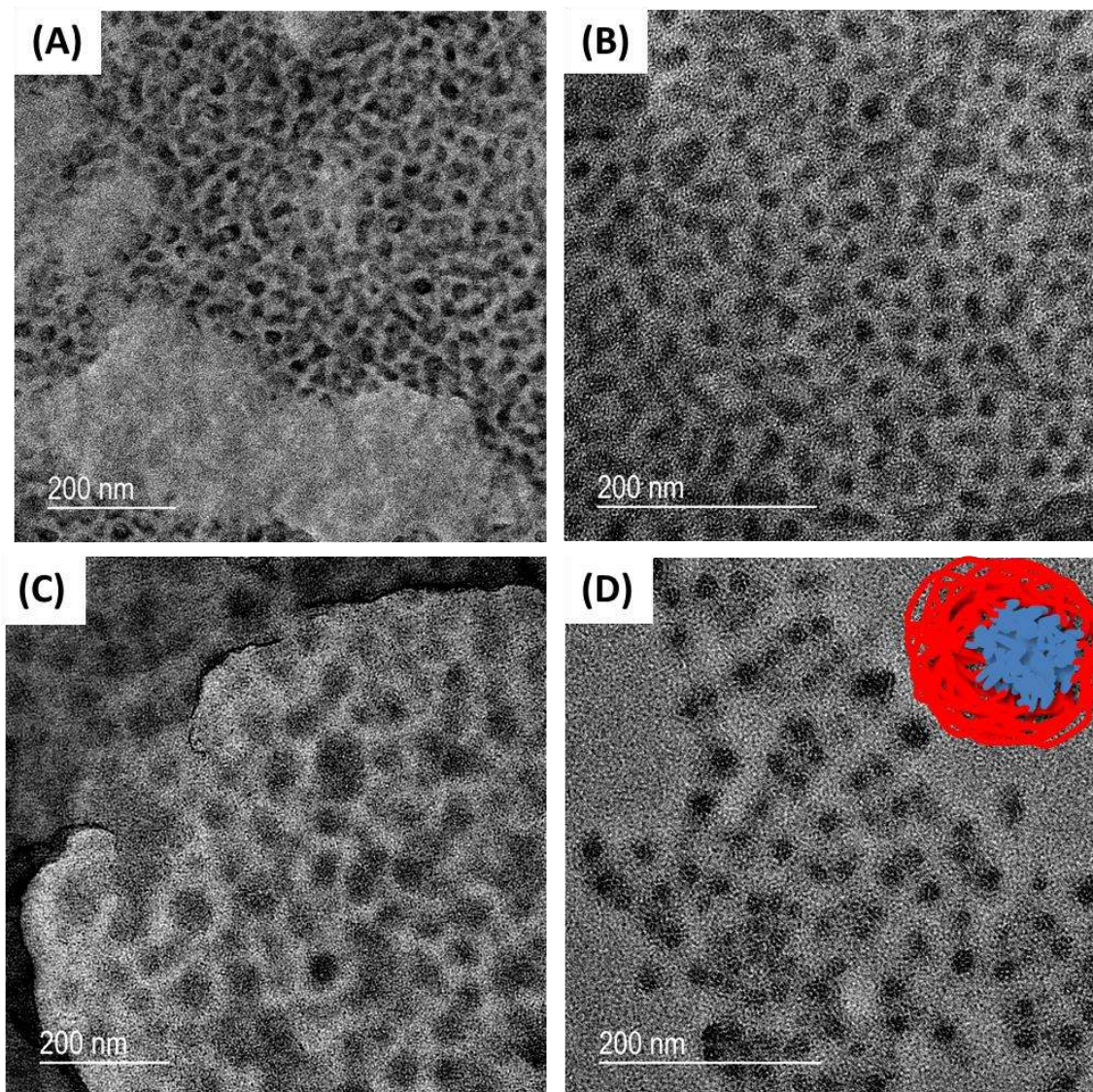


Figure 4-5. TEM images of (A) the 40-arm star $[\text{PS}_{53.8}\text{-PVP}_{53.8}]_{40}$, and (B) the 26-arm star $[\text{PS}_{50}\text{-PVP}_{50}]_{26}$ drop cast from toluene solutions with PVP blocks stained by iodine vapor. TEM image of (C) $[\text{PS}_{53.8}\text{-PVP}_{53.8}]_{40}$ drop cast from toluene solution with both PS and PVP blocks stained using RuO_4 . TEM image of doubly-stained (D) $[\text{PS}_{53.8}\text{-PVP}_{53.8}]_{40}$ deposited from a toluene solution containing gold (III), which coordinates with PVP blocks. The dried film is subsequently exposed to RuO_4 vapors. This double staining method renders the PVP blocks

appear darker than the PS blocks, as described in text. Based on this series of images, a drawing (inset) of how the stars rearrange in toluene, a selective solvent for the PS (red) blocks, is developed.

4.5 Conclusions

The solution properties of six architecturally complex 26- and 40-arm star block copolymers of varying molecular weight, and S/V ratio have been investigated. DLS and SLS experiments suggest that highly dense, architecturally-complex stars with a large number of arms resist aggregation in solution with the overall molecular weight and the large number of arms dictating their solution properties. Basic physical and thermodynamic properties were measured and the phase behavior of the macromolecular structure was established in a selective and non-selective good solvent. The intramolecular interactions dominate the solution self-assembly and phase behavior of high molecular weight multi-arm star block copolymers, helping to keep the stars isolated and minimizing hydrodynamic interactions between stars. It is possible that these behaviors are enabled by an unusual intramolecular rearrangement that allows long PVP blocks to be shielded, rather than collapsed and decorating the outer periphery of the star. These studies highlight the notions that the behaviors of topologically-complex amphiphilic block copolymers differ in unexpected ways from the behaviors of their linear analogs and offer new and unusual structures by self-assembly. From a practical point-of-view, these results suggest that high molecular weight and highly branched star block copolymer systems may be advantageous when used as nanocarriers because they remain disperse and do not disassemble as they are diluted.

**Chapter 5: Effects of Sequence and Composition on the Self-assembly of
Poly(lactic acid)-Poly(ethylene glycol) Bottlebrush Copolymers**

5.1 Abstract

To understand links between macromolecular topology, composition, and self-assembly, a series of bottlebrush copolymers differing in sequence and composition were synthesized by ring opening metathesis polymerization (ROMP) starting from norbornenyl functionalized poly(ethylene glycol) (PEG) and norbornenyl functionalized poly(lactic acid) (PLA) macromonomers. Solution self-assembly properties of the resulting PLA-PEG random and diblock bottlebrush copolymers were investigated in various solvent conditions at 25 °C. The hydrodynamic sizes of the random bottlebrush copolymers were more sensitive to concentration changes in the selective solvent methanol as compared to the selective solvent water. The block bottlebrush copolymer maintained its characteristic hydrodynamic sizes in methanol and water, and readily formed large compound micelles (LCMs) at very low concentrations. The critical micelle concentration (CMC) of micellar aggregates formed by the random bottlebrushes was tuned according to the PLA/PEG composition and, in aqueous solution conditions, the structures were more stable due to the extremely low CMC. The PLA-PEG bottlebrush copolymers interfacial curvature remained constant as spherical micellar aggregates were formed by all of the samples in both solvents. However, different spherical core-shell structures were observed above the CMC depending on the side-chain ratios, solvent type, and block sequence. These studies highlight how macromolecular design impacts self-assembly behaviors, and as PLA-PEG bottlebrush copolymers are biocompatible, these types of studies are important for developing therapeutic systems that could function as nanocarriers for drug delivery within the human body.

5.2 Introduction

Bottlebrush polymers are comb-like or branched macromolecules with densely grafted polymeric side-chains arrayed along a linear backbone.¹⁴⁵⁻¹⁴⁹ The combination of sterics, size and topology of bottlebrush copolymers provides a variety of ways to tune structure and properties. As a result, bottlebrush copolymers have found use in drug delivery, molecular templating, tumor detection, and biological imaging.^{146,148,150-151} The unusual architecture of polymeric bottlebrushes can also provide novel ways to tune rheological or lubricative properties in various solvent conditions.¹⁵² The three main methods used to synthesize bottlebrush macromolecules are: (1) grafting onto, (2) grafting from, and (3) grafting through. In the first method, polymer chains having a reactive end group are attached to a linear backbone displaying complementary functional groups to create the bottlebrush. The grafting-from method involves creating a macroinitiator with active sites that are used to initiate the polymerization of the side chains. The third method, known as grafting-through, uses macromonomers with polymerizable end groups to create the graft topology.¹⁵³

Bottlebrush copolymers contain at least two chemically different polymeric side-chains. As block copolymers are known to undergo microphase segregation to produce novel nanoscale structures, recent efforts have been devoted to exploring the diverse self-assembly properties and functions of bottlebrush copolymers in solution.^{149,154-156} Similar to amphiphilic block copolymers,^{8,27,157} amphiphilic bottlebrush block copolymers can self-assemble, forming micelles in solution. Fenyves *et al.* synthesized amphiphilic bottlebrush block copolymers containing polylactide (PLA) and poly(ethylene oxide) (PEO) side chains by the grafting from method. The self-assembled properties were investigated upon varying the length of the PLA and

PEO side chains while the backbone length and symmetry was kept constant. In aqueous solution, cryo-TEM images revealed that PLA-PEO bottlebrush copolymers self-assembled into shape-dependent spherical and cylindrical micelles, as well as into bilayer structures. The transition in morphology was explained along the lines of changes in interfacial curvature and packing constraints, which were as a result of the changes in PLA and PEO composition as the backbone length was kept constant.¹⁵⁴

The sequence of the side chains (block versus random topology) in bottlebrush copolymers has been demonstrated to have a considerable impact on their self-assembly properties in solution.¹⁵⁸ Shao *et al.* synthesized a series of block and random bottlebrush copolymers consisting of poly(oligo ethylene glycol) and poly(cholic acid) side-chains of similar molecular weights and comonomer ratios via ring-opening metathesis polymerization (ROMP) of their norbornene derivatives. In aqueous solution, both the random and block bottlebrush copolymers self-assembled into spherical micelles, as observed from dynamic light scattering (DLS) measurements and TEM imaging. The average micellar size and aggregation number (N_{agg}) of the bottlebrush block copolymer were much larger than those of the random copolymer. This difference in micellar size was a direct result of the sequence of the side chains, which led to dissimilar self-assembled core-shell structures.¹⁵⁸

Beyond this investigation, comparing the self-assembly behaviors, structure, and properties of random and block bottlebrush copolymers of similar composition and overall molecular weight remains a subject open for investigation. With this in mind, we pursue studies of bottlebrush copolymer design on self-assembly and structure. Four poly(lactic acid)-poly(ethylene glycol) *g*-[PLA-PEG] bottlebrush copolymers differing in side chain composition

and block sequence but having similar overall molecular weights were synthesized and studied in different solvent conditions. The random bottlebrush copolymers investigated in this study were made by simultaneously copolymerizing norbornenyl functionalized PEG and norbornenyl functionalized PLA as two macromonomers via ROMP; this is a grafting through approach. Stoichiometric control of the two macromonomers allows for tuning the composition of the random bottlebrush copolymers. In contrast, the block bottlebrush copolymers in this study were made by polymerization of norbornenyl functionalized PLA, then subsequent addition of the norbornenyl functionalized PEG. Conceptually, these studies offer a way to link polymer topology and design with structure and properties. From a practical point-of-view, this theme of research is important because PLA and PEG are useful for biomedical applications because PEG is biocompatible and PLA is biodegradable, as proven through previous studies with linear and branched PLA and PEG materials.¹⁵⁹⁻¹⁶²

5.3 Experimental

5.3.1 Materials

A third generation Grubbs' catalyst $[(H_2IMes)(pyr)_2(Cl)_2RuCHPh]$ was synthesized as described previously¹⁶³ and used quickly after synthesis, rather than storing for a long period of time. N,N-dimethylformamide (DMF, 99.8%) and methanol (MeOH, 99.8%) were purchased from Fisher Scientific and used as received. All other reagents were used as received unless noted otherwise.

5.3.2 Materials synthesis

Norbornenyl-functionalized poly(ethylene glycol) (PEG macromonomer) and norbornenyl-functionalized poly(D,L-lactide) (PLA macromonomer) were made following methods reported previously¹⁶⁴⁻¹⁶⁵ and characterized by ¹H NMR for end-group analysis. To synthesize random bottlebrush copolymers, PLA macromonomer (0.019 mmol) and the PEG macromonomer (0.2095 mmol) were added to a scintillation vial that had been previously oven dried. The vial was then capped with a rubber septum. To this vial, 3.5 mL of dry dichloromethane (DCM) was added and purged with nitrogen. In a separate vial, a stock solution (0.0023 mmol) of (H₂IMes)(pyr)₂(Cl)₂RuCHPh in dry DCM (3.0 mL) was prepared and purged with nitrogen. Then, a portion of the catalyst solution (0.0023 mmol, 1 mL) was transferred via clean, dry syringe to the vial containing the macromonomer solution. The mixture was stirred for 90 min at room temperature, after which time an excess of ethyl vinyl ether (EVE) (0.1 mL) was added via syringe to terminate the reaction. The crude reaction mixture was concentrated by rotary evaporation, precipitated into diethyl ether (DEE) and methanol and filtered. An excess of DEE was then added and the mixture was centrifuged to collect the precipitate. The solvent was decanted and the precipitate was isolated by vacuum-drying overnight at room temperature. Throughout this Chapter I refer to the bottlebrushes by specifying numerical subscripts for each block that indicates the volume fraction of either PLA or PEG side chains in the copolymer, and using *r* to indicate a random incorporation of the macromonomers and *b* to indicate a diblock bottlebrush.

5.3.3 Methods and characterization

^1H NMR spectroscopy was performed using a Varian Unity 500 wide bore multinuclear spectrometer with deuterated chloroform as solvent. Size Exclusion Chromatography (SEC) was performed using an Agilent 1260 Infinity Binary pump equipped with Agilent 1200 Series PDA detector, a Wyatt Dawn Heleos II 18-angle laser light scattering detector. THF was used as eluent and ASTRA 6.1 software was used to calculate absolute molecular weight from light scattering. dn/dc for SLS was determined separately (as described in Chapter 2) on a Wyatt Optilab T-rEX refractometer.

Dynamic light scattering (DLS) measurements were performed using methods previously described¹³³ on an ALV-CGS-3 Compact Goniometer System equipped with a linearly polarized 22 mW HeNe laser operating at a wavelength, λ , of 632.8 nm. The signal is processed using an ALV 7000 multiple tau (τ) digital correlator with an initial sampling time of 125 ns and the temperature is maintained at 25 ± 0.1 °C in all experiments. Approximately 1.5 mL of polymer solution at concentrations ranging from ~0.1 – 10.0 mg/mL was added to previously cleaned, dust-free 10 mm borosilicate glass cuvettes and these were sealed with a Teflon cap. DLS measurements were made at 16 angles ranging from 20° to 146° and a counting time of 600 s was used at each angle for solutions having a concentration of 5.0 mg/mL or greater. As the concentration was decreased from that level, the counting time was increased in order to obtain reliable statistics for the light intensity autocorrelation function, $g_2(q,\tau)$.

Transmission electron microscopy (TEM) samples were prepared by drop casting ~20 μL of solution onto copper supported carbon film grids, and each film was allowed to dry. The films were directly imaged without staining. Images were obtained from a Zeiss Libra 200 MC

transmission electron microscope and Gatan UltraScan US1000XP CCD camera was used to record the images using the Digital Micrograph software package.

For cryogenic-transmission electron microscopy (cryo-TEM) imaging, the micellar solution was first cooled to 4 °C in order to slow the evaporation of the solvent while blotting the excess liquid from the lacey carbon films. Droplets of the solution were deposited onto lacey carbon film grids, and excess fluid was blotted to create ultrathin layers of the solution spanning the holes of perforated carbon films. The grids were immediately plunged into liquid ethane. Vitrified samples were transferred under liquid nitrogen into the microscope using the Gatan 626 cryo-holder and stage, which maintains sample temperature at -175 °C throughout imaging.

5.4 Results and Discussions

5.4.1 Synthesis of bottlebrush copolymers

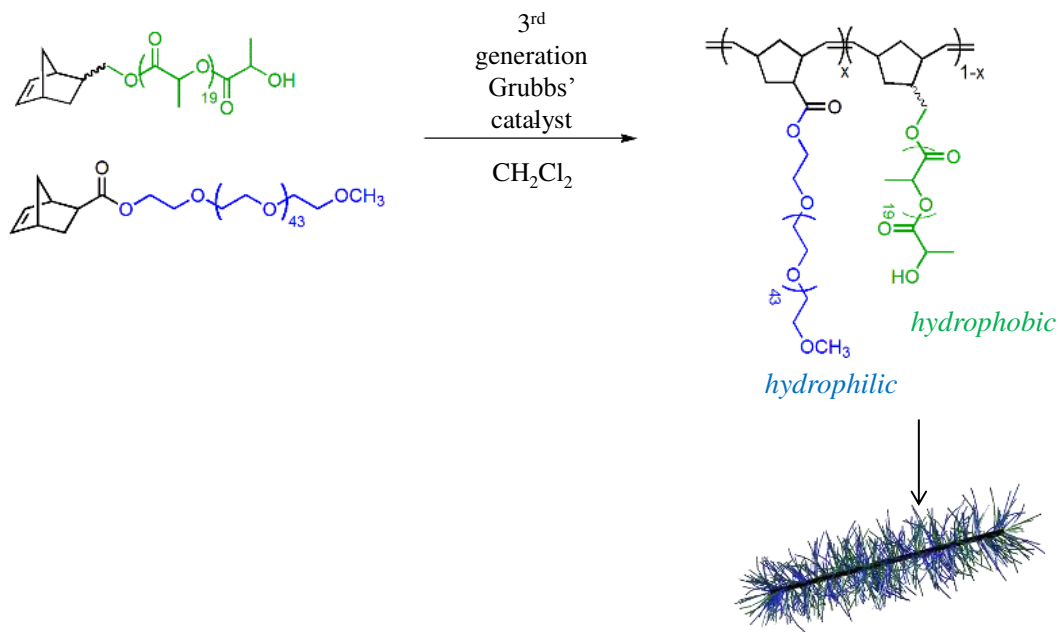
A bottlebrush diblock copolymer and a series of random bottlebrush copolymers were synthesized by ROMP using norbornenyl functionalized PEG and norbornenyl functionalized PLA as two macromonomers as shown in Scheme 5-1 and Scheme 5-2. PEG and PLA macromonomers were synthesized separately. The bottlebrush copolymers were characterized by NMR and is described in previous publications.¹⁶⁴⁻¹⁶⁶ The composition of the random bottlebrush copolymers was altered by simply adjusting the stoichiometry of PEG and PLA macromonomers in the feed. The molecular characteristics of the macromonomers, *g*-[PLA-*r*-PEG] (where *g* stands for bottlebrush and *r* stands for random) and *g*-[PLA-*b*-PEG] (where *g* stands for

bottlebrush and *b* stands for block) are given in Table 5-1. The subscripts indicate the volume fraction of each type of side chain within the bottlebrush.

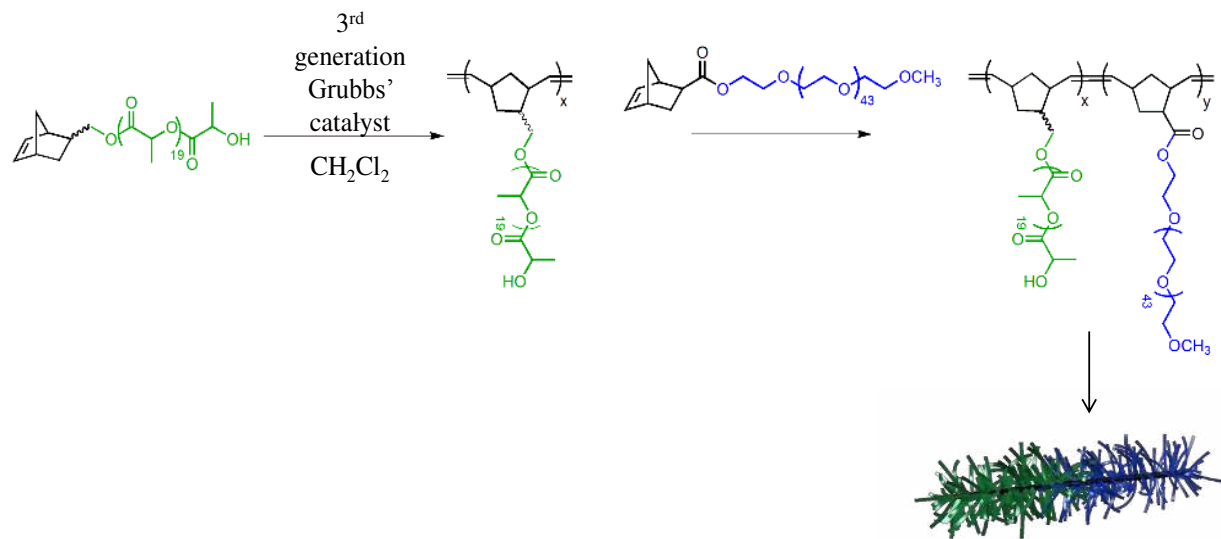
Table 5-1. Molecular characteristics of PLA-PEG bottlebrush copolymers, where *r* indicates random and *b* indicates a block copolymer and their macromonomers.

Sample ID	Mol _{PLA} (%) ^a	Mol _{PEG} (%) ^a	Vol _{PLA} (%) ^b	Vol _{PEG} (%) ^b	M_n^c (kDa)	M_w^c (kDa)	\mathcal{D}^c
PLA macromonomer	--	--	--	--	1.57 ^a	--	--
PEG macromonomer	--	--	--	--	2.10 ^a	--	--
<i>g</i> -[PLA ₃₆ - <i>b</i> -PEG ₆₄]	44	56	36	64	164.3	188.8	1.14
<i>g</i> -[PLA ₄₁ - <i>r</i> -PEG ₅₉]	49	51	41	59	144.6	153.0	1.06
<i>g</i> -[PLA ₁₃ - <i>r</i> -PEG ₈₇]	17	83	13	87	178.0	196.8	1.10
<i>g</i> -[PLA ₇ - <i>r</i> -PEG ₉₃]	9	91	7	93	162.4	179.4	1.10

^aDetermined by ¹H NMR. ^bDetermined by ¹H NMR using density of PLA (1.25 g/cm³)¹⁶⁷ and PEG (1.20 g/cm³)¹⁶⁸. ^cDetermined by refractive index detector considering *dn/dc* of PLA and PEG bottlebrush copolymers in DMF using poly(ethylene oxide) standards.



Scheme 5-1. Reaction scheme used to make PLA-*r*-PEG bottlebrush random copolymers.



Scheme 5-2. Reaction scheme used to make PLA-*b*-PEG bottlebrush block copolymers.

5.4.2 Effect of composition and concentration on self-assembly in solution

The solution self-assembly properties of the three g -[PLA- r -PEG] copolymers were studied by DLS at four different concentrations in methanol, a selective solvent for the PEG side chains. The DLS data for g -[PLA₄₁- r -PEG₅₉] are shown in Figure 5-1 and summarized in Table 5-2. Figure 5-1A shows the normalized light intensity autocorrelation functions at 25.0 ± 0.1 °C for g -[PLA₄₁- r -PEG₅₉] at concentrations of 1.0, 2.0, 5.0, and 10.0 mg/mL (nominal values). The light intensity autocorrelation function starts at a lower value for $c = 1.0$ mg/mL but gradually increases as concentration increases. The data also shows that as concentration increases, the correlation in scattered intensity increases, which indicates an increase in the size and the number of scattering particles in solution. This increase in size is also seen in the normalized amplitude distribution of decay rates, which are shown in Figure 5-1B. At low concentrations, the normalized amplitude distribution of decay rates is very narrow and well defined, and as a result, the light intensity autocorrelation functions for sample g -[PLA₄₁- r -PEG₅₉] at $c = 1.0$ and 2.0 mg/mL are well-fit with a single exponential decay function. At these low concentrations where only a single decay mode is observed, the angularly-dependent mean decay rate, Γ , normalized by the square of the scattering wave vector, Γ/q^2 , can be plotted versus q^2 as shown in Figure 5-1C, with the best-fit line extrapolated to zero scattering angle used to obtain the concentration dependent z -average apparent diffusion coefficient (D_{app}). The apparent hydrodynamic radius (R_{h1}) can be calculated from D_{app} using the Stokes-Einstein relation: $R_{h1} = 9.0$ and 10.0 nm at $c = 1.0$ and 2.0 mg/mL, respectively. These data analysis procedures, including permutations used to handle situations where there is more than one population of

scatterers as described in Chapter 2, were performed for all of the g -[PLA- r -PEG] bottlebrush copolymers, and the results are given in Table 5-2.

DLS and SLS measurements were also made on g -[PLA₄₁- r -PEG₅₉], g -[PLA₁₃- r -PEG₈₇] and g -[PLA₇- r -PEG₉₃] in DMF (a thermodynamically non-selective good solvent) at 1.0 mg/mL, 3.0 mg/mL, and 9.0 mg/mL. The apparent hydrodynamic radius at $c = 9.0$ mg/mL was found to be ~ 10 nm (see Appendix C), which is in good agreement with results obtained in the selective solvent methanol. Therefore, these measurements indicated that the R_{h1} values determined at 1.0, 2.0, 5.0 and 10.0 mg/mL for g -[PLA₄₁- r -PEG₅₉] represent single chains in methanol. Static light scattering (SLS) measurements were also conducted on g -[PLA₄₁- r -PEG₅₉], g -[PLA₁₃- r -PEG₈₇] and g -[PLA₇- r -PEG₉₃] in DMF, and Zimm plots and results extracted from extrapolations (M_w , A_2 , and R_g) for g -[PLA₄₁- r -PEG₅₉], g -[PLA₁₃- r -PEG₈₇], g -[PLA₇- r -PEG₉₃] can be found in Appendix C.

As the concentration of g -[PLA₄₁- r -PEG₅₉] is increased to 5.0 mg/mL in methanol, the normalized amplitude distribution functions begin to broaden and there is a shift to larger size. There is also a clear indication of the formation of a second peak indicating a second population of scatterers. As a result, the light intensity autocorrelation functions determined at 5.0 and 10.0 mg/mL each were fit with and well-described by a double exponential function, and the results of the fits are shown in Figure 5-1D. Here, the mean decay rate associated with the fast mode yields a D_{app} consistent with hydrodynamic size of single chains, R_{h1} , in solution, while the characteristic decay rate associated with the slow mode, which describes the second population of scatterers yields a R_{h2} that is larger, as shown in Table 5-2. This indicates that this population is micellar aggregates.

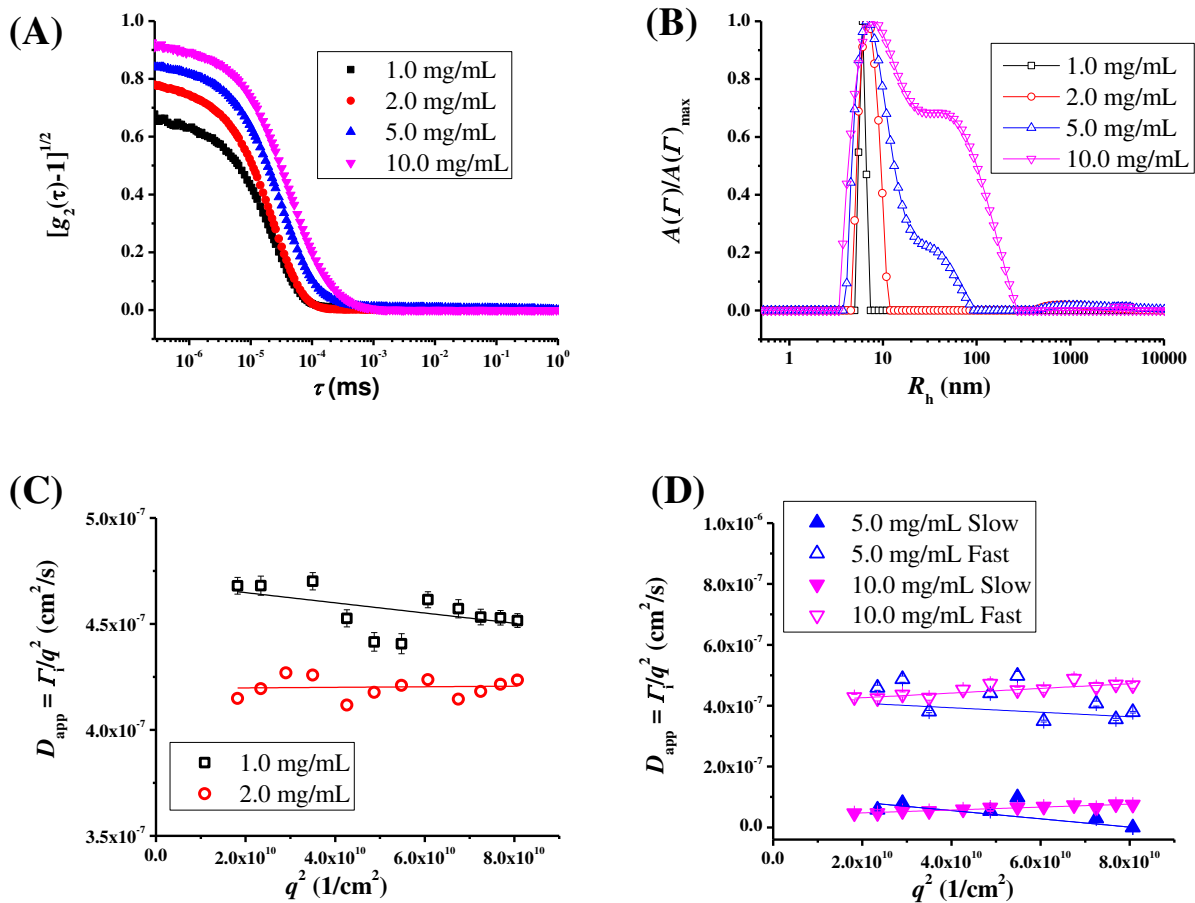


Figure 5-1. Results from DLS measurements on g -[PLA₄₁- r -PEG₅₉], including (A) normalized light intensity autocorrelation function for g -[PLA₄₁- r -PEG₅₉] and the corresponding (B) normalized amplitude distribution of decay rates. In plots (C) and (D), D_{app} is obtained by extrapolating the best fit line through the data cast as Γ/q^2 versus q^2 to $q^2 = 0$. Resulting apparent R_h values are presented in Table 5-2.

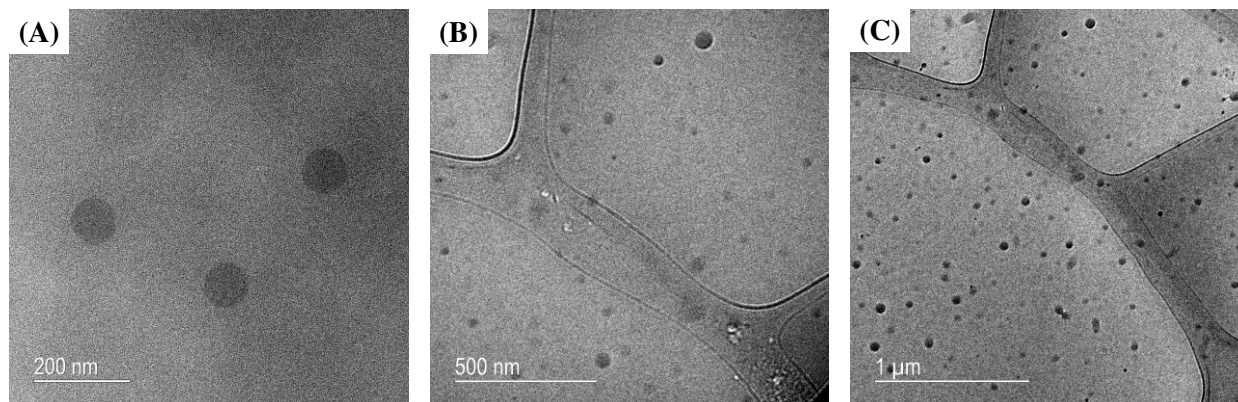


Figure 5-2. Representative TEM image showing aggregates formed from g -[PLA₄₁- r -PEG₅₉] at (A) 5.0 mg/mL, and (B) and (C) cryo-TEM images acquired from solutions at 10.0 mg/mL in methanol at two different size scales.

The TEM image in Figure 5-2A shows the self-assembled micellar aggregates formed in methanol for the g -[PLA₄₁- r -PEG₅₉] bottlebrush copolymer, which incorporates both macromonomers in roughly equal amounts, at 5.0 mg/mL. The DLS results suggest that the critical micelles concentration (CMC) is greater than 2.0 mg/mL but less than 5.0 mg/mL. The micelle structure is spherical in shape, ostensibly with the PLA block (which is not soluble in MeOH) forming the core and PEG blocks stabilizing the micelle by forming the corona. The diameter of the micelles determined from the TEM image is ~90 nm, which is in good agreement with the diameter determined from light scattering measurements. This is an indication of stable core-shell structures being formed, likely due to the uniform distribution of PLA and PEG side chains along the polynorbornene backbone. Cryo-TEM images in Figures 5-2B and 5-2C show that the stable core-shell spherical solution morphology of the g -[PLA₄₁- r -PEG₅₉] is maintained

at 10.0 mg/mL in methanol. From the cryo-TEM images it is seen that there is a broad distribution of micellar sizes within the sample, and this is in good agreement with the DLS data at 10.0 mg/mL, which shows a broad distribution.

Table 5-2. Hydrodynamic sizes of PLA-PEG bottlebrush copolymers in methanol as a function of concentration.

Concentration (mg/mL)	<i>g</i> -[PLA ₄₁ - <i>r</i> - PEG ₅₉]		<i>g</i> -[PLA ₁₃ - <i>r</i> - PEG ₈₇]		<i>g</i> -[PLA ₇ - <i>r</i> - PEG ₉₃]		<i>g</i> -[PLA ₃₆ - <i>b</i> - PEG ₆₄]	
	R_{h1} (nm)	R_{h2} (nm)	R_{h1} (nm)	R_{h2} (nm)	R_{h1} (nm)	R_{h2} (nm)	R_{h1} (nm)	R_{h2} (nm)
1.0	9	-	14	-	12	-	115	483
2.0	10	-	12	-	11	-	100	449
5.0	8	48	10	156	10	-	74	637
10.0	10	102	10	183	9	136	72	694

The effect of composition on the self-assembly behavior of *g*-[PLA-*r*-PEG] bottlebrush copolymers was examined by increasing the incorporation of soluble PEG grafts relative to the insoluble PLA grafts. *g*-[PLA₁₃-*r*-PEG₈₇] was also studied in the selective solvent methanol using DLS at four different concentrations, $c = 1.0, 2.0, 5.0, 10.0$ mg/mL (nominal), and the results are presented in Table 5-2. At this copolymer composition, the solution concentration seems to have a minimal effect on the value of the normalized light intensity autocorrelation functions at short lag times, τ , as shown in Figure 5-3A. However, the shape of the

autocorrelation function seems to change at longer lag times as concentration increases. These distinctive behaviors evident in the light intensity autocorrelation functions suggest stronger scattering as concentration increases that evolves to a bimodal mixture of single chains and micellar aggregates in solution. This is borne out by the distributions of decay rates shown in Figure 5-3B, where the double distribution of the normalized amplitude distribution of decay rates suggests that single chains and micellar aggregates are present at all four concentrations. If, in fact, micelles are present at 1.0 mg/mL, then one would conclude that the CMC for *g*-[PLA₁₃-*r*-PEG₈₇] is lower than the CMC for the *g*-[PLA₄₁-*r*-PEG₅₉] bottlebrush, which has a higher level of incorporation of PLA, which is insoluble in methanol. This aspect was investigated thoroughly in the analyses of DLS data. The light intensity autocorrelation functions for *g*-[PLA₁₃-*r*-PEG₈₇] at 1.0 and 2.0 mg/mL was fit with a single exponential function (Figure 5-3C) and the results are shown in Table 5-2. The results from the double exponential fit of the light intensity autocorrelation functions *g*-[PLA₁₃-*r*-PEG₈₇] at 1.0 mg/mL and 2.0 mg/mL are shown in Figure C8 of Appendix C. As seen in Appendix C, data acquired at many of the scattering angles has been omitted in order to obtain the best fit line to the data in plots of Γ/q^2 versus q^2 to achieve hydrodynamic that are consistent with those suggested by the normalized amplitude distribution of decay rates. In view of this, it seems that the data do not support the claim that two distributions are, in fact, present at $c = 1.0$ and 2.0 mg/mL – simply put, one is asking too much from the light scattering data to create a story that is consistent with two scattering modes. As a result, a single decay mode representing a single population of scatterers is more appropriate. The normalized light intensity autocorrelation functions at 5.0 and 10.0 mg/L were well-fit with a double exponential function, and the results plotted as Γ/q^2 versus q^2 are shown in

Figure 5-3D. In both Figure 5-3C and 5-3D, best-fit lines extrapolated to $q^2 = 0$ were used to find D_{app} values, and from these, apparent R_h values were calculated and are presented in Table 5-2. Similar procedures were followed for g -[PLA₇- r -PEG₉₃] and g -[PLA₃₆- b -PEG₆₄] copolymers to complete Table 5-2. The data show that micellar aggregates formed by self-assembly for g -[PLA₁₃- r -PEG₈₇] are much larger compared to those formed from g -[PLA₄₁- r -PEG₅₉]. Because the total molecular weight of the copolymer was fixed and the random bottlebrushes are made from the same macromonomers, it stands to reason that the micelles are larger because the thickness of the PEG shell increases as the PEG to PLA ratio increases.

The relative composition of the g -[PLA₁₃- r -PEG₈₇] bottlebrush copolymer in which the corona forming PEG blocks are more prevalent than the core forming PLA blocks suggests a highly swollen corona with stretched PEG chains that leads to an increase in the hydrodynamic radius. TEM images at 5.0 mg/mL in Figure 5-4A and 5-4B shows non-spherical micellar structures. The aggregate sizes taken from TEM are slightly smaller than the DLS sizes due to either difficulty in imaging a strongly swollen corona or because the highly swollen coronal side chains collapse upon solvent removal. Cryo-TEM images also show aggregates having curved interfaces but slightly irregular structures at 10.0 mg/mL. The micellar structures formed by the g -[PLA₄₁- r -PEG₅₉] bottlebrush are more regular as compared to those formed by the g -[PLA₁₃- r -PEG₈₇] bottlebrush.

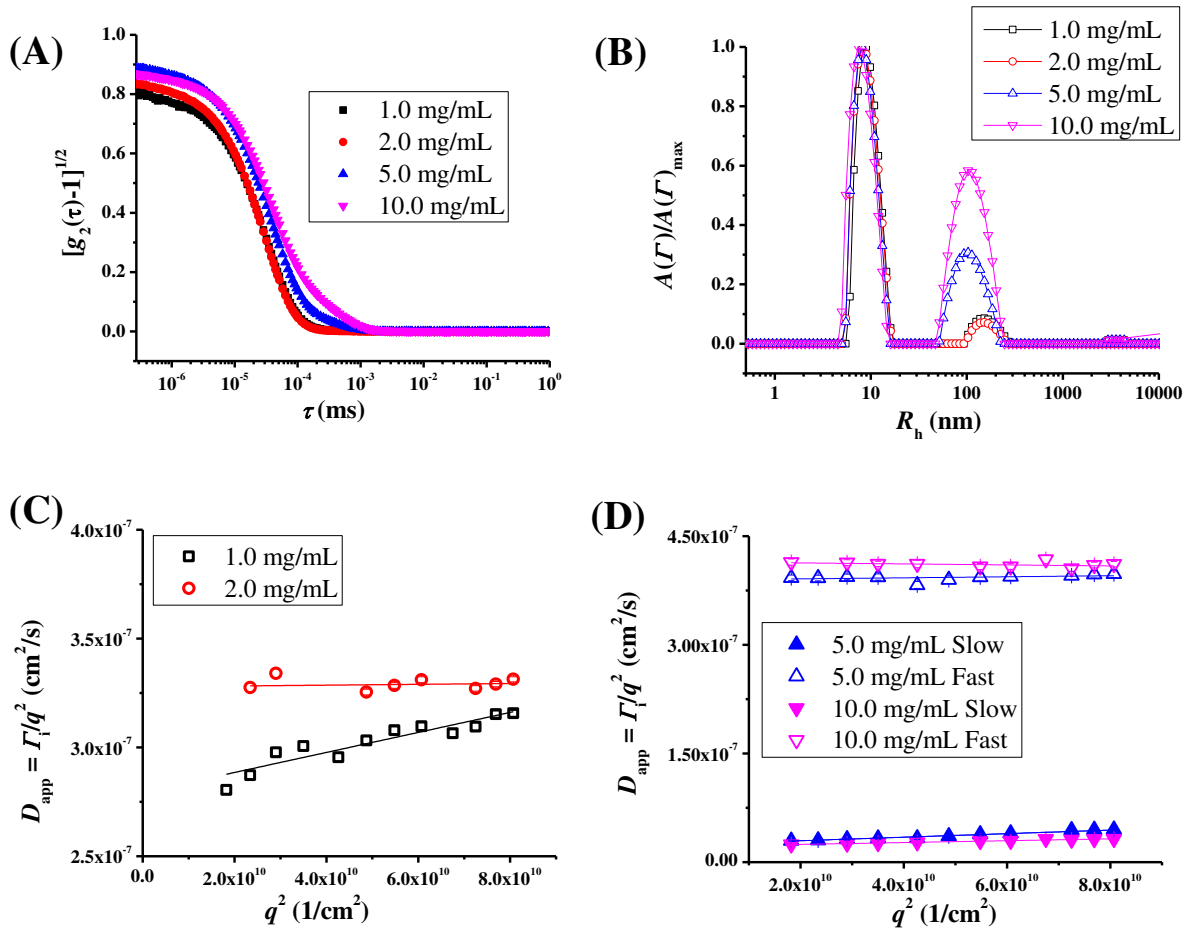


Figure 5-3. (A) Normalized light intensity autocorrelation function and (B) normalized amplitude distribution of decay rates for g -[PLA₁₃- r -PEG₈₇] in methanol as a function of concentration. For plots (C) and (D), D_{app} is obtained by extrapolating the best fit line through data cast as Γ/q^2 versus q^2 to $q^2 = 0$. Resulting apparent R_h values are presented in Table 5-2. While a small population of larger scatterers seems to be present at 1.0 and 2.0 mg/mL, as described in the text, careful data analysis at all scattering angles does not support the conclusion that both modes are, in fact, present.

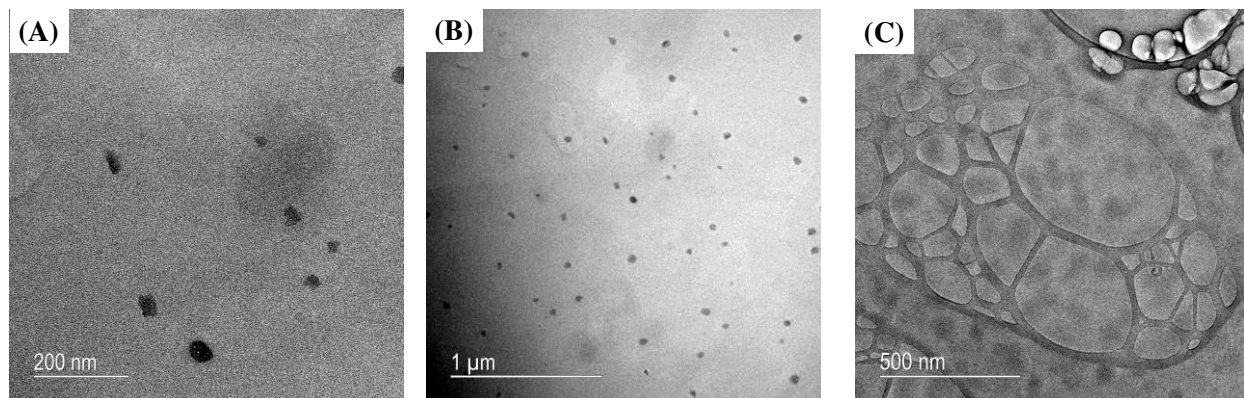


Figure 5-4. Representative TEM images for g -[PLA₁₃- r -PEG₈₇] in methanol at (A) and (B) 5.0 mg/mL at two different image size scales and (C) a cryo-TEM image for g -[PLA₁₃- r -PEG₈₇] at 10.0 mg/mL.

Further decreasing the PLA to PEG ratio leads to a considerable change in the self-assembly properties in methanol. As shown in Figure 5-5B, the g -[PLA₇- r -PEG₉₃] resists aggregation, displaying very narrow, well defined distributions centered at ~ 10 nm until the concentration is increased to 10.0 mg/mL. As shown in Figure 5-5A, at all concentrations studied the normalized light intensity autocorrelation functions begin at similar values and decay at similar lag times. However, the correlation function at 10.0 mg/mL has a slightly different shape at longer lag times, which suggests the onset of micellization. Each of the normalized light intensity autocorrelation functions produced at $c = 1.0, 2.0,$ and 5.0 mg/mL was well-fit with a single exponential function. The data shown in Figure 5-5C is plotted as I/I_0 versus q^2 , as previously described, and the D_{app} values determined by extrapolation were used with the Stokes-Einstein relation to produce the apparent R_h values, which are summarized in Table 5-2. At 10.0 mg/mL the normalized light intensity autocorrelation function was fit with a double

exponential function; however, the data was extremely noisy indicating that this concentration may be close to the CMC. At this concentration, values of D_{app} were extracted from the best fit line to the data extrapolated to $q^2 = 0$ using only data acquired at large scattering angles. Because of this and as described earlier, the hydrodynamic sizes should be examined very closely. Nevertheless, the data are suggesting that the CMC has increased as the content of solvophobic PLA decreases in the random copolymer. This increase in CMC is likely a direct result of the bottlebrush having improved solubility due to the PEG content. Furthermore, it may be anticipated that there would be a large entropic penalty that results from reorganization of the sidechains to enable the solvophobic PLA blocks to aggregate, driving self-assembly. In other words, the soluble PEG side chains do an excellent job of shielding and preventing the PLA blocks from coalescing. Despite the resistance of the g -[PLA_{7- r} -PEG₉₃] toward micellization, both DLS and cryo-TEM provide evidence of micelle formation. The cryo-TEM images acquired at 10.0 mg/mL (shown in Figure 5-6) reveal that the morphology of the weakly aggregating g -[PLA_{7- r} -PEG₉₃] appears to be spherical. While there are a large number of micelles shown in this image, that was not the case over the entire lacey carbon film grid – many areas had few, if any, micelles.

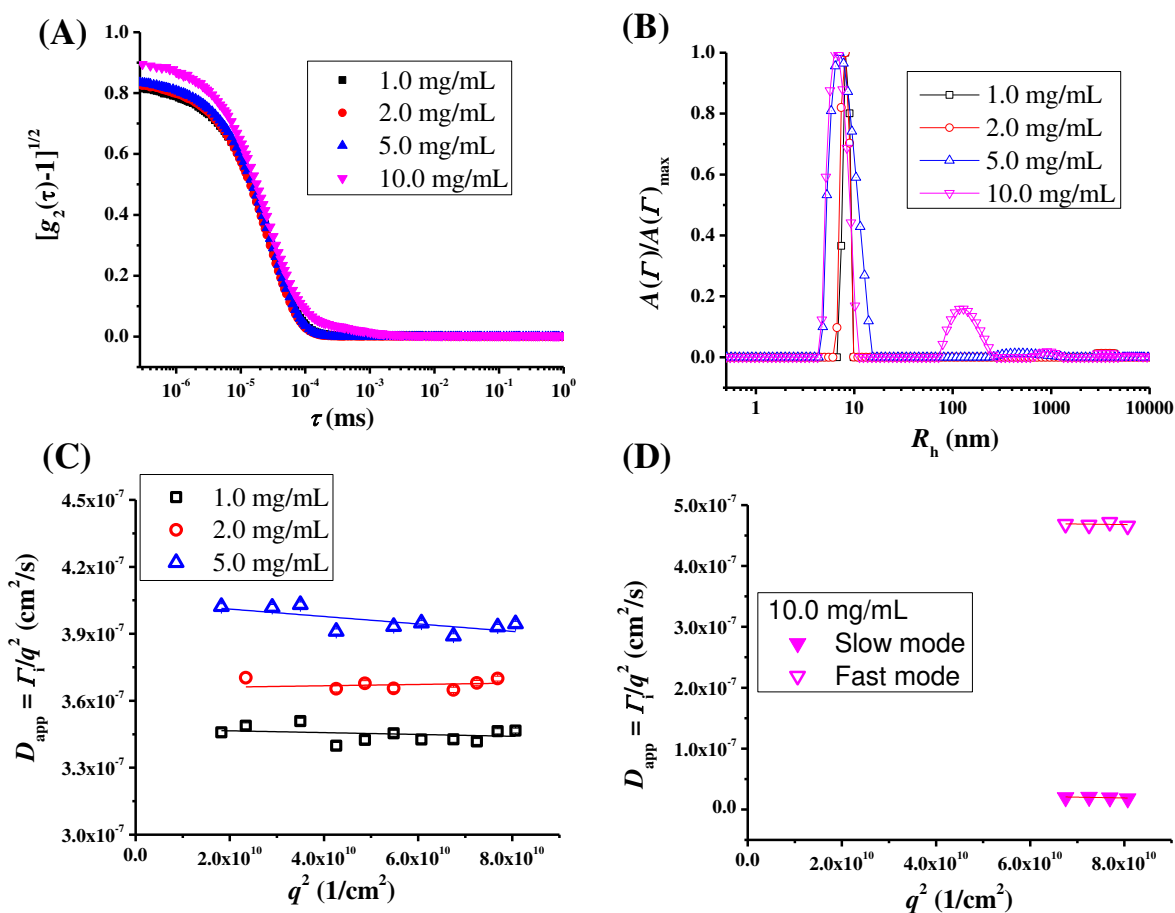


Figure 5-5. (A) Light intensity autocorrelation function for g -[PLA₇- r -PEG₉₃] and (B) normalized amplitude distribution of decay rates. For plots (C) and (D), D_{app} for g -[PLA₇- r -PEG₉₃] is obtained by extrapolating the best fit line through the data cast as Γ/q^2 versus q^2 to $q^2 = 0$. The apparent hydrodynamic radii are given in Table 5-2.

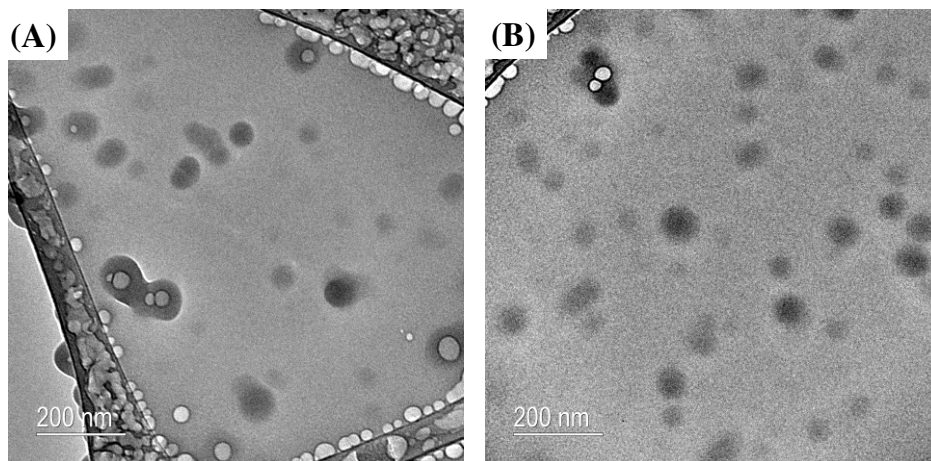


Figure 5-6. Cryo-TEM images acquired from a region on a lacy carbon film grid where there was a high density of aggregates. Images (A) and (B) are acquired for g -[PLA₇- r -PEG₉₃] at 10.0 mg/mL in methanol.

5.4.3 Effect of sequence on self-assembly

Random copolymers often behave like simple single component systems, while linear diblock copolymers are well known and often studied for their ability to undergo microphase segregation. In the case of bottlebrush copolymers, the sequence of side chains in bottlebrush copolymers can dictate the hydrodynamics of the self-assembled aggregates in solution.¹⁵⁸ To examine sequence effects, a single diblock bottlebrush was synthesized and studied.

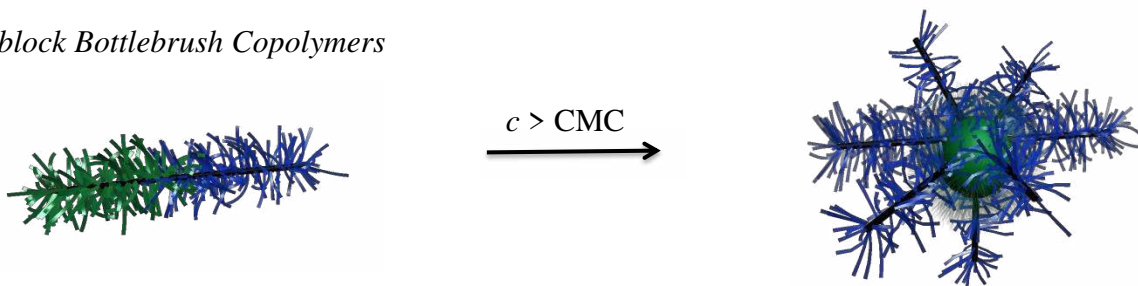
As seen in Figure 5-7B, the g -[PLA₃₆- b -PEG₆₄] bottlebrush diblock copolymer formed micellar structures at very low concentrations. Furthermore, the normalized amplitude distributions of decay rates at all four concentrations are very broad – broader than distributions determined for any of the random copolymer bottlebrushes. This breadth is an indication of very high polydispersity of the micellar aggregates formed in solution. The normalized light intensity

autocorrelation functions at all concentrations were well-fit with double exponential functions. Values of D_{app} were obtained from the best fit line through the data cast as Γ/q^2 versus q^2 extrapolated to $q^2 = 0$. (See Figures 5-7D, E, and F.) The Stokes-Einstein relation was used to calculate $R_{\text{h,app}}$ and the results are shown in Table 5-2. The hydrodynamic radii are larger for the g -[PLA₃₆- b -PEG₆₄] diblock bottlebrush copolymer as compared to those obtained for the random bottlebrush copolymers. From the TEM images shown in Figure 5-8, it is seen that there is a coexistence of large compound micelles (LCMs) with smaller micellar structures. The LCMs collapse upon drying on the carbon film TEM grids and as a result, the shape of the structure may be slightly changed compared to their solution structure. However, a spherical morphology is observed for the LCMs formed by self-assembly of g -[PLA₃₆- b -PEG₆₄] in methanol.

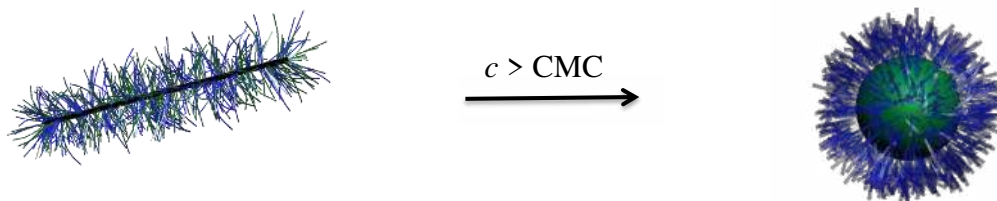
In thinking about the characteristic sizes ($R_{\text{h,app}}$ values) determined from DLS data analysis, it is important to bear in mind that $R_{\text{h,app}}$ is a single value that characterizes the entire distribution. It describes the characteristic size of a hard sphere that has the same diffusional behavior of the population of scattering particles. Thus, while it is often useful to compare and contrast properties of different samples, it is important to always keep in mind the physical basis of numbers being compared. The increase in $R_{\text{h,app}}$ may represent an increase in the number of chains that form the micellar structure. This change could be driven by fundamental differences between how random bottlebrushes and diblock bottlebrushes organize themselves into micellar structures formed in a selective solvent. In the case of the diblock bottlebrush, a core-shell structure could easily be formed because the two “halves” of the diblock arrange themselves across the core-corona interface without the side chains needing to stretch as shown in Scheme 5-3. On the other hand, in a random bottlebrush, it is more difficult to form an interface by

segregating solvophobic and solvophilic blocks. It may be possible for the two types of chains to segregate to opposite sides of the backbone, but the expected entropy cost would be significant. Moreover, as the relative amount of solvophobic block decreases, it would seemingly be more difficult for the highly grafted bottlebrush to distort so that the solvophobic blocks can pack (minimize their contact with the solvent). Nevertheless, these basic thoughts about how random and diblock bottlebrushes undergo microphase segregation are consistent with the observed trends. The larger $R_{h,app}$ observed for the diblock g -[PLA₃₆- b -PEG₆₄] compared to the corresponding random bottlebrushes may also be because the PLA chains within the core are more loosely packed within the structure, or a combination of both factors.

(1) *Diblock Bottlebrush Copolymers*



(2) *Random Bottlebrush Copolymers*



Scheme 5-3. Schematic representation of how block and random bottlebrush copolymers self-assemble to form single micelles in a solvent that is selective for the blue side chains.

It is observed from DLS results and TEM images for the bottlebrush copolymers studied that tuning side chain sequence affects the size and shape of the micellar structures, and in addition to regular traditional micelles, large compound micelles also are formed in methanol. Changing the bottlebrush copolymer sequence and composition seems to have negligible impact on the interfacial curvature of the micellar structures formed in methanol, as both the random and block form spherical micellar aggregates. When examining the effect of random bottlebrush composition, the composition of the graft copolymer seemed to have a remarkable effect on the CMC. Furthermore, the block bottlebrush copolymer seemed to form the most stable structures as compared to the random bottlebrush copolymers because of its remarkably low CMC. Generally speaking, dilution is one way to break micellization; however the block bottlebrush copolymers formed well-defined micellar aggregates at very low concentrations, whereas the random bottlebrushes seemed to remain as single chains in solution at low concentrations.

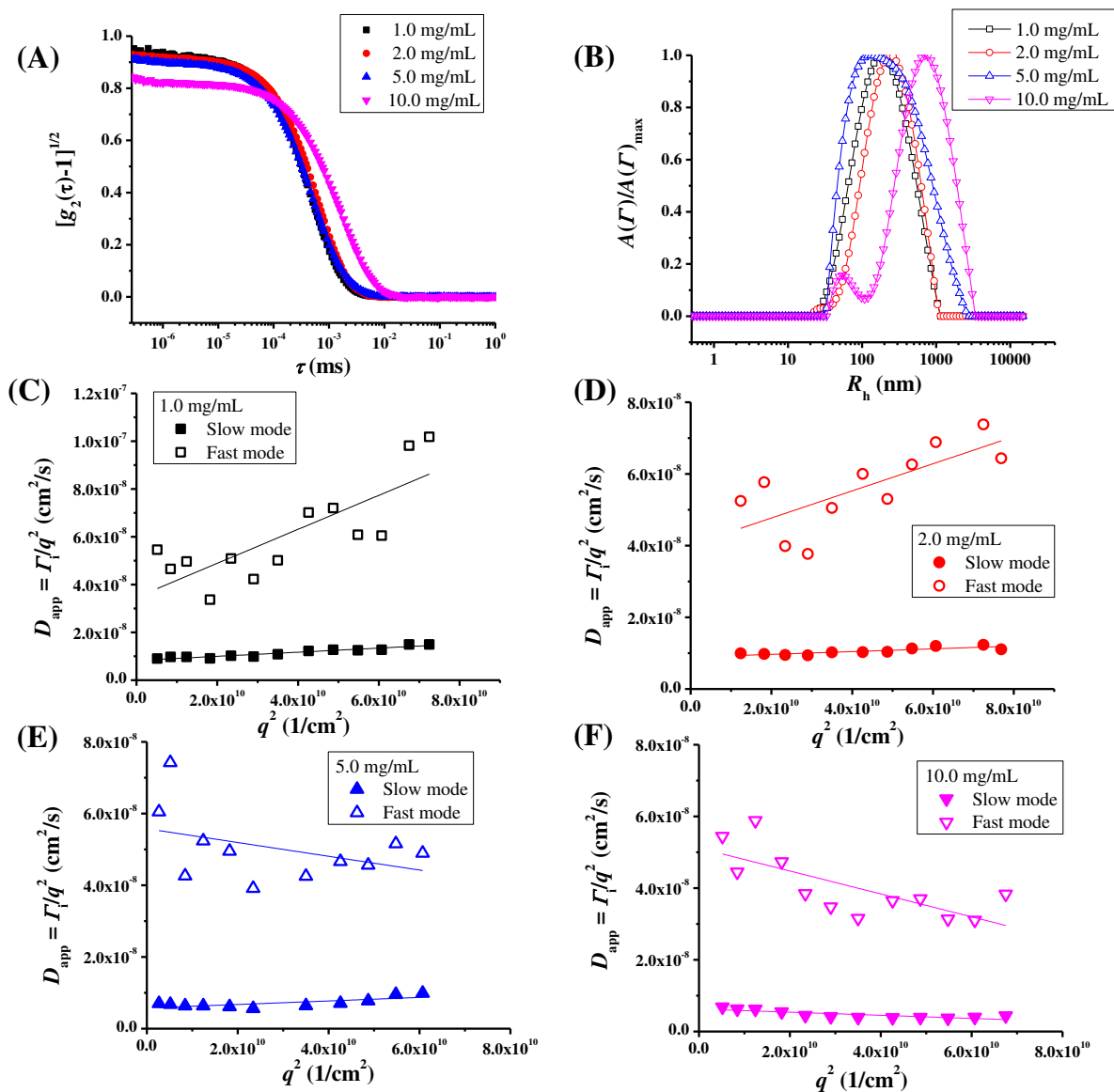


Figure 5-7. (A) Light intensity autocorrelation functions for g -[PLA₃₆- b -PEG₆₄] at various concentrations in methanol, and (B) normalized amplitude distribution of decay rates, which suggest that micelles are formed at all of the concentrations studied. For plots (C), (D), (E) and (F), D_{app} is obtained by extrapolating the best fit line through the data cast as Γ/q^2 versus q^2 to $q^2 = 0$ for g -[PLA₃₆- b -PEG₆₄]. Values of $R_{h,\text{app}}$ are presented in Table 5-2.

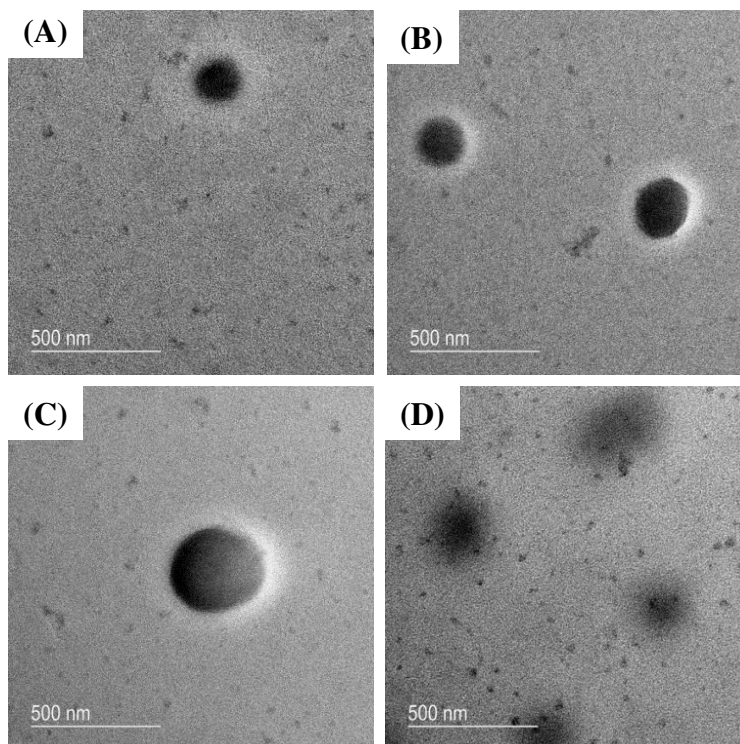


Figure 5-8. TEM images for g -[PLA₃₆- b -PEG₆₄] in methanol at (A) 1.0 mg/mL (B) 2.0 mg/mL, (C) 5.0 mg/mL, and (D) 10.0 mg/mL. The large aggregates are large compound micelles and smaller aggregates are also observed.

5.3.4 Self-assembly in aqueous solution

The self-assembly of the bottlebrush copolymers was also investigated in aqueous solution, which is strongly selective for PEG, using DLS measurements. Hydrodynamic radii determined for the three random and diblock bottlebrush copolymer are given in Table 5-3, but details are omitted because the data analysis follows the same protocols used throughout this chapter. It was observed that the PLA-PEG random and block bottlebrushes form micellar aggregates in water at very low concentration: Figure 5-9 shows results from a typical light

scattering experiment for g -[PLA₄₁- r -PEG₅₉] at $c = 0.5$ mg/mL in aqueous solution. This sample was studied at a very low concentration because its solubility is significantly decreased due to the large PLA content. The DLS results indicate a bimodal mixture of single chains and micellar aggregates with hydrodynamic sizes that were much larger than those measured for the micellar aggregates formed from this random copolymer in methanol. In addition and for comparison purposes, the g -[PLA₃₆- b -PEG₆₄] bottlebrush copolymer of similar composition also adopted a bimodal distribution of sizes, with large micellar structures and single chains both being present at very low concentration ($c = 0.1$ mg/mL). Results are presented in Appendix C. This change in micellization behavior is as a direct result of the substantial decrease in solubility of PLA in water, which drives system to micellize at much lower concentrations.

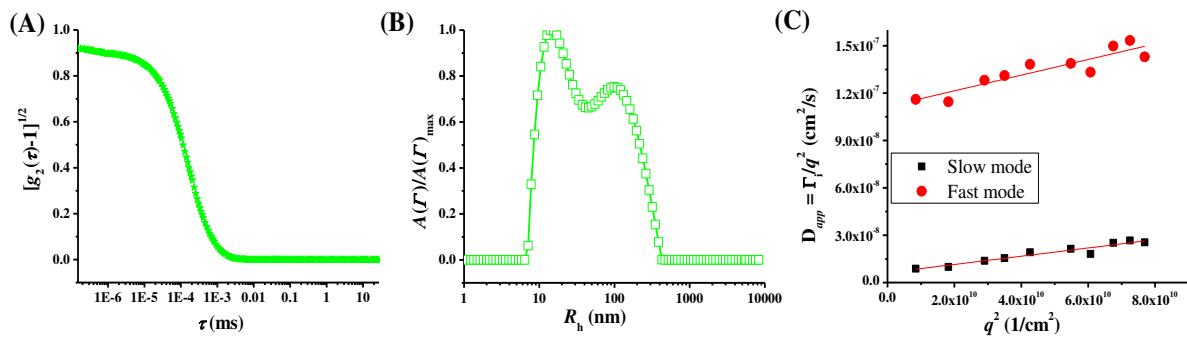


Figure 5-9. (A) Normalized light intensity autocorrelation function, and (B) normalized amplitude distribution of decay rates for g -[PLA₄₁- r -PEG₅₉] at $c \approx 0.5$ mg/mL in water. (C) D_{app} for g -[PLA₄₁- r -PEG₅₉] in aqueous solution at $c \approx 0.5$ mg/mL is obtained by extrapolating the best fit line through the data cast as Γ/q^2 versus q^2 to $q^2 = 0$. Data presented in (B) and (C) clearly indicate two populations of scatterers of different size. Values of $R_{h,app}$ are presented in Table 5-2.

Table 5-3. Hydrodynamic radii of PLA-PEG random and block bottlebrush copolymers in water as a function of copolymer design and concentration.

Concentration (mg/mL)	<i>g</i> -[PLA ₄₁ - <i>r</i> -PEG ₅₉]		<i>g</i> -[PLA ₁₃ - <i>r</i> -PEG ₈₇]		<i>g</i> -[PLA ₇ - <i>r</i> -PEG ₉₃]		<i>g</i> -[PLA ₃₆ - <i>b</i> -PEG ₆₄]	
	<i>R</i> _{h1} (nm)	<i>R</i> _{h2} (nm)	<i>R</i> _{h1} (nm)	<i>R</i> _{h2} (nm)	<i>R</i> _{h1} (nm)	<i>R</i> _{h2} (nm)	<i>R</i> _{h1} (nm)	<i>R</i> _{h2} (nm)
0.1	N/A	N/A	10	83	N/A	N/A	104	512
0.5	22	394	16	122	N/A	N/A	×	×
1.0	×	×	16	142	15	215	×	×
5.0	×	×	19	223	13	260	×	×
10.0	×	×	20	249	14	391	×	×

N/A indicates that light scattering experiments were not done at these concentrations. × Indicates that the bottlebrush copolymer was not soluble in aqueous solution at the particular concentration.

Because of solubility issues, only the self-assembly behavior of the *g*-[PLA₁₃-*r*-PEG₈₇] and *g*-[PLA₇-*r*-PEG₉₃] bottlebrush copolymers could be investigated over a wide concentration range, as evident from the results shown in Table 5-3. Figure 5-10A shows the normalized light intensity autocorrelation functions for *g*-[PLA₁₃-*r*-PEG₈₇] at concentrations of 0.1, 0.5, 1.0, 5.0, and 10.0 mg/mL (nominal values) in water. For all concentrations, the light intensity autocorrelation functions start at similar values, indicating high coherence, and decay similarly in terms of lag times and shape. This suggests that the structures formed by the *g*-[PLA₁₃-*r*-PEG₈₇] bottlebrush copolymer in aqueous solution are very stable throughout the concentration range studied. As observed from Figure 5-10B, the normalized amplitude distribution of decay rates are very broad, spanning from *R*_h ~10 nm to ~250 nm, but there is a clear indication of a second

distribution at small sizes, which suggests a bimodal system of single chains and micellar aggregates for g -[PLA₁₃- r -PEG₈₇] copolymer at all concentrations studied. The plots of the best fit line to the data cast as Γ/q^2 versus q^2 for g -[PLA₁₃- r -PEG₈₇] are shown in Appendix C.

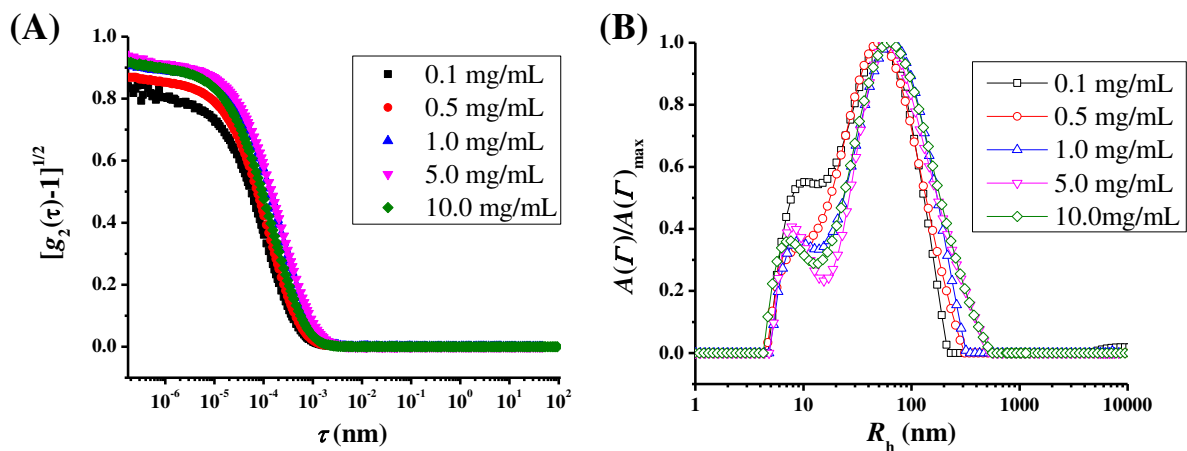


Figure 5-10. (A) Normalized light intensity autocorrelation function at five different concentrations for g -[PLA₁₃- r -PEG₈₇] in aqueous solution, and (B) normalized amplitude distribution of decay rates at five different concentrations for g -[PLA₁₃- r -PEG₈₇]. Both plots reflect similar behaviors at all concentrations studied.

The self-assembly behavior of the g -[PLA₇- r -PEG₉₃] random bottlebrush copolymer in aqueous solution is very similar to that of g -[PLA₁₃- r -PEG₈₇], as seen in Figures 5-11A and B. The normalized light intensity autocorrelation functions show strong coherence and basically overlap one another at all concentrations studied. This suggests similar diffusive behavior across the concentration range studied, which is also reflected in the normalized amplitude distribution

of decay rates shown in Figure 5-11B. The distribution of hydrodynamic sizes shows there are bimodal distributions with sizes corresponding to single chains (characteristic $R_h \sim 13$ nm) and micellar aggregates having characteristic sizes of ~ 394 nm. (Plots of I/q^2 versus q^2 that were used to determine D_{app} and from that, $R_{h,app}$, for g -[PLA_{7- r} -PEG₉₃] are provided in Appendix C.) The results presented in Table 5-3 indicate that there is an increase in the hydrodynamic radius of the large aggregates as the concentration is increased; however, this increase seems most likely due to an increase in the breadth of the hydrodynamic radius distribution. In consideration of the self-assembly properties of the both g -[PLA_{13- r} -PEG₈₇] and g -[PLA_{7- r} -PEG₉₃] bottlebrush copolymers in both solvents studied, it is clear that aqueous solutions readily promote the formation of large compound micelles (LCMs), even at low concentrations.

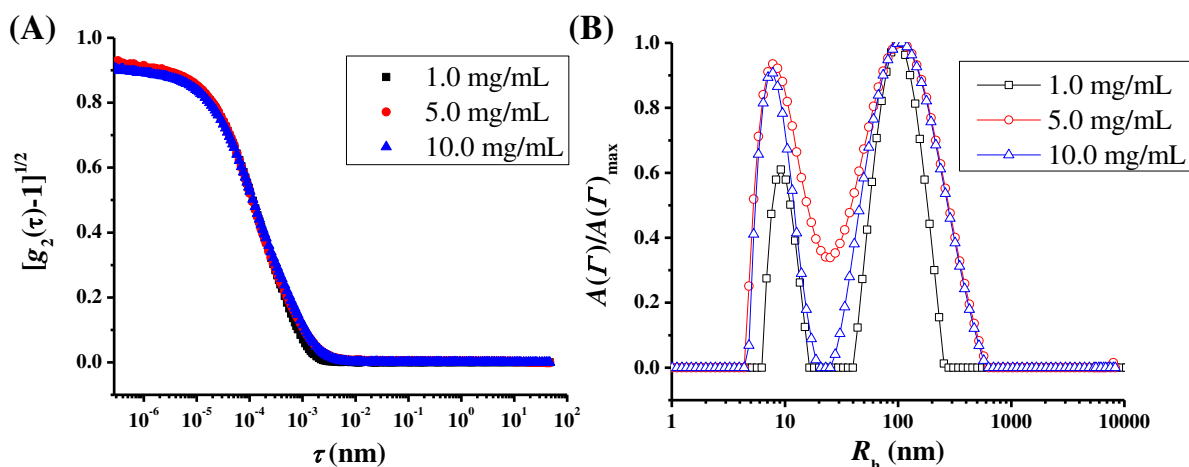


Figure 5-11. (A) Normalized light intensity autocorrelation function at three different concentrations for sample g -[PLA₇- r -PEG₉₃] in aqueous solution, and (B) normalized amplitude distribution of decay rates at three different concentrations for sample g -[PLA₇- r -PEG₉₃] in aqueous solution. The data reflect strong micellization behavior.

5.5 Conclusions

The concentration- and solvent-dependent self-assembly behavior of a series of g -[PLA-PEG] bottlebrush copolymers were investigated in two selective solvents for the PEG side chains, methanol and water. This study reveals that the basic design of the g -[PLA-PEG] bottlebrush copolymers has a significant effect on self-assembly properties in solution. In general, as the solvophobic PLA content was significantly decreased, the bottlebrush copolymer became more soluble and this resulted in an increase in the CMC in methanol. This behavior is speculated to be due in large part to the large entropic penalty that results from bringing the PLA side chains together to form the core of the micellar structure. In aqueous solution, the bottlebrush copolymers readily formed micellar aggregates at very low concentrations, which,

indicates an increase in micellar stability in water as compared to methanol. However, it should be noted that as the insoluble PLA content was increased the solubility of the bottlebrush copolymer significantly decreases in aqueous solution. In water and methanol, the composition and sequence of the side chains influence the size of the self-assembled structures and the micellar stability and, as a result, the formation of different core shell micellar structures and large compound micelles was seen. In total, these results demonstrate that topological design is a useful way to alter self-assembly behaviors.

Chapter 6: Summary, Conclusions and Future Work

6.1 Summary and conclusions

The ability to control the self-assembly properties of amphiphilic block copolymers in solution and at surfaces through the synthetic design of the monomeric building blocks to produce novel and interesting structures or develop systems useful for devices based on soft-matter remains a significant challenge for scientists. For example, the capability to create well-ordered structures from binary mixtures of architecturally- and compositionally-complex amphiphilic block copolymers, to advance technologies such as drug delivery, and surface patterning for processes such as nanolithography, and highly integrated nanoscale electronic devices without the need to synthesize new polymers remains attractive and stimulating, but needs the fundamental science to understand options and possibilities.^{10,16,122,169-171} The work in this dissertation sheds light on this notion and answers some of the most pressing fundamental questions in self-assembly processing using architecturally- and compositionally-complex block copolymers. My work reveals important links between polymer design and the properties of the self-assembled structures and their binary mixtures in solution and at surfaces. Nineteen different amphiphilic block copolymers were used in my thesis work, including six linear poly(styrene-*block*-vinylpyridine) (PS-PVP) diblock and triblock copolymers with varying block lengths; nine PS-PVP star diblock copolymers varying by overall molecular weight, arm number, and block composition; and four poly(lactic acid)-poly(ethylene glycol) PLA-PEG bottlebrush copolymers differing by side chain composition and sequence. Static and dynamic light scattering, atomic force microscopy, and cryogenic and regular transmission electron microscopy with several staining techniques were used to examine self-assembled structures in solution and at surfaces in these studies.

The self-assembly behavior of PS-PVP block copolymers was investigated by SLS and DLS in a thermodynamically non-selective good solvent (THF) and in a selective solvent for PS (toluene). The linear amphiphilic block copolymers in THF remained as isolated single chains in solution with hydrodynamic radii ranging from 8.0 nm to 14.0 nm. In toluene and above the CMC, the block copolymers formed micellar structures in accordance to the closed association model. The organization of the aggregates is such that the insoluble PVP blocks form the core and the soluble PS chains forms the micellar corona. The CMC of the triblock copolymers were higher as compared to the diblock copolymers because of the entropic penalty of looping of PS chains in order to organize PVP chains into the core of the ensembles. The triblock copolymers form flower-like micelles as compared to the star-like micelles formed by its diblock counterpart. This micellar behavior was also seen for triblock copolymers comprising of polyethylene oxide (PEO) and polybutylene oxide (PBO) constituents in the fashion of PBO-PEO-PBO in water (a solvent selective for PEO).¹⁷²⁻¹⁷³ At surfaces, thin films created by spin casting PS-PVP linear diblock and triblock copolymer solutions formed well defined spherical aggregates. However, as the S/V ratio was increased the particle sizes became smaller, and the film thicknesses decreased and became more uniform.

In toluene, the 8-arm star PS-PVP diblock copolymers formed bimodal systems of unimolecular and multimolecular star aggregates at low and medium S/V ratios, as measured by DLS. However, at high S/V ratio the 8-arm stars resist aggregation due to the shielding effects (sterics) brought about by the well solvated PS-chains that prevent the PVP chains from aggregating. In contrast, 26- and 40-arm star diblock copolymers form unimolecular stars independent of block composition both in toluene and THF, the former being selective for PS

and the latter being a non-selective good solvent. Furthermore, SLS and DLS measurements and analyses show that the phase behavior and hydrodynamic behaviors of the 26- and 40-arm star diblock copolymers remain constant through a wide concentration range and exhibit similar sizes and properties in toluene and THF. The hydrodynamic sizes were directly related to the overall molecular weight of the stars, and the 40-arm stars displayed greater R_h values as compared to the 26-arm stars. Stained TEM images on copper-supported carbon film grids revealed an unusual intramolecular microphase-segregated unimolecular star structure that is driven by a thermodynamic balance between the chemically incompatible PS and PVP blocks and the interactions of each block with solvent toluene.

In solution and at surfaces, the self-assembly of the single component PS-PVP block copolymers from toluene solution leads to the formation of either simple spherical micellar ensembles or unimolecular star structures depending on the molecular architecture and block composition. In contrast, binary mixtures of diblock, triblock, and star block copolymers self-assemble into very interesting structures depending on the overall copolymer blend composition, block architecture, and solution concentration. AFM analyses showed that 1:1 binary mixtures of diblock and triblock copolymer pairs formed spherical aggregates from toluene solution. However, DLS measurements showed much higher hydrodynamic radii values for these mixtures as compared to its single component parent systems. AFM analyses of 1:1 binary mixtures of diblock and star block copolymers also showed simple spherical aggregates at surfaces. However, a binary mixture of a diblock and an 8-arm star displayed a network of worm-like aggregates or bicontinuous structures. Though most of the binary mixtures of diblock and star block copolymers form spherical aggregates at surfaces, DLS measurements and analyses for

some of the mixtures show triple distribution functions. This was as a direct result of the increase in polydispersity that is introduced into the micellar system by mixing and, in so doing, the kinetics of micelle formation is significantly altered.

Binary mixtures of triblock and star block copolymers cast from toluene solutions formed the most complex and interesting structures at surfaces compared to those formed by mixing diblock and stars. Specifically, a novel “brain coral-like” hierarchical aggregate consisting of primary spherical and secondary worm-like structures is observed in a blend created from a mixture of a triblock and an 8-arm PS-PVP star block copolymer. Cryo-TEM images show that the hierarchical structures do not exist in solution; they form due to the substantial collapse of PS microdomains during the solvent removal process. In general, the AFM results prove that there are three typical morphologies (spherical, worm-like, and hierarchical) adopted in thin films of PS-PVP block copolymer binary mixtures from toluene solution created when binary mixtures are blended using a premixing method.

To understand the links between block composition and sequence on the self-assembled properties of amphiphilic bottlebrush copolymers, a series of PLA-PEG bottlebrush copolymers were synthesized by ring-opening metathesis polymerization, or “ROMP”. The solution properties of four PLA-PEG bottlebrush copolymers differing by side chain composition and sequence were investigated in methanol and water over a wide concentration range. According to DLS measurements and analyses, in methanol, the random bottlebrush copolymer samples exhibit higher CMCs and smaller hydrodynamic radii as compared to the diblock bottlebrush copolymer. From cryo-TEM and regular TEM images, the bottlebrush copolymers form spherical micelles independent of block composition or block sequence. In aqueous solution

PLA-PEG random and diblock bottlebrush copolymers form large compound micelles and exhibited lower CMC values. The decrease in CMC values in water indicates that the micellar structures are more stable in aqueous solution. However, under aqueous conditions the diblock and random bottlebrush copolymer with a large PLA content was only soluble at very low solution concentrations.

In summary, through this body of results, my research has shown specifically that architecture, composition, sequence, and concentration can have a significant impact on the phase behavior and self-assembled properties of amphiphilic block copolymers in solution and at surfaces. Perhaps more importantly, my work has revealed specific links and correlations between copolymer design, composition, self-assembled structure and properties in solution and thin films. Additionally, my work has demonstrated that binary mixtures of architecturally- and compositionally complex block copolymers in solution can lead to interesting and exotic self-assembled structures at surfaces. This research has also shown that special attention has to be given to the choice of solvent and fabrication process of micelle formation, as this can significantly affect and change the self-assembly properties of micellar systems.

6.2 Future work

Detailed insight into the links between macromolecular architecture, composition, and block sequence and the behavior of amphiphilic block copolymer systems have been gained through this work; however, many fundamental questions that need to be addressed remain. Therefore, I expect that additional studies will be helpful to advance the understanding of the

self-assembly of single component architecturally complex macromolecular systems and their binary mixtures in solution and at surfaces. The following research is recommended:

- I. A more detailed understanding of the links between the processing method used to make binary amphiphilic copolymer mixtures and the resulting self-assembled structures can be gained by changing the mixing protocol.⁵⁶ In Chapter 3, the premixing method was used to create binary blends of novel polymeric ensembles in solution and at surfaces. It would be very interesting to make a comparison between mixing protocols by investigating the postmixing method. Here, (micellar) solutions of each copolymer are made independently and subsequently mixed after equilibration. In so doing, the kinetics and thermodynamics of micelle formation between the block copolymers are likely to change. This change in processing method is expected to alter the properties of the resulting micellar system, and probing issues of copolymer design, size, composition and concentration would help clarify the role of processing and potentially provide useful routes to useful or unusual self-assembled structures.
- II. Although several cryo-TEM and regular TEM staining techniques are available and were used in my thesis work, other techniques may be useful in order to better understand the location and rearrangement of the chains within the micellar structures formed in solution. For example, a more detailed picture of the conformation and location of PS and PVP blocks within the single component and mixed micellar systems could be achieved if one of the blocks was isotopically labeled by substituting deuterium for hydrogen. By doing this, specifically for the

high molecular weight 26- and 40-arm stars, the conformation and exact location of each block can be better determined using small-angle neutron scattering techniques.¹⁷⁴ In the case of PLA-PEG bottlebrush copolymer, the volume fraction of PLA side chains inside the core and the organization of the PEG side chains in the corona could be better resolved.

- III. Currently there are no studies in the literature on binary mixtures of bottlebrush copolymers from a thermodynamically selective solvent for one of the side chains. Because the solution self-assembly behavior of the PLA-PEG single component bottlebrush copolymers has been investigated in my thesis work. It would be of great interest to augment those studies by examining binary mixtures containing the PLA-PEG bottlebrushes used in this study. Such studies should be performed using methanol and water as selective solvents, focusing on the role of composition and sequence in both polymers used in this work.

In total, these themes of study would further elaborate links between polymer topology, solution properties, and structure via self-assembly. This body of work would help to advance the development of novel nanostructured polymer systems by self-assembly, and inspire new ideas about how to translate molecular structures to larger-scale soft objects to create useful systems.

List of References

1. Whitesides, G. M.; Grzybowski, B., Self-Assembly at All Scales. *Science* **2002**, 295 (5564), 2418-2421.
2. Lodge, T. P., Block Copolymers: Past Successes and Future Challenges. *Macromolecular Chemistry and Physics* **2003**, 204 (2), 265-273.
3. Ozin, G. A.; Hou, K.; Lotsch, B. V.; Cademartiri, L.; Puzzo, D. P.; Scotognella, F.; Ghadimi, A.; Thomson, J., Nanofabrication by Self-assembly. *Materials Today* **2009**, 12 (5), 12-23.
4. Singamaneni, S.; Bliznyuk, V. N.; Binek, C.; Tsybal, E. Y., Magnetic Nanoparticles: Recent Advances in Synthesis, Self-Assembly and Applications. *Journal of Materials Chemistry* **2011**, 21 (42), 16819-16845.
5. Higgins, A. M.; Jones, R. A. L., Anisotropic Spinodal Dewetting as a Route To Self-Assembly of Patterned Surfaces. *Nature* **2000**, 404 (6777), 476.
6. Gelain, F.; Horii, A.; Zhang, S., Designer Self-Assembling Peptide Scaffolds for 3-D Tissue Cell Cultures and Regenerative Medicine. *Macromolecular Bioscience* **2007**, 7 (5), 544-551.
7. Matsen, M. W.; Schick, M., Self-assembly of Block Copolymers. *Current Opinion In Colloid & Interface Science* **1996**, 1 (3), 329-336.
8. Mai, Y.; Eisenberg, A., Self-assembly of Block Copolymers. *Chemical Society Reviews* **2012**, 41 (18), 5969-5985.
9. Kotaka, T.; Tanaka, T.; Hattori, M.; Inagaki, H., Block Copolymer Micelles in Dilute Solution. *Macromolecules* **1978**, 11 (1), 138-145.

10. Riess, G., Micellization of Block Copolymers. *Progress in Polymer Science* **2003**, *28* (7), 1107-1170.
11. Albert, J. N. L.; Epps Iii, T. H., Self-assembly of Block Copolymer Thin Films. *Materials Today* **2010**, *13* (6), 24-33.
12. Darling, S. B., Directing the Self-assembly of Block Copolymers. *Progress in Polymer Science* **2007**, *32* (10), 1152-1204.
13. Tsukruk, V. V., Assembly of Supramolecular Polymers in Ultrathin Films. *Progress in Polymer Science* **1997**, *22* (2), 247-311.
14. Nagarajan, R.; Ganesh, K., Block Copolymer Self-Assembly in Selective Solvents: Theory of Solubilization in Spherical Micelles. *Macromolecules* **1989**, *22* (11), 4312-4325.
15. Ian, W.; GuoJun, L., Self-Assembly and Chemical Processing of Block Copolymers: A Roadmap Towards a Diverse Array of Block Copolymer Nanostructures. *Sci. China Life Sci.* **2013**, 1-27.
16. Tsai, H.; Pitera, J. W.; Miyazoe, H.; Bangsaruntip, S.; Engelmann, S. U.; Liu, C.-C.; Cheng, J. Y.; Bucchignano, J. J.; Klaus, D. P.; Joseph, E. A.; Sanders, D. P.; Colburn, M. E.; Guillorn, M. A., Two-Dimensional Pattern Formation Using Graphoepitaxy of PS-b-PMMA Block Copolymers for Advanced FinFET Device and Circuit Fabrication. *ACS Nano* **2014**, *8* (5), 5227-5232.
17. Berret, J.-F.; Schonbeck, N.; Gazeau, F.; El Kharrat, D.; Sandre, O.; Vacher, A.; Airiau, M., Controlled Clustering of Superparamagnetic Nanoparticles Using Block Copolymers: Design of New Contrast Agents for Magnetic Resonance Imaging. *Journal of the American Chemical Society* **2006**, *128* (5), 1755-1761.

18. Forster, S.; Konrad, M., From Self-organizing Polymers to Nano- and Biomaterials. *Journal of Materials Chemistry* **2003**, *13* (11), 2671-2688.
19. Rösler, A.; Vandermeulen, G. W.; Klok, H.-A., Advanced Drug Delivery Devices Via Self-Assembly of Amphiphilic Block Copolymers. *Advanced Drug Delivery Reviews* **2012**.
20. Pavía-Sanders, A.; Zhang, S.; Flores, J. A.; Sanders, J. E.; Raymond, J. E.; Wooley, K. L., Robust Magnetic/Polymer Hybrid Nanoparticles Designed for Crude Oil Entrapment and Recovery in Aqueous Environments. *ACS Nano* **2013**, *7* (9), 7552-7561.
21. Neoh, K. G.; Kang, E. T., Functionalization of Inorganic Nanoparticles with Polymers for Stealth Biomedical Applications. *Polymer Chemistry* **2011**, *2* (4), 747-759.
22. Bates, F. S.; Hillmyer, M. A.; Lodge, T. P.; Bates, C. M.; Delaney, K. T.; Fredrickson, G. H., Multiblock Polymers: Panacea or Pandora's Box? *Science* **2012**, *336* (6080), 434-440.
23. Szwarc, M.; Levy, M.; Milkovich, R., Polymerization Initiated by Electron Transfer to Monomer. A New Method of Formation of Block Polymers¹. *Journal of the American Chemical Society* **1956**, *78* (11), 2656-2657.
24. Ji, H.; Sakellariou, G.; Advincula, R. C.; Smith, G. D.; Kilbey, S. M.; Dadmun, M. D.; Mays, J. W., Synthesis and Characterization of Well-defined [polystyrene-*b*-poly(2-vinylpyridine)]_n Star-block Copolymers with Poly(2-vinylpyridine) corona blocks. *Journal of Polymer Science Part A: Polymer Chemistry* **2007**, *45* (17), 3949-3955.
25. Isono, T.; Satoh, Y.; Miyachi, K.; Chen, Y.; Sato, S.-i.; Tajima, K.; Satoh, T.; Kakuchi, T., Synthesis of Linear, Cyclic, Figure-Eight-Shaped, and Tadpole-Shaped Amphiphilic Block Copolyethers via *t*-Bu-P4-Catalyzed Ring-Opening Polymerization of Hydrophilic and Hydrophobic Glycidyl Ethers. *Macromolecules* **2014**.

26. Hong, K.; Mays, J. W., 1,3-Cyclohexadiene Polymers. 3. Synthesis and Characterization of Poly(1,3-cyclohexadiene-block-styrene). *Macromolecules* **2001**, *34* (11), 3540-3547.
27. Jain, S.; Bates, F. S., Consequences of Nonergodicity in Aqueous Binary PEO–PB Micellar Dispersions. *Macromolecules* **2004**, *37* (4), 1511-1523.
28. Hamley, I. W., *Block Copolymers in Solution: Fundamentals and Applications*. Wiley New York: 2005.
29. Zhulina, E. B.; Borisov, O. V., Theory of Block Polymer Micelles: Recent Advances and Current Challenges. *Macromolecules* **2012**, *45* (11), 4429-4440.
30. Borisov, O.; Zhulina, E.; Leermakers, F. M.; Müller, A. E., Self-Assembled Structures of Amphiphilic Ionic Block Copolymers: Theory, Self-Consistent Field Modeling and Experiment. In *Self Organized Nanostructures of Amphiphilic Block Copolymers I*, Müller, A. H. E.; Borisov, O., Eds. Springer Berlin Heidelberg: 2011; Vol. 241, pp 57-129.
31. Hayward, R. C.; Pochan, D. J., Tailored Assemblies of Block Copolymers in Solution: It Is All about the Process. *Macromolecules* **2010**, *43* (8), 3577-3584.
32. Zamfir, M.; Patrickios, C. S.; Montagne, F.; Abetz, C.; Abetz, V.; Oss-Ronen, L.; Talmon, Y., Styrene–Vinyl Pyridine Diblock Copolymers: Synthesis by RAFT Polymerization and Self-Assembly in Solution and in the Bulk. *Journal of Polymer Science Part A: Polymer Chemistry* **2012**, *50* (8), 1636-1644.
33. Fredrickson, G. H.; Bates, F. S., Dynamics of Block Copolymers: Theory and Experiment. *Annual Review of Material Science* **1996**, *26*, 501-550.

34. Tenbrinke, G.; Hadziioannou, G., Topological Constraints and their Influence on the and the Properties of Synthetic Macromolecular Systems .2. Micelle Formation of Triblock Copolymers. *Macromolecules* **1987**, *20* (3), 486-489.
35. Kotaka, T.; Tanaka, T.; Inagaki, H., Thermodynamic and Conformational Properties of Styrene-Methyl Methacrylate Block Copolymers in Dilute-Solution .4. Behavior of Diblock and Triblock Copolymers in Selective Solvents. *Polymer Journal* **1972**, *3* (3), 327-&.
36. Balsara, N. P.; Tirrell, M.; Lodge, T. P., Micelle formation of BAB Triblock Copolymers in Solvents that Preferentially Dissolve the A block. *Macromolecules* **1991**, *24* (8), 1975-1986.
37. Krause, S., Dilute Solution Properties of a Styrene—Methyl Methacrylate Block Copolymer. *The Journal of Physical Chemistry* **1964**, *68* (7), 1948-1955.
38. Wang, X.; Li, L.; Ye, X.; Wu, C., Comparative Study of Solution Properties of Amphiphilic 8-Shaped Cyclic-(Polystyrene-b-Poly(acrylic acid))₂ and Its Linear Precursor. *Macromolecules* **2014**, *47* (7), 2487-2495.
39. Williams, R. J.; Dove, A. P.; O'Reilly, R. K., Self-assembly of Cyclic Polymers. *Polymer Chemistry* **2015**, *6* (16), 2998-3008.
40. Geiser, D.; Höcker, H., Synthesis and Investigation of Macrocyclic Polystyrene. *Macromolecules* **1980**, *13* (3), 653-656.
41. Minatti, E.; Viville, P.; Borsali, R.; Schappacher, M.; Deffieux, A.; Lazzaroni, R., Micellar Morphological Changes Promoted by Cyclization of PS-b-PI Copolymer: DLS and AFM Experiments. *Macromolecules* **2003**, *36* (11), 4125-4133.

42. Zhulina, E. B.; Borisov, O. V., Effect of Block Copolymer Architecture on Morphology of Self-Assembled Aggregates in Solution. *ACS Macro Letters* **2013**, *2* (4), 292-295.
43. Sheng, Y.-J.; Nung, C.-H.; Tsao, H.-K., Morphologies of Star-Block Copolymers in Dilute Solutions. *The Journal of Physical Chemistry B* **2006**, *110* (43), 21643-21650.
44. Hinestrosa, J. P.; Alonzo, J.; Osa, M.; Kilbey, S. M., Solution Behavior of Polystyrene–Polyisoprene Miktoarm Block Copolymers in a Selective Solvent for Polyisoprene. *Macromolecules* **2010**, *43* (17), 7294-7304.
45. Alonzo, J.; Hinestrosa, J. P.; Mays, J. W.; Kilbey, S. M., Kinetics of Preferential Adsorption of Amphiphilic Star Block Copolymers that Tether by Their Corona Blocks at the Solid/Fluid Interface. *Macromolecules* **2014**, *47* (12), 4048-4055.
46. Roovers, J.; Zhou, L. L.; Toporowski, P. M.; van der Zwan, M.; Iatrou, H.; Hadjichristidis, N., Regular Star Polymers with 64 and 128 Arms. Models for Polymeric Micelles. *Macromolecules* **1993**, *26* (16), 4324-4331.
47. Nese, A.; Mosnáček, J.; Juhari, A.; Yoon, J. A.; Koynov, K.; Kowalewski, T.; Matyjaszewski, K., Synthesis, Characterization, and Properties of Starlike Poly(n-butyl acrylate)-b-poly(methyl methacrylate) Block Copolymers. *Macromolecules* **2010**, *43* (3), 1227-1235.
48. Jang, S.; Moon, H. C.; Kwak, J.; Bae, D.; Lee, Y.; Kim, J. K.; Lee, W. B., Phase Behavior of Star-Shaped Polystyrene-block-poly(methyl methacrylate) Copolymers. *Macromolecules* **2014**, *47* (15), 5295-5302.

49. Shim, J. S.; Kennedy, J. P., Novel Thermoplastic Elastomers. II. Properties of Star-block Copolymers of PSt-b-PIB Arms Emanating from Cyclosiloxane Cores. *Journal of Polymer Science Part A: Polymer Chemistry* **1999**, *37* (6), 815-824.
50. Pang, X.; Zhao, L.; Akinc, M.; Kim, J. K.; Lin, Z., Novel Amphiphilic Multi-Arm, Star-Like Block Copolymers as Unimolecular Micelles. *Macromolecules* **2011**, *44* (10), 3746-3752.
51. Pang, X.; Feng, C.; Xu, H.; Han, W.; Xin, X.; Xia, H.; Qiu, F.; Lin, Z., Unimolecular Micelles Composed of Inner Coil-Like Blocks and Outer Rod-Like Blocks Crafted by Combination of Living Polymerization with Click Chemistry. *Polymer Chemistry* **2014**, *5* (8), 2747-2755.
52. Vyhnanekova, R.; Müller, A. H. E.; Eisenberg, A., Control of Morphology and Corona Composition in Aggregates of Mixtures of PS-b-PAA and PS-b-P4VP Diblock Copolymers: Effects of Solvent, Water Content, and Mixture Composition. *Langmuir* **2014**, *30* (44), 13152-13163.
53. Wang, X.; Davis, J. L.; Hinestrosa, J. P.; Mays, J. W.; Kilbey, S. M., Control of Self-Assembled Structure through Architecturally and Compositionally Complex Block Copolymer Surfactant Mixtures. *Macromolecules* **2014**, *47* (20), 7138-7150.
54. Li, Z.; Hillmyer, M. A.; Lodge, T. P., Control of Structure in Multicompartment Micelles by Blending μ -ABC Star Terpolymers with AB Diblock Copolymers. *Macromolecules* **2005**, *39* (2), 765-771.

55. Zhu, J.; Hayward, R. C., Wormlike Micelles with Microphase-Separated Cores from Blends of Amphiphilic AB and Hydrophobic BC Diblock Copolymers. *Macromolecules* **2008**, *41* (21), 7794-7797.
56. Yoo, S. I.; Sohn, B.-H.; Zin, W.-C.; Jung, J. C.; Park, C., Mixtures of Diblock Copolymer Micelles by Different Mixing Protocols. *Macromolecules* **2007**, *40* (23), 8323-8328.
57. Yoo, S. I.; Yun, S. H.; Kim, H. K.; Sohn, B.-H., Highly Ordered Hexagonal Arrays of Hybridized Micelles from Bimodal Self-Assemblies of Diblock Copolymer Micelles. *Macromolecular Rapid Communications* **2010**, *31* (7), 645-650.
58. Voulgaris, D.; Tsitsilianis, C.; Esselink, F. J.; Hadziioannou, G., Polystyrene/poly(2-vinylpyridine) Heteroarm Star Copolymer Micelles in Toluene: Morphology and Thermodynamics. *Polymer* **1998**, *39* (25), 6429-6439.
59. Alonzo, J.; Huang, Z.; Liu, M.; Mays, J. W.; Toomey, R. G.; Dadmun, M. D.; Kilbey, S. M., Looped Polymer Brushes Formed by Self-Assembly of Poly(2-vinylpyridine)-Polystyrene-Poly(2-vinylpyridine) Triblock Copolymers at the Solid-Fluid Interface. Kinetics of Preferential Adsorption. *Macromolecules* **2006**, *39* (24), 8434-8439.
60. Kilbey, S. M.; Watanabe, H.; Tirrell, M., Structure and Scaling of Polymer Brushes Near the Theta Condition. *Macromolecules* **2001**, *34* (15), 5249-5259.
61. Chu, B., *Laser Light Scattering, Basic Principles and Practices*. Academic Press: 1974.
62. Hiemenz, P. C.; Lodge, T. P., *Polymer Chemistry, Second Edition*. Taylor & Francis: 2007.
63. Schärfl, W., *Light Scattering from Polymer Solutions and Nanoparticle Dispersions*; Springer: Berlin, 2007.

64. Provencher, S. W., CONTIN: A General Purpose Constrained Regularization Program for Inverting Noisy Linear Algebraic and Integral Equations. *Computer Physics Communications* **1982**, 27 (3), 229-242.
65. Brown, W., *Light Scattering: Principles and Development*. Clarendon Press: 1996.
66. Burchard, W., Solution Properties of Branched Macromolecules. In *Branched Polymers II*, Roovers, J., Ed. Springer Berlin Heidelberg: 1999; Vol. 143, pp 113-194.
67. Russo, P., *Dynamic Light Scattering*. Louisiana State University, 2009.
68. Ahmed, R.; Patra, S. K.; Hamley, I. W.; Manners, I.; Faul, C. F. J., Tetragonal and Helical Morphologies from Polyferrocenylsilane Block Polyelectrolytes via Ionic Self-Assembly. *Journal of the American Chemical Society* **2013**, 135 (7), 2455-2458.
69. Schacher, F. H.; Rugar, P. A.; Manners, I., Functional Block Copolymers: Nanostructured Materials with Emerging Applications. *Angewandte Chemie-International Edition* **2012**, 51 (32), 7898-7921.
70. Cai, Y.; Aubrecht, K. B.; Grubbs, R. B., Thermally Induced Changes in Amphiphilicity Drive Reversible Restructuring of Assemblies of ABC Triblock Copolymers with Statistical Polyether Blocks. *Journal of the American Chemical Society* **2011**, 133 (4), 1058-1065.
71. Dou, H. J.; Jiang, M.; Peng, H. S.; Chen, D. Y.; Hong, Y., pH-dependent Self-assembly: Micellization and Micelle-hollow-sphere Transition of Cellulose-based Copolymers. *Angewandte Chemie-International Edition* **2003**, 42 (13), 1516-1519.
72. Jang, S. G.; Audus, D. J.; Klinger, D.; Krogstad, D. V.; Kim, B. J.; Cameron, A.; Kim, S. W.; Delaney, K. T.; Hur, S. M.; Killops, K. L.; Fredrickson, G. H.; Kramer, E. J.; Hawker,

- C. J., Striped, Ellipsoidal Particles by Controlled Assembly of Diblock Copolymers. *Journal of the American Chemical Society* **2013**, *135* (17), 6649-6657.
73. Jang, S. G.; Kramer, E. J.; Hawker, C. J., Controlled Supramolecular Assembly of Micelle-Like Gold Nanoparticles in PS-*b*-P2VP Diblock Copolymers via Hydrogen Bonding. *Journal of the American Chemical Society* **2011**, *133* (42), 16986-16996.
74. Li, Z.; Zhang, Y.; Fullhart, P.; Mirkin, C. A., Reversible and Chemically Programmable Micelle Assembly with DNA Block-Copolymer Amphiphiles. *Nano Letters* **2004**, *4* (6), 1055-1058.
75. Ma, N.; Li, Y.; Xu, H.; Wang, Z.; Zhang, X., Dual Redox Responsive Assemblies Formed from Diselenide Block Copolymers. *Journal of the American Chemical Society* **2010**, *132* (2), 442-443.
76. Ramanathan, M.; Kilbey, S. M.; Ji, Q. M.; Hill, J. P.; Ariga, K., Materials Self-assembly and Fabrication in Confined Spaces. *Journal of Materials Chemistry* **2012**, *22* (21), 10389-10405.
77. Ren, L. X.; Hardy, C. G.; Tang, C. B., Synthesis and Solution Self-Assembly of Side-Chain Cobaltocenium-Containing Block Copolymers. *Journal of the American Chemical Society* **2010**, *132* (26), 8874-+.
78. Zhang, K.; Jiang, M.; Chen, D., DNA/Polymeric Micelle Self-Assembly Mimicking Chromatin Compaction. *Angewandte Chemie International Edition* **2012**, *51* (35), 8744-8747.

79. Gu, X. D.; Liu, Z. W.; Gunkel, I.; Chourou, S. T.; Hong, S. W.; Olynick, D. L.; Russell, T. P., High Aspect Ratio Sub-15 nm Silicon Trenches From Block Copolymer Templates. *Advanced Materials* **2012**, *24* (42), 5688-5694.
80. Hardy, C. G.; Ren, L. X.; Ma, S. G.; Tang, C. B., Self-assembly of Well-defined Ferrocene Triblock Copolymers and their Template Synthesis of Ordered Iron Oxide Nanoparticles. *Chemical Communications* **2013**, *49* (39), 4373-4375.
81. Kastle, G.; Boyen, H. G.; Weigl, F.; Lengl, G.; Herzog, T.; Ziemann, P.; Riethmuller, S.; Mayer, O.; Hartmann, C.; Spatz, J. P.; Moller, M.; Ozawa, M.; Banhart, F.; Garnier, M. G.; Oelhafen, P., Micellar Nanoreactors - Preparation and Characterization of Hexagonally Ordered Arrays of Metallic Nanodots. *Advanced Functional Materials* **2003**, *13* (11), 853-861.
82. Suntivich, R.; Choi, I.; Gupta, M. K.; Tsitsilianis, C.; Tsukruk, V. V., Gold Nanoparticles Grown on Star-Shaped Block Copolymer Monolayers. *Langmuir* **2011**, *27* (17), 10730-10738.
83. Kim, B. S.; Park, S. W.; Hammond, P. T., Hydrogen-bonding Layer-by-layer Assembled Biodegradable Polymeric Micelles as Drug Delivery Vehicles from Surfaces. *ACS Nano* **2008**, *2* (2), 386-392.
84. Kim, J. O.; Kabanov, A. V.; Bronich, T. K., Polymer Micelles With Cross-Linked Polyanion Core for Delivery of a Cationic Drug Doxorubicin. *Journal of Controlled Release* **2009**, *138* (3), 197-204.

85. Rosler, A.; Vandermeulen, G. W. M.; Klok, H. A., Advanced Drug Delivery Devices Via Self-Assembly of Amphiphilic Block Copolymers. *Advanced Drug Delivery Reviews* **2012**, *64*, 270-279.
86. Ternat, C.; Ouali, L.; Sommer, H.; Fieber, W.; Velazco, M. I.; Plummer, C. J. G.; Kreutzer, G.; Klok, H. A.; Manson, J. A. E.; Herrmann, A., Investigation of the Release of Bioactive Volatiles from Amphiphilic Multiarm Star-Block Copolymers by Thermogravimetry and Dynamic Headspace Analysis. *Macromolecules* **2008**, *41* (19), 7079-7089.
87. Cho, J.; Hong, J. K.; Char, K.; Caruso, F., Nanoporous Block Copolymer Micelle/micelle Multilayer Films with Dual Optical Properties. *Journal of the American Chemical Society* **2006**, *128* (30), 9935-9942.
88. Joo, W.; Park, M. S.; Kim, J. K., Block Copolymer Film with Sponge-like Nanoporous Structure for Antireflection Coating. *Langmuir* **2006**, *22* (19), 7960-7963.
89. Kang, Y.; Walish, J. J.; Gorishnyy, T.; Thomas, E. L., Broad-wavelength-range Chemically Tunable Block-Copolymer Photonic Gels. *Nature Materials* **2007**, *6* (12), 957-960.
90. Lu, Y. X.; Choi, Y. J.; Lim, H. S.; Kwak, D.; Shim, C.; Lee, S. G.; Cho, K., pH-Induced Antireflection Coatings Derived from Hydrogen-Bonding-Directed Multi layer Films. *Langmuir* **2010**, *26* (22), 17749-17755.
91. Hentschel, J.; Kushner, A. M.; Ziller, J.; Guan, Z. B., Self-Healing Supramolecular Block Copolymers. *Angewandte Chemie-International Edition* **2012**, *51* (42), 10561-10565.
92. Matyjaszewski, K.; Tsarevsky, N. V., Nanostructured Functional Materials Prepared by Atom Transfer Radical Polymerization. *Nature Chemistry* **2009**, *1* (4), 276-288.

93. Petzetakis, N.; Robin, M. P.; Patterson, J. P.; Kelley, E. G.; Cotanda, P.; Bomans, P. H. H.; Sommerdijk, N.; Dove, A. P.; Epps, T. H.; O'Reilly, R. K., Hollow Block Copolymer Nanoparticles through a Spontaneous One-step Structural Reorganization. *ACS Nano* **2013**, *7* (2), 1120-1128.
94. Rupar, P. A.; Chabanne, L.; Winnik, M. A.; Manners, I., Non-Centrosymmetric Cylindrical Micelles by Unidirectional Growth. *Science* **2012**, *337* (6094), 559-562.
95. Stals, P. J. M.; Li, Y. C.; Burdynska, J.; Nicolay, R.; Nese, A.; Palmans, A. R. A.; Meijer, E. W.; Matyjaszewski, K.; Sheiko, S. S., How Far Can We Push Polymer Architectures? *Journal of the American Chemical Society* **2013**, *135* (31), 11421-11424.
96. Hinestrosa, J. P.; Uhrig, D.; Pickel, D. L.; Mays, J. W.; Kilbey, S. M., Hydrodynamics of Polystyrene-Polyisoprene Miktoarm Star Copolymers in a Selective and a Non-Selective Solvent. *Soft Matter* **2012**, *8* (39), 10061-10071.
97. Stepanek, M.; Matejcek, P.; Humpolickova, J.; Havrankova, J.; Podhajecka, K.; Spirkova, M.; Tuzar, Z.; Tsitsilianis, C.; Prochazka, K., New Insights on the Solution Behavior and Self-Assembly of Polystyrene/Poly(2-Vinylpyridine) 'Hairy' Heteroarm Star Copolymers with Highly Asymmetric Arms in Polar Organic and Aqueous Media. *Polymer* **2005**, *46* (23), 10493-10505.
98. Tsitsilianis, C.; Voulgaris, D.; Stepanek, M.; Podhajecka, K.; Prochazka, K.; Tuzar, Z.; Brown, W., Polystyrene/Poly(2-vinylpyridine) Heteroarm Star Copolymer Micelles in Aqueous Media and Onion Type Micelles Stabilized by Diblock Copolymers. *Langmuir* **2000**, *16* (17), 6868-6876.

99. Won, Y. Y.; Davis, H. T.; Bates, F. S., Molecular Exchange in PEO-PB Micelles in Water. *Macromolecules* **2003**, *36* (3), 953-955.
100. Borovinskii, A. L.; Khokhlov, A. R., Micelle Formation in the Dilute Solution Mixtures of Block-copolymers. *Macromolecules* **1998**, *31* (22), 7636-7640.
101. Cai, P.; Wang, C. Q.; Ye, J.; Xie, Z. W.; Chi, W., Hybridization of Polymeric Micelles in a Dispersion Mixture. *Macromolecules* **2004**, *37* (9), 3438-3443.
102. Esselink, F. J.; Dormidontova, E. E.; Hadziioannou, G., Redistribution of Block Copolymer Chains between Mixed Micelles in Solution. *Macromolecules* **1998**, *31* (15), 4873-4878.
103. Honda, C.; Yamamoto, K.; Nose, T., Comicellization of Binary Mixtures of Block Copolymers with Different Block Lengths in a Selective Solvent. *Polymer* **1996**, *37* (10), 1975-1984.
104. Kang, N.; Perron, M. E.; Prud'homme, R. E.; Zhang, Y. B.; Gaucher, G.; Leroux, J. C., Stereocomplex Block Copolymer Micelles: Core-shell Nanostructures with Enhanced Stability. *Nano Letters* **2005**, *5* (2), 315-319.
105. Konak, C.; Helmstedt, M., Comicellization of Diblock and Triblock Copolymers in Selective Solvents. *Macromolecules* **2003**, *36* (12), 4603-4608.
106. Stepanek, M.; Podhajecka, K.; Tesarova, E.; Prochazka, K.; Tuzar, Z.; Brown, W., Hybrid Polymeric Micelles with Hydrophobic Cores and Mixed Polyelectrolyte/Nonelectrolyte Shells in Aqueous Media. 1. Preparation and Basic Characterization. *Langmuir* **2001**, *17* (14), 4240-4244.
107. Tian, M. M.; Qin, A. W.; Ramireddy, C.; Webber, S. E.; Munk, P.; Tuzar, Z.; Prochazka, K., Hybridization of Block-Copolymer Micelles. *Langmuir* **1993**, *9* (7), 1741-1748.

108. Matsen, M. W., Polydispersity-induced Macrophase Separation in Diblock Copolymer Melts. *Physical Review Letters* **2007**, *99* (14).
109. Schmitt, A. L.; Repollet-Pedrosa, M. H.; Mahanthappa, M. K., Polydispersity-Driven Block Copolymer Amphiphile Self-Assembly into Prolate-Spheroid Micelles. *ACS Macro Letters* **2012**, *1* (2), 300-304.
110. Widin, J. M.; Schmitt, A. K.; Schmitt, A. L.; Im, K.; Mahanthappa, M. K., Unexpected Consequences of Block Polydispersity on the Self-Assembly of ABA Triblock Copolymers. *Journal of the American Chemical Society* **2012**, *134* (8), 3834-3844.
111. Zhu, J.; Zhang, S.; Zhang, K.; Wang, X.; Mays, J. W.; Wooley, K. L.; Pochan, D. J., Disk-Cylinder and Disk-Sphere Nanoparticles Via a Block Copolymer Blend Solution Construction. *Nature Communications* **2013**, *4*.
112. Lefevre, N.; Daoulas, K. C.; Muller, M.; Gohy, J. F.; Fustin, C. A., Self-Assembly in Thin Films of Mixtures of Block Copolymers and Homopolymers Interacting by Hydrogen Bonds. *Macromolecules* **2010**, *43* (18), 7734-7743.
113. Court, F.; Yamaguchi, D.; Hashimoto, T., Morphological Studies of Binary Mixtures of Block Copolymers: Temperature Dependence of Cosurfactant Effects. *Macromolecules* **2006**, *39* (7), 2596-2605.
114. Jiang, N.; Xu, Y.; He, N.; Chen, J.; Deng, Y.; Yuan, C.; Han, G.; Dai, L., Synthesis of Walnut-Like Hierarchical Structure with Superhydrophobic and Conductive Properties. *Journal of Materials Chemistry* **2010**, *20* (48), 10847-10855.

115. Qin, S.; Li, H.; Yuan, W. Z.; Zhang, Y., Fluorine-Containing Block Copolymer Particles with Surface and Internal Hierarchical Microphase Separation Structures. *Soft Matter* **2012**, 8 (8), 2471-2476.
116. van Zoelen, W.; ten Brinke, G., Thin Films of Complexed Block Copolymers. *Soft Matter* **2009**, 5 (8), 1568-1582.
117. Urban, C.; Schurtenberger, P., Characterization of Turbid Colloidal Suspensions using Light Scattering Techniques Combined with Cross-Correlation Methods. *Journal of Colloid and Interface Science* **1998**, 207 (1), 150-158.
118. Zhulina, E. B.; Adam, M.; LaRue, I.; Sheiko, S. S.; Rubinstein, M., Diblock Copolymer Micelles in a Dilute Solution. *Macromolecules* **2005**, 38 (12), 5330-5351.
119. Cameron, N. S.; Corbierre, M. K.; Eisenberg, A., 1998 E.W.R. Steacie Award Lecture Asymmetric Amphiphilic Block Copolymers in Solution: a Morphological Wonderland. *Canadian Journal of Chemistry* **1999**, 77 (8), 1311-1326.
120. Lo, C. L.; Lin, K. M.; Huang, C. K.; Hsiue, G. H., Self-Assembly of a Micelle Structure from Graft and Diblock Copolymers: An Example of Overcoming the Limitations of Polyions in Drug Delivery. *Advanced Functional Materials* **2006**, 16 (18), 2309-2316.
121. Alexandridis, P.; Lindman, B., *Amphiphilic Block Copolymers: Self-Assembly and Applications*. Elsevier Science: 2000.
122. Patri, A. K.; Majoros, I. J.; Baker Jr, J. R., Dendritic Polymer Macromolecular Carriers for Drug Delivery. *Current Opinion in Chemical Biology* **2002**, 6 (4), 466-471.
123. Segalman, R. A., Patterning with Block Copolymer Thin Films. *Materials Science and Engineering: R: Reports* **2005**, 48 (6), 191-226.

124. Roovers, J.; Toporowski, P.; Martin, J., Synthesis and Characterization of Multiarm Star Polybutadienes. *Macromolecules* **1989**, *22* (4), 1897-1903.
125. Zhou, L. L.; Hadjichristidis, N.; Toporowski, P. M.; Roovers, J., Synthesis and Properties of Regular Star Polybutadienes with 32 Arms. *Rubber Chemistry and Technology* **1992**, *65* (2), 303-314.
126. Herman, D. S.; Kinning, D. J.; Thomas, E. L.; Fetters, L. J., A Compositional Study of the Morphology Of 18-Armed Poly(Styrene-Isoprene) Star Block Copolymers. *Macromolecules* **1987**, *20* (11), 2940-2942.
127. Kreutzer, G.; Ternat, C.; Nguyen, T. Q.; Plummer, C. J. G.; Månson, J.-A. E.; Castelletto, V.; Hamley, I. W.; Sun, F.; Sheiko, S. S.; Herrmann, A.; Ouali, L.; Sommer, H.; Fieber, W.; Velazco, M. I.; Klok, H.-A., Water-Soluble, Unimolecular Containers Based on Amphiphilic Multiarm Star Block Copolymers. *Macromolecules* **2006**, *39* (13), 4507-4516.
128. Iatridi, Z.; Tsitsilianis, C., Water-Soluble Stimuli Responsive Star-Shaped Segmented Macromolecules. *Polymers* **2011**, *3* (4), 1911-1933.
129. Nguyen, A. B.; Hadjichristidis, N.; Fetters, L. J., Static light Scattering Study of High-Molecular Weight 18-Arm Star Block Copolymers. *Macromolecules* **1986**, *19* (3), 768-773.
130. Strandman, S.; Hietala, S.; Aseyev, V.; Koli, B.; Butcher, S. J.; Tenhu, H., Supramolecular Assemblies of Amphiphilic PMMA-Block-PAA Stars in Aqueous Solutions. *Polymer* **2006**, *47* (19), 6524-6535.

131. Strandman, S.; Zarembo, A.; Darinskii, A. A.; Laurinmäki, P.; Butcher, S. J.; Vuorimaa, E.; Lemmetyinen, H.; Tenhu, H., Effect of the Number of Arms on the Association of Amphiphilic Star Block Copolymers. *Macromolecules* **2008**, *41* (22), 8855-8864.
132. Strandman, S.; Zarembo, A.; Darinskii, A. A.; Löflund, B.; Butcher, S. J.; Tenhu, H., Self-Assembling of Star-Like Amphiphilic Block Copolymers with Polyelectrolyte Blocks. Effect of pH. *Polymer* **2007**, *48* (24), 7008-7016.
133. Wang, X.; Davis, J. L.; Hinestrosa, J. P.; Mays, J. W.; Kilbey, S. M., Control of Self-Assembled Structure through Architecturally and Compositionally Complex Block Copolymer Surfactant Mixtures. *Macromolecules* **2014**, *47* (20), 7138-7150.
134. Spatz, J. P.; Mössmer, S.; Hartmann, C.; Möller, M.; Herzog, T.; Krieger, M.; Boyen, H.-G.; Ziemann, P.; Kabius, B., Ordered Deposition of Inorganic Clusters from Micellar Block Copolymer Films. *Langmuir* **1999**, *16* (2), 407-415.
135. Lei, L.; Gohy, J.-F.; Willet, N.; Zhang, J.-X.; Varshney, S.; Jérôme, R., Morphology of Core-Shell-Corona Aqueous Micelles: II. Addition of Core-Forming Homopolymer. *Polymer* **2004**, *45* (13), 4375-4381.
136. Mössmer, S.; Spatz, J. P.; Möller, M.; Aberle, T.; Schmidt, J.; Burchard, W., Solution Behavior of Poly(styrene)-block-poly(2-vinylpyridine) Micelles Containing Gold Nanoparticles. *Macromolecules* **2000**, *33* (13), 4791-4798.
137. Cong, R.; Temyanko, E.; Russo, P. S.; Edwin, N.; Uppu, R. M., Dynamics of Poly(styrenesulfonate) Sodium Salt in Aqueous Solution. *Macromolecules* **2005**, *39* (2), 731-739.
138. Debye, P., Light Scattering in Solutions. *Journal of Applied Physics* **1944**, *15* (4), 338-342.

139. Galaev, I.; Mattiasson, B., *Smart Polymers: Applications in Biotechnology and Biomedicine*. CRC Press: 2007.
140. Wang, F.; Bronich, T. K.; Kabanov, A. V.; Rauh, R. D.; Roovers, J., Synthesis and Characterization of Star Poly(ϵ -caprolactone)-*b*-Poly(ethylene glycol) and Poly(*l*-lactide)-*b*-Poly(ethylene glycol) Copolymers: Evaluation as Drug Delivery Carriers. *Bioconjugate Chemistry* **2008**, *19* (7), 1423-1429.
141. Sotiriou, K.; Nannou, A.; Velis, G.; Pispas, S., Micellization Behavior of PS(PI)₃ Miktoarm Star Copolymers. *Macromolecules* **2002**, *35* (10), 4106-4112.
142. Huber, K.; Burchard, W.; Fetters, L. J., Dynamic Light-Scattering from Regular Star-Branched Molecules. *Macromolecules* **1984**, *17* (4), 541-548.
143. Adam, M.; Fetters, L. J.; Graessley, W. W.; Witten, T. A., Concentration-Dependence of Static and Dynamic Properties for Polymeric Stars in a Good Solvent. *Macromolecules* **1991**, *24* (9), 2434-2440.
144. Hammond, M. R.; Li, C.; Tsitsilianis, C.; Mezzenga, R., Hierarchical Self-Organization in Polyelectrolyte-Surfactant Complexes Based on Heteroarm Star Block Copolyampholytes. *Soft Matter* **2009**, *5* (12), 2371-2377.
145. Gu, W.; Huh, J.; Hong, S. W.; Sveinbjornsson, B. R.; Park, C.; Grubbs, R. H.; Russell, T. P., Self-Assembly of Symmetric Brush Diblock Copolymers. *ACS Nano* **2013**, *7* (3), 2551-2558.
146. Verduzco, R.; Li, X.; Pesek, S. L.; Stein, G. E., Structure, Function, Self-Assembly, and Applications of Bottlebrush Copolymers. *Chemical Society Reviews* **2015**, *44* (8), 2405-2420.

147. Rzayev, J., Molecular Bottlebrushes: New Opportunities in Nanomaterials Fabrication. *ACS Macro Letters* **2012**, *1* (9), 1146-1149.
148. Lee, H. I.; Pietrasik, J.; Sheiko, S. S.; Matyjaszewski, K., Stimuli-Responsive Molecular Brushes. *Progress in Polymer Science* **2010**, *35* (1-2), 24-44.
149. Sheiko, S. S.; Sumerlin, B. S.; Matyjaszewski, K., Cylindrical Molecular Brushes: Synthesis, Characterization, and Properties. *Progress in Polymer Science* **2008**, *33* (7), 759-785.
150. Sun, G.; Cho, S.; Yang, F.; He, X.; Pavía-Sanders, A.; Clark, C.; Raymond, J. E.; Verkhoturov, S. V.; Schweikert, E. A.; Thackeray, J. W.; Trefonas, P.; Wooley, K. L., Advanced Photoresist Technologies by Intricate Molecular Brush Architectures: Diblock Brush Terpolymer-Based Positive-Tone Photoresist Materials. *Journal of Polymer Science Part A: Polymer Chemistry* **2015**, *53* (2), 193-199.
151. Riley, T.; Heald, C. R.; Stolnik, S.; Garnett, M. C.; Illum, L.; Davis, S. S.; King, S. M.; Heenan, R. K.; Purkiss, S. C.; Barlow, R. J.; Gellert, P. R.; Washington, C., Core-Shell Structure of PLA-PEG Nanoparticles Used for Drug Delivery. *Langmuir* **2003**, *19* (20), 8428-8435.
152. Banquy, X.; Burdyńska, J.; Lee, D. W.; Matyjaszewski, K.; Israelachvili, J., Bioinspired Bottle-Brush Polymer Exhibits Low Friction and Amontons-like Behavior. *Journal of the American Chemical Society* **2014**, *136* (17), 6199-6202.
153. Rathgeber, S.; Pakula, T.; Wilk, A.; Matyjaszewski, K.; Beers, K. L., On the Shape of Bottle-Brush Macromolecules: Systematic Variation of Architectural Parameters. *The Journal of Chemical Physics* **2005**, *122* (12), 124904.

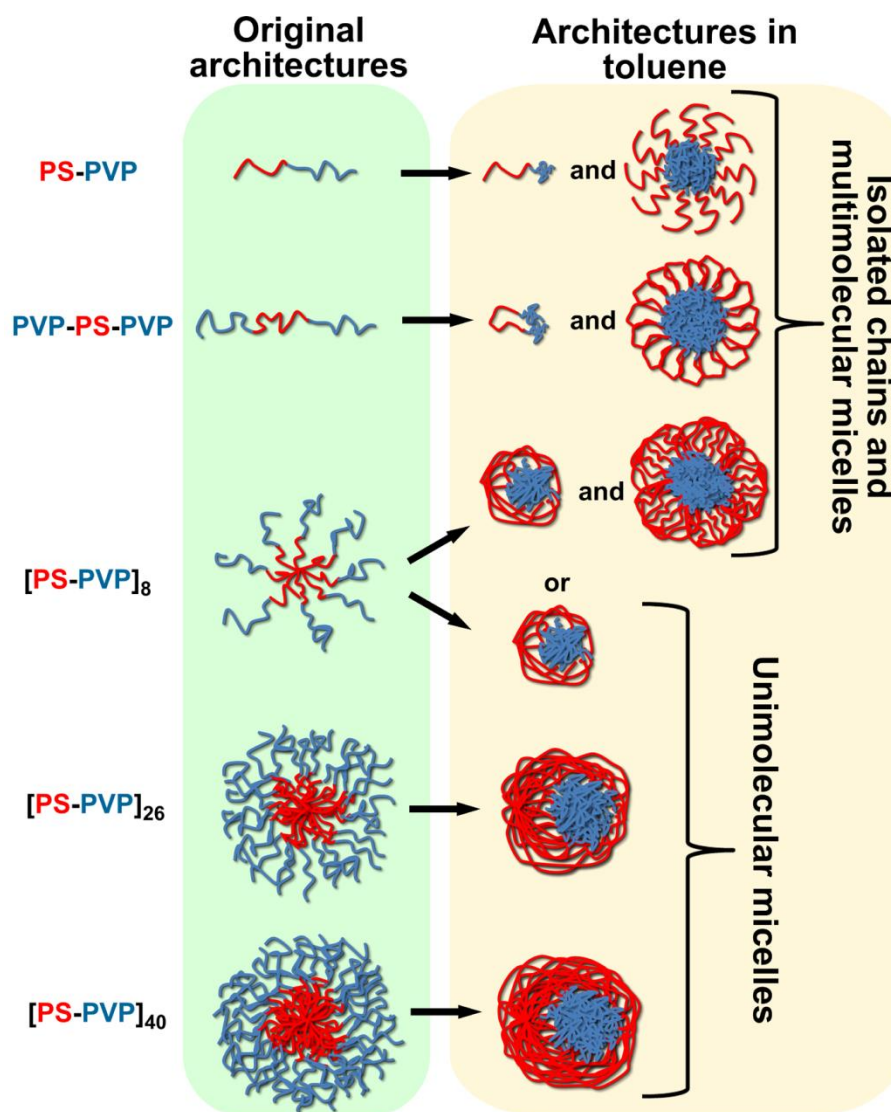
154. Fenyves, R.; Schmutz, M.; Horner, I. J.; Bright, F. V.; Rzaev, J., Aqueous Self-Assembly of Giant Bottlebrush Block Copolymer Surfactants as Shape-Tunable Building Blocks. *Journal of the American Chemical Society* **2014**, *136* (21), 7762-7770.
155. Li, Z.; Ma, J.; Cheng, C.; Zhang, K.; Wooley, K. L., Synthesis of Hetero-Grafted Amphiphilic Diblock Molecular Brushes and Their Self-Assembly in Aqueous Medium. *Macromolecules* **2010**, *43* (3), 1182-1184.
156. Desvergne, S.; Héroguez, V.; Gnanou, Y.; Borsali, R., Polymacromonomers: Dynamics of Dilute and Nondilute Solutions. *Macromolecules* **2005**, *38* (6), 2400-2409.
157. Jain, S.; Bates, F. S., On the Origins of Morphological Complexity in Block Copolymer Surfactants. *Science* **2003**, *300* (5618), 460-464.
158. Shao, Y.; Jia, Y.-G.; Shi, C.; Luo, J.; Zhu, X. X., Block and Random Copolymers Bearing Cholic Acid and Oligo(ethylene glycol) Pendant Groups: Aggregation, Thermosensitivity, and Drug Loading. *Biomacromolecules* **2014**, *15* (5), 1837-1844.
159. Hiemstra, C.; Zhong, Z.; Li, L.; Dijkstra, P. J.; Feijen, J., In-Situ Formation of Biodegradable Hydrogels by Stereocomplexation of PEG-(PLLA)₈ and PEG-(PDLA)₈ Star Block Copolymers. *Biomacromolecules* **2006**, *7* (10), 2790-2795.
160. M Saffer, E.; N Tew, G.; R Bhatia, S., Poly (lactic acid)-poly (ethylene oxide) Block Copolymers: New Directions in Self-Assembly and Biomedical Applications. *Current Medicinal Chemistry* **2011**, *18* (36), 5676-5686.
161. Surita, R. B.; Gregory, N. T., PLA-PEO-PLA Hydrogels: Chemical Structure, Self-Assembly and Mechanical Properties. In *Degradable Polymers and Materials: Principles and Practice (2nd Edition)*, American Chemical Society: 2012; Vol. 1114, pp 313-324.

162. Khemani, K.; Scholz, C., *Degradable Polymers and Materials: Principles and Practice (2nd Edition)*. American Chemical Society: 2012; Vol. 1114, pp XI-XI.
163. Love, J. A.; Morgan, J. P.; Trnka, T. M.; Grubbs, R. H., A Practical and Highly Active Ruthenium-Based Catalyst that Effects the Cross Metathesis of Acrylonitrile. *Angewandte Chemie International Edition* **2002**, *41* (21), 4035-4037.
164. Ahn, S.-k.; Carrillo, J.-M. Y.; Han, Y.; Kim, T.-H.; Uhrig, D.; Pickel, D. L.; Hong, K.; Kilbey, S. M.; Sumpter, B. G.; Smith, G. S.; Do, C., Structural Evolution of Poly lactide Molecular Bottlebrushes: Kinetics Study by Size Exclusion Chromatography, Small Angle Neutron Scattering, and Simulations. *ACS Macro Letters* **2014**, *3* (9), 862-866.
165. Sutthasupa, S.; Shiotsuki, M.; Sanda, F., Recent Advances in Ring-Opening Metathesis Polymerization, and Application to Synthesis of Functional Materials. *Polymer Journal* **2010**, *42* (12), 905-915.
166. Ahn, S.-k.; Pickel, D. L.; Kochemba, W. M.; Chen, J.; Uhrig, D.; Hinestrosa, J. P.; Carrillo, J.-M.; Shao, M.; Do, C.; Messman, J. M.; Brown, W. M.; Sumpter, B. G.; Kilbey, S. M., Poly(3-hexylthiophene) Molecular Bottlebrushes via Ring-Opening Metathesis Polymerization: Macromolecular Architecture Enhanced Aggregation. *ACS Macro Letters* **2013**, *2* (8), 761-765.
167. Xia, Y.; Olsen, B. D.; Kornfield, J. A.; Grubbs, R. H., Efficient Synthesis of Narrowly Dispersed Brush Copolymers and Study of Their Assemblies: The Importance of Side Chain Arrangement. *Journal of the American Chemical Society* **2009**, *131* (51), 18525-18532.

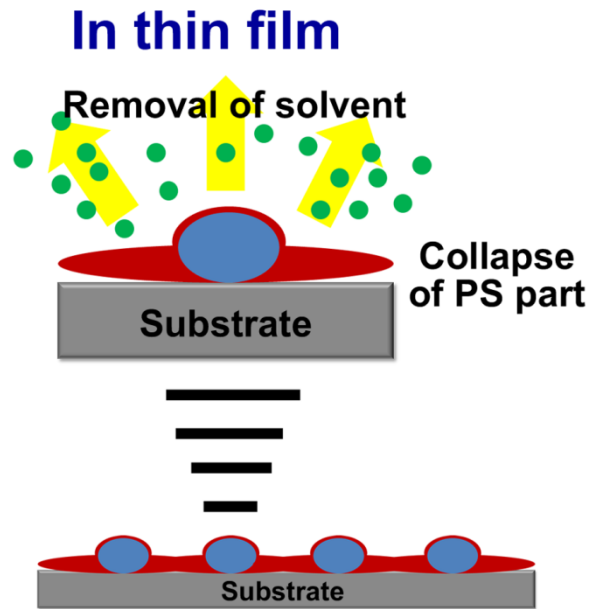
168. Polyethylene glycol [MAK Value Documentation, 1998]. In *The MAK-Collection for Occupational Health and Safety*, Wiley-VCH Verlag GmbH & Co. KGaA: 2002.
169. Chang, J. B.; Choi, H. K.; Hannon, A. F.; Alexander-Katz, A.; Ross, C. A.; Berggren, K. K., Design Rules for Self-Assembled Block Copolymer Patterns using Tiled Templates. *Nature Communications* **2014**, *5*.
170. Zhang, J.; Ma, P. X., Host-guest Interactions Mediated Nano-Assemblies using Cyclodextrin-Containing Hydrophilic Polymers and Their Biomedical Applications. *Nano Today* **2010**, *5* (4), 337-350.
171. Albrecht, T. R.; Bedau, D.; Dobisz, E.; Gao, H.; Grobis, M.; Hellwig, O.; Kercher, D.; Lille, J.; Marinero, E.; Patel, K.; Ruiz, R.; Schabes, M. E.; Wan, L.; Weller, D.; Wu, T. W., Bit Patterned Media at 1 Tdot/in(2) and Beyond. *IEEE Transactions on Magnetics* **2013**, *49* (2), 773-778.
172. Yang, Z.; Pickard, S.; Deng, N. J.; Barlow, R. J.; Attwood, D.; Booth, C., Effect Of Block Structure on the Micellization and Gelation of Aqueous-Solutions of Copolymers of Ethylene-Oxide and Butylene Oxide. *Macromolecules* **1994**, *27* (9), 2371-2379.
173. Yang, Y. W.; Yang, Z.; Zhou, Z. K.; Attwood, D.; Booth, C., Association of Triblock Copolymers of Ethylene Oxide and Butylene Oxide in Aqueous Solution. A Study of $B_nE_mB_n$ Copolymers. *Macromolecules* **1996**, *29* (2), 670-680.
174. Hammouda, B., Probing Nanoscale Structures-The SANS Toolbox. National Institute for Standards and Technology: Gaithersburg, MD, 2004.

Appendices

**Appendix A - Chapter 3: Control of Self-Assembled Structure through
Architecturally and Compositionally Complex Block Copolymer Surfactant
Mixtures**



Scheme A-1. Model architectures of different PS-PVP block copolymers. The unimolecular micelles formed from multiarm stars generally have asymmetrical PVP-PS core-corona structures in toluene, the detailed self-assembly behaviors of multiarm stars in selective/non-selective solvents is more complex as described in Chapter 4.



Scheme A-2. Effect of solvent removal on the self-assembly behaviors of PS-PVP block copolymers in thin films. In these drawings, the color red represents PS domains and the color blue represents PVP domains.

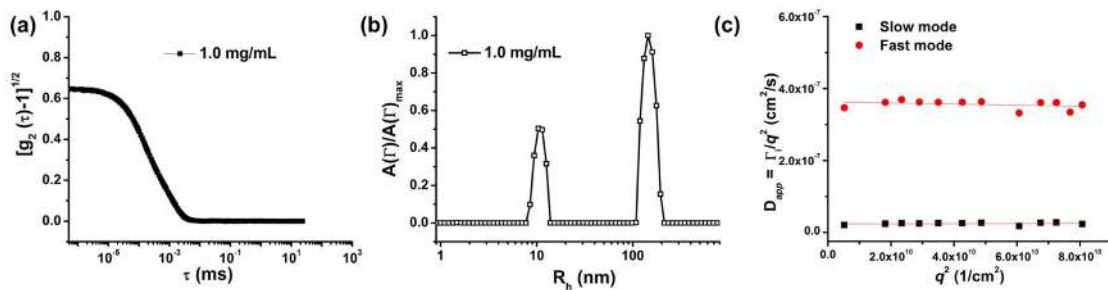


Figure A-1. Light intensity autocorrelation function (a), hydrodynamic radii, R_h , distributions (b) and apparent diffusion coefficient D_{app} versus q^2 (c) for sample D1 in toluene at $c = 1.0$ mg/mL.

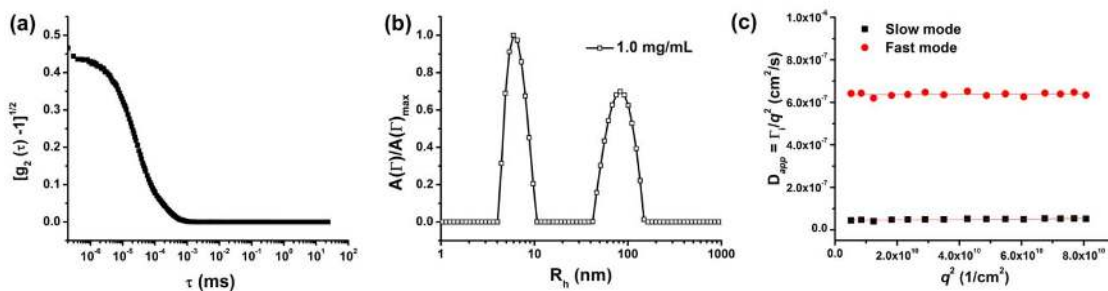


Figure A-2. Light intensity autocorrelation function (a), hydrodynamic radii, R_h , distributions (b) and apparent diffusion coefficient D_{app} versus q^2 (c) for sample D2 in toluene at $c = 1.0$ mg/mL.

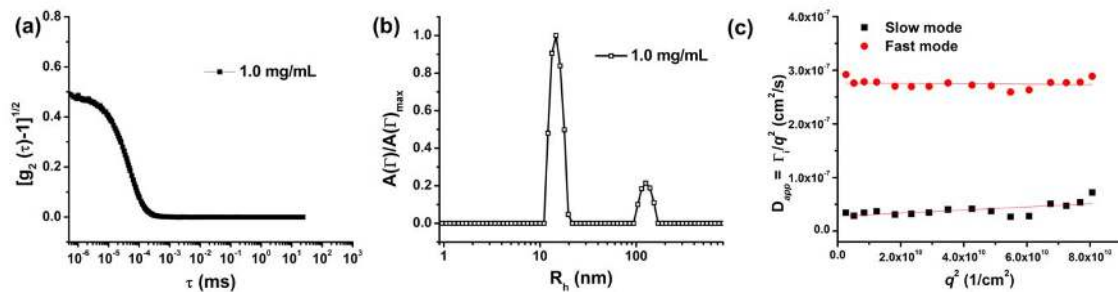


Figure A-3. Light intensity autocorrelation function (a), hydrodynamic radii, R_h , distributions (b) and apparent diffusion coefficient D_{app} versus q^2 (c) for sample D3 in toluene at $c = 1.0$ mg/mL.

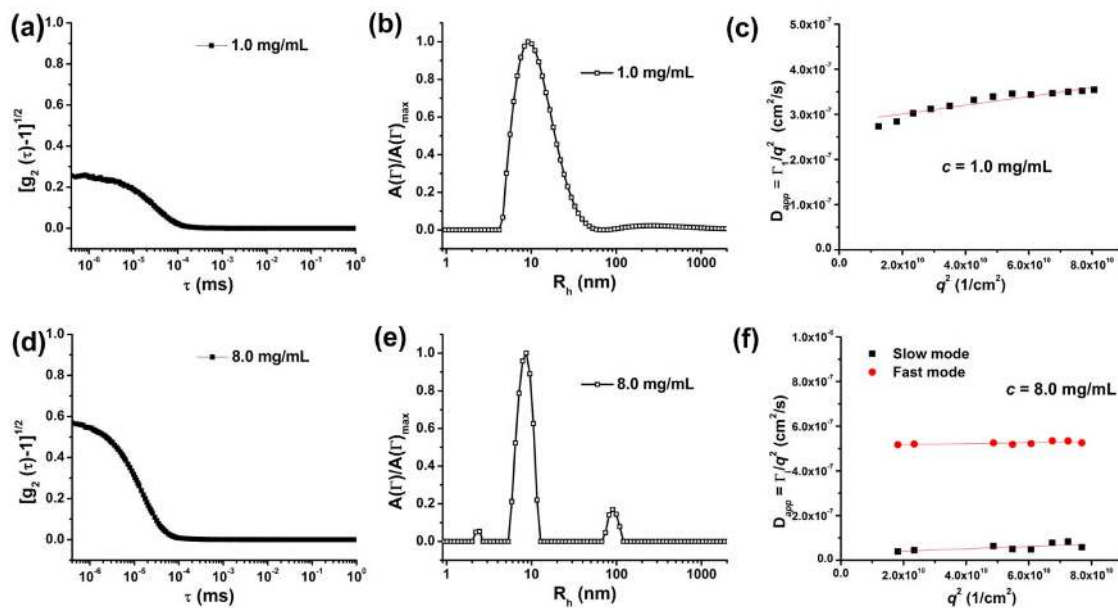


Figure A-4. Light intensity autocorrelation function (a, d), hydrodynamic radii, R_h , distributions (b, e) and apparent diffusion coefficient D_{app} versus q^2 (c, f) for sample T2 in toluene at $c = 1.0$ mg/mL (a, b, c) and at $c = 8.0$ mg/mL (d, e, f).

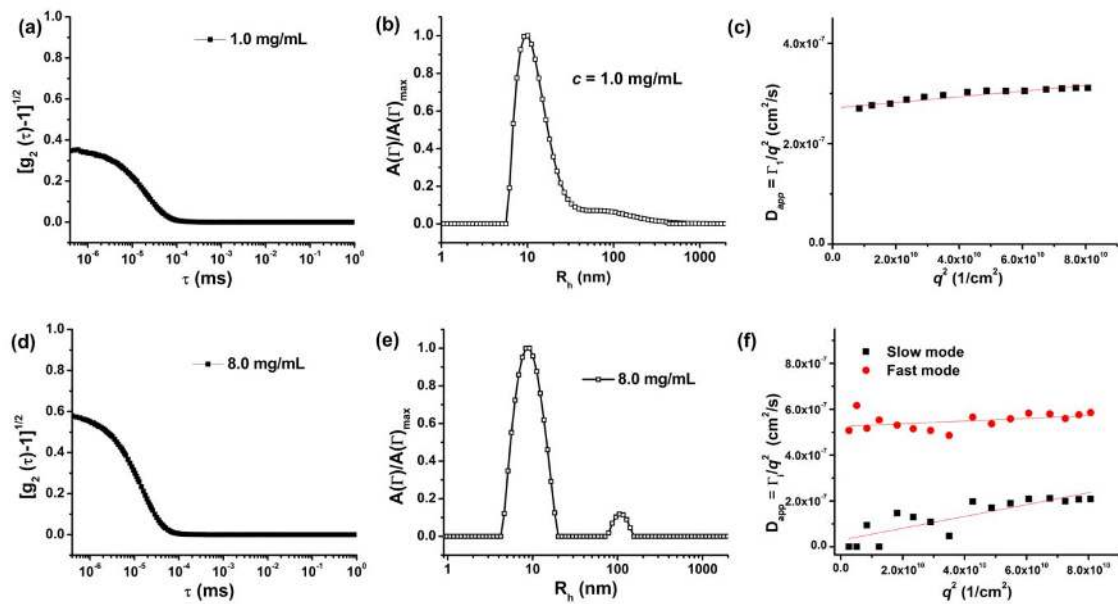


Figure A-5. Light intensity autocorrelation function (a, d), hydrodynamic radii, R_h , distributions (b, e) and apparent diffusion coefficient D_{app} versus q^2 (c, f) for sample T3 in toluene at $c = 1.0$ mg/mL (a, b, c) and at $c = 8.0$ mg/mL (d, e, f).

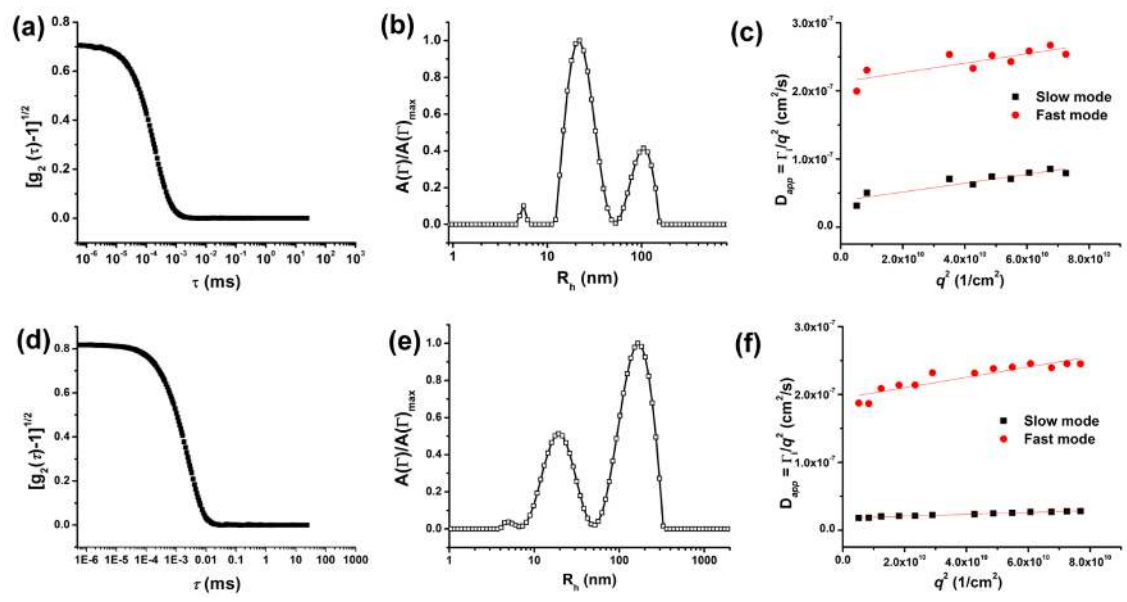


Figure A-6. Light intensity autocorrelation function (a, d), hydrodynamic radii, R_h , distributions (b, e) and apparent diffusion coefficient D_{app} versus q^2 (c, f) for sample S1 in toluene at $c = 1.0$ mg/mL (a, b, c) and at $c = 8.0$ mg/mL (d, e, f).

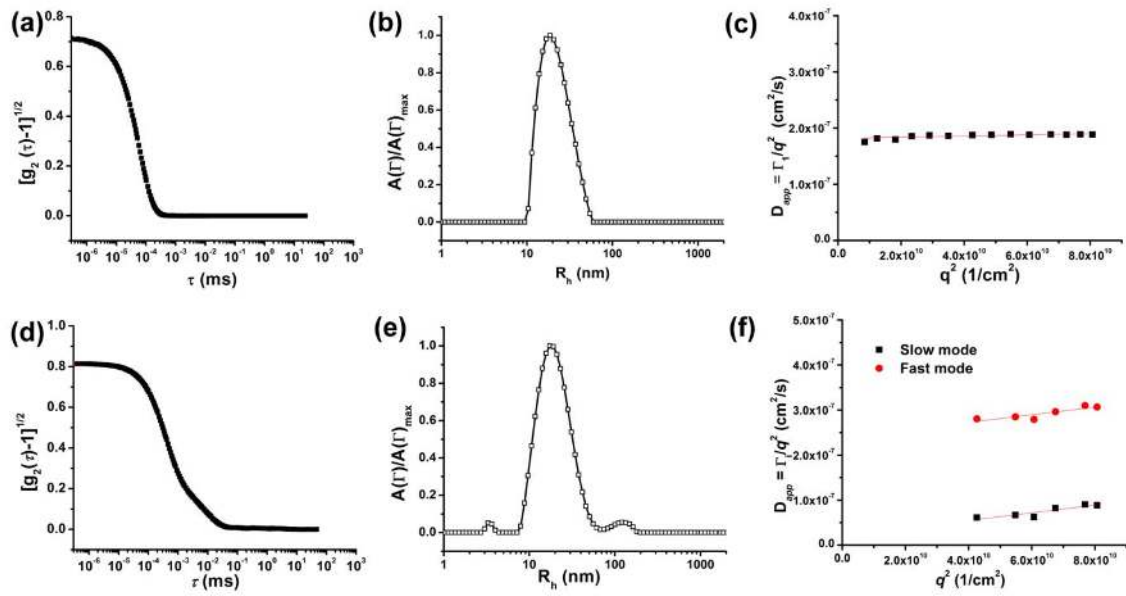


Figure A-7. Light intensity autocorrelation function (a, d), hydrodynamic radii, R_h , distributions (b, e) and apparent diffusion coefficient D_{app} versus q^2 (c, f) for sample S2 in toluene at $c = 1.0$ mg/mL (a, b, c) and at $c = 8.0$ mg/mL (d, e, f).

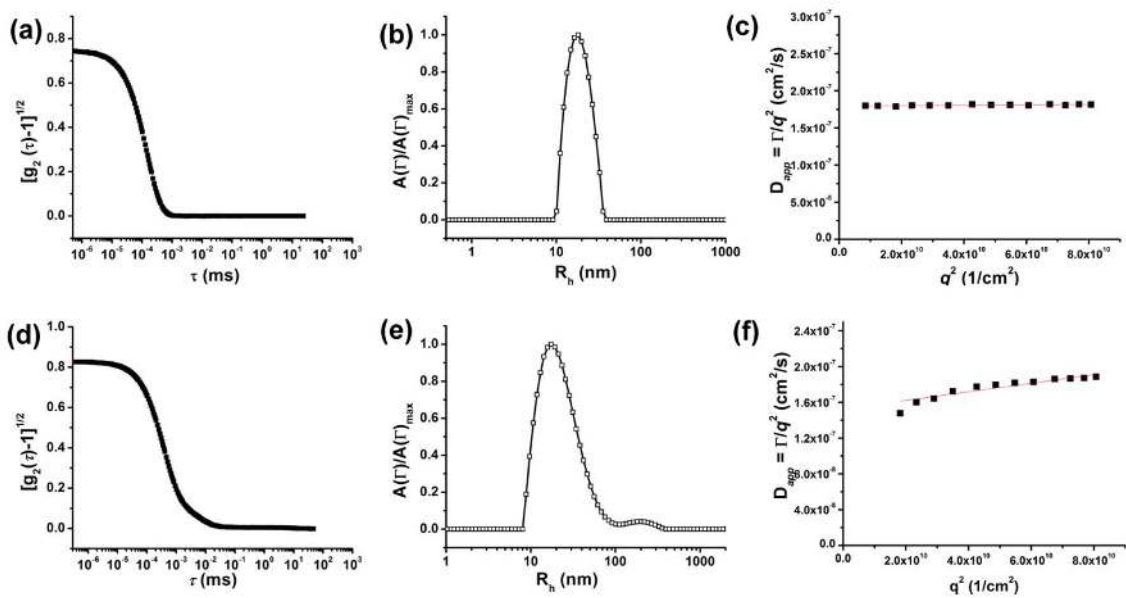


Figure A-8. Light intensity autocorrelation function (a, d), hydrodynamic radii, R_h , distributions (b, e) and apparent diffusion coefficient D_{app} versus q^2 (c, f) for sample S3 in toluene at $c = 1.0$ mg/mL (a, b, c) and at $c = 8.0$ mg/mL (d, e, f).

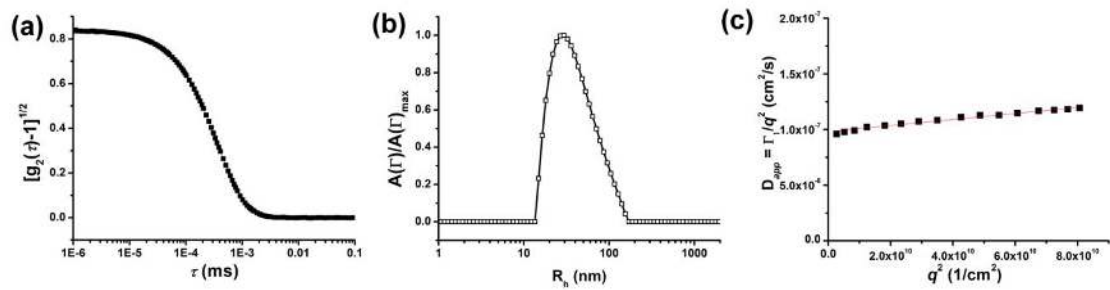


Figure A-9. Light intensity autocorrelation function (a), hydrodynamic radii, R_h , distributions (b) and apparent diffusion coefficient D_{app} versus q^2 (c) for sample S4 in toluene at $c = 1.0$ mg/mL.

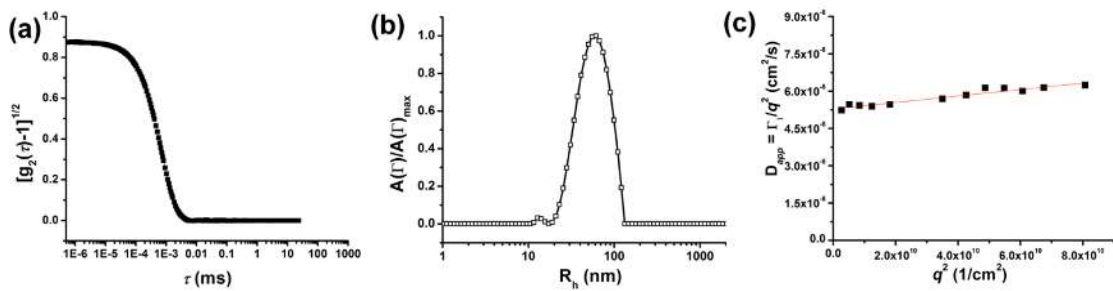


Figure A-10. Light intensity autocorrelation function (a), hydrodynamic radii, R_h , distributions (b) and apparent diffusion coefficient D_{app} versus q^2 (c) for sample S5 in toluene at $c = 1.0$ mg/mL.

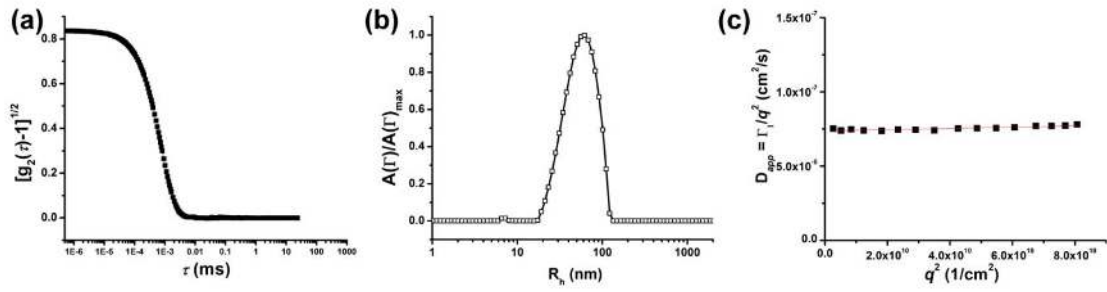


Figure A-11. Light intensity autocorrelation function (a), hydrodynamic radii, R_h , distributions (b) and apparent diffusion coefficient D_{app} versus q^2 (c) for sample S6 in toluene at $c = 1.0$ mg/mL.

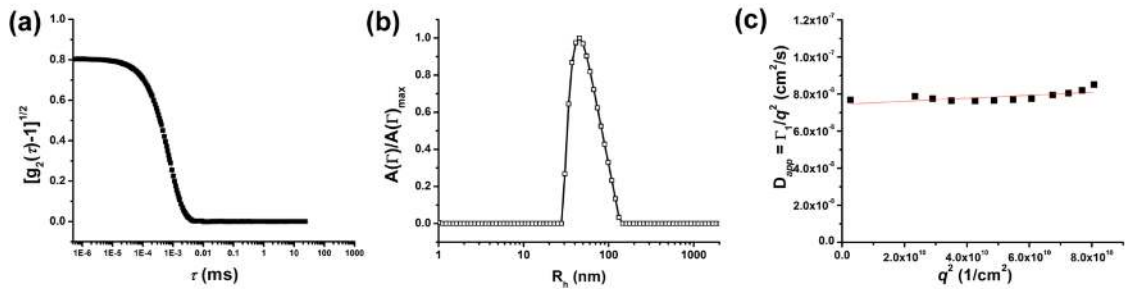


Figure A-12. Light intensity autocorrelation function (a), hydrodynamic radii, R_h , distributions (b) and apparent diffusion coefficient D_{app} versus q^2 (c) for sample S7 in toluene at $c = 1.0$ mg/mL.

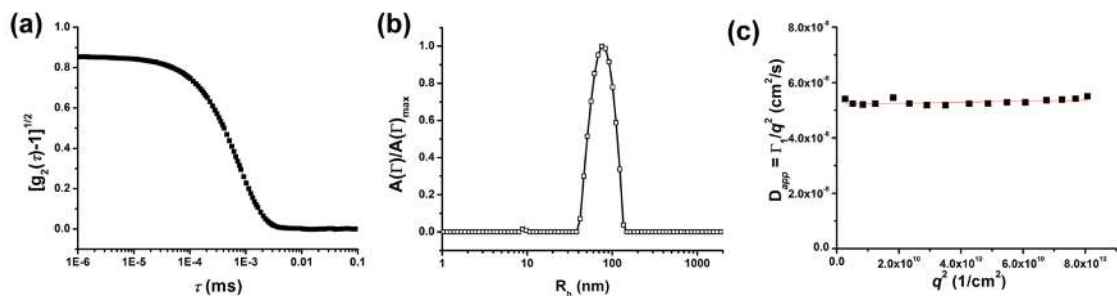


Figure A-13. Light intensity autocorrelation function (a), hydrodynamic radii, R_h , distributions (b) and apparent diffusion coefficient D_{app} versus q^2 (c) for sample S8 in toluene at $c = 1.0$ mg/mL.

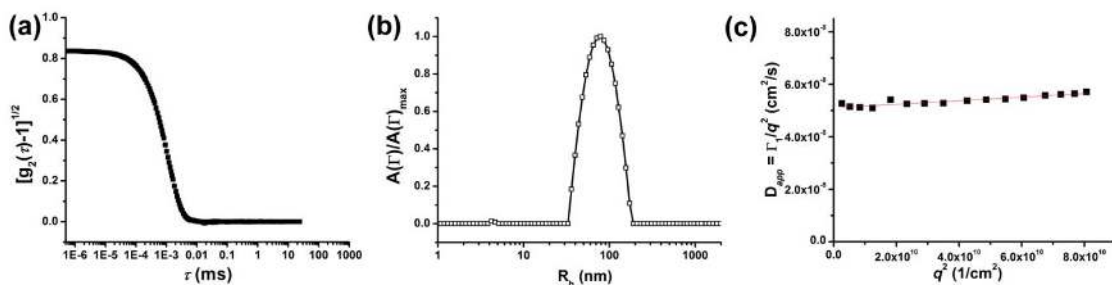


Figure A-14. Light intensity autocorrelation function (a), hydrodynamic radii, R_h , distributions (b) and apparent diffusion coefficient D_{app} versus q^2 (c) for sample S9 in toluene at $c = 1.0$ mg/mL.

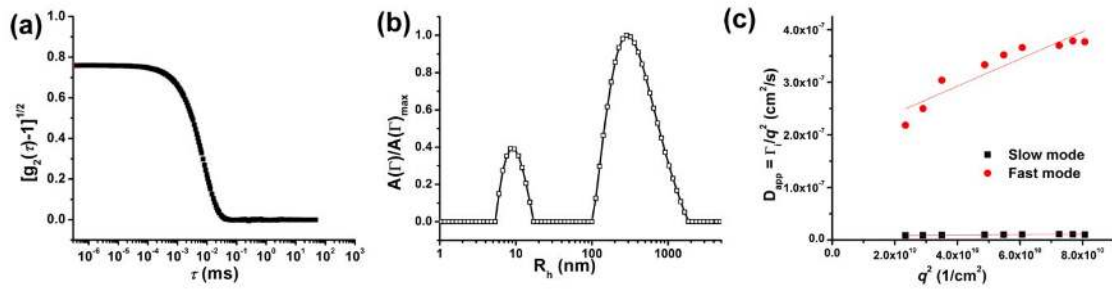


Figure A-15. Light intensity autocorrelation function (a), hydrodynamic radii, R_h , distributions (b) and apparent diffusion coefficient D_{app} versus q^2 (c) for mixture D1+T1 in toluene at $c = 8.0$ mg/mL.

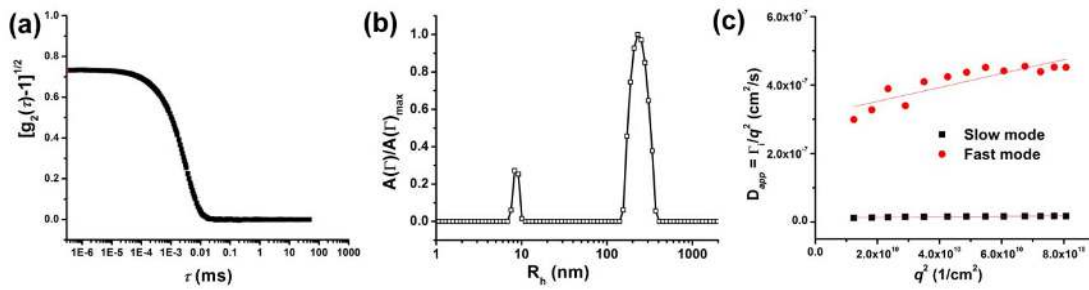


Figure A-16. Light intensity autocorrelation function (a), hydrodynamic radii, R_h , distributions (b) and apparent diffusion coefficient D_{app} versus q^2 (c) for mixture D1+T2 in toluene at $c = 8.0$ mg/mL.

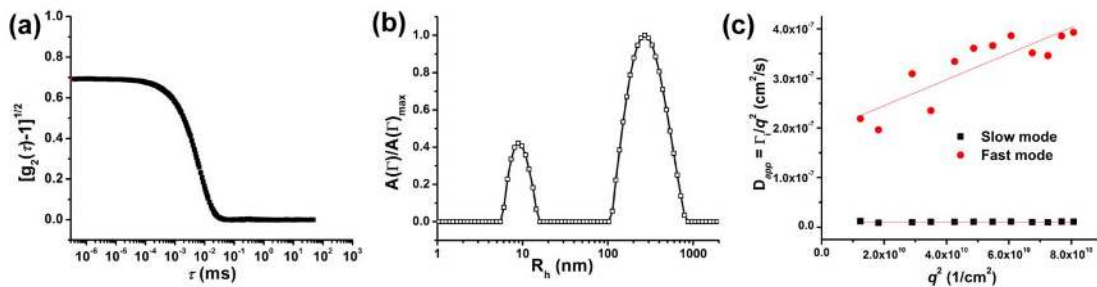


Figure A-17. Light intensity autocorrelation function (a), hydrodynamic radii, R_h , distributions (b) and apparent diffusion coefficient D_{app} versus q^2 (c) for mixture D1+T3 in toluene at $c = 8.0$ mg/mL.

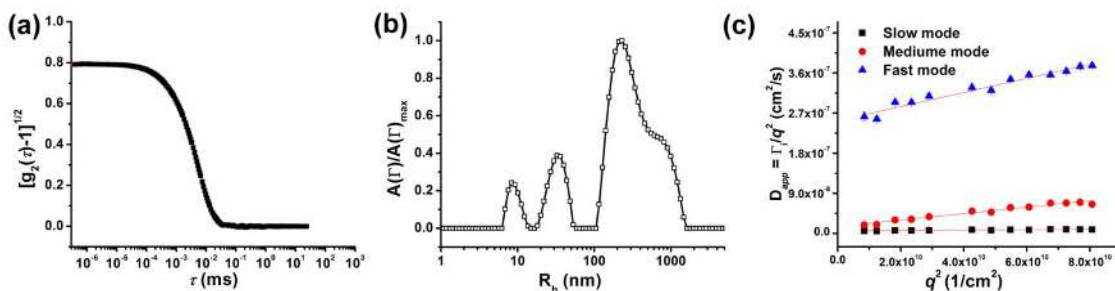


Figure A-18. Light intensity autocorrelation function (a), hydrodynamic radii, R_h , distributions (b) and apparent diffusion coefficient D_{app} versus q^2 (c) for mixture D1+S1 in toluene at $c = 8.0$ mg/mL.

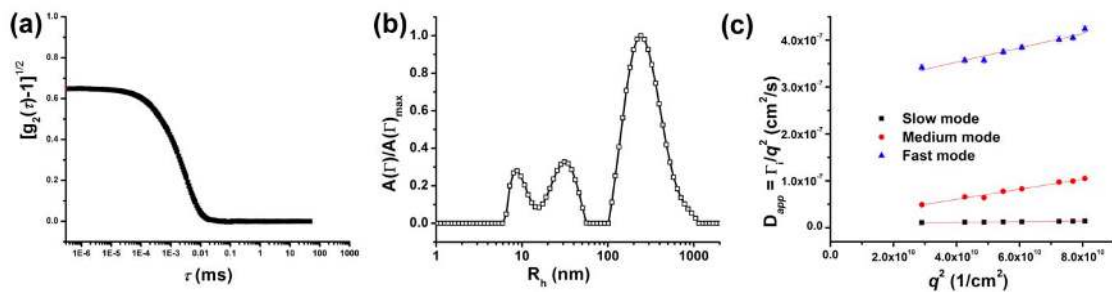


Figure A-19. Light intensity autocorrelation function (a), hydrodynamic radii, R_h , distributions (b) and apparent diffusion coefficient D_{app} versus q^2 (c) for mixture D1+S2 in toluene at $c = 8.0$ mg/mL.

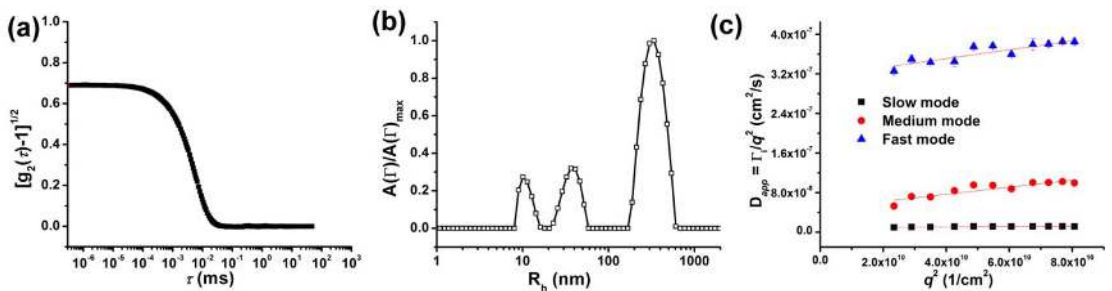


Figure A-20. Light intensity autocorrelation function (a), hydrodynamic radii, R_h , distributions (b) and apparent diffusion coefficient D_{app} versus q^2 (c) for mixture D1+S3 in toluene at $c = 8.0$ mg/mL.

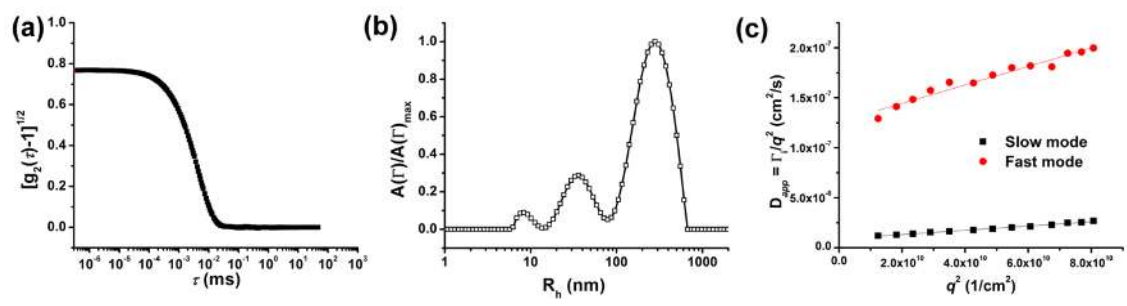


Figure A-21. Light intensity autocorrelation function (a), hydrodynamic radii, R_h , distributions (b) and apparent diffusion coefficient D_{app} versus q^2 (c) for mixture D1+S4 in toluene at $c = 8.0$ mg/mL.

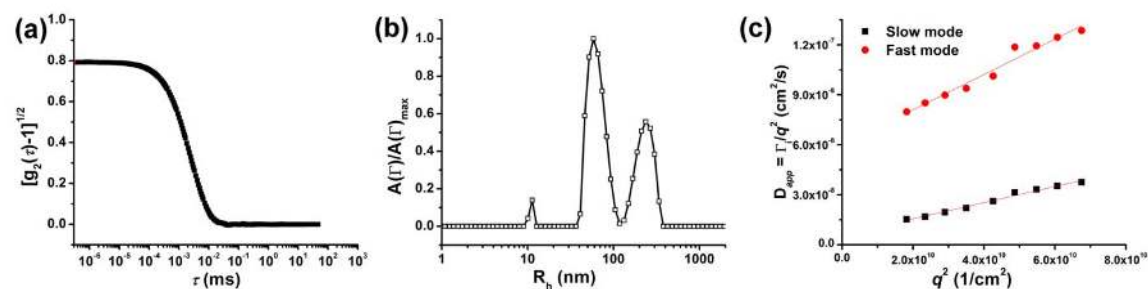


Figure A-22. Light intensity autocorrelation function (a), hydrodynamic radii, R_h , distributions (b) and apparent diffusion coefficient D_{app} versus q^2 (c) for mixture D1+S7 in toluene at $c = 8.0$ mg/mL.

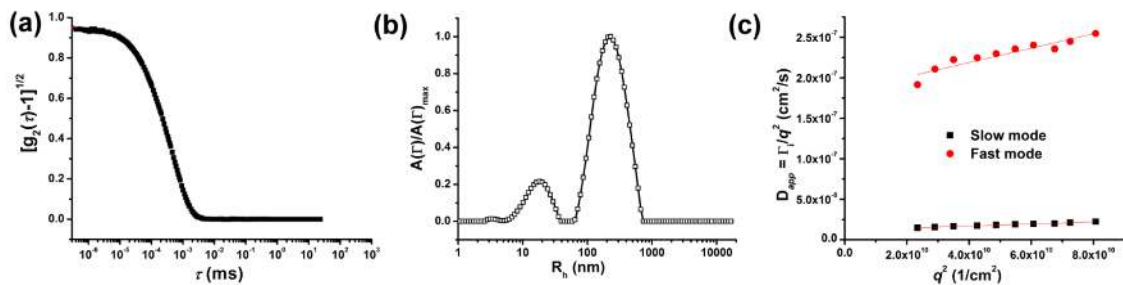


Figure A-23. Light intensity autocorrelation function (a), hydrodynamic radii, R_h , distributions (b) and apparent diffusion coefficient D_{app} versus q^2 (c) for mixture T1+S1 in toluene at $c = 8.0$ mg/mL.

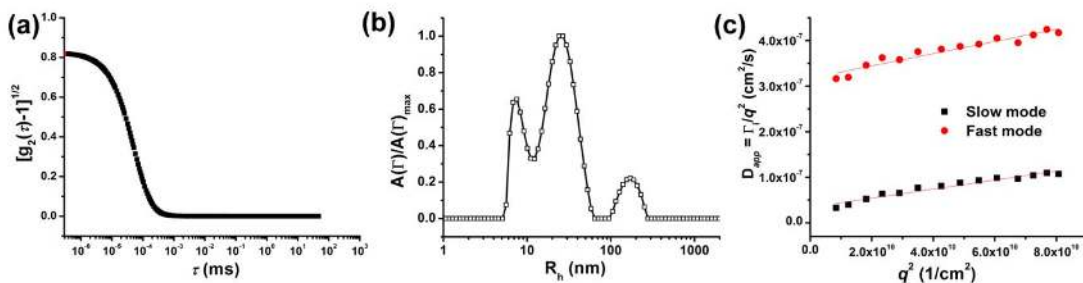


Figure A-24. Light intensity autocorrelation function (a), hydrodynamic radii, R_h , distributions (b) and apparent diffusion coefficient D_{app} versus q^2 (c) for mixture T1+S2 in toluene at $c = 8.0$ mg/mL.

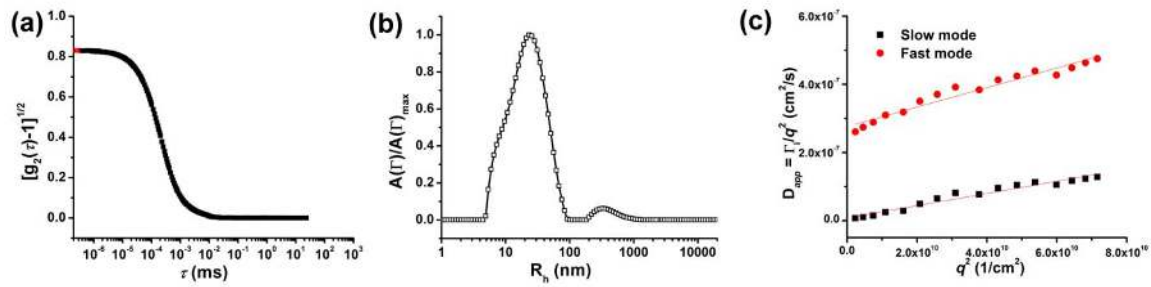


Figure A-25. Light intensity autocorrelation function (a), hydrodynamic radii, R_h , distributions (b) and apparent diffusion coefficient D_{app} versus q^2 (c) for mixture T1+S3 in toluene at $c = 8.0$ mg/mL.

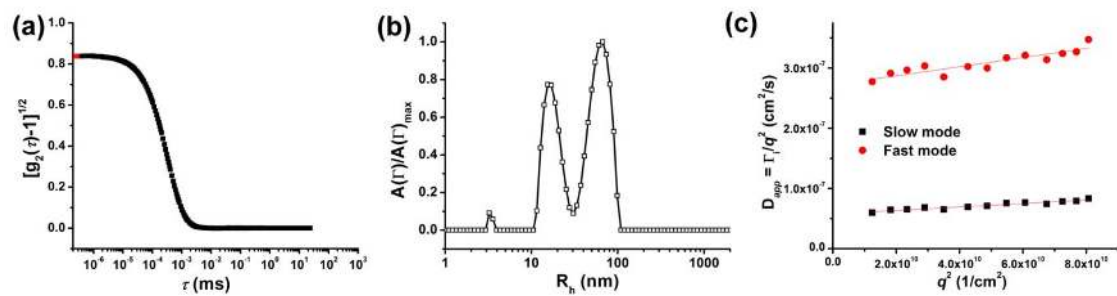


Figure A-26. Light intensity autocorrelation function (a), hydrodynamic radii, R_h , distributions (b) and apparent diffusion coefficient D_{app} versus q^2 (c) for mixture T1+S4 in toluene at $c = 8.0$ mg/mL.

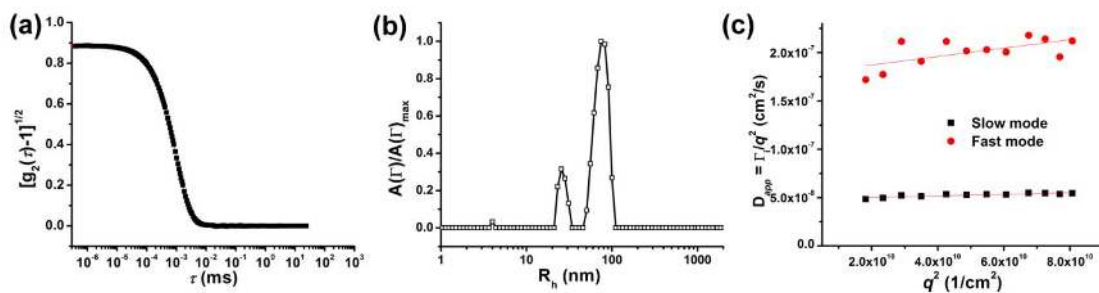


Figure A-27. Light intensity autocorrelation function (a), hydrodynamic radii, R_h , distributions (b) and apparent diffusion coefficient D_{app} versus q^2 (c) for mixture T1+S7 in toluene at $c = 8.0$ mg/mL.

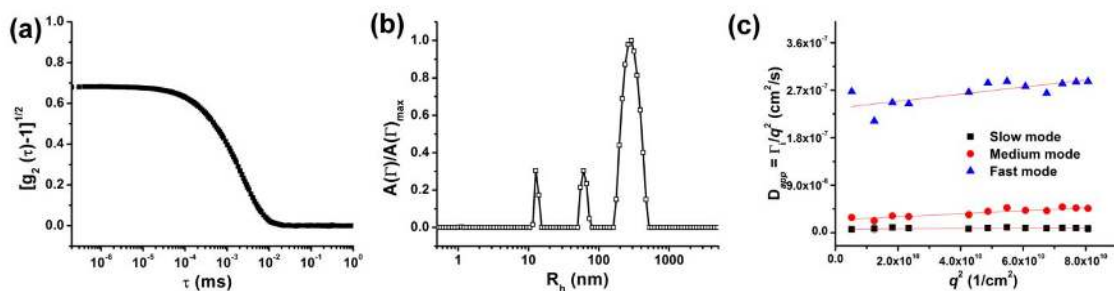


Figure A-28. Light intensity autocorrelation function (a), hydrodynamic radii, R_h , distributions (b) and apparent diffusion coefficient D_{app} versus q^2 (c) for mixture S1+T2 in toluene at $c = 8.0$ mg/mL.

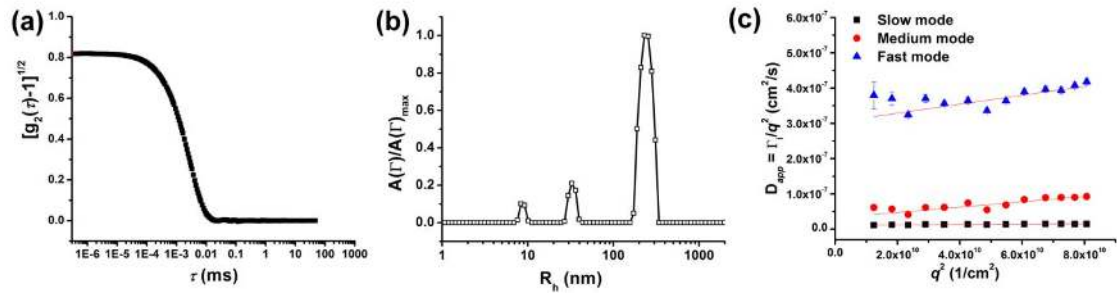


Figure A-29. Light intensity autocorrelation function (a), hydrodynamic radii, R_h , distributions (b) and apparent diffusion coefficient D_{app} versus q^2 (c) for mixture S1+T3 in toluene at $c = 8.0$ mg/mL.

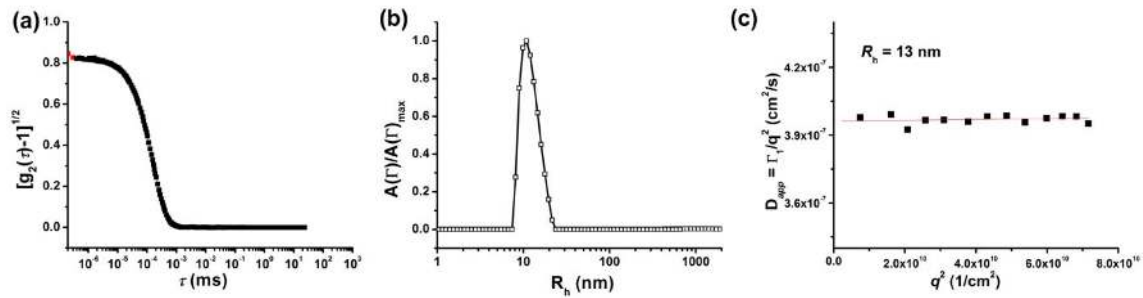


Figure A-30. Light intensity autocorrelation function (a), hydrodynamic radii, R_h , distributions (b) and apparent diffusion coefficient D_{app} versus q^2 (c) for sample T1 in THF at $c = 1.0$ mg/mL.

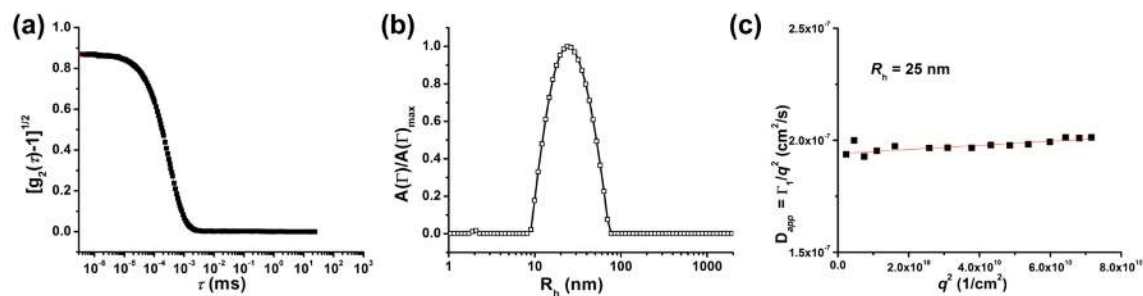


Figure A-31. Light intensity autocorrelation function (a), hydrodynamic radii, R_h , distributions (b) and apparent diffusion coefficient D_{app} versus q^2 (c) for sample S1 in THF at $c = 0.5$ mg/mL.

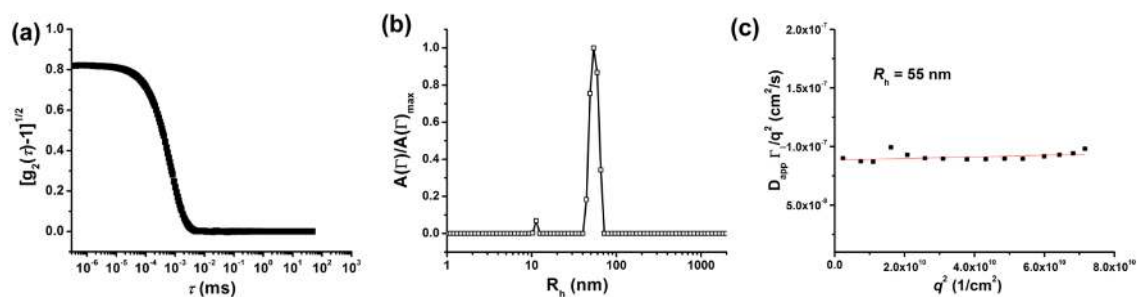


Figure A-32. Light intensity autocorrelation function (a), hydrodynamic radii, R_h , distributions (b) and apparent diffusion coefficient D_{app} versus q^2 (c) for sample S6 in THF at $c = 0.5$ mg/mL.

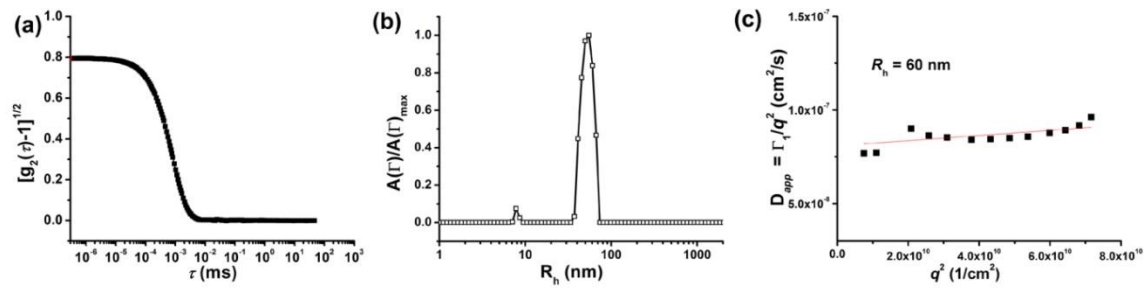


Figure A-33. Light intensity autocorrelation function (a), hydrodynamic radii, R_h , distributions (b) and apparent diffusion coefficient D_{app} versus q^2 (c) for sample S8 in THF at $c = 0.5$ mg/mL.

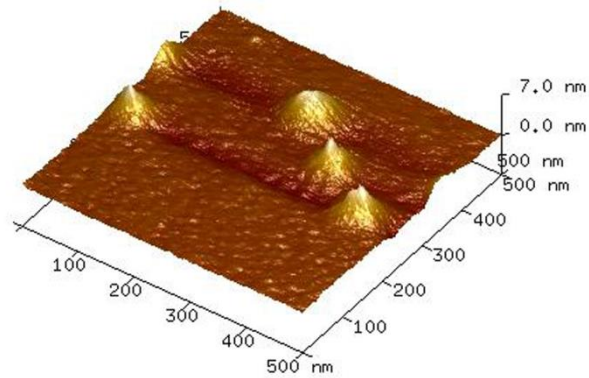


Figure A-34. 3D AFM image of disperse micelles made by drop-casting from S7 toluene solution at $c = 3.0$ $\mu\text{g/mL}$ on a silicon substrate.

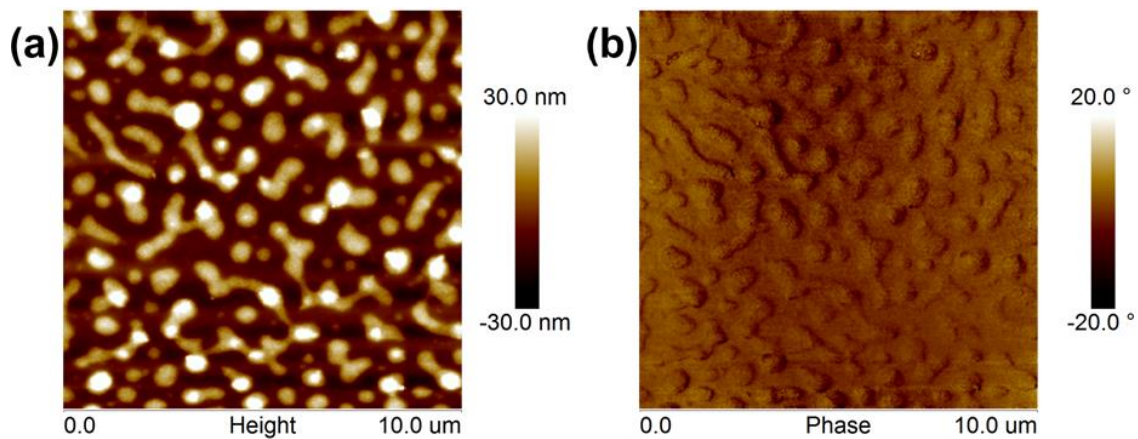


Figure A-35. AFM height (a) and phase (b) images ($10\ \mu\text{m} \times 10\ \mu\text{m}$) of the film made from T1+S2 block copolymer mixture at a mixing ratio of 1:1 by weight.

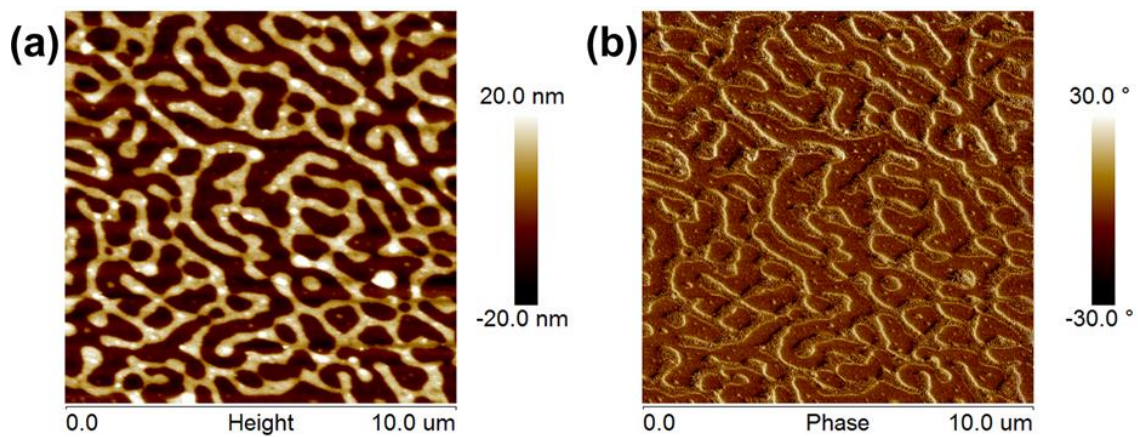


Figure A-36. AFM height (a) and phase (b) images ($10\ \mu\text{m} \times 10\ \mu\text{m}$) of the film made from S1+T3 block copolymer mixture at a mixing ratio of 1:1 by weight.

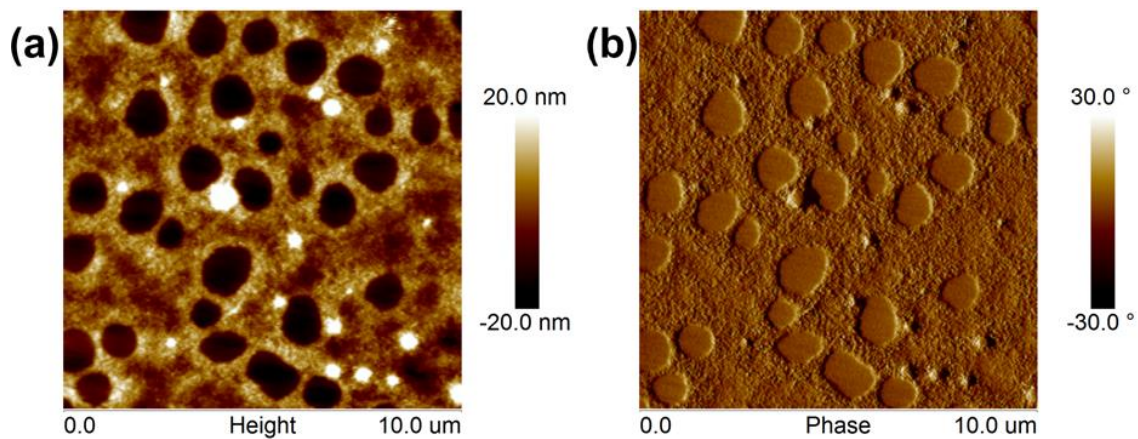


Figure A-37. AFM height (a) and phase (b) images ($10\ \mu\text{m} \times 10\ \mu\text{m}$) of the film made from T1+S3 block copolymer mixture at a mixing ratio of 3:1 by weight.

Table A-1. Hydrodynamic radii of PS-PVP block copolymer mixtures (polymer I:polymer II = 1:1, w:w) in toluene at a concentration of 1.0 mg/mL.

mixture ID	polymer I	polymer II	R_{h1} (nm)	R_{h2} (nm)	R_{h3} (nm)
D1+T1	D1	T1	14	212	
D1+T2	D1	T2	14	271	
D1+T3	D1	T3	11	52	
D1+S1	D1	S1	14	50	
D1+S2	D1	S2	17	247	
D1+S3	D1	S3	19	295	
D1+S4	D1	S4	28	262	
D1+S7	D1	S7	42	220	
T1+S1	T1	S1	17	176	
T1+S2	T1	S2	16	119	
T1+S3	T1	S3	15	52	
T1+S4	T1	S4	14	47	272
T1+S7	T1	S7	75	205	
S1+T2	S1	T2	17	193	
S1+T3	S1	T3	18	198	

**Appendix B - Chapter 4: Solution Properties of Architecturally Complex
Multiarm Star Diblock Copolymers in Non-selective and Selective Solvents for
the Inner Block**

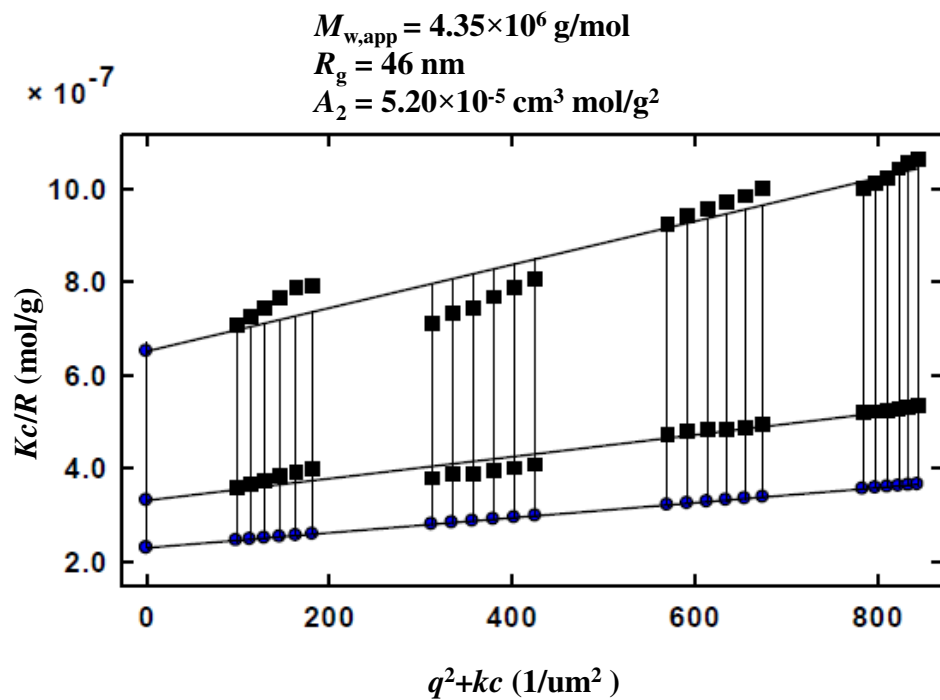


Figure B-1. Zimm plot for $[\text{PS}_{50}\text{-PVP}_{50}]_{26}$ in toluene, a selective solvent for the inner PS block. Properties determined from the extrapolations to zero scattering angle, $q^2 = 0$, and to zero concentration, $c = 0$, are set above the Zimm plot.

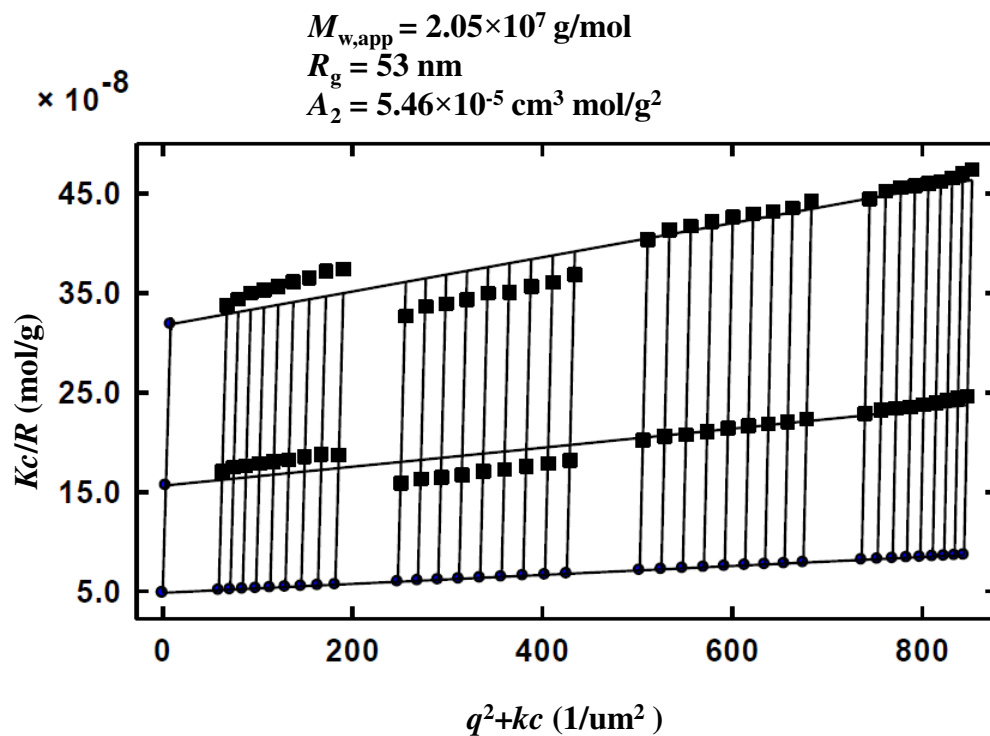


Figure B-2. Zimm plot for $[\text{PS}_{102.5}\text{-PVP}_{20.5}]_{26}$ in toluene, a selective solvent for the inner PS block. Properties determined from the extrapolations to zero scattering angle, $q^2 = 0$, and to zero concentration, $c = 0$, are set above the Zimm plot.

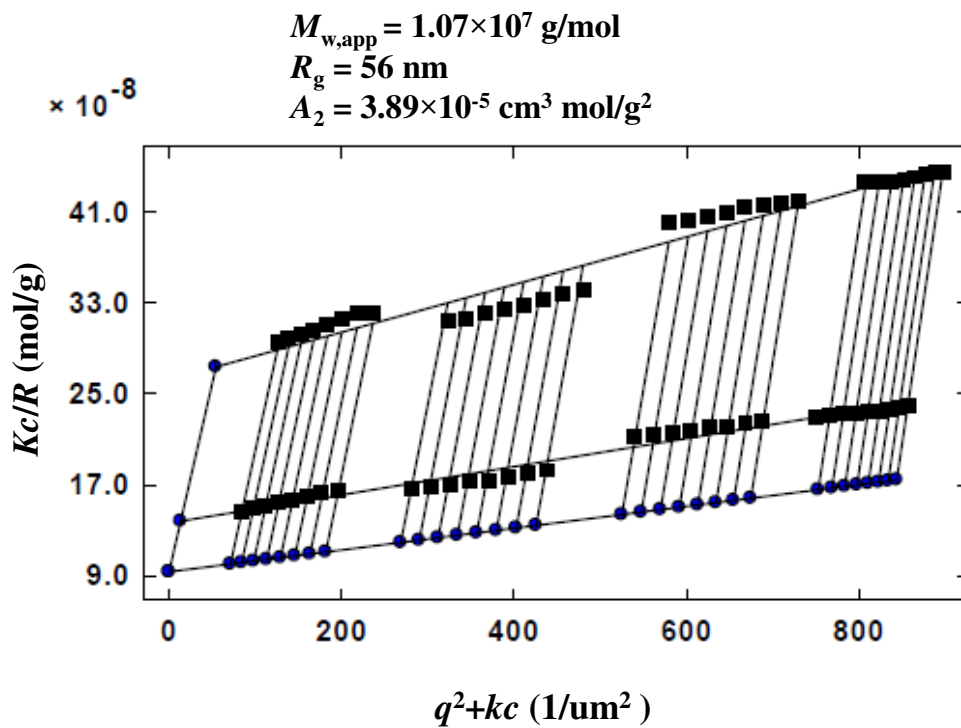


Figure B-3. Zimm plot for $[\text{PS}_{53.8}\text{-PVP}_{53.8}]_{40}$ in toluene, a selective solvent for the inner PS block. Properties determined from the extrapolations to zero scattering angle, $q^2 = 0$, and to zero concentration, $c = 0$, are set above the Zimm plot.

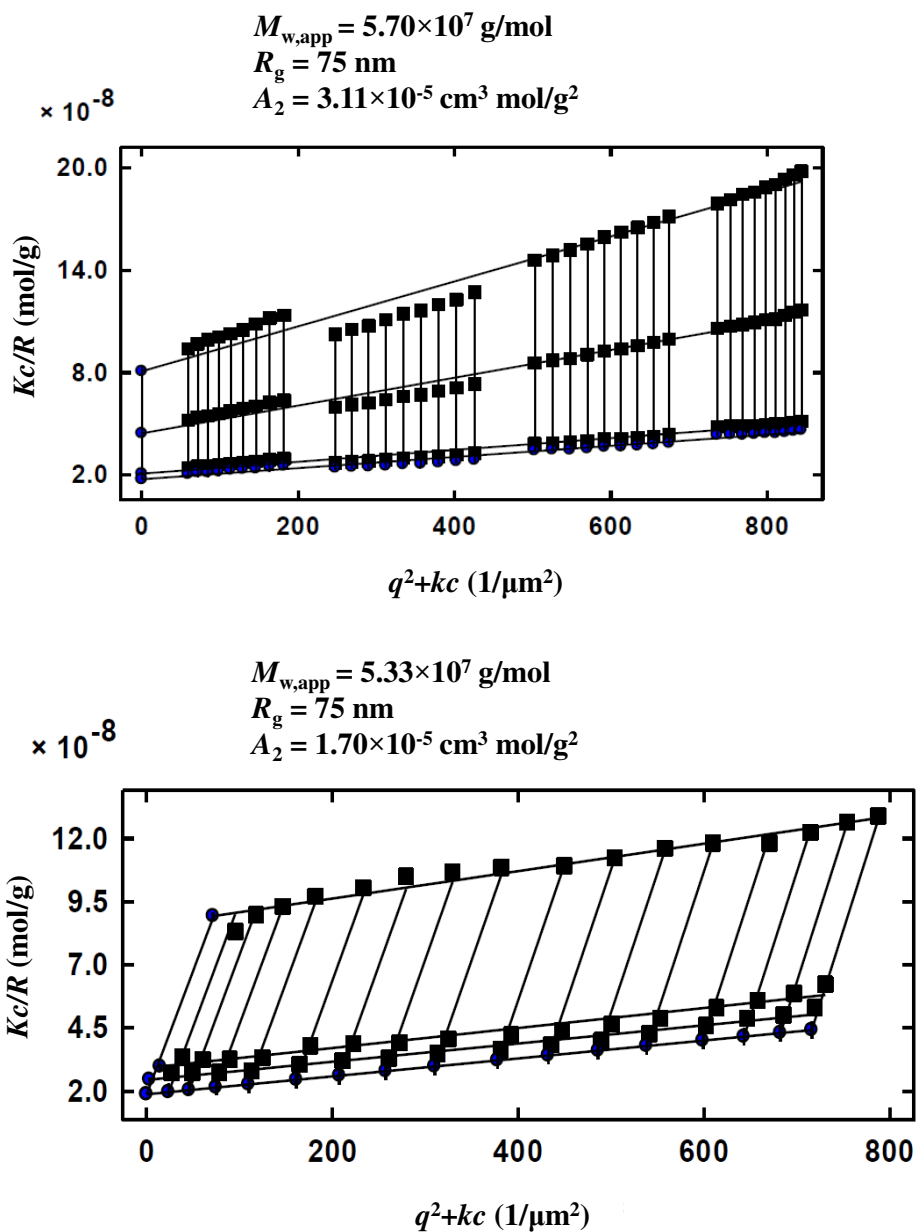


Figure B-4. Zimm plot for sample $[\text{PS}_{106.3}\text{-PVP}_{21.3}]_{40}$ in toluene, a selective solvent for the inner block (top), and THF a non-selective solvent (bottom), with results from the extrapolation to zero scattering angle, $q^2 = 0$, and zero concentration, $c = 0$, are set above the Zimm plot.

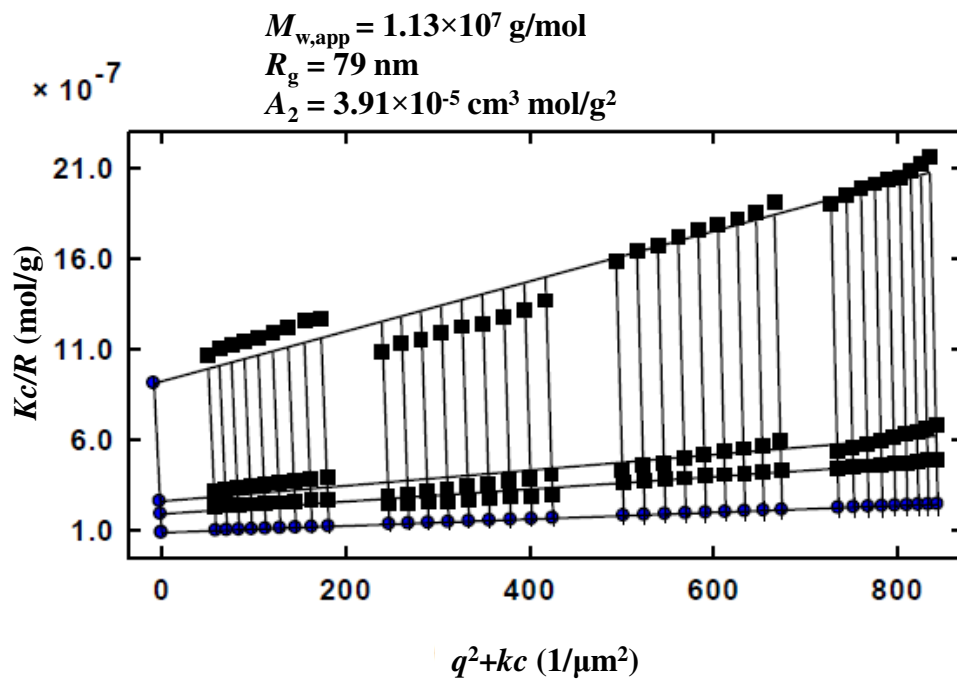


Figure B-5. Zimm plot for $[\text{PS}_{108}\text{-PVP}_{12}]_{40}$ in toluene, a selective solvent for the inner PS block. Properties determined from the extrapolations to zero scattering angle, $q^2 = 0$, and to zero concentration, $c = 0$, are set above the Zimm plot.

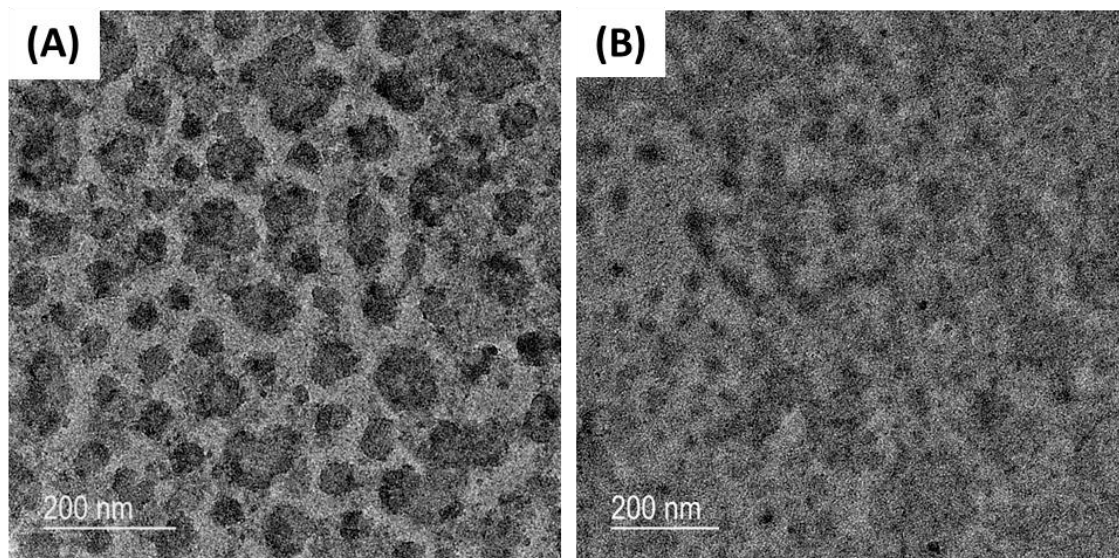
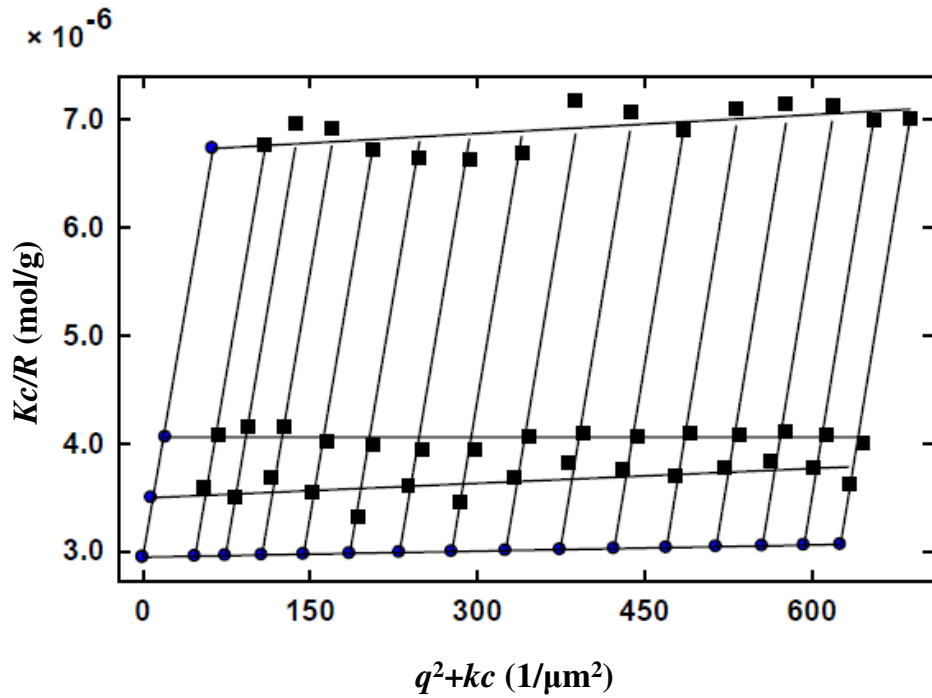


Figure B-6. These two images show a comparison of the morphology of the 40-arm star $[\text{PS}_{53.8}\text{-PVP}_{53.8}]_{40}$ from THF solution (a thermodynamically good solvent for both blocks) obtained from two different staining techniques. (A) TEM image of the 40-arm star $[\text{PS}_{53.8}\text{-PVP}_{53.8}]_{40}$ drop cast from a THF solution with both PS and PVP blocks stained with RuO_4 . Here, RuO_4 stains the double bonds in the PS and PVP blocks allowing the entire structure on the copper supported carbon film TEM grid to be imaged. (B) TEM image of the 40-arm star $[\text{PS}_{53.8}\text{-PVP}_{53.8}]_{40}$ drop cast from THF solution with only the PVP blocks stained by iodine vapor.

Appendix C - Chapter 5: Effects of Sequence and Composition on the Self-assembly of Poly(lactic acid)-Poly(ethylene glycol) Bottlebrush Copolymers



$$M_w(c) = 3.397 \times 10^5 \text{ g/mol } (\pm 4.78\%) \quad M_w(q^2) = 3.397 \times 10^5 \text{ g/mol } (\pm 1.56\%)$$

$$A_2 = 2.202 \times 10^{-4} \text{ mol cm}^3/\text{g}^2 (\pm 6.11\%)$$

$$R_g = 14.0 \text{ nm } (\pm 32.1\%)$$

Figure C-1. Zimm plot produced from SLS measurements on sample g -[PLA₄₁- r -PEG₅₉] in DMF, a non-selective good solvent, at three different concentrations ($c = 1.0, 3.0,$ and 9.0 mg/mL). Set below the plot are results from the extrapolation to zero scattering angle, $q^2 = 0$, and zero concentration, $c = 0$. $M_w(c)$ is the molecular weight that is calculated from extrapolation to $c = 0$ and $M_w(q^2)$ is the molecular weight that is calculated from the extrapolation to $q^2 = 0$. Concentrations are nominal values.

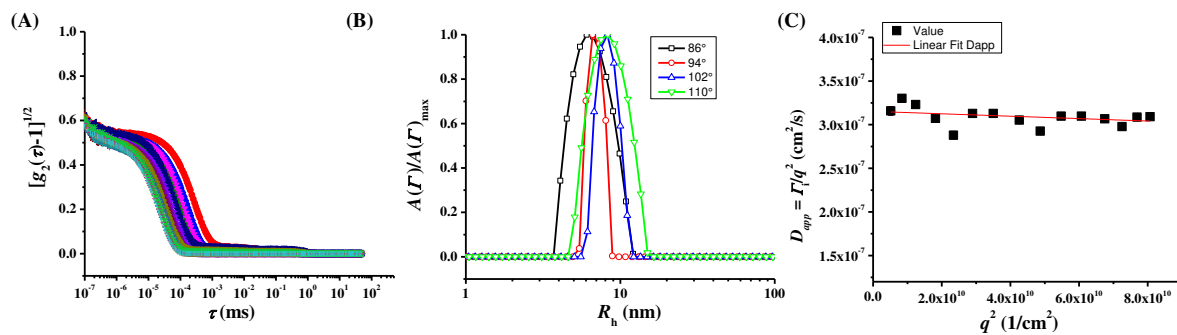
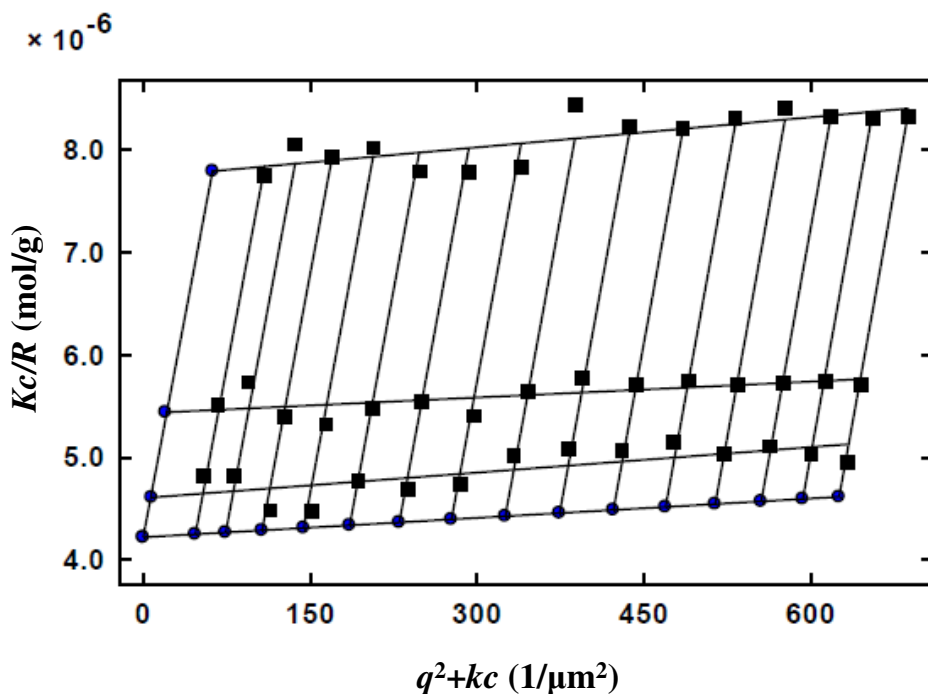


Figure C-2. (A) Normalized light intensity autocorrelation function and (B) normalized amplitude distribution of decay rates for g -[PLA₄₁- r -PEG₅₉] in DMF at $c = 9.0$ mg/mL. (C) angularly-dependent characteristic decay rate, Γ , for g -[PLA₄₁- r -PEG₅₉] in DMF at $c = 9.0$ mg/mL, plotted as Γ/q^2 versus q^2 . Extrapolating the best fit line through the data to $q^2 = 0$ yields the z -average apparent diffusion coefficient, D_{app} . The numerical value of D_{app} is then substituted into the Stokes-Einstein equation to calculate $R_h = 9.0$ nm. Concentrations are nominal values.



$$M_w(c) = 2.368 \times 10^5 \text{ g/mol } (\pm 1.74 \%) \quad M_w(q^2) = 2.368 \times 10^5 \text{ g/mol } (\pm 1.0 \%)$$

$$A_2 = 2.074 \times 10^{-4} \text{ mol cm}^3/\text{g}^2 \text{ } (\pm 3.35 \%)$$

$$R_g = 21.0 \text{ nm } (\pm 1.0 \%)$$

Figure C-3. (A) Zimm plot produced from SLS measurements on sample g -[PLA₁₃- r -PEG₈₇] in DMF, a non-selective good solvent, at three different concentrations ($c = 1.0, 3.0,$ and 9.0 mg/mL). Set below the plot are results from the extrapolation to zero scattering angle, $q^2 = 0$, and zero concentration, $c = 0$. $M_w(c)$ is the molecular weight that is calculated from extrapolation to $c = 0$ and $M_w(q^2)$ is the molecular weight that is calculated from the extrapolation to $q^2 = 0$. Concentrations are nominal values.

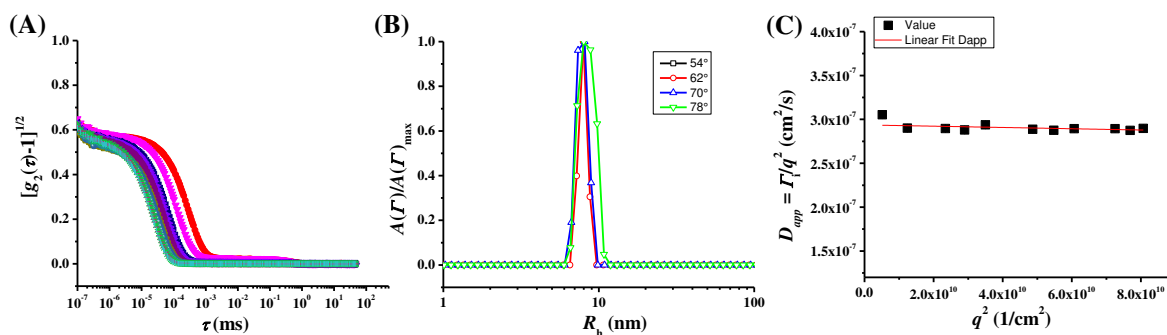
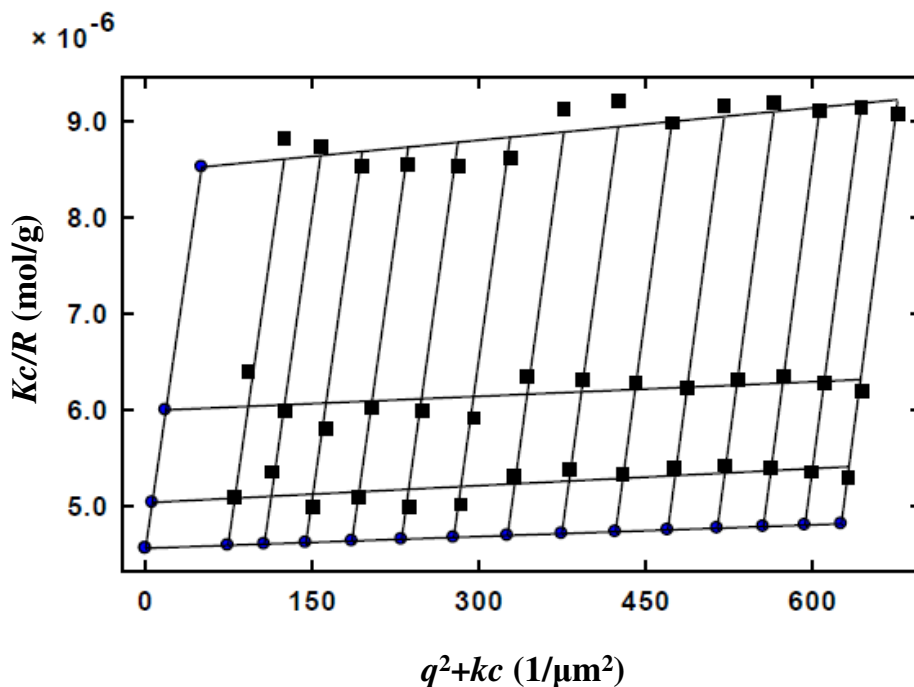


Figure C-4. (A) Normalized light intensity autocorrelation function and (B) normalized amplitude distribution of decay rates for g -[PLA₁₃- r -PEG₈₇] in DMF at $c = 9.0$ mg/mL. (C) angularly-dependent characteristic decay rate, Γ , for g -[PLA₁₃- r -PEG₈₇] in DMF at $c = 9.0$ mg/mL, plotted as Γ/q^2 versus q^2 . Extrapolating the best fit line through the data to $q^2 = 0$ yields the z -average apparent diffusion coefficient, D_{app} . The numerical value of D_{app} is then substituted into the Stokes-Einstein equation to calculate $R_h = 9.0$ nm. Concentrations are nominal values.



$$M_w(c) = 2.192 \times 10^5 \text{ g/mol } (\pm 0.52\%) \quad M_w(q^2) = 2.192 \times 10^5 \text{ g/mol } (\pm 1.0 \%)$$

$$A_2 = 2.292 \times 10^{-4} \text{ mol cm}^3/\text{g}^2 \text{ } (\pm 6.11 \%)$$

$$R_g = 16.0 \text{ nm } (\pm 1.0 \%)$$

Figure C-5. Zimm plot produced from SLS measurements on sample g -[PLA₇- r -PEG₉₃] in DMF, a non-selective good solvent, at three different concentrations ($c = 1.0, 3.0,$ and 9.0 mg/mL). Set below the plot are results from the extrapolation to zero scattering angle, $q^2 = 0$, and zero concentration, $c = 0$. $M_w(c)$ is the molecular weight that is calculated from extrapolation to $c = 0$ and $M_w(q^2)$ is the molecular weight that is calculated from the extrapolation to $q^2 = 0$. Concentrations are nominal values.

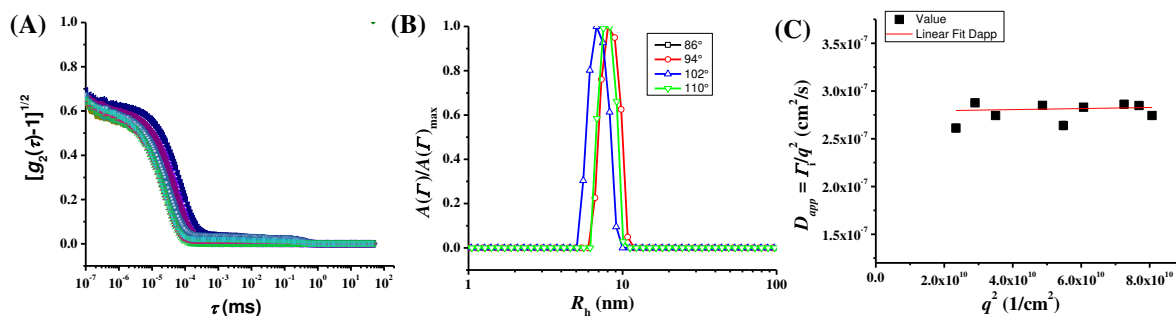


Figure C-6. (A) Normalized light intensity autocorrelation function and (B) normalized amplitude distribution of decay rates for g -[PLA₇- r -PEG₉₃] in DMF at $c = 9.0$ mg/mL. (C) angularly-dependent characteristic decay rate, Γ , for g -[PLA₇- r -PEG₉₃] in DMF at $c = 9.0$ mg/mL, plotted as Γ/q^2 versus q^2 . Extrapolating the best fit line through the data to $q^2 = 0$ yields the z -average apparent diffusion coefficient, D_{app} . The numerical value of D_{app} is then substituted into the Stokes-Einstein equation to calculate $R_h = 9.0$ nm. Concentrations are nominal values.

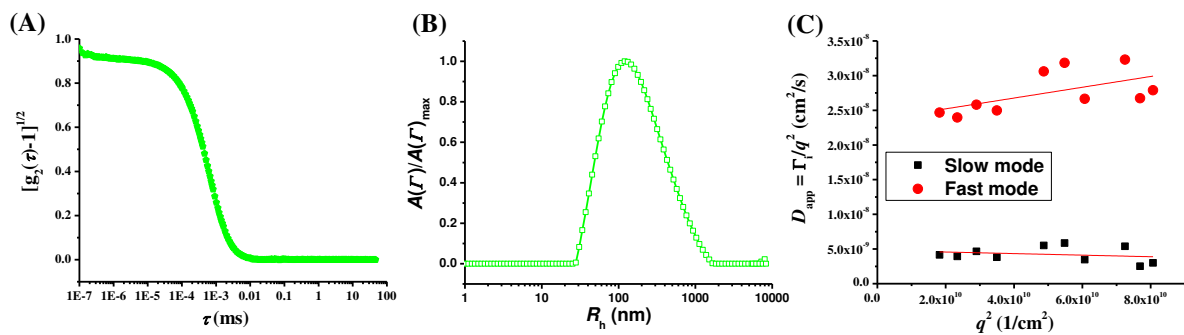


Figure C-7. (A) Normalized light intensity autocorrelation function and (B) normalized amplitude distribution of decay rates for g -[PLA₃₆- b -PEG₆₄] in aqueous solution at $c = 0.1$ mg/mL. (C) angularly-dependent characteristic decay rate, Γ , for g -[PLA₃₆- b -PEG₆₄] in aqueous solution at $c = 0.1$ mg/mL, plotted as Γ/q^2 versus q^2 . Extrapolating the best fit line through the data to $q^2 = 0$ yields the z -average apparent diffusion coefficient, D_{app} . Concentrations are nominal values.

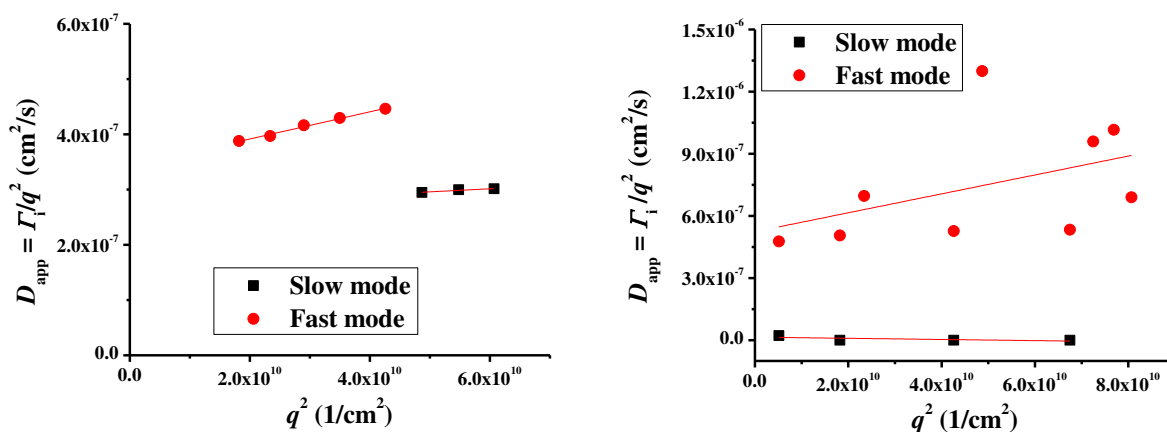


Figure C-8. Plots showing the angular dependence of the characteristic decay rates, Γ , cast as Γ/q^2 versus q^2 . (A) g -[PLA₁₃- r -PEG₈₇] in MeOH at $c = 1.0$ mg/mL. D_{app} is obtained by extrapolating the best fit lines through the data to $q^2 = 0$. From those intercepts, Stokes-Einstein relation gives $R_{h,slow\ mode} = 12$ nm, and $R_{h,fast\ mode} = 150$ nm. (B) g -[PLA₁₃- r -PEG₈₇] in MeOH at $c = 2.0$ mg/mL. D_{app} is obtained by extrapolating the best fit line through the data to $q^2 = 0$, and the resulting D_{app} values give $R_{h,fast\ mode} = 8.0$ nm, and $R_{h,slow\ mode} = 270$ nm. Concentrations are nominal values. As explained in Chapter 5 (Section 5.4.2), the need to select only certain scattering angles to obtain R_h values for the slow mode that are (nearly) consistent with the size range suggested by the amplitude distribution function make it difficult to conclude that the second (slow) mode is real.

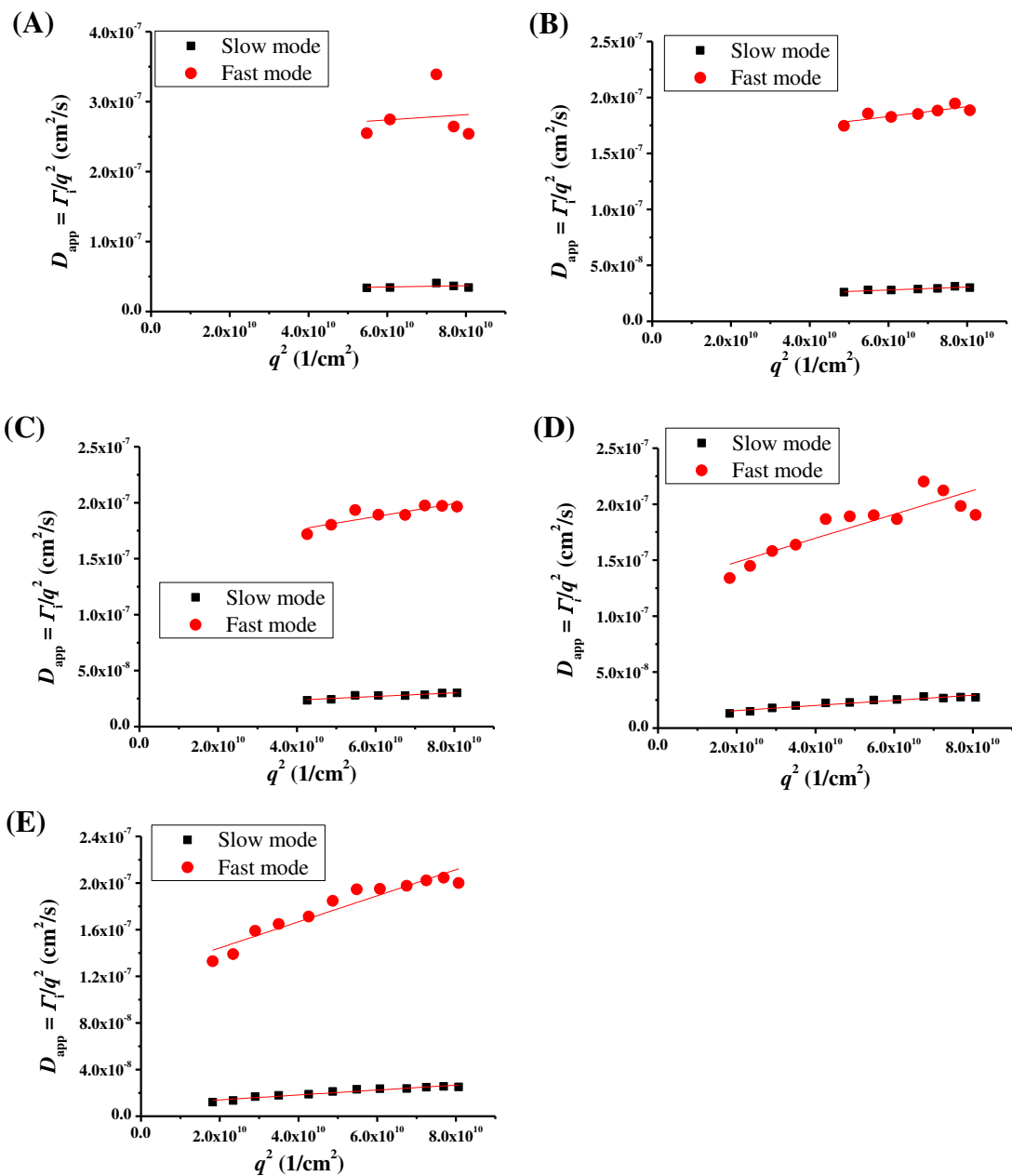


Figure C-9. Plots showing the angular dependence of the characteristic decay rates, Γ , cast as Γ/q^2 versus q^2 for g -[PLA₁₃- r -PEG₈₇] in aqueous solution at (A) $c = 0.1$ mg/mL, (B) $c = 0.5$ mg/mL, (C) $c = 1.0$ mg/mL (D) $c = 5.0$ mg/mL, and (E) $c = 10.0$ mg/mL. Concentrations are nominal values.

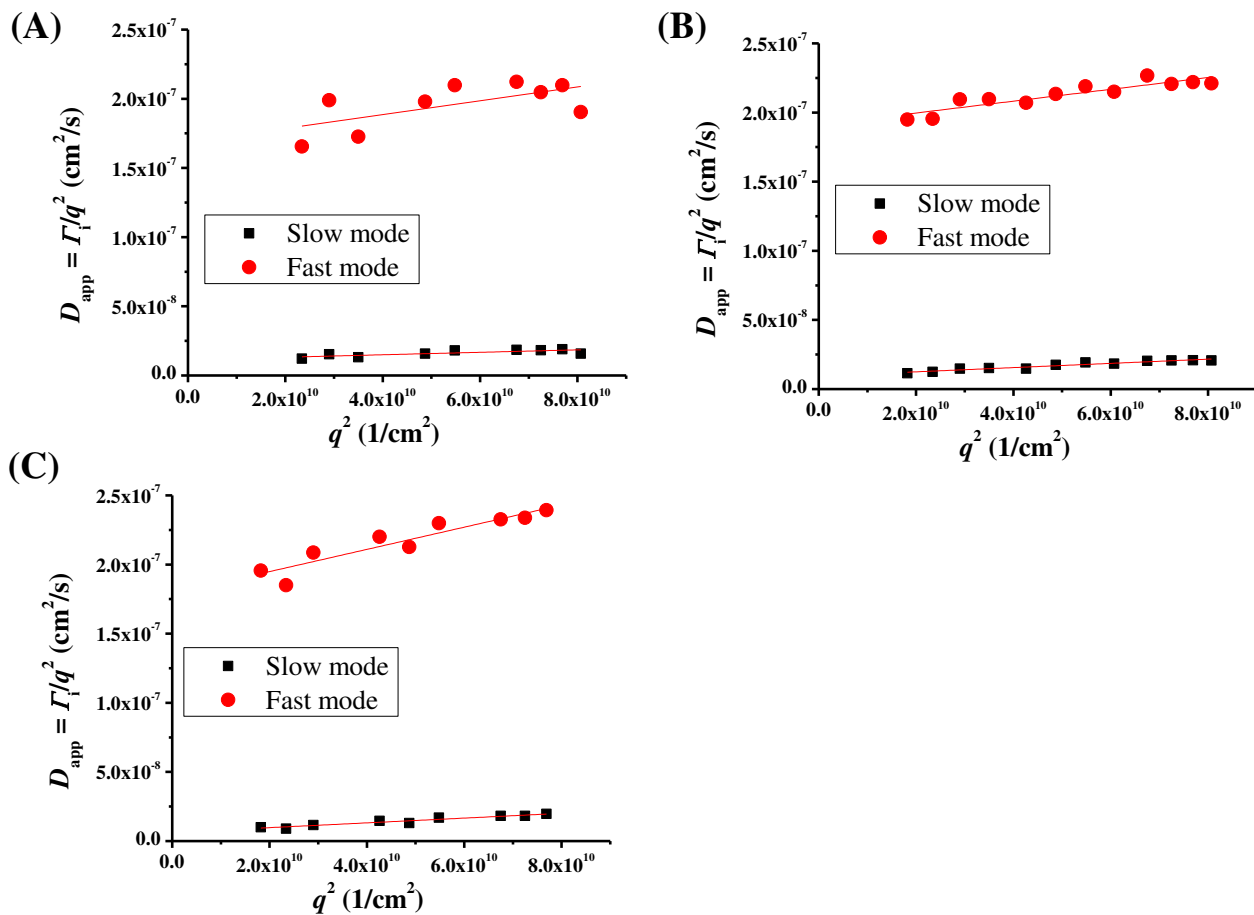


Figure C-10. Plots showing the angular dependence of the characteristic decay rates, Γ , cast as Γ/q^2 versus q^2 for g -[PLA₇- r -PEG₉₃] in aqueous solution at (A) $c = 1.0$ mg/mL, (B) $c = 5.0$ mg/mL, and (C) $c = 10.0$ mg/mL. Concentrations are nominal values.

Vita

Jesse Lawrence Davis was born and raised on the island of Trinidad and Tobago. Jesse attended Saint Joseph Boys' R.C. Elementary School, and after scoring well on the Secondary Entrance Assessment exam, he was placed at San Juan Government Secondary School. Directly following this, he enrolled at Saint Augustine Senior Secondary Comprehensive School where, his studies concentrated in Chemistry and Geography in preparation for the General Certificate of Education Advanced Level Examinations. In 2006 he earned a soccer scholarship to attend South Georgia College in Douglas, Georgia. He transferred to Georgia Southwestern State University in Americus, Georgia, where he earned a B.S. in Chemistry. He came to the University of Tennessee in 2011 and joined the research group of Prof. S. Michael Kilbey II where his research has focused on self-assembly of architecturally complex amphiphilic block copolymers and their binary mixtures.